The Assembly History of Disc Galaxies

Sarah Holmes Miller

New College

University of Oxford

A thesis submitted for the degree of

Doctor of Philosophy

Trinity Term 2012

I dedicate this thesis to
my loving and supportive parents,
Barbara and Amp;
my dear grandparents,
Barbara, Ruth, William, and Amp;
my wonderful brother, Amp William;
and to the love of my life,
my husband, Oliver.

Acknowledgements

I thank the Rhodes Trust, the British Federation of Women Graduates, New College, the University of Oxford and its sub-department of Astrophysics, and the California Institute of Technology for supporting this work.

I thank also K. Bundy, R. Ellis, T. Treu, S. Moran, N. Miller, G. Mikelsons, and K. Chiu for organisation of the initial DEIMOS dataset of this project. I thank P. Capak for generously procuring his SSA22 photometry catalog, A. Benson for preliminary results from the GALACTICUS model to compare to observations, and C. Peng for supplying GALFIT. I thank A. B. Newman for the reduction of the LRIS dataset, as well as C. Bridge and K. Bundy for a subset of its observation.

I acknowledge useful discussions with R. Allen, G. Besla, A. Brooks, J. Bullock, A. Bunker, M. Bureau, B. Catinella, C. Conroy, R. Davies, V. Debattista, A. Dutton, J. R. Fisher, F. Fraternalli, H. Flores, R. Giovanelli, N. Gnedin, F. Governato, J. Greene, J. Gunn, F. Hammer, M. Haynes, L. Hernquist, R. Hlozek, S. Jogee, S. Kannapan, S. Kassin, A. Kravtsov, C. Lackner, A. Loeb, B. Madore, S. McGaugh, L. Miller, M. Puech, J. Read, R. Reyes, J. Silk, E. Shaya, J. Simon, M. Strauss, P. Tissera, R. B. Tully, M. Verheijen, R. Wechsler, B. Weiner, and B. Willman at various points over the course of this work.

I give a special thanks to co-authors M. Sullivan, K. Bundy, R. S. Ellis, T. Treu, and A. B. Newman for significant discussions on, and dedication to, this project, highlighting the substantial effort of my supervisors M. Sullivan and R. S. Ellis.

The spectroscopic data was secured with the W.M. Keck Observatory on Mauna Kea, and I thank the observatory staff for their dedication and support. I acknowledge the cultural role and reverence that the summit of Mauna Kea has always had with the indigenous Hawaiian community, and the astronomical community is most fortunate to have the opportunity to conduct observations from this mountain.

More personally, I must thank my amazing friends and loving family for their endless support. I could not have done this without them. They are my all, and I owe them everything.

Finally, I wish to thank the universe, for beautifully unravelling itself to the amusement of bipedal primates on the planet Earth (and whomever else may look out towards its vast banks of hydrogen nuclei and their fiery furnaces aglow). We are after all a small part of that universe, and in studying the stars, we hope to better understand ourselves.

Statement of Originality

The analysis from section 'Stellar mass estimates' (§3.3) was not lead by the author of this thesis, but by co-author[1][2] Kevin Bundy, with software he developed for his thesis[3]. All other analyses have been conducted by the author.

[1]from Miller, S. H., Ellis, R. S., Sullivan, M., Bundy, K., Newman, D., & Treu, T., 2012, *The Astrophysical Journal*, 753, 74: 'The Assembly History of Disk Galaxies: II - Probing the Emerging Tully-Fisher Relation Scientific to $z \sim 1.7$'

[2]from Miller, S. H., Bundy, K., Sullivan, M., Ellis, R. S., & Treu, T., 2011, *The Astrophysical Journal*, 741, 115: 'The Assembly History of Disk Galaxies: I. - The Tully-Fisher Relation to $z \sim 1.3$ from Deep Exposures with DEIMOS'

[3]Bundy, Kevin 2006 'The mass assembly history of field galaxies.' Dissertation (Ph.D.), California Institute of Technology.

Abstract

We present new measures of the rotation curves of disc galaxies from $z\sim0.2$ to $z\sim1.7$, using deep exposures from both DEIMOS and LRIS spectrographs on the Keck telescopes in combination with multi-band imaging from the Hubble Space Telescope. We do this with a new modelling code, CURVATION, which has been optimised to extract the rotation velocity measurements from galaxies at intermediate and high redshift. To this end, we conduct a bulge-to-disc decomposition to allow us to de-project observed velocities to extract a model of the intrinsic rotation curve. We demonstrate the improved accuracy and precision of these measurements via a number of tests, but primarily in recovering an intrinsic scatter of the high-redshift Tully-Fisher relation which is similar to that found locally. We show for the first time that the stellar mass Tully-Fisher relation is tightly in place at $z \sim 1$, the normalisation of which has evolved less than 0.02 ± 0.02 dex in stellar mass from $z \sim 1.7$ to $z \sim 0.2$. We do however see evidence for evolution in classic B-band Tully-Fisher relation, which is brighter at $z \sim 1$ by 0.85 ± 0.28 magnitudes than that at $z \sim 0.3$. This trend is consistent with what was previously known about the evolving star-formation rates of disc galaxies. We then explore the potential drivers of these trends in the Tully-Fisher relation by estimating the baryonic and dark matter content of our galaxies. We also discover a surprising trend in the bulgeless disc galaxies at high redshift, which may be evolving differently from other rotationally supported galaxies. In the context of work which has been conducted at $z \sim 2$, we discuss our results of a stellar mass Tully-Fisher relation which is strikingly similar over two-thirds of the age of the Universe.

Contents

List of Figures

List of Tables

Basic Motivation

This prologue is written to motivate the work of this thesis at the most fundamental level, as we attempt to improve our physical understanding of the Universe. It is written in language which is accessible to anyone who has studied physics at A-levels in the UK or the equivalent (e.g., high-school) for the rest of the English-speaking world.

How does the matter in our universe evolve and assemble over time? Before we can attempt to address this question, we must first determine a reliable method of identifying mass in the universe, whether it is visible or not. Preferable to just one method, we rather seek several independent methods that give consistent results.

As the galaxies of stars, dust, and gas, like our own Milky Way galaxy, are the dominant matter assembly points when we look deep into the night sky, they are our reasonable starting point of inquiry. Although greater structures of galaxy clusters make up even larger filament-like superstructures, individual galaxies typify the building blocks of the cosmic distribution of mass. The more we understand the physics and make-up of individual galaxies, the more we understand the universe at large.

How do we measure the mass of a galaxy? One way is to observe the galaxy with a variety of filters and use the combinations of luminosities measured to deduce how much mass must be emitting the light. For this we must have independent evidence for how many of which stars emit light at which frequencies

in a galaxy. The literature is rich in studies of this nature in the Milky Way as well as a few galaxies nearest to us. For a given balance of luminosities from the observations in different filters of a galaxy, we can work out a probability distribution of the likely stellar populations and thus a distribution of likely stellar masses. The geometry of the galaxy must also be taken under consideration, to account for any affect of an inclined disc, and we also need to account for any light that has been hidden by opaque material, like dust and dense gas.

But what if not all mass emits light?

Another method we have at our disposal uses our theoretical understanding of gravity to calculate how much mass should be in a particular galaxy based on observable properties. For a rotationally-supported galaxy, or a disc galaxy, the galaxy's mass will determine the speed at which the matter in the disc travels around the centre, if the galaxy is roughly in equilibrium.

In the most simple toy model of a galaxy's gravitational field, we can drop a trace particle into a spherically symmetric distribution of mass which is spinning. This is probably not a good approximation for many types of galaxies which are not spherically symmetric, but this is the traditional form of the calculation made, which we address in more detail in this thesis. For a particle of mass m, velocity v, and circular orbit radius r, the centripetal force needed to describe the disc galaxy motion is:

$$F_c = \frac{mv^2}{r}. \tag{1}$$

The force provided by gravity is:

$$F_g = -\frac{1}{2}\frac{GM(r)m}{r^2}, \tag{2}$$

where M(r) is the total mass inside radius r. If the galaxy is roughly in equilibrium, then the potential energy in a system (from the gravitational force in Eq. 2) should be equal to twice the kinetic energy (which can be calculated using Eq. 1). All together this means that:

$$M(r) \propto \frac{v_c^2(r)}{r} \tag{3}$$

for the total mass of the galaxy inside radius r, where the circular velocity of the mass at r is v_c.

Another way to think about this concept is by charting of rotational velocity as a function of position from the galactic centre, which is called a rotation curve. In describing a rotation curve, we often reference the change in velocity from the lowest to highest amplitude along the length of the galaxy (ΔV), or the maximum velocity reached with respect to the its centre (V_{max}); $2V_{max}$ should equal ΔV if properly calibrated.

A curious feature of rotation curves is that at large radii, the velocity with respect to position remains *flat*. While the luminosity curve of the galaxy falls off exponentially with respect to radius, the velocity stays constant (or close to it), indicating a spherically symmetric distribution of mass, whereas in a simple Keplerian gravitational potential (how we calculate the orbits of the planets), the velocity should fall off $\propto \frac{1}{\sqrt{r}}$.

Where then is the mass needed to keep the rotation curves at large r flat while surface brightness dies out? The answer may lie in a spherically distributed halo of dark matter, making up most of the galactic mass.

It turns out that there is a tight relation of the galaxies in the Universe, between their maximal rotation speed and the absolute magnitude or luminosity they emit, called the Tully-Fisher relation:

$$L \propto (V_{max})^{\alpha}. \tag{4}$$

where α tends to be measured at about 4.

By the implied relation between the mass and luminosity of a galaxy, the Tully-Fisher relation may be used to further understand how much mass is distributed throughout the galaxy and to study the evolution of galaxies, similarly to the Hertzsprung-Russell diagram for stars. The Tully-Fisher relation can also be used as a distance indicator.

The idea is that the relation could be calibrated for galaxies of known V_{max} and luminosity L in order to get β and C in Eq. 1.1. For galaxies of unknown

distance, you could measure V_{max} by observing the rotation curve, and then deduce L from the previously calibrated relation. By measuring the actual flux f of the galaxy of unknown distance, where:

$$f = \frac{L}{4\pi d^2}, \tag{5}$$

or by measuring the apparent magnitude m, where:

$$m - M = 5\log(\frac{d}{10pc}), \tag{6}$$

one could then obtain a distance d to the given galaxy.

Ultimately we would like to determine the true rotation curves of galaxies by understanding their mass distribution and dynamics at an unprecedented level. By doing this over cosmic distances with unmatched depth in our observations and by obtaining accurate measurements of the luminosity of these galaxies, we will further constrain the Tully-Fisher relation on a path of better understanding the evolution of matter, both baryonic and dark, through the age of the universe.

Chapter 1

Introduction

Morton S. Roberts (1969) posed two questions in his article on the 'Integral Properties of Spiral and Irregular Galaxies':

1. Why are there different types of galaxies?

2. What is the evolutionary history of a galaxy?

Research in galaxy formation and evolution over the past decades has largely sought to answer these questions. Significant progress has been made in the last 15 years in observationally charting the history of cosmic star formation (Hopkins & Beacom, 2006; Ellis, 2008). Attention has now shifted to interpreting the stellar mass assembly history of galaxies (e.g., Bundy et al., 2006) in a framework whereby cold dark matter (CDM) halos merge under gravitational instability (White & Rees, 1978). With the established presence of an accelerated expansion force of the universe in Λ (Riess et al., 1998; Perlmutter et al., 1999), a coherent theory of galaxy assembly is emerging within the concordance cosmology framework (ΛCDM).

A major challenge for ΛCDM structure formation lies in understanding how the baryonic components of galaxies assemble within dark matter halos. Although baryons represent only one-sixth of the gravitating matter in WMAP cosmology (Spergel et al., 2007; Seljak et al., 2005), their dissipative properties suggest they dominate the inner regions of luminous galaxies (Blumenthal et al., 1986). Determining the interplay between dark matter and baryons is

critical for predicting the evolution of density profiles, substructure, shapes, and angular momentum of galaxies (Governato et al., 2007; Shlosman, 2009). One of the most significant challenges is reproducing the detailed characteristics of rotationally supported disc galaxies which represent the dominant fraction of present-day luminous systems (Ellis & Silk, 2009).

Early N-body simulations as well as semi-analytic models produced galaxies that rotate too fast at a given luminosity (van den Bosch, 2000; Mo & Mao, 2000; Eke et al., 2001; Benson et al., 2003; Dutton et al., 2007). Caused by a transfer of angular momentum from baryons to the dark matter halo, this deficiency has since been mitigated by improved resolution, as well as the introduction of feedback (Steinmetz & Navarro, 1999), e.g. from supernovae (Governato et al., 2007; Piontek & Steinmetz, 2011; Governato et al., 2010; Pontzen & Governato, 2012). However, reproducing the absolute zero point of the various scaling relation has remained problematic.

Observational efforts in this challenge have focused on the Tully-Fisher (TF) relation (Tully & Fisher, 1977) and its past evolution, which provides an essential benchmark for verifying theoretical models. We review the discovery and progress of this important relation in the following section (§1.1), and explain its unique features in the context of other galaxy scaling relations (§1.2). We then review work that has been done in constraining the evolution of the TF relation (§1.3), before we describe the plan for this thesis (§1.4).

1.1 The Tully-Fisher relation

In 1977, Brent Tully and J. Richard Fisher published a sample of ten nearby spirals along with galaxies from the Virgo and Ursa Major clusters to calibrate a relation between the absolute magnitude (M) and the total change in rotation velocity (ΔV) across spiral galaxies:

$$M = C - \beta \log \Delta V, \tag{1.1}$$

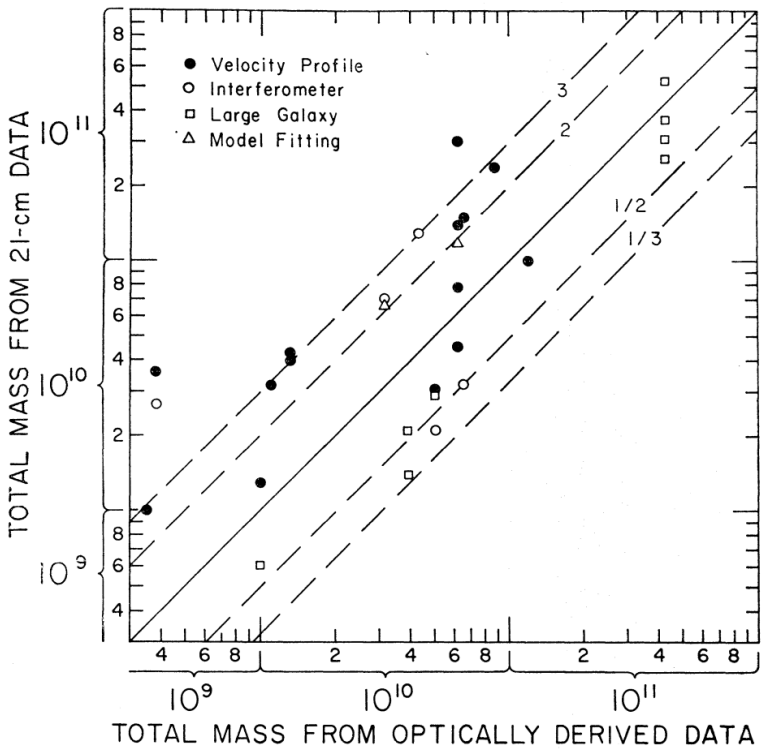

Figure 1.1 **From Roberts (1969):** We reproduce an early 'Tully-Fisher-like' figure before the Tully-Fisher paper. The rotational velocity axis is given in the ordinate, and the luminosity based component in the abscissa. The solid line shows the exact 1:1 correspondence between masses, and the dashed lines show factors of 2 and 3 in the mass determination.

where C is a constant (the zero-point), and β is the slope of the relation. Correlations between the total mass (via distance-independent HI profile widths) and luminosity of rotationally-supported galaxies had been studied by, *e.g.*, Balkowski et al. (1974); Rogstad & Shostak (1972); Shostak (1975), and even explored as a distance tool by, *e.g.*, Dieter (1962b,a); Roberts (1962); Heidmann (1969); Allen (1970). We reproduce an early demonstration of this relation by Roberts (1969) in Fig. 1.1.

The promise of the Tully and Fisher paper was the extent to which they were able to calibrate the relation— using both local galaxies with Cepheid variables (Leavitt, 1908) to determine absolute magnitudes, as well as galaxies known to be at relatively similar distance, *i.e.* clusters.

With the striking tightness of the intrinsic relation revealed by the calibra-

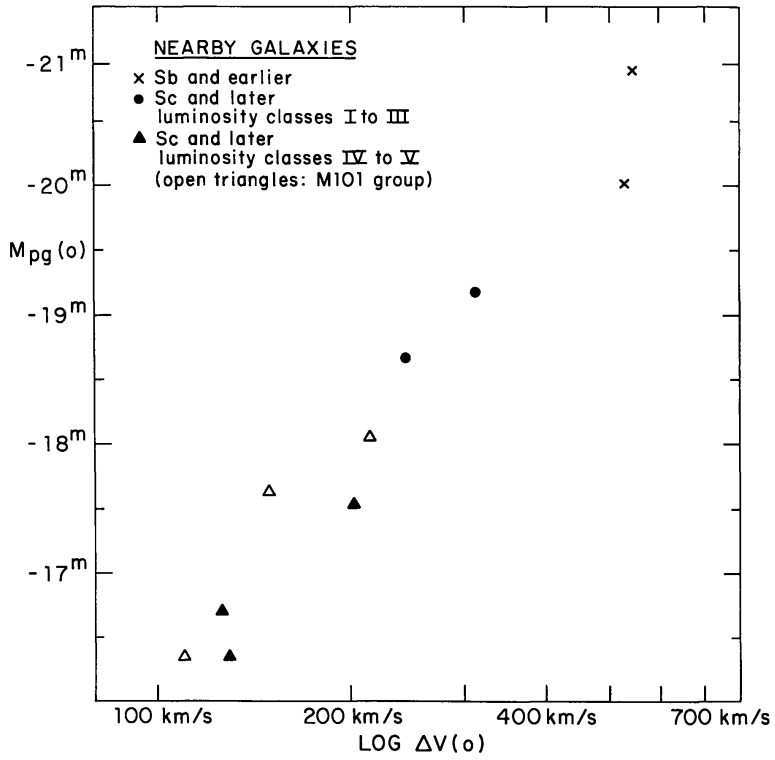

Figure 1.2 **From (Tully & Fisher, 1977)**: Reproduction of their absolute magnitude verses the global profile width for local galaxies, where crosses are the M31 and M81 spirals, dots are M33 and NGC 2403, filled triangles are smaller M81-group members, and finally open triangles are smaller M101-group members.

tion of Tully & Fisher (see Fig. 1.2), emphasis was necessarily placed on the sensitivity of the relation (in Eq. 1.1: C, β, & scatter— root mean square or rms) to the method of velocity extraction and to correction factors for effects, *e.g.*, inclination, dust extinction, and internal absorption.

After determining the correlated distance modulus for both Virgo and Ursa Major cluster galaxies, their detail-oriented calibration allowed them to determine the Hubble constant as $H_0 = 80$ km/s/Mpc, which was the closest estimate to the presently accepted value at the time. In fact, the Tully-Fisher (TF) relation soon became regarded as the most robust distance indicator at 'intermediate' distances, beyond the reach of Cepheid variables, but not yet to the Hubble flow (Aaronson et al., 1979).

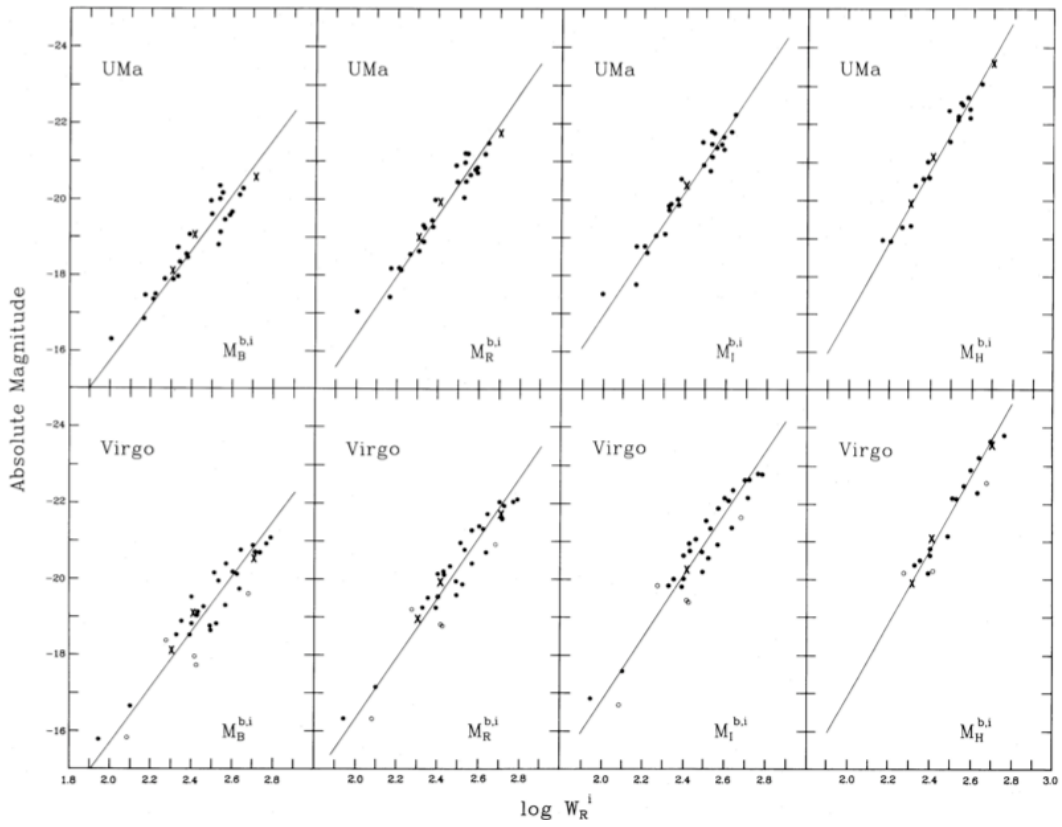

Figure 1.3 **From Pierce & Tully (1988):** Luminosity–linewidth relations on an absolute scale established by the nearby galaxies, M31, NGC 2403, and M33, for both the Ursa Major and Virgo Clusters. The heavy crosses mark the local calibrators; the open circles in the Virgo figures mark the galaxies with distances more than 2 σ from the mean and are excluded from the fit. The fit is the single regression based on minimised residuals in the line widths. I-band data was not obtained for M31 or M33, so only NGC2403 is used in the fit for the I-band.

With improvements in detector technology and the implementation of multicolour CCD photometry to the TF relation, Pierce & Tully (1988) were able to further minimise the dispersion in the TF relation with more accurate absolute magnitudes and inclination measurements. Techniques in Cepheid variable calibration had improved (*e.g.*, Madore et al., 1985; Freedman, 1985), and more precise inclination measurements to de-project the line widths meant that a wider range of galaxies with inclinations as low as 30° could be included in the sample (whereas the original paper could only include galaxies with inclinations

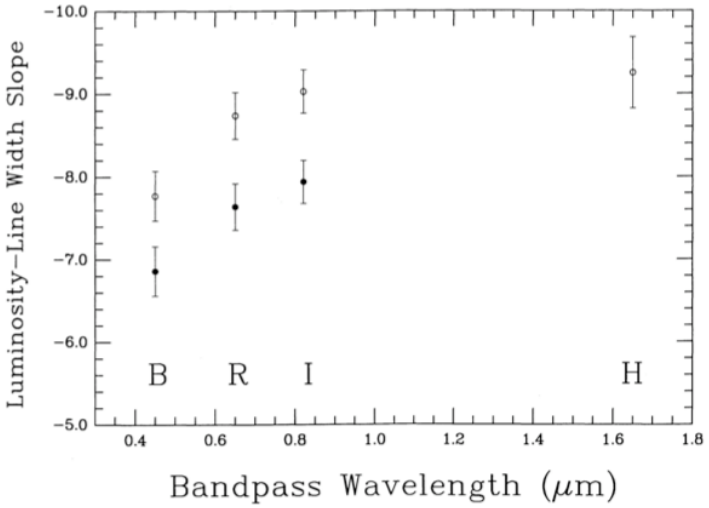

Figure 1.4 **Also from Pierce & Tully (1988):** Shows the dependence of the slope of the luminosity–linewidth relation as a function of wavelength. Solid points are the slopes derived from total or asymptotic magnitudes. Open points are from aperture magnitudes where $\log \frac{A}{D} = -0.5$.

between 45° and 85°).

Examining the relation in different bandpass filters (Fig. 1.3 & Fig. 1.4) revealed the difference in slope in the relation between wavelength regimes of light, and they were the first to see how the scatter of the relation in the R and I bands was less than the B band. They suggested that this was due to variations in the global stellar population of the galaxies at a given total mass, which has been reproduced and confirmed in studies which followed Bell & de Jong (2001); Courteau et al. (2007). They found only a slight indication that morphological-type dependence was present in the TF relation, and suggest that such an effect was only secondary, contrary to previous studies which suggested, without sufficient proof, that morphological-type played a much more prominent role in the relation. Another important implication of this result was that the relation could be applied not only to the cluster environment, but to field galaxies as well.

1.2 The elusive third parameter

With the importance of the TF relation established, attention turned to fully quantifying its scatter and possibly improving upon it with a missing 'third parameter' (*e.g.*, Strauss & Willick, 1995). A significant contribution to this effort was made by Courteau & Rix (1999a), demonstrating the use of TF-relation residuals as estimates to the relative mass contribution of the stellar disc and the dark halo at the peak of the disc rotation. The TF-relation in fact appears to be independent of surface brightness for the highest surface brightness galaxies, which they suggested was due to large quantities of dark matter in the $r < r_{disc}$ portion of disc galaxies (Sprayberry et al., 1995; Zwaan et al., 1995).

In modelling the adiabatic infall of baryonic matter into dark matter halos, TF-relation residuals require a mean value of $V_{disc} \approx 0.6V_{total}$, a result which appears to largely ignore the presence of a bulge and the initial dark matter details of the halo. The only assumptions made are that of adiabatic contraction and the initially rising dark matter rotation curve, ultimately resulting in a flat rotation curve. A continuity is understood between high surface brightness and low surface brightness galaxies, where the latter become increasingly more dark matter dominated, even towards their galactic centres.

The Courteau & Rix (1999a) result, when combined with empirical TF-relations, invalidates the 'maximal disc' theory for most high surface brightness, late-type spirals, a theory which had gained much popularity until this time (*e.g.*, Buchhorn, 1992; Freeman, 1993; Zhao et al., 1995; Kuijken & Dubinski, 1995; Sackett, 1997). From this point, the stellar disc scale radius, r_s, became an important piece of the TF-relation puzzle, and we move beyond this two-parameter relation, to a larger family of 'scaling relations'. Disc formation models seek to successfully reproduce the properties of empirical scaling relations at any wavelength.

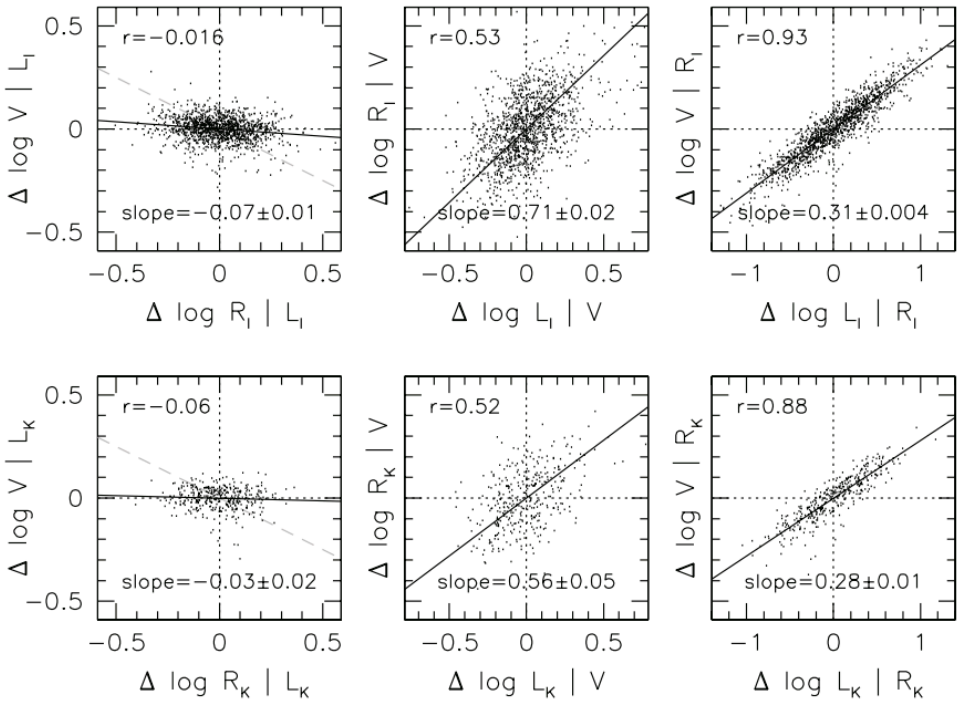

Figure 1.5 **From Courteau et al. (2007):** Correlations between the residuals of the various VLR relations for both I-band (**top**) and K-band (**bottom**). Best-fitting slopes with 1σ uncertainties are given in the bottom of each panel, and the correlation coefficient is given in the top right corner of each panel. The pure disc model prediction is given in the light grey dashed line (slope of -0.5) of the V—L and R—L panels (**left**). Only a weak correlation is shown, not at the predicted level. The significant correlations observed in the **middle** and **right** panels is simply the TF relation in a differential form.

Courteau et al. (2007) collected extensive structural and dynamical parameters ($N \sim 1300$ field and cluster spirals), in both the I-band and K-band using the wealth of data from the 2MASS catalog, in order to further constrain the disc-size(R)-luminosity(L)-velocity(V) scaling relations. A dependence on morphological type, with shallower slopes for later-type discs, especially in the RL-relation, was found. Trends in colour were also found, as well as a quantification of residuals.

Following the surprising independence of the TF relation on surface density, Courteau et al. confirm that the TF residuals do not depend on disc scale radius (see Fig. 1.5). While this study is a significant effort in the constraining

scaling relations with statistical robustness, Courteau et al. concede that further progress must be made with an even larger sample ($N > 1000$), with deep multi-wavelength imaging so that scattering and absorption effects can be minimised (near-IR necessary), high resolution spectroscopy, controlled selection criteria, accurate and homogeneous measurements of structural parameters, as well as accurate measurements of luminous mass (complete with chemical information to constrain stellar population effects). This challenge would be met by the work of Reyes et al. (2011b), which presents a fully calibrated set of Tully-Fisher and scaling relations from SDSS, and whose results are largely consistent with these earlier results.

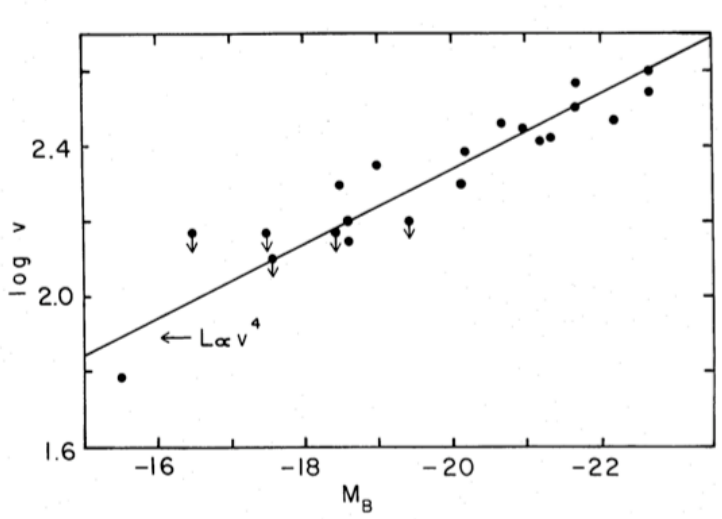

Figure 1.6 **From Faber & Jackson (1976)**: Velocity dispersions (line-of-sight) verses absolute magnitude. Such a correlation ($L \propto v^4$) was proposed by Minkowski (1962).

This lack of a third parameter in the Tully-Fisher relation is in stark contrast to the other major scaling relation developed at the same time as a counterpart for elliptical galaxies: The Faber-Jackson relation. While the Tully-Fisher relation compares orbital velocities to absolute luminosities in spiral and disc galaxies, the Faber-Jackson relation correlates parameters in elliptical galaxies. Faber & Jackson (1976) measured velocity dispersions and mass-to-light

(M/L_B) ratios of 25 galaxies, and found that both luminosity, L_B, and M/L_B increased with velocity dispersion, showing that ellipticals are nearly a one-parameter family, where total mass is the most important independent variable. An advantage of the Faber-Jackson relation is its firmer physical basis via its interpretation using the virial theorem, where the mean square random velocity directly relates to the mass of the galaxy.

Moreover, the predicted third parameter dependence of radius in the Faber-Jackson relation does exist, in the form of the Fundamental Plan (Djorgovski & Davis, 1987), making the lack of dependence on the third parameter in the Tully-Fisher relation all the more mysterious. Efforts have been made to unify these relations with the Tully-Fisher relation into one coherent framework (*e.g.*, Catinella et al., 2012; Dutton et al., 2011a). While progress has been made, a fully consistent framework from first gravitational principals has not yet been found.

1.3 Previous work on the evolution of the TF relation

Naturally as the measurements of local scaling relations began to take shape and their utility established as a basic correlation probe of dark matter halos and baryonic mass within them (Verheijen, 2001), interest began to shift to the rotation curves and scaling relations of galaxies at cosmological distances. An early paper from Keck data presented nine field galaxies in the redshift range $0.1 < z < 1$ (Vogt et al., 1996).

At this point, empirical evidence was sought from counts of faint blue galaxies to constrain galaxy evolution models. Interpretations ranged from luminosity brightening at high redshifts (Gronwall & Koo 1995) to more complex, luminosity-dependent changes (*e.g.*, Broadhurst et al., 1988; Colless et al., 1990; Glazebrook et al., 1995) in order to explain the abundance of faint blue galaxies. Vogt et al. (1996) sought to constrain the global brightening of disc

galaxies at higher redshift. Vogt et al. concluded that the only difference seen between the past and now is a modest increase in luminosity, ΔM_B <0.6 (however, it is shown later that this increase could be even more dramatic, *e.g.*, Böhm & Ziegler, 2007).

Vogt et al. discover that all of the rotation curves appear similar to local curves in form and amplitude, with the exception of one disc that was undergoing a probable merger. This would imply that the spirals that we see in the local universe were already in place around $z \sim 1$. Although no statistically-significant trends were secured with this initial study, Vogt et al. demonstrated in their pioneering paper the potential for studying rotation curves to $z \sim 1$.

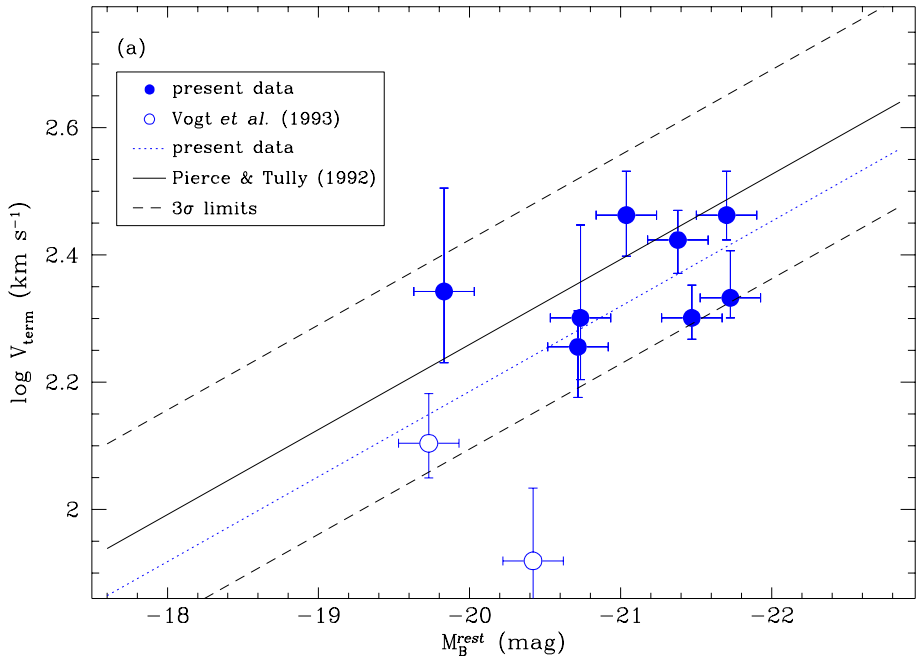

Figure 1.7 **From Vogt et al. 1996:** data at $z \sim 1$ compared to the local TF relation (Pierce & Tully 1988, 1992). The slight offset of $\Delta M_B < 1.6$ is demonstrated by the fitted lines.

Despite the substantial challenges introduced at the beginning of this chapter, the theoretical understanding of disc galaxy scaling relations and their

evolution has made some improvement over the past decades. Using an adjustment to the rotational velocity derived from their hydrodynamic simulations to account for over-merging, Portinari & Sommer-Larsen (2007) were able to match the observed local TF relation, and predict a modest evolution to $z \sim 1$. However the predictive power is tempered by an unknown dependence on redshift of this adjustment.

Semi-analytic models have also worked to match observations and provide further insight on the physical interpretation of evolution in the TF relation. Some controversy remains over whether the central regions of galaxy halos are subject to adiabatic contraction (Somerville et al., 2008), broadly maintain a non-evolving density profile (Wechsler et al., 2002), or permit adiabatic expansion (Dutton et al., 2010b).

Regardless of the exact evolutionary response of the inner halo, the persistent picture is one in which the baryonic component grows in tandem with the dynamical mass (Fall & Efstathiou, 1980; Dalcanton et al., 1997; Mo et al., 1998). Gas may cool from the halo or from externally-sourced streams, increasing the disc scale length as stars form. In this framework, while any given galaxy is predicted to grow by factors of 1.2-2 in stellar mass, dynamical mass, scale radius, and luminosity since $z \sim 1$ (modulo evolutionary corrections), this growth typically occurs along scaling relations, reducing the evolutionary signals accessible to observations.

Observational progress in testing these pictures of disc assembly has been similarly slow. There are significant technical challenges in making the necessary measurements at intermediate redshift and, as a result, there are discrepant conclusions with regard to evolutionary trends in the literature. In part, this may reflect different ways in which intermediate redshift disc galaxies are selected. Subsequent optical-based studies since Vogt et al. (1996) have presented mixed conclusions.

A key uncertainty is whether to address evolution in the overall mass-to-light ratio independent of luminosity (i.e. a zero-point shift with redshift) as

discussed by Rix et al. (1997a), Bamford et al. (2006), and Fernández Lorenzo et al. (2009, 2010), or whether to permit luminosity dependent evolution (i.e. changes in the TF slope) as discussed by Ziegler et al. (2002) and Böhm et al. (2004). TF studies at infrared wavelengths are less affected by biases induced by short-term star formation activity and early surveys found no convincing evolution (Conselice et al., 2005; Flores et al., 2006). However, by contrast, Puech et al. (2008) claim from near-IR measures that discs were overall less luminous in the past. Clearly the rest wavelength at which the luminosity is sampled is a key parameter: Fernández Lorenzo et al. (2010) claim evolution in the B-band but none in redder bands, while Weiner et al. (2006a,b) find evolution in the slope of the infrared TF relation consistent with that seen in the blue relation, however they observe little evolution in infrared zero-point. Moran et al. (2007) have emphasised the importance of environmental influences which can be deduced by considering the scatter in the TF relation as a function of local density.

In view of this, a more physically-relevant approach for understanding the assembly history of discs may be to consider the **stellar mass Tully-Fisher relation** (M_*-TF) which, notwithstanding the difficulty of estimating gas fractions, provides the most robust route to understanding the interplay between baryons and dark matter in disc galaxies. Stellar masses are derived using population model fits to multi-color photometry for galaxies of known redshift, assuming an initial stellar mass function (Brinchmann & Ellis, 2000; Bundy et al., 2005). Although the low redshift M_*-TF relation is well-constrained (Bell & de Jong, 2001; Pizagno et al., 2005; Meyer et al., 2008), those at intermediate redshift (Conselice et al., 2005; Flores et al., 2006; Atkinson et al., 2007) reveal a larger scatter than seen in the traditional TF relations, suggestive of additional uncertainties.

A recurrent topic of discussion in the literature is sample selection and whether evolution seen in both the TF relation and its scatter is driven by redshift-dependent selection criteria. The inclusion of more early types and

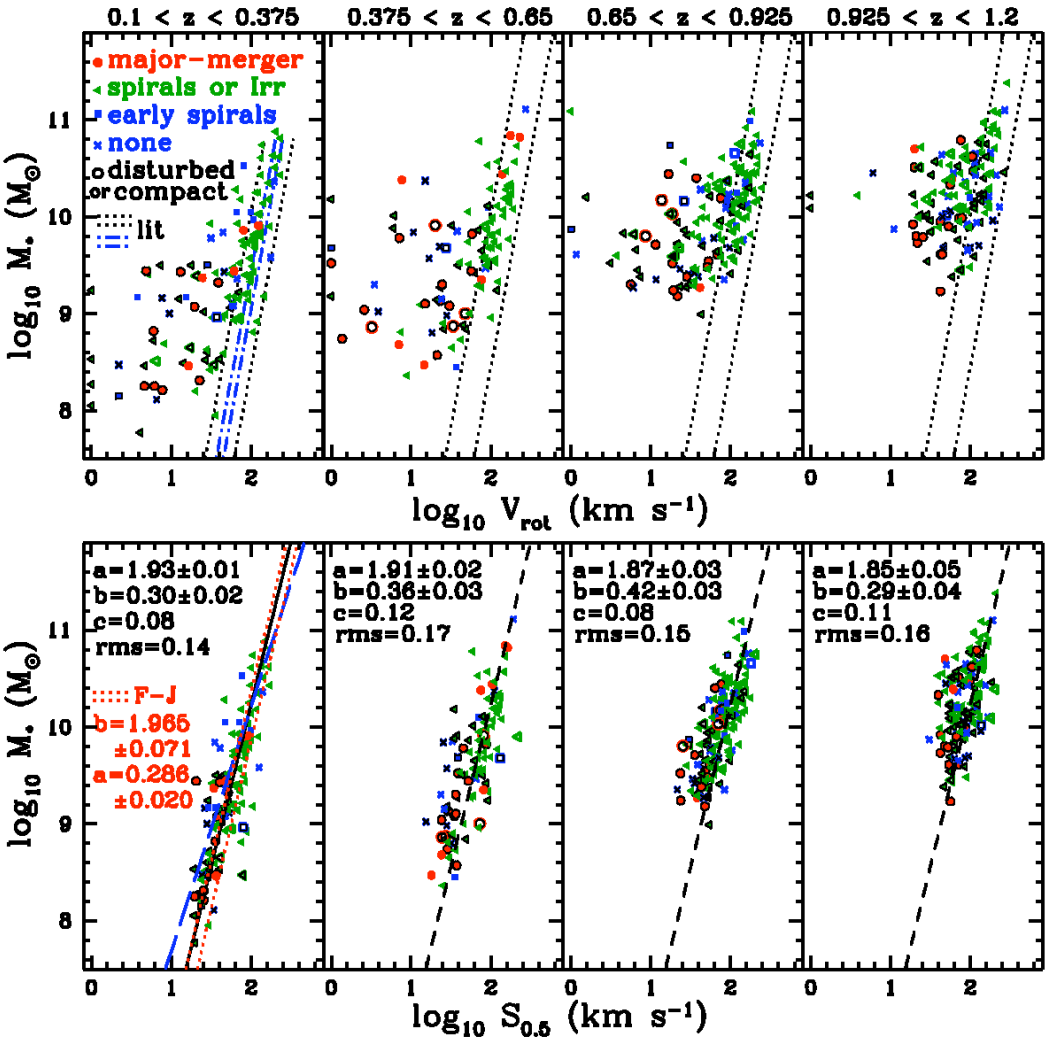

Figure 1.8 **From Kassin et al. (2007):** The state-of-the-art on the intermediate to high redshift study of the stellar mass Tully-Fisher relation, leading up to this thesis. The **top** panels show the stellar mass Tully-Fisher relation broken down into 4 redshift bins, while the **bottom** panels show the $S_{0.5}$ relation, which combines the gas dispersion with the rotational velocity to construct a 'kinematic tracer', which is compared to the Faber-Jackson relation in the bottom left panel.

dynamically disturbed galaxies likely broadens the intrinsic scatter. In an attempt to include more kinematically-disturbed galaxies, often excluded without good cause in TF studies, Weiner et al. (2006b) and Kassin et al. (2007) have included an additional kinematic term, $S_{0.5}$, defined as $\sqrt{0.5V_{rot}^2 + \sigma_g^2}$, where V_{rot} is the rotational velocity and σ_g is the velocity dispersion in the ionised gas, meant to accommodate the isotropic velocity width of the observed emission lines and reduces the scatter from their classic M_*-rotational velocity relation. Kassin et al. (2007) detect no significant evolution in the TF relation, including the $S_{0.5}$ relation, over $0.1 < z < 1.2$. However, combining a measure of the velocity dispersion with the disc angular momentum may obscure information about the rotational support of the disc.

Using integral field unit (IFU) spectrographs, Flores et al. (2006) and Puech et al. (2008) have produced intensity, velocity, and dispersion maps of galaxies at intermediate redshifts that demonstrate the unique advantage of a second spatial dimension in modelling the velocity field and accounting for projection effects. So far, the IFU-based samples are fairly modest in size and sample brighter sources compared to those reached with multi-slit techniques. Moreover, the spaxel resolution is often lower than for the highest-resolution slit spectroscopy. As we will show in this paper, the spectroscopic signal-to-noise is an equally important factor in making progress because it determines the radial extent to which emission lines can be traced and as a result, whether the adopted velocity measure requires extrapolation.

Both IFUs and slit spectroscopy have been successfully employed at $z \approx 2 - 3$, where near-IR studies can take advantage of redshifted Hα lines—the brightest kinematic tracer—as well as improved spatial resolution from adaptive optics. Results at these redshifts may indicate the emergence of regular scaling relations from more complex and disordered dynamical states. With adequate sampling, at least one-third of $z \simeq$ 2-3 star-forming galaxies show ordered rotation (Shapiro et al., 2008; Stark et al., 2008; Jones et al., 2010) and reveal significantly higher velocity dispersions than local counterparts (e.g., Genzel

et al. (2006)). Cresci et al. (2009) have measured the stellar mass TF relation at $z \approx 2$ using SINFONI observations of 18 rotation-dominated systems in the SINS survey (Förster Schreiber et al., 2009). The slope of their measured relation is consistent with that seen in local observations but offset towards lower M_* at fixed velocity by ∼0.5 dex. While necessarily biased toward massive systems with well-ordered rotation, these may be representative of gas rich systems in transition to z∼1 discs (Tacconi et al., 2010). Gnerucci et al. (2011) have recently measured the TF relation at $z \sim 3$ from SINFONI IFU data, but because of the large scatter observed, they suggest the TF relation has not yet been established. However, all points on the relation are consistent with the favoured vector of disc assembly theory, with a lower average stellar-to-dynamical mass ratio than found in the local universe.

1.4 Plan for the thesis

The present survey was motivated by our desire to chart and understand the apparent evolution from a prevalence of disturbed and complex dynamical states observed at high z to the well-ordered rotation of local spirals. To make progress, we seek to determine the stellar mass TF relation over the redshift range $0.2 < z < 1.7$ with spectroscopic exposures 3 to 8 times that of previous studies. By including disc systems selected from HST ACS data with irregular or distorted morphologies as well as more normal morphologies, we hope to avoid biases based on selecting mature, well-ordered discs (Vogt et al., 1996, 1997; Conselice et al., 2005).

Our study not only allows us to chart evolution in a large sample down to fainter limits and masses than is possible at $z \sim 2$, but the improved precision we demonstrate enables us to measure a robust TF relation only a gigayear (Gyr) later and onwards. The scatter we observe should provide a valuable indication of the rate at which discs settle onto the local TF relation. To fully utilise the gains in signal-to-noise ratio from long exposures, we develop an

improved method for extracting the rotation curves of galaxies at intermediate redshift via a new modelling code.

While our results are based on slit spectroscopy, unlike most previous slit-based studies (Weiner et al., 2006a; Kassin et al., 2007; Böhm & Ziegler, 2007), we are able to align the spectral slits on our masks with the HST-measured major axis, significantly improving the fidelity of our recovered rotation curves at $z \sim 1$. We aim to avoid introducing a bias towards aligning the often more extended and brighter objects at lower redshift over the higher redshift objects observed at smaller angular scales, since doing so could introduce an extraneous evolution in the offset and scatter of the Tully-Fisher relation with redshift.

We also take the opportunity, given the resolved measurements of the rotation curves, to conduct a more detailed, radially-dependent analysis of the likely dark matter distribution in our discs. We also utilise the radially-dependent V/σ measurements to test various interpretive hypotheses which our results could imply.

A plan of this thesis is as follows:

- In Chapter 2, we review the measurement of rotation curves in galaxies, as well as introduce, explain, and justify our chosen method of rotation curve fitting for this thesis.

- In Chapter 3, we introduce the dataset of this thesis, explaining sample selection and photometrically derived measurements of this thesis, including the stellar mass estimates and rotation velocity extractions.

- In Chapter 4, we present our results on the Tully-Fisher relation from $0.2 < z < 1.7$, including the stellar mass Tully-Fisher relation as well as the original B-band magnitude relation.

- In Chapter 5, we explore various implications of both the kinematical nature of the disc galaxies studied, as well as the TF relations tracked to

$z \sim 1.7$ in a wider context of our understanding of disc galaxy assembly and evolution.

- In Chapter 6, we review the conclusions of this thesis, and contemplate future prospects for further work on disc galaxy assembly and the evolution of the Tully-Fisher relation.

Chapter 2

Rotation Curve Modelling

The cornerstone of this thesis is an innovative method to extract rotation curves of high redshift galaxies. Drawing on earlier research, we have constructed a flexible method appropriate for both intermediate and high redshift data of a range of qualities, to extract fiducial velocities for application to studies of the redshift evolution of the Tully-Fisher (TF) relation.

We begin with a historical review of rotation curves (§2.1), and justify the functional form and fiducial TF velocity chosen for this work in light of previous rotation curve studies, especially at high redshift (§2.2). We then detail the specific rotation curve fitting procedure developed for this thesis (CURVATION), written in IDL and based on a variety of experiments and tests using both simulated and real data (§2.3). The code was developed to work independently of any specific spectroscopic dataset, and its application to the specific Keck data presented in thesis is described in Chapter 3, along with the description of the dataset itself.

2.1 The historical context

Remarkably, the rotation of galaxies was observed and confirmed before the Great Debate of Shapley and Curtis in 1920, when the size and extent of our Milky Way as well as the true identities of the 'spiral nebulae' were famously disputed (see Trimble, 1995). Left unsettled until Hubble (1925) applied the

Cepheid variable techniques developed by Leavitt (1908) to the ubiquitous 'spiral nebulae', a consensus was reached then finally that they were distant galaxies beyond our own. Yet as early as 1912, V. M. Slipher had systematically observed spectra of the nearest galaxies with the Lowell Observatory 24-inch reflector, discovering tilted spectral lines which he correctly interpreted as the rotation of these systems (Slipher, 1914).

In 1917, F. G. Pease observed M31 for 79 hours (over the course of 3 months) with the Mt. Wilson 60-in, using 2 plates: one where the slit was placed along the galaxy's major axis, and one along its minor axis (Pease, 1918). He saw clear Doppler shifting along the major axis and none along the minor axis, confirming that rotation must be responsible for Slipher's tilted lines. A century later the rotation curves of galaxies are still often observed in a similar way— with slit spectroscopy along the galaxy major axis to track the maximal Doppler shifting of spectral features.

Nearly half a century after the first rotation curves were observed, less than 10 resolved rotation curves were available in the literature, due in large part to the challenging nature of the observations. The discovery of galactic radio emission in the 1930s, and later the Hydrogen 21 cm emission line by Ewen & Purcell (1951), would reveal an alternative way to track rotation in galaxies to even greater radii than optical techniques, although it would be some time until arrays of dishes and improved interferometric techniques could sufficiently resolve them spatially. In the review of de Vaucouleurs (1959), the only 8 resolved rotation curves in the literature at the time were together described as consisting of a solid body inner part linearly rising to a maximum, beyond which the rotation slowed according to Kepler's laws: $V(r) \propto \frac{1}{\sqrt{r}}$, where V is the rotational velocity in the disc and r is the radial distance from the centre of the galaxy. However, this conclusion was limited by the poor signal-to-noise ratio (S/N) beyond the solid-body portion of the rotation curve.

As observations improved in statistics and sensitivity by orders of magnitude with various technological advances (*e.g.*, the invention of the CCD for optical

astronomy) the seminal work by Vera Rubin and her colleagues throughout the 1970s and 1980s revealed that almost no rotation curves exhibit Keplerian behaviour (Rubin et al., 1978; Bosma, 1978; Giovanelli & Haynes, 1983; Rubin et al., 1985; Sancisi & van Albada, 1987), most remaining more or less flat to large distances from galaxy centres. In fact Oort (1940) had noted that the dynamics of the Milky Way suggested a flat, non-Keplerian rotation curve in his local Galactic kinematical analysis. This surprising feature of rotation curves is celebrated now as some of the earliest and most important evidence for dark matter, whereby an extensive halo is invoked to explain the lack of Keplerian behaviour in the outer disc. As exemplified by De Vaucouleurs' review, the planetary-driven Keplerian paradigm heavily influenced both expectations and interpretations of kinematic observations. We will explore the implicit spherical symmetry in both Keplerian and dark halo paradigms in the penultimate chapter of this thesis.

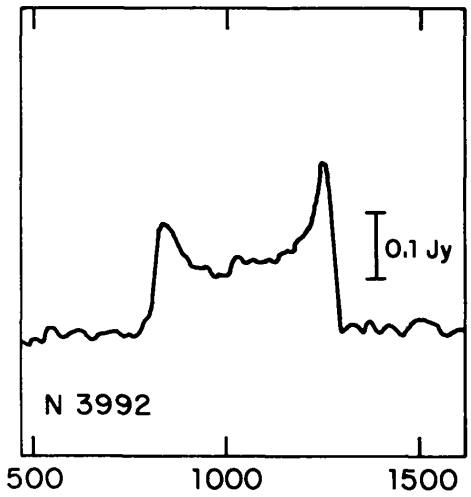

Figure 2.1 **From Tully & Fisher (1977):** The 'double horned' 21 cm HI emission line from an example galaxy (NGC 3992). The vertical scale is denoted in Jansky and the horizontal scale is in km s^{-1} with respect to the sun, and the resolution is 22 km s^{-1}.

The 'double horned'-shaped 21 cm HI global profiles (see Fig. 2.1) were observed with early arrays and single-dish instruments revealing the maximal rotation velocity (X2) in a disc, applied for instance in the relation of Tully

& Fisher (1977). Even with present technology, the 21 cm emission line is impossible to detect in individual galaxies much beyond $z\sim0.2$, let alone $z\sim1$, and rotation curves measured from the rotationally-excited CO lines take tens of hours to resolve on pre-ALMA (Atacama Large Millimetre Array— see Ch 6, *Future Directions*) millimetre wavelength arrays. Since the redshift range of interest in this thesis is $z>0.2$, we must use a different approach for measuring rotation curves than with radio or millimetre wavelengths.

To this day the vast majority of intermediate-to-high redshift ($z>0.2$) rotation curves are fit using optical emission lines from the discs of galaxies (mostly from ionised Hydrogen (Hα & Hβ, the Balmer series), and/or forbidden lines of ionised Oxygen (the [O II] λ3727 doublet and the [O III] λ5007 line), due to their relative brightnesses in the optical wavelengths. This allows the disc to be traced further in radius than with absorption lines in the stellar continuum. However emission line studies rely on ionised gas and thus star-formation to be occurring throughout the disc, excluding populations of galaxies whose star formation has largely shut down.

This analysis is ideally performed with resolved spectra, but often velocities are extracted from an integrated profile similar to studies of the spatially unresolved HI 21 cm line profile. Line width studies of this nature were some of the earliest full kinematical analyses of optical emission lines conducted (Dressler & Faber, 1990), and made a concerted effort to demonstrate their equivalence to HI 21 cm profiles. Even recently, line width studies have been carried out for the sake of efficiency in building large sample sizes or when resolution is not sufficient for resolved rotation curve analysis. Weiner et al. (2006a) analysed 1,191 galaxies, extracting 1,089 integrated optical emission line widths, and concluded such measurements represent a fairly robust way to characterise rotational velocities in galaxies. Their conclusion here is debatable, since the scatter in the correlation between line widths and velocities from more resolved rotation curves range from 0.5 dex to >1 dex depending on whether the veloci-

ties of galaxies are dominated by rotation or dispersion (respectively), and the correlation appears offset from the 1:1 relation by eye.

In this thesis we focus solely on spatially-resolved spectral observations, to diagnose the shape of rotation curves as well as the extent to which discs of galaxies are being probed. This is important at high redshifts, as high S/N can be difficult to attain, especially in the outer discs where rotation curves tend to flatten.

2.2 High-redshift methodologies

The measurement of rotation curves at intermediate-to-high redshift was pioneered by Nicole Vogt in her thesis, Vogt (1995), and in subsequent papers. In Vogt et al. (1996), optical spectra were taken of 9 galaxies from $0.1<z<1$ from 30 minutes to 3 hour co-adds with the Low Resolution Imaging Spectrograph (LRIS, Oke et al., 1995) on Keck, depending on their relative brightness. A functional form of the rotation curves is needed to fit to the data for the velocity extraction analysis. Vogt et al. adopted the 'universal rotation curve' of Persic & Salucci (1991):

$$V(r) \simeq 200 \left(\frac{L_B}{L_{B*}}\right)^{1/4} \left(1 + \left[0.12 - 0.24 \log\left(\frac{L_B}{L_{B*}}\right)\right]\left[\frac{r}{R_{\max}} - 1\right]\right) \text{km s}^{-1} \tag{2.1}$$

where L_{B*} is parameterised by Persic & Salucci as $6 \times 10^{10} h_{50}^{-2} L_{B\odot}$. This rises linearly to 1 disc scale radius (r_s, where the surface brightness $\Sigma(r) = \Sigma_0 e^{-r/r_s}[\text{L}_\odot/\text{pc}^2]$), expressed in the function as the $R_{\max}$ parameter, at which point the velocity gradient flattens depending on the B-band luminosity (L_B) of the galaxy. Constructing their model based on the functional form of Eq. 2.1, Vogt et al. additionally assume that the emission line brightness profile across the disc follows the exponential disc starlight profile, augmented by an factor of 1.5 multiplied to the HST-measured disc scale (this factor from Ryder & Dopita, 1994, comparing line emission to continuum flux).

Vogt et al. then convolve this model with atmospheric seeing and mock-observe it through a slit mask equivalent to that of the observations, varying the circular velocity of the model by hand until the simulated rotation curve matches the observed data at the extremes. The asymptotic limit of Eq. 2.1, termed by Vogt *et al.* as the terminal velocity, is claimed to not substantially change when varying the disc scale radius by 25%, although this change is not quantified. Their 9 intrinsic terminal velocity measurements are applied in a TF analysis, the first ever attempted at $z\sim1$.

This first high-redshift rotation curve fitting procedure of Vogt *et al.* highlights many of the important factors that determine the optimal methods in optical rotation curve analyses, including:

- contamination of the emission line from skylines and galaxy continuum,
- incorporating all available emission lines into a single best fit,
- adaptive binning techniques where S/N is low,
- the characterisation of both the spectral and spatial emission profile,
- relying on manual or automated methods in finding the best-fit, and
- accounting for inclination, atmospheric seeing, instrument resolution and intrinsic velocity dispersion of the emission line with additional information beyond what the spectrum alone provides.

At high redshift, where the relative scales of seeing and line dispersion are a significant fraction of the overall rotation curve structure, further important requirements to consider are:

1. a functional form which well represents line emission from rotating discs, preferably with some physical basis (§2.2.1); and,
2. a characterisation of this function form with a fiducial velocity that is reliably detected across a sample of rotationally supported galaxies and

that minimises the need for extrapolation to radii where direct velocity information does not exist (§2.2.2).

2.2.1 Functional form

Several functional forms have been discussed in the literature, such as the 'universal rotation curve' of Persic & Salucci (1991, Eq. 2.1), where the entire parameterisation rests on the galaxy luminosity. Purely phenomenological, yet less restrictive, the 'multi-parameter function' has been applied in works such as Schlegel (1995), Rix et al. (1997b), Kravtsov et al. (1998) and Courteau (1997):

$$V(r) = V_0 + V_a \frac{(1+x)^\beta}{(1+x^\gamma)^{1/\gamma}}, \tag{2.2}$$

where $x = r_t/(r - r_0)$, and V_0 is the central or systematic velocity, r_0 is the dynamical centre, V_a is the asymptotic velocity, and r_t is the turnover radius—the transitional point between the rising and flattening part of the rotation curve.

Both of these functional forms contain more free parameters than the most widely adopted model, which is the empirically-motivated arc-tangent or 'arc-tan' function:

$$V = V_0 + \frac{2}{\pi} V_a \arctan(\frac{r - r_0}{r_t}), \tag{2.3}$$

where V_0 , r_0, V_a, and r_t are defined similarly to those of Eq. 2.2 (Gilmore et al., 1990; Schlegel, 1995; Courteau, 1997; Willick, 1999). Both simple yet flexible enough to fit most observed rotation curves shapes (see Fig. 2.2), this form also arises naturally from parameterisations of haloes formed in simulations (e.g., Gilmore et al., 1990). We adopt this function in our analysis.

While our adopted arctan function is not able to account for a sharp peak near the turnover radius found locally in resolved rotation curves of bulge dominated galaxies, rarely is this feature observed in intermediate-high redshift sample, and Weiner *et al.* confirm this. Nevertheless, velocities extracted

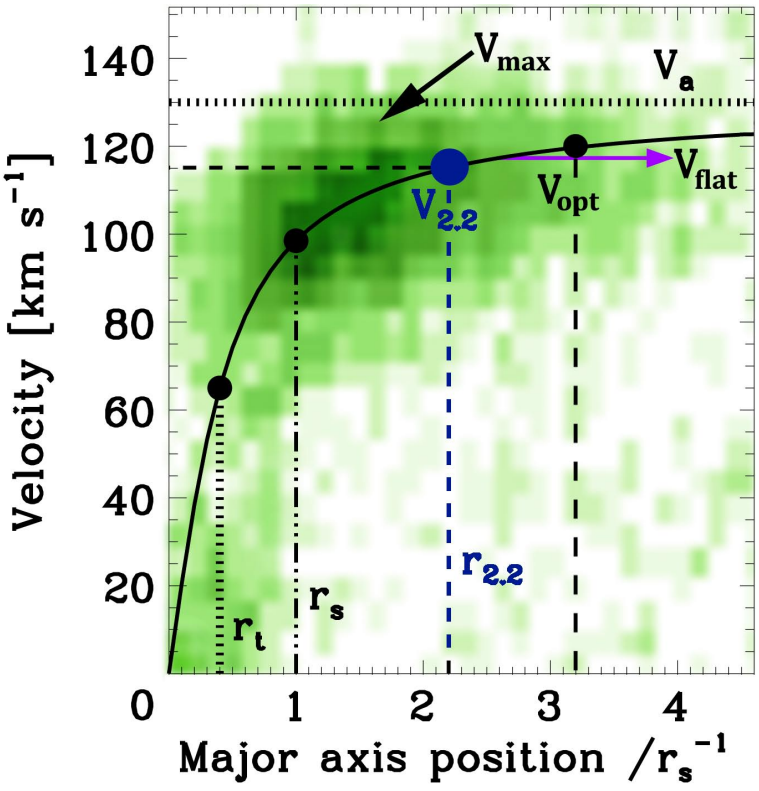

Figure 2.2 A functional arctan rotation curve with various characteristic radii (discussed in the text) shown as dimensionless factors of the disc scale radius (r_s, marked with the dot-dashed line). We plot an example emission line spectrum in green behind the arctan functional form to demonstrate the resolution which is achievable at intermediate-high redshift spectra. The example shown has a functional parameters, turnover radius $r_t = 0.4\,r_s$ (marked with the dotted vertical line), and an asymptotic velocity $V_a = 130$ km s^{-1} (marked with a horizontal vertical line), which are typical parameter values for rotation curves of galaxies found in disc galaxies. The region where the rotation curve turns over is extensive, and the so-called turnover radius, r_t, is mathematically defined and does not clearly indicate the elbow of the rotation curve by eye. The maximum velocity, $V_{\rm max}$, of the emission line data (not the functional form) is indicated with the black arrow. The velocity at the optical radius $V_{\rm opt}$ is at 3.2 times the disc scale radius and denoted with a long dashed line. The velocity with which the rotation curve flattens $V_{\rm flat}$ is marked with a purple arrow. As a consistent and fiducial radius for velocity extraction, we adopt $r_{2.2}$ or 2.2 disc scale radii, with its corresponding velocity as $V_{2.2}$, marked in blue with the short dashed line.

from less than one disc scale radius while adopting this model could be problematic due to the possible confusion of bulge dispersion with the disk rotation, which may be blurred out from the seeing and/or instrumental dispersion. By extracting key TF values from the rotation curve beyond potential bulge contribution, significant biases are avoided due to this possible confusion, bringing us to the second critical point: fiducial velocity selection.

2.2.2 Fiducial velocity selection

After a panel discussion regarding the ideal TF velocity at a meeting celebrating 35 years of the TF relation (held at the Green Bank National Radio Astronomy Observatory in West Virginia), the expert consensus was that the velocity at which a rotation curve flattens ($V_{\rm flat}$) was the ideal fiducial velocity of a rotation curve. Largely, this is because rotation curves share the general characteristic of becoming asymptotically flat with radius, but this is only ever directly measurable in galaxies with a resolved, low dispersion tracer out to large radii, such as spatially-resolved HI 21 cm studies (Verheijen, 1997; McGaugh et al., 2000). The ideal $V_{\rm flat}$ in most galaxies is not directly observable, so other fiducial velocities must be adopted in order to characterise the rotation velocity for analyses like the TF relation, especially in optical emission line studies like ours.

Studies such as Flores et al. (2006) and Weiner et al. (2006b) advocate the use of the circular rotational velocity ($V_{\rm circ}$, which is $\propto \sqrt{M/r}$ where M is total mass enclosed within radius r, assuming spherical symmetry). Typically then $V_{\rm circ}$ is equated to the circular velocity of the halo where dark matter dominates the total halo mass in the favoured cold dark matter (CDM) paradigm. However in practical application, this is assumed to be the asymptotic velocity from Eq. 2.3, V_a of the best-fit arctan function, or a similar terminal or flattening velocity of more complex models in studies such as Vogt et al. (1996, 1997); Flores et al. (2006); Weiner et al. (2006a); Kassin et al. (2007). While the arctan

function can closely match the observable extent of rotation curves, by definition the mathematically-extrapolated asymptote is never directly observed in real data, no matter how extended the observable emission is in the outer disc. Small offsets in the extrapolated velocity curve will lead to large changes towards the asymptotic limit, especially when emission is only detected in the more solid-body portion of the rotation curve, and emission line dispersion and seeing distort the terminal emission. In this respect, if $V_{\rm circ}$ is represented by an under-constrained V_a, the extrapolation can lead to a severe over or under prediction (Courteau, 1997). We confirm this in the simulations and tests to be introduced in the next section.

Past studies have also adopted $V_{\rm max}$, or the maximum measured velocity along the disc, as a fiducial TF velocity (*e.g.*, Conselice et al., 2005; Cresci et al., 2009). This choice is motivated by the ideal case where the maximum in a rotation curve is the velocity to which it flattens. The disadvantage with $V_{\rm max}$ is its relative inconsistency across the variety of discs observed in ionised gas studies such as this, since $V_{\rm max}$ is highly dependent on the location of ionising star-formation across a given disc. In terms of the disc scale radius, there is a range of a factor $\simeq$5 or more in the associated radius, and $V_{\rm max}$ is found to be a poor proxy for the HI 21 cm profiles width (Courteau, 1997). Many hours of exposure time on a disc which has little emitting gas may leave the underlying bulk rotation undetected. In this case $V_{\rm max}$ would largely underestimate $V_{\rm flat}$, which could explain the scatter bias towards lower velocities in the study of Flores et al. (2006) for objects where the S/N ratio is $<$5 in their optical emission data maps. $V_{\rm max}$ can also over-estimate $V_{\rm flat}$ when detectable emission only occurs in a more central bulge-like component which is greatly broadened by velocity dispersion.

There is no perfect fiducial velocity or functional form to meet all needs of all datasets, and trade-offs are made with one selection or another. Because of the variety of emission extents observed in disc galaxies, we have selected a physically motivated fiducial radius to which emission typically can be detected

over our wide redshift range: the intrinsic velocity at 2.2 times the exponential disc scale radius ($r_{2.2}$), which we will refer to as $V_{2.2}$. This has a good physical basis corresponding to the location of peak rotational amplitude for a pure exponential disc (Freeman, 1970; Binney & Tremaine, 1987; Courteau & Rix, 1999a). Although few discs are likely to be perfectly exponential, the $r_{2.2}$ approximation as the point at which rotation curves flatten is visually confirmed in most galaxies. TF velocities based upon $V_{2.2}$ result in the smallest internal scatter and provide the best match to HI 21 cm line widths for local galaxies (Courteau, 1997), which is important in comparing the high redshift results to the majority of local TF work that is from HI data. Also this fiducial velocity has been adopted in recent literature, e.g., Pizagno et al. (2005), Dutton et al. (2010a), Reyes et al. (2011b), & Reyes et al. (2011a), in determining the kinematic connection between late-type galaxies and dark matter halos, which we will explore in Chapter 5.

A similar parameter to $V_{2.2}$ is $V_{\rm opt}$: the velocity at the optical radius (typically defined as 3.2 $\times$ the disc scale radius, enclosing 83% of the light in a pure exponential disc). Another similar parameter is V_{80}, the velocity at the radius enclosing 80% of the disc light (favoured in Reyes et al., 2011a,b), which are both fractionally further out in the disc than $V_{2.2}$ ($r_{2.2} = 1.45 r_{\rm opt}$). Velocity extracted anywhere from $\sim$2—4 times the disc scale radius leads to results which are marginally quantitatively different results, yet qualitatively similar (*e.g.*, Courteau, 1997; Reyes et al., 2011b), so that the choice is ultimately left to the discretion of those conducting the analysis.

In conclusion, we have adopted the arctan function, primarily for its simplicity given the nature of high redshift data. For fiducial velocity extraction, our preference has been towards a choice which relies less on extrapolation, rather than a velocity which may be marginally closer to an idealised terminal velocity that may or may not exist in a given rotation curve. That is to say, we have adopted $V_{2.2}$ rather than a similarly acceptable choice of $V_{\rm opt}$ or V_{80},

which is preferable a V_a or $V_{\rm max}$ when adopting the arctan function or similar at intermediate to high redshifts.

2.3 curvation: a rotation curve fitting code

Now we turn to how we will be specifically fitting emission line data in this thesis to obtain intrinsic rotation curves for each galaxy disc, using the arctan function. The IDL code CURVATION attempts to reproduce the observed spectra with as few assumptions as possible. Thus de-projecting for inclination and other effects occurs *a posteriori* and depends on the specific dataset in use, so we explain this aspect of the analysis in Chapter 3. The code calls on a number of the standard procedures in the IDL Astronomy User's Library as well as the Markwardt (2009) MPFIT library.

In explaining the steps of the procedure and justifying the various decisions made about the method, we will be referring to tests using both observed and simulated data. The simulations allow us to test whether a method or piece of code can recover various characteristics of the rotation curve, which can be directly compared to the known intrinsic form. However, inevitably real data must be used as well, since there are innumerable features of real spectroscopic observations of emission lines that elude simulated data. We thus test our procedure and code with a balance of both real and simulated data.

The simulations attempt to realistically emulate the observed spectroscopic data at the resolution of the DEIMOS instrument on Keck ($0\farcs1185$ per spatial pixel and $\Delta v \sim 30$ km s^{-1}). The simulated emission line spectra vary according to the characteristics of both literature data and preliminary considerations of our own data (Ch. 3). These include the emission line S/N per pixel from 3 to 15, the emission extent from 0.1 to 30 times the turnover radius, and the intrinsic shape of the emission line, varying the parameters V_a (40 - 300 km s^{-1}) and r_t ($0\farcs01$ - $4\farcs5$) from Eq. 2.3. We reproduce the natural correlation observed between V_a and r_t by making V_a a function of r_t in the simulated emission

lines. However the S/N and emission extent are not correlated with the other parameters and so are freely drawn from our input distributions. We assume either a flat or exponentially decreasing intrinsic emission brightness profile, and a constant intrinsic velocity dispersion of the emission line with respect to position along the major axis. These are the most unrealistic components of the simulations. Real emission lines are clumpy, vary unpredictably in brightness across the disc, and are typically not amenable to functional description. This is the major reason why tests are also conducted with real spectroscopic data, even though the intrinsic emission distribution is not known. Real data are also useful to test the performance of the code in the presence of skyline residuals and other spurious features from the instrument or from the reduction.

The basic procedure described in Vogt et al., which has been an important guide for our work as well as various emission line fitting analyses which followed, *e.g.*, Simard & Pritchet (1998); Rigopoulou et al. (2002); Ziegler et al. (2002); Milvang-Jensen et al. (2003); Böhm et al. (2004); Jäger et al. (2004); Bamford et al. (2006); Metevier et al. (2006); Moran et al. (2007), is similar also to optical analyses of more local galaxy rotation curves which preceded it, *e.g.*, Courteau (1992). A somewhat simplified tactic can be found in the large body of work of Weiner et al. (2006a, b), which yielded 380 spatially-resolved rotation curves that have also been used in various other Team Keck Redshift Survey (TKRS) galaxy studies, such as Kassin et al. (2007). They also adopt the arctan function, and motivated by a desire to analyse large samples of kinematics with only the information contained in the 2D spectra, they further simplify the Vogt *et al.* -style method. They correct only for the effect of seeing, without compensation for disk inclination or effects of slit position angle offsets, and also fix turnover radii in the arctan models at $0\farcs2$. These restrictions demand careful testing, which was included in their papers. However, further comparisons and tests in this thesis call into question some of their conclusions.

We have attempted to improve upon these methods, partly to take advantage of the increased detail in our deep spectroscopic data, but also to ensure that key steps on the procedure are as empirically-driven as possible. A simple outline of the fitting code is as follows:

1. Trace the observed 2D emission line in wavelength as a function of spatial position (§2.3.1),

2. Construct a model 2D spectrum with an arctan-shaped emission line profile, implementing features traced in step 1 (§2.3.2),

3. Trace the model spectrum, varying the arctan model parameters V_a and r_t (as well as the dynamical centre and a seeing-dispersion beam correction factor) until the model trace optimally fits that of the data (§2.3.3),

4. Extract and de-project $V_{2.2}$ at $r_{2.2}$ from the best-fit arctan models (§3.6).

2.3.1 Step 1: Emission line tracing

In order to cleanly trace the Doppler shifting emission line, we begin by subtracting the galaxy continuum on a reduced and rectified 2D spectral frame. Due to the smoothness of the continuum over the scales of the emission lines, removing the continuum is equivalent to modelling the continuum along with the emission line (see Fig. 2.3 for an example). However for the sake of simplicity, this is performed by linearly interpolating in wavelength across the emission line region, treating each spatial row independently.

We next fit each emission line as a function of spatial position. This procedure returns the central wavelength, line width, and peak flux in each spatial row of pixels, or 'bin'. We fit two half-Gaussians to the line profile in the wavelength direction, and use an adaptive binning procedure in the spatial direction to ensure a consistent S/N to the extent of the trace. After N rows have been included in the spatial bin (where N is some maximum binning limit), if the

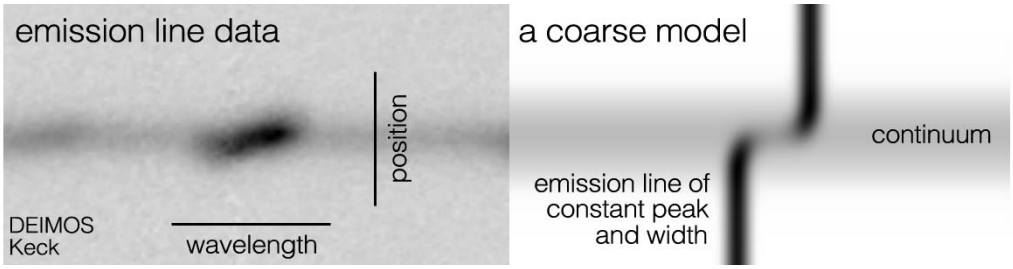

Figure 2.3 An example of an Hα emission line (left) with an example of a fairly crude rotation curve model, consisting of a model continuum and an emission line which extends the entire extent of the slit. The latter aspect of this model is similar to that of Weiner et al. (2006a) and Kassin et al. (2007).

S/N criterion has still not been met, then the trace is terminated. This maximum binning limit is adjusted based on the nature of the dataset, and the intrinsic scale of the features one wishes to trace. For instance if a spectrograph has a spatial scale of $0\farcs1185$ per pixel (such as DEIMOS on Keck) and the seeing is typically $0\farcs9$, then resolved features will be Nyquist sampled if the maximum binning limit is 3 (=$0\farcs3555$). The blurring effect of seeing in the spatial direction, compounded by dispersion in the wavelength direction, can affect the emission line in a particular spatial bin by mixing flux from neighbouring bins. We use two half-Gaussians with differing sigmas joined at the same peak to account for these effects, ensuring that the position of the peak flux is always traced (see comparison of two methods in Fig. 2.4).

The results of a tracing code with a single, symmetric Gaussian fit to each spatial bin (rather than 2 half-Gaussians) can be seen in Fig. 2.5. By eye, the traces look acceptable, but the subtle offsets propagate through the modelling process and compound in final velocity extractions, as seen in Fig. 2.6. Ultimately, this is best exemplified by tracing simulated data, where the intrinsic emission line centroid is known. We see a clear departure of the symmetric Gaussian trace from the intrinsic emission line (initially one pixel across in the simulations, which is then blurred by some simulated seeing and dispersion to mock the degenerate blurring we see in the real data). This departure propagates through to the model as well by a factor of 2-3 scatter in the attempted

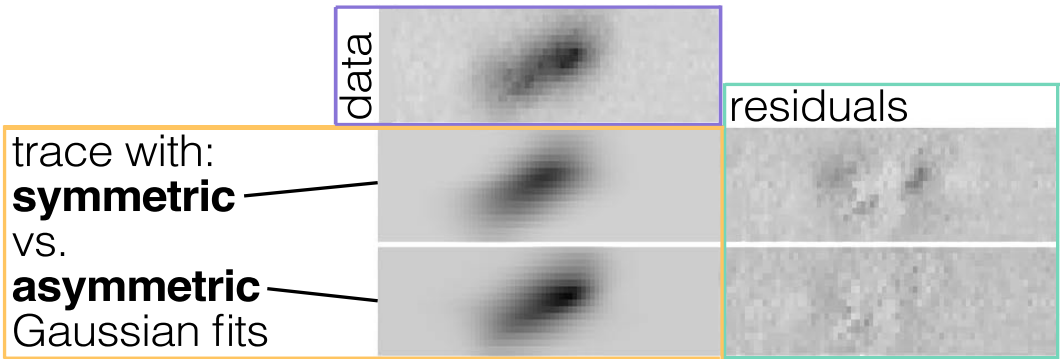

Figure 2.4 Comparing the data/trace/residuals of an emission line **(top)** where the line profile across spatial bins has been assumed as symmetric **(middle)** compared to asymmetric, or rather 2 half-Gaussian line profiles in the trace **(bottom)**, with respective residuals shown here in the same dynamic range **(right)**. This change in the tracing code, accounting for instrumental blurring between spatial bins, marked a 30% reduction in residuals. The added flexibility helps to avoid biasing of the rotation curve towards the systematic velocity due to the effects of seeing, which compounds the blurred light from the line dispersion.

recovery of V_a from the symmetric Gaussians. Asymmetric Gaussians reduce this departure significantly, and averaging over the range of simulated emission lines, can lead to an improved recovery rate (output V_a within 1σ of intrinsic V_a) of 50%, which jumps to 70% when attempting to recover $V_{2.2}$.

The trace terminates when the emission is no longer detected above the local noise level, which is determined by the variance map of the reduced data. We experimented with various methods of modelling the extent of the emission, such as attempting to trace the entire spatial extent of the slit, merely de-weighting those bins which have insufficient S/N based on the variance of the Gaussian fit (similar to Weiner et al., 2006a, see Fig. 2.3 for an example). However, the effects of blurring by seeing and dispersion propagate differently when the model emission line flux has a constant intrinsic peak, than when the intrinsic emission brightness varies spatially, such as a drop in emission towards the outer edge of the optical disc. Without taking this into account, these models often induce a flattening of the rotation curve when none was actually present in the intrinsic emission line of the simulated spectrum.

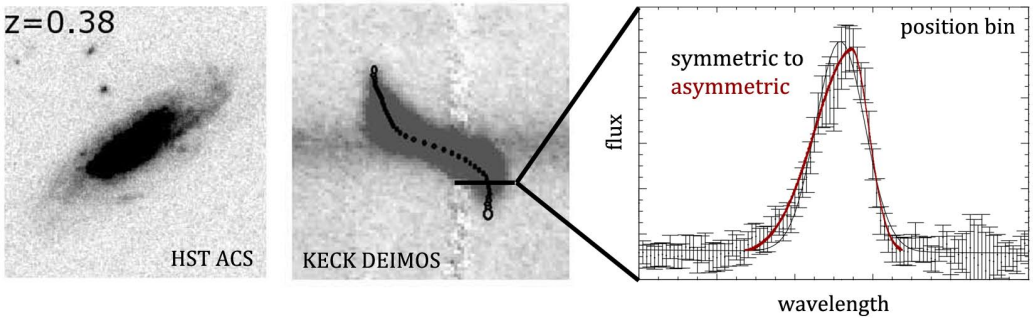

Figure 2.5 **Left:** The HST ACS image of the galaxy, with redshift noted. **Centre:** a cutout of the spectrum around the Hα line of interest, where flux is plotted as a function of wavelength (abscissa) verses spatial position (ordinate). The wavelength centroids of the symmetric Gaussian trace are overlaid on each emission line with black circles, the width of which are the uncertainties in the wavelength centroid and the height of which indicate the spatial binning. One of the challenges in constructing this code is the relative subtlety of the differences the various features make. By eye this tracing code appears to work well, however the subtle biasing that the symmetric Gaussians cause propagate through the modelling process as a substantial scatter in whatever application to which they are applied (*e.g.*, Fig. 2.6). **Right:** An example of the difference between the symmetric Gaussian and asymmetric (2 half-Gaussian) tracing code implemented in a given spatial bin (of flux vs. wavelength).

The procedure produces an array of wavelength values as a function of spatial position (see Fig. 2.7 and left side of Fig. 2.8), as well as the position-dependent emission peak flux and 2 half-Gaussian line width. The emission peak profile relays the star formation rate across the disc modified by foreground absorbing gas and dust. The varying line widths contain information on the local ionised gas velocity dispersion, any unresolved random motion, and the projected, line-of-sight spread of velocities which depend on the inclination and intrinsic thickness of the disc. Confounding this spread of dispersive degeneracies and muddled emission profiles are the seeing and instrumental dispersion. With the observed emission characterised by the trace at this integrated level, we attempt to recover the intrinsic emission distribution, or at least approach it at the resolution of the observations, with the modelling procedure described further in the next section.

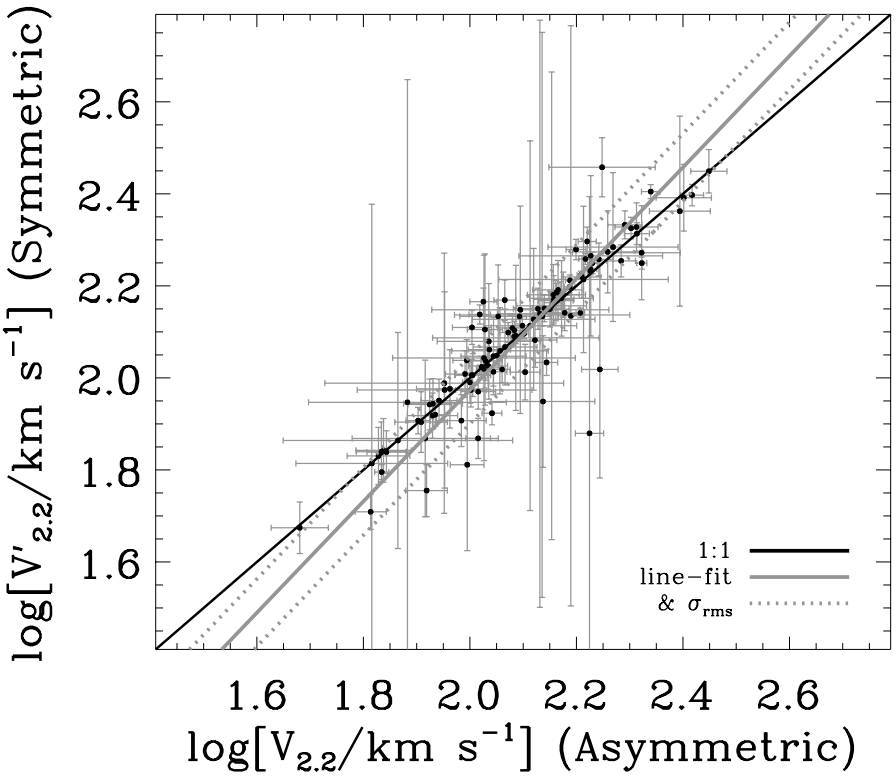

Figure 2.6 Comparing velocities extracted at $V_{2.2}$ from using tracing procedures which assume the spatial bin emission line profiles are **Symmetric vs. Asymmetric**. The traces are applied in models to recover the rotation curves of real data since simulations reveal that symmetric Gaussians improve the recovery rate by 70%, and so assuming asymmetric Gaussians better reveal the intrinsic emission, we may assess what gain is made by this implementation in the final TF velocities. While the scatter between the two methods is only about 0.1 dex, accumulating various gains in precision of this nature will ultimately lead to a much tighter TF relation, simply due to minimising uncertainties in the velocity extraction method.

2.3.2 Step 2: Model construction

We next construct a model to best reproduce the trace. Some previous methods fit an arctan function directly to the trace points (*e.g.*, Stark et al., 2008; Jones et al., 2010; Reyes et al., 2011b, see Fig. 2.9). However without accounting for the effects of seeing and emission line dispersion beyond the instrumental dispersion, these rotation curves are not modelled such that the intrinsic velocities

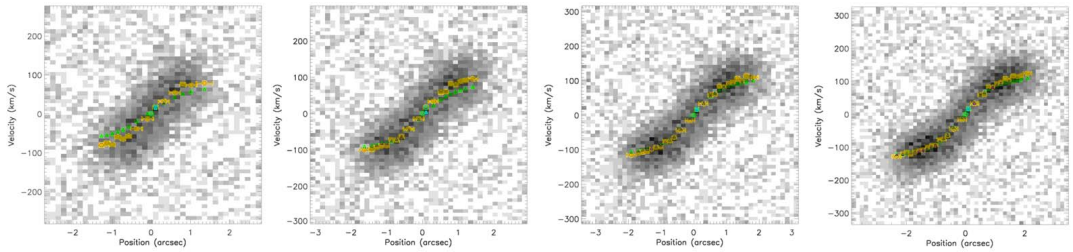

Figure 2.7 An example of our fitting procedure for a series of simulated emission line spectra with varying emission extension, V_a, and r_t. The panels show a grey scale representing flux as a function of velocity with respect to position. Orange circles show the trace centroids of the emission line (bars along the positional dimension indicate bin size, not error), and the green triangles show the equivalent centroids for the constructed model.

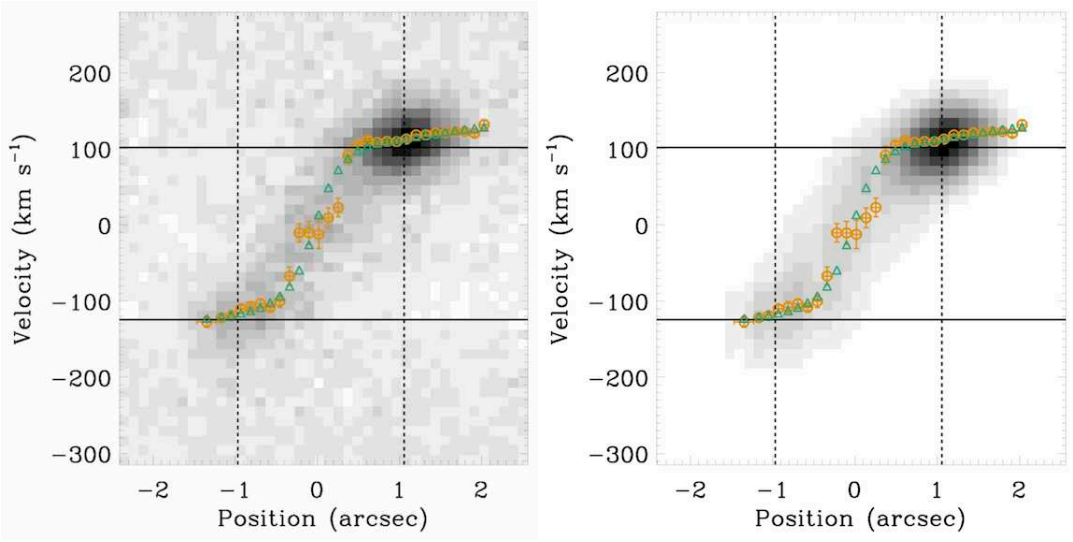

Figure 2.8 An example of our fitting procedure for a galaxy with asymmetric emission and medium extension. The **left** panel shows the observed 2-D spectral data in the region of $H\alpha$, and the **right** panel is the equivalent section of the constructed model spectrum. Both show a grey scale representing flux as a function of velocity with respect to position. Similar to that of Fig. 2.7, orange circles show the trace centroids of the emission line (bars along the positional dimension indicate bin size, not error), and the green triangles show the equivalent centroids for the constructed model. The $r_{2.2}$ radius is marked by vertical dotted lines and the extracted $V_{2.2}$ velocity is marked by horizontal solid lines. These lines of fiducial measurements do not cross directly through the trace because they are extracted from the best-fit model's intrinsic arctan function, prior to distortion by seeing and dispersion.

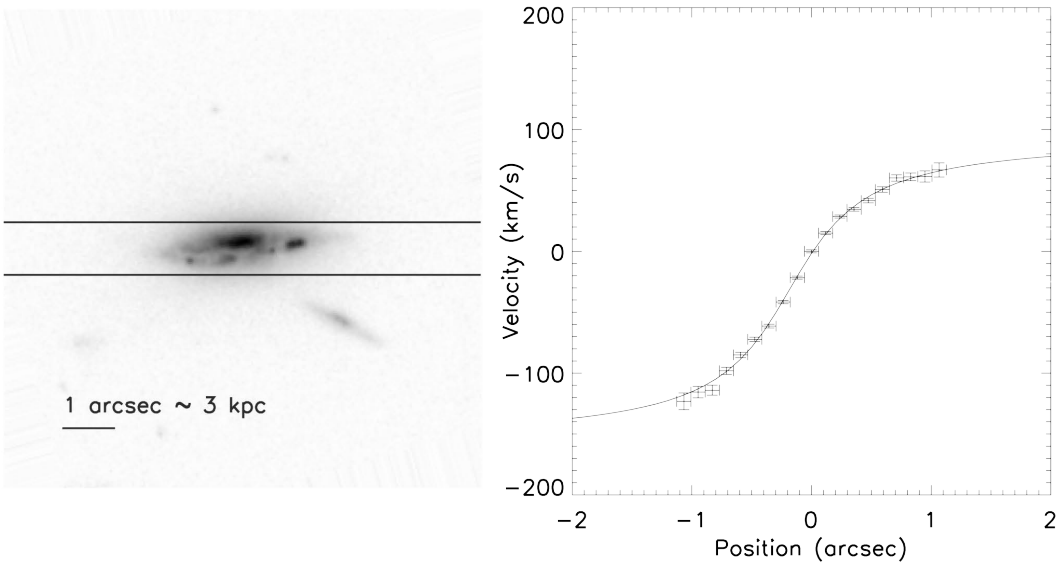

Figure 2.9 To the **left** is an HST ACS image of the galaxy kinematically modelled, and to the **right** is the result from a simple modelling code which does not take into account the effects of blurring by seeing to extract an intrinsic rotation curve, and rather fits an arctan model directly to the observed trace of the emission line.

can be extracted. Rather we construct a model 2D spectrum based on the arctan function of Eq. (2.3), which is then convolved with seeing and dispersion, and then compared to the trace of the observed data before subjected to an iterative process to find the best fit in Step 3 (§2.3.3).

A simple algorithm initially guesses values of V_a and r_t for the arctan parameters to approximately match the flat portion of the outer trace of the observed data. We lay this model rotation curve on a 2D grid, adjusting the brightness and line width in each spatial bin to match that of the trace, *i.e.* using the parameters from the two half-Gaussians in each bin. Simpler models assume a spatially-constant intrinsic line dispersion across the entire disc (Vogt et al., 1996; Weiner et al., 2006b; Metevier et al., 2006). Yet because of the widely varying intrinsic line dispersions within many of the galaxies, we implement the position-dependent dispersion measurement from the trace in the model, which accounts for spatially varying intrinsic line dispersions (see Fig. 2.10). Whereas the simulations which are constructed with constant velocity dispersion cannot

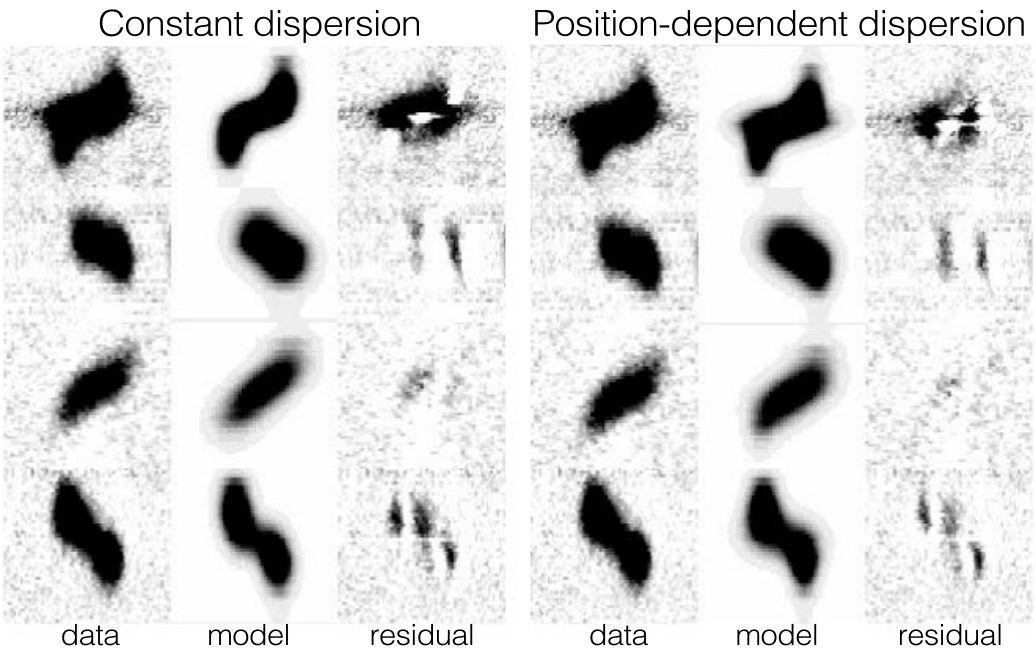

Figure 2.10 Comparing the data/trace/residuals of emission lines where the dispersion has been fixed to the median best-fit dispersion traced across the disc **(left)**, and where dispersion is allowed to vary **(right)**. The residuals are greatly reduced in the latter, by 60% on average.

assess this feature of the code, it largely improves residuals between real data and their models by 60% on average.

We finally convolve the resulting rotation curve with an independent measurement of the seeing, and the resulting peak model brightness is re-normalised, bin by bin, to that observed (see Fig 2.8). Ideally we would start with the pre-blurred emission brightness spatial profile, but that is unknown. Assuming an emission brightness profile which is substantially different from the intrinsic profile can seed a fundamental systematic flaw in the modelling process. We found that this induced a variety of biases in the rotation curve shape fitting due to the degeneracy in blurring by seeing and dispersion, which is particularly troublesome for galaxies with irregular emission line brightness profiles.

The position-dependent dispersion measured (dispersion profile) is blurred by the seeing, but we need to attempt to remove this effect so that we can blur the model by both the separate measurement of the seeing (from the alignment

stars) and by the dispersion profile (and not effectively blur by seeing twice). We can attempt to remove this effect of the blurring by seeing in the dispersion profile by fitting for a multiplicative factor. This correction factor is used to multiply the dispersion implemented in the model, and it is always less than or equal to 1. This allows the model to approach the intrinsic, 'de-convolved' rotation curve, although it will never completely recover it. This method is more successful than alternative approaches we attempted, for example adopting the collapsed light profile from the closest (in wavelength) broad-band HST image as observed through the slit, or simple functional forms of emission brightness profiles (constant, linear, exponential). We find many emission lines that are brighter at the disc edge than towards the centre, as well as asymmetric or clumpy emission distributions.

Emission brightness profiles tend to not match the broad-band flux distribution that enters the slit, neither for the band closest to the emission line of interest or for the B_{F435W} (rest-frame ultra-violet). This is due mostly to differing behaviours of dust and gas absorption between the broader-band light and the emission, and the markedly different distribution of ionising star formation compared to the underlying total stellar population. In the most extreme cases, the emission lines contribute less than 30% of the total light in a typical broad-band image of a star-forming galaxy, so emission itself would not drive the broad-band flux.

We now turn to how we apply this constructed model in a χ^2 minimisation procedure to find a best-fit for V_a and r_t of the arctan function assumed for the intrinsic rotation curve.

2.3.3 Step 3: Finding a best-fit

For finding a best-fit model, we use a robust non-linear least squares fitting algorithm based on MPFIT (Markwardt, 2009). The 5 parameters which are varied are the 2 defining arctan parameters, V_a and r_t, as well as the position of the dynamical centre (2 more parameters) and the seeing-dispersion beam

correction factor (1 parameter). The χ^2 values are calculated between the model trace and the data trace, rather than on the entire 2D frame.

Not only is this method much faster, but it results in smaller residuals because we focus the fit, in a sense, on the information that is most pertinent to the shape of the rotation curve. Simard & Pritchet (1998), Milvang-Jensen et al. (2003), Bamford et al. (2006), and Chiu et al. (2007) use the full 2D flux of the modelled spectrum to compute the χ^2 and iterate on a best-fit using a Metropolis algorithm. Yet since they must assume an intrinsic emission brightness profile (*i.e.,* exponential) which is often dissimilar to the true intrinsic emission profile, as discussed in the previous section, this places added weight in the minimisation process on extraneous portions of the model, easily pulling the fit into a local minimum away from the fiducial velocity of interest. Since this is not simply a parameter which is easily marginalised in a Bayesian method, a practical solution is to perform a χ^2 minimisation on the 1D trace itself.

However since this is not immediately evident, we conducted both 1D and 2D χ^2 minimisation procedures on a grid of simulated data, to compare how the two methods were able to recover the known intrinsic function. Out of the array of simulated rotation curves (varying in V_a, r_t, S/N, and emission extent, as described in the preamble of §2.3) a summary of pertinent slices of these simulations and subsequent degrees of model recovery can be seen in Fig. 2.11. This figure shows the output velocity (from the best-fit model) subtracted from the input velocity (intrinsic value from the arctan function before the blurring effects of seeing and dispersion are applied), and while the improved recovery by the 1D method is not dramatic, it is significant. The recovery rates of the 2D method are more likely to be overestimated in the simulations as compared to real data, since the more pristine simulated data do not adequately reproduce the irregular emission brightness profiles and various asymmetries found in real rotation curves. These features are more pronounced in the residuals used for the 2D χ^2 minimisation, whereas they are largely

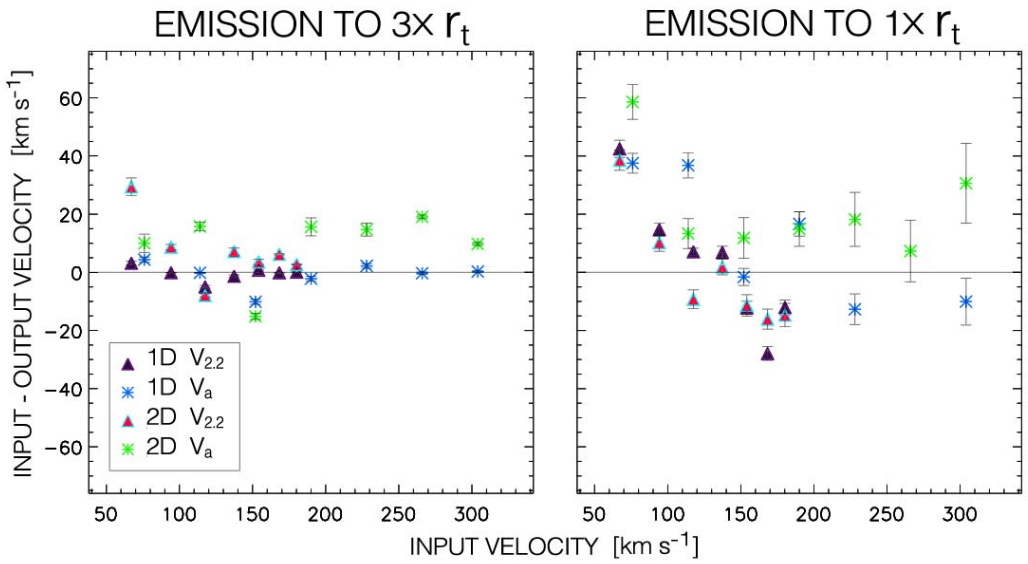

Figure 2.11 Simulations of rotation curves of varying the arctan V_a (asterisks) and extracted $V_{2.2}$ (triangles) values are attempted to be recovered by two modelling codes (1D vs 2D, see text) at two different emission extents: where emission extends to 3 times the arctan r_t **left** and 1 times the r_t **right**. Not only do these simulations demonstrate the superior performance of the 1D algorithm verses the 2D version, we also confirm that the $V_{2.2}$ values tend to be a safer velocity to extract than V_a. Note that the differences between the input and modelled output velocities in these simulations and their subsequent models are likely under-estimates of the true recovery expected in modelling real data, with its many more sources of uncertainty, asymmetry, and irregularity.

ignored by the 1D trace method, which helps to avoid the local minima which irregular and asymmetric features can create. One manifestation of this effect is seen in the error bars (errors on the mean) in Fig. 2.11, which shows how the spread in output velocities from the 2D method is consistently about 2 times larger than that of the 1D method, indicating a wider range of local minima in the former that are confirmed upon visual inspection.

To quantify uncertainties in modelling the observed spectral emission lines with their array of irregular features, we propagate the error from the measured input parameters (emission profile, seeing, and dispersion) by using a Monte Carlo approach. We simultaneously alter input parameters from random Gaussian distributions with widths matching the error in the observed parameters for each galaxy. After 100 iterations, we add the uncertainty from the resulting

distribution of output velocities to the formal fitting errors.

2.4 Summary of Chapter 2

In this chapter we have reviewed major milestones in the history of galaxy rotation curves, including the early work at high redshift. Both faint and difficult to spatially resolve, intermediate to high redshift data present a number of challenges in extracting intrinsic disc velocities for application to the TF relation.

To aid in this challenge, we aim to reduce added uncertainty and bias in selecting a fiducial velocity to extract from our modelled rotation curves at 2.2 times the scale length of the galaxy disc, selected primarily to avoid extrapolation to velocities untraced by the observed emission lines. We have adopted the arctan model for an intrinsic functional form of the rotation curve given its simplicity and utility.

We describe a method of modelling intrinsic rotation curves of 2D spectroscopic data, CURVATION, which is an innovative attempt to further reduce sources of systematic bias and uncertainty in this challenging task.

We now turn in Chapter 3 to describe the specific dataset to which we will apply this method, including the implementations of the final corrections to de-project our extracted measurements to the intrinsic fiducial velocities we seek for tracking the evolution of the TF relation.

Chapter 3

The Disc Galaxy Sample and Derived Data Products

In this chapter, we describe the observations and data on this thesis to track the mass assembly history of disc galaxies to $z \sim 1.7$ via the TF relation. The key measurements for this goal are the disc kinematics via rotation curves models, introduced in the previous chapter, and stellar mass estimates from photometric data. For the latter we employ high-resolution Hubble Space Telescope imaging in multiple filters, as well as ground-based photometry in the near infra-red. For the kinematics to model rotation curves, we use Keck spectroscopy from the DEep Imaging Multi-Object Spectrograph (DEIMOS Faber et al., 2003) as well as the Low Resolution Imaging Spectrograph (LRIS Oke et al., 1995).

Multi-object observational capability is essential in creating a large sample to address questions such as those posed in this thesis, but these capabilities until recently have been largely at optical wavelengths. The DEIMOS instrument provides state-of-the-art performance in high resolution multi-slit spectroscopy over 4,100–11,000 Å, although performance and throughput fall off past 8,000 Å. The challenge of tracking emission in disc galaxies considerably deepens much beyond $z \sim 0.9$, where the brightest singlet emission lines from star-forming galaxies, i.e., Hα, [O III], and Hβ, shift out of the typical high-performance ranges of optical spectrographs, and [O II] 3727 Å, shifts into the skyline-dominated region of red and near infra-red (NIR) spectra.

The installation of a deep depletion, red-sensitive CCD on the red arm of the LRIS has significantly improved the efficiency in the wavelength interval 8,000 Å to 10,000 Å corresponding to [O II] in the redshift interval $1.0 \lesssim z < 1.7$. This allows us to extend the initial DEIMOS dataset spanning $0.2 < z < 1.3$ to higher redshifts, to try to understand the transition from the dispersion-dominated systems observed above $z \simeq 2$, and to evaluate the nature of the M_*-TF relation 2 Gyr earlier than that probed by our DEIMOS sample.

A unique feature of this dataset is the extended time of integration for the spectroscopy. Especially at high redshift, line emission signal-to-noise (S/N) at the furthest radial reaches of galaxy discs is typically low (often <3, depending on the exact method of determining S/N) for standard integration times on 10-metre class telescopes (typically ∼1 hour, e.g., Vogt et al., 1997; Conselice et al., 2005; Weiner et al., 2006b; Kassin et al., 2007). For this reason we have observed most galaxies in this dataset for ∼6–8 hours, considerably improving S/N compared to earlier work. This makes a significant difference in whether emission lines are detected to the flattening of rotation curves, or whether they are detected at all.

Recent there has been a concerted effort to secure data from integral field unit (IFU) spectrographs. These produce 3D data (spectra across a 2D array of positions or 'spaxels') thereby yielding the full 2D velocity field as opposed to a 1D velocity curve across an axis probed by a long-slit of multi-slit spectrograph. While impressive new multi-IFU instruments are commissioning (to be discussed in 'Future Directions' section in Ch. 6), multi-slit spectrographs retain several advantages for delivering kinematics for large samples of galaxies over a wide redshift range, which is a key advantage in survey efficiency that can be leveraged to target a lower average stellar mass range than the many extant IFU samples (i.e., IMAGES, SINS: Förster Schreiber et al., 2006; Flores et al., 2006).

In this chapter we first introduce our sample selection criteria from the available photometric datasets (§3.1), and then describe the photometric mod-

elling and bulge/disc decomposition of the targets (§3.2). We explain how the stellar masses were estimated from the available photometry (§3.3), which helps to further characterise the sample and constitutes one axis of the Tully-Fisher relation of primary interest in this work. With the photometric component of the dataset described, we then move on to the spectroscopic observations (§3.4), including a simple classification scheme of the spectra which identifies the galaxies that are necessarily precluded from kinematical analysis (§3.5). We then describe the application of the rotation curve modelling scheme to the sub-set of galaxies for which it is appropriate (§3.6), including how the fiducial $V_{2.2}$ velocities were extracted and de-projected to derive intrinsic rotation speeds for application to the TF relation. We present a number of tests and checks of this method on the primary dataset (§3.7), and then discuss the special considerations of applying the modelling method to our secondary sample at high redshift (§3.8).

3.1 Sample selection

Prerequisites for constructing a multi-slit spectroscopic sample suitable for disc evolution studies are:

1. resolved morphologies — to select rotationally-supported galaxies,
2. broad-band photometry — to make a magnitude or estimated stellar mass cut for potential targets, and
3. accurate disc position angles — for slitlet placement.

Galaxies at intermediate and high redshift are challenging to resolve due to increasing angular diameter distance to $z\sim1$, compounded also by their intrinsically smaller size. Thus measurements of features of galaxies, like the orientation of the major axis, are difficult to resolve from the ground without AO due to the scale of seeing ($\sim$1 arcsec) compared to their angular extent ($\sim$1–3 arcsec). Our spectroscopic campaign is thus selected from deep imaging that

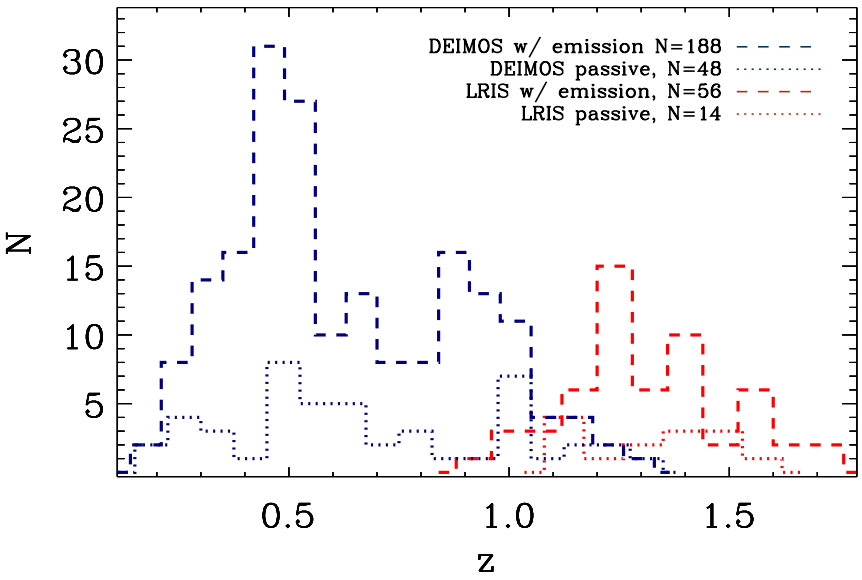

Figure 3.1 The redshift distribution of our two sub-samples (DEIMOS: 236 and LRIS: 70 galaxies). Line emission was detected in most of the galaxies targeted as shown with the dashed lines (blue and red, respectively). While all galaxies have photometric redshifts and most have significant S/N in the collapsed 1D spectra, the dotted lines show the distribution for those galaxies without significant S/N in emission as measured from the 2D slit spectra, which makes it impossible for those targets to enter the rotation curve analysis (again, blue and red, respectively).

meets these requirements from the Hubble Space Telescope Advanced Camera for Surveys (HST ACS), and a number of fields already have extensive multi-wavelength coverage suitable for extra-galactic astronomy at intermediate and high redshifts.

We focus on five fields with some of the deepest imaging and widest wavelength range of data available: (1) the Great Observatories Origins Deep Survey (GOODS) North and (2) GOODS South fields (Giavalisco et al., 2004), (3) the Small Selected Area 22 (SSA22) field (Lilly et al., 1991; Chapman et al., 2004; Abraham et al., 2007), (4) the Extended Groth Strip (EGS) field (Davis et al., 2005), and (5) the Cosmic Evolution Survey (COSMOS) field (Scoville et al., 2007). The primary sample from $z \sim 0.2 - 1.3$ (intermediate redshift, N=236), targeted with DEIMOS, is selected from the GOODS North and South fields. Our secondary $z \sim 1 - 1.7$ (high redshift, N=70) sample is targeted with LRIS

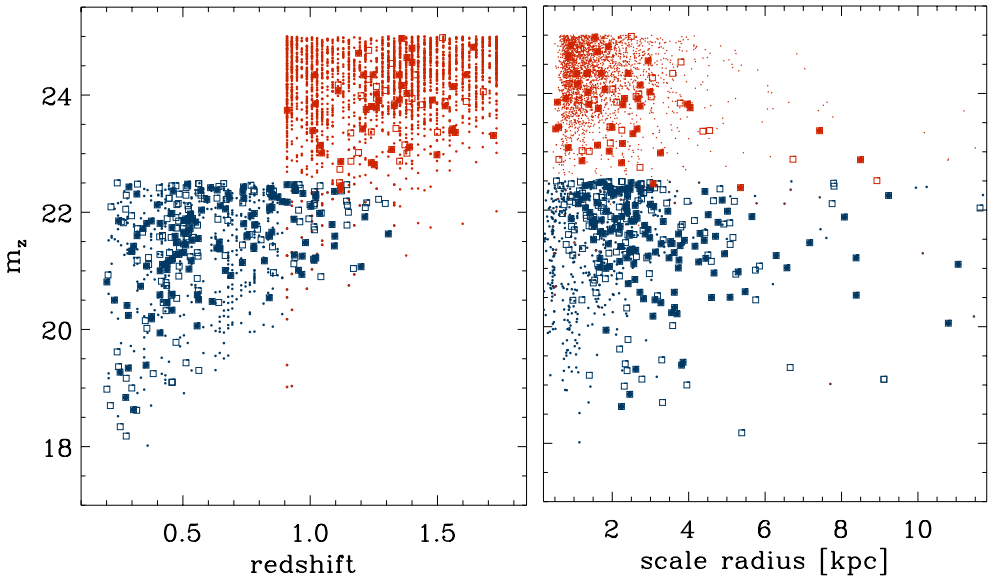

Figure 3.2 Displaying how the total underlying field population relates to the sample by plotting apparent z magnitudes verses both redshift (**left**) and size (**right**), we denote targeted galaxies with open boxes and final sample galaxies (extended emission galaxies, explained in §3.5) with filled circles, and all other field population galaxies are denoted with points. Again, the DEIMOS sample is shown in blue and the LRIS sample is shown in red. The DEIMOS field includes both m_z cuts as well as a K-band cut, explained in the text.

and spans all five survey fields listed. A summary of masks, targets, spectroscopic observations and available space and ground-based imaging in each field can be found in Table 3.1 & 3.2.

We selected our sample of spectroscopic targets to span a broad stellar mass and luminosity range. Our goal in the morphological selection of disc targets is to be inclusive of all galaxies with disc-like structure, avoiding selection of only the most relaxed and "well-behaved" spirals in favour of a more complete census, including the disturbed and morphologically abnormal population. Our sample includes visually irregular systems with elongated features, as well as galaxies with asymmetric and clumpy light distributions. We also included discs with dominant bulges. This inclusivity is a key difference in our sample as compared with earlier work (*i.e.*, Vogt et al., 1996, 1997; Conselice et al., 2005), and the main aim of broadening the morphological selection criteria was to avoid potential biases associated with selecting only symmetric spirals that

could represent only the end point of evolution and consequently bias us to locating mature systems. An inclusive sample of this type is also seen in the work of Weiner et al. (2006a) and Kassin et al. (2007).

To conduct this morphological screening, sources were visually inspected by Richard S. Ellis, Kevin Bundy, and/or SHM so that potential targets with compact morphology, without diffuse extension, were given low priority but not excluded. The DEIMOS targets were selected from a $z_{F850LP} < 22.5$ sample in the GOODS North and South fields, discussed by Bundy et al. (2005). For the LRIS targets, we applied an apparent magnitude limit of $i_{AB} < 25$ and selected sources in the redshift range $1.0 \lesssim z < 1.7$ (using photometric redshifts when a spectroscopic redshift was unavailable). This led to a sample of 50 targets per LRIS pointing. These magnitude cuts were set according to predicted sensitivity of the instruments based on prior experience with the instrument and the performance of the instrument in many previous studies in the literature. To get a sense of how the underlying field population relates to the sample, we plot both redshift and size with apparent magnitude in Figure 3.2, and denote targeted and final sample galaxies apart from the total underlying sample. The final sample galaxies (extended emission) will be explained in §3.5.

For the DEIMOS sample, within the z-band limited sample, a further photometric selection was applied, $K_s \leq 22.2$ (eliminating half of the suitable sample), to ensure a high fraction of reliable stellar mass (M_*) estimates (see §3.3). We did not apply a near-infrared magnitude cut to our LRIS sample, which makes the mass range in our highest redshift bin wider than the highest redshift bin of the DEIMOS sample.

Although spectroscopic redshifts are available for many of our targets, especially in the GOODS fields from the Team Keck Redshift Survey (TKRS) program (Wirth et al., 2004) in GOODS-N and from the VIMOS VLT Deep Survey (Le Fèvre et al., 2004) in GOODS-S, targets were not excluded when only photometric redshifts were available. Selecting within the target redshift range of $0.2<z<1.3$, photometric redshifts from COMBO17 (Wolf et al., 2004),

Bundy et al. (2005), and the respective catalogs listed in Table 3.1 & 3.2 were used wherever photometric redshifts were needed to fill in for missing spectroscopic redshifts. We have found 88% of the photometric redshifts to be within 0.05 of the spectroscopic redshifts for our targets.

Several galaxies within our sample can be found in earlier kinematic surveys, *i.e.*, Flores et al. (2006) and Weiner et al. (2006a). This is explored further in §3.7.

3.2 Photometric modelling: Bulge-disc decomposition

The HST ACS imaging (see Table 3.1 & 3.2 for filter availability per field) provides valuable structural information that can be used for translating the observed rotation curves into physically-based properties. Key requirements for both observing and de-projecting rotation curves in their analysis are the inclination, position angle (PA) and effective radius of each galaxy. We also need to separate, where possible, the light of the central bulge from the extended galaxy disc. Without this extra step, the disc sizes are in danger of being under-estimated due to the bright central peak of the bulge biasing the disc scale length towards the centre of the galaxy.

Parametric fitting, where analytic functions are applied as models for the light distributions of galaxies, was first used by de Vaucouleurs (1948) who found that the function $\exp(-R^{1/4})$ worked well to describe the projected light profile of elliptical galaxies. Later, de Vaucouleurs (1959) found that many more galaxies were accurately described as having both an inner spheroidal component, or bulge, with surface brightness Σ going as:

$$\log \Sigma(R) \propto R^{1/4} \tag{3.1}$$

with respected to projected radius R, in addition to an outer exponential disc-like component as well, going as:

$$\Sigma(R) = \Sigma(R_s) \exp[-R/R_s]. \tag{3.2}$$

parameterised by R_s, or the exponential scale length (R_s denotes the projected radius, whereas r_s denotes the true, intrinsic radius). It was later that Freeman (1970) showed sufficient evidence that the bulge component was typically constituted of dynamically 'hot' stars with large velocity dispersions, whereas the dynamically 'cooler' disc components were far flatter and largely rotationally supported.

Since then, numerous works in the literature have used parametric representations of galaxy light distributions to play an integral part of our descriptions of galaxies in assembly and evolution studies. Out of the number of procedural choices available for bulge-disc decomposition, we derive these quantities using GALFIT3 (Peng, 2010), which is a 2D parametric galaxy light fitting program, using a nonlinear least-squares algorithm. We chose GALFIT after consulting the Häussler et al. (2007) study, which compares the GIM2D (Simard et al., 2002) results with that of GALFIT of 41,495 objects in the GEMS (Galaxy Evolution from Morphology and SEDs) survey, with similar HST ACS imaging of galaxies at a similar redshift range to this study. Their tests reveal that GALFIT performs better in fitting more concentrated components (such as the bulges in our sample) than other programs written in the same spirit (*e.g.*, Simard & Pritchet, 1998; Simard et al., 2002). Also GALFIT is more resistant to crashing and computes at a faster runtime, both important features for application within a Monte-Carlo analysis, which we conduct in this study.

Before we describe the GALFIT procedure in further detail, we will first motivate the importance of accurately characterising the functional form which describes the appearance of a point in an image ('point spread function' or PSF) for the bulge-disc decomposition we seek.

3.2.1 Point spread functions

The point spread function (PSF) should account for the entire distortion of the wavefront from source to image, and for space telescope imaging, this is primarily due to instrumental effects and imperfect optics. In attempting to

parametrically model the light of an object, one must account for how the PSF will blur and possibly distort the image. We will do this by convolving the model component with a PSF to compare to the data in a nonlinear least-squares fitting algorithm like GALFIT.

There are standard codes to extract PSFs in the IDL Astronomy User's Library, but we found better results were extracted with an adapted Fortran code by Mark Sullivan. This code takes in a list of coordinates of preselected stars from the science images and produces a highly sampled PSF. We experimented with using different stars of various magnitudes and sampling area sizes. Stars were selected to be isolated with high S/N (without saturation), and in areas where the background flux was consistent with no flux gradient (*i.e.* avoiding the edges of a given HST ACS image tile). The sampling area size of the PSF is important since it determines how long GALFIT will take to convolve model components of the galaxies, which is one of the most time-consuming parts of the procedure. We determined that a PSF which was 85×85 pixels was an acceptable balance between the need for a fast runtime and a sufficiently sampled PSF for a convergent result. This was roughly where the amplitude of the wing fell below 1% of the peak flux, and experimenting with larger PSFs at 100 and 200 pixel stamp lengths made no significant difference in the GALFIT solutions.

We ran GALFIT on a variety of PSFs from different PSF extraction methods to test the difference, and the residuals were consistently and significantly smaller with the PSFs derived from the Fortran code than any of the PSFs constructed from the standard AstroLib IDL codes. A spatially dependent PSF was also attempted, *i.e.* by obtaining a PSF per HST pointing, but two problems arose: (1) unsurprising in HST fields, there are not enough good quality PSF stars to make a robust, position dependent PSF, and (2) the various pointings which had enough quality stars for individual PSFs do not differ in PSF significantly from pointing to pointing. Since the extracted PSF will not be used for anything as delicate as a gravitational lensing analysis, we do not require a further detailed PSF analysis, *e.g.*, that from the Tiny Tim software

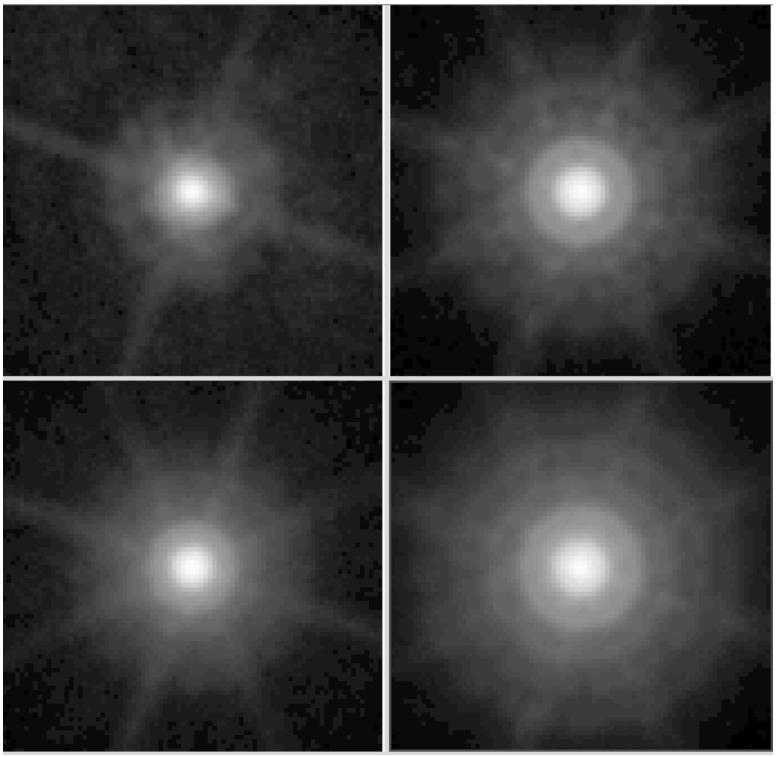

Figure 3.3 Example PSFs in the B_{F435W} (**top left**), V_{F606W} (**bottom left**), i_{F775W} (**top right**), and z_{F850LP} (**bottom right**) filters from the HST ACS GOODS North fields, extracted with the Fortran code described in the text. Note the difference in the dithering pattern from the fewer diffraction spikes in the B_{F435W} filter imaging as compared to that from the rest of the filters.

(Krist, 1993; Krist et al., 2011). By extracting stars directly as PSFs we can ensure no loss of important information due to the unique stacking in the HST field as displayed by the non-regular diffraction lines (see in Fig. 3.3).

3.2.2 GALFIT analysis

For each galaxy we extracted a 9.″03 x 9.″03 (301 x 301 pixels) postage stamp centered on the object. Neighbours were individually masked out by hand to eliminate confusion with the target of interest. For the bulge-disc decomposition, we first fit an exponential surface brightness disc component plus a 'classical' bulge component (de Vaucouleurs' profile) to every galaxy. The de Vaucouleurs (1948) profile is a special case of the more general Sérsic (1963) profile, where surface brightness (Σ) goes with respected to projected radius R

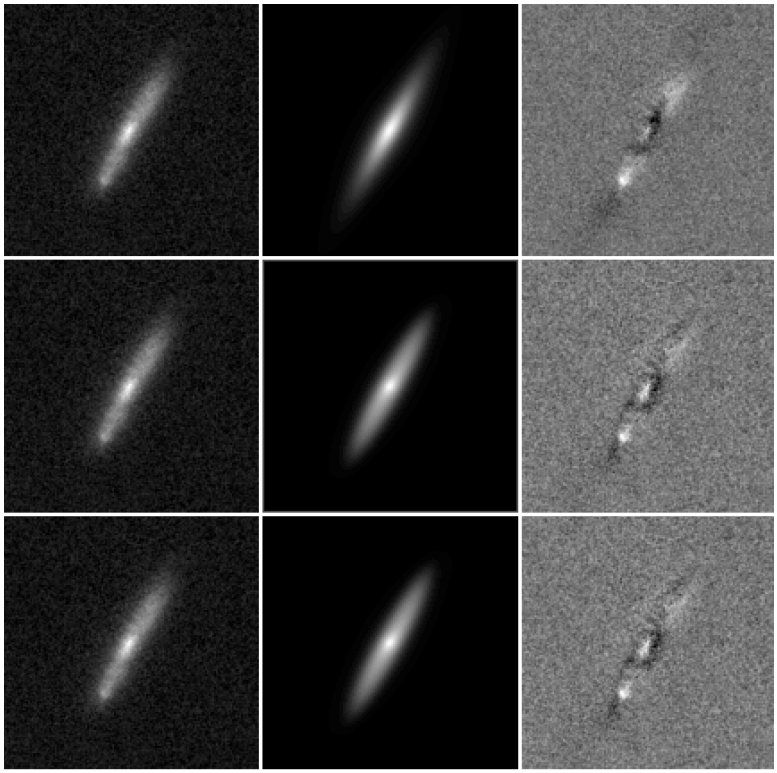

Figure 3.4 Example of GALFIT output of a galaxy (gs_B galaxy 1126 $z = 0.5$) in our sample in GOODS South, with HST ACS z_{F850LP} imaging. Shown is the observed image (left column), GALFIT model (middle column), and residuals (right column) and 'Most Constrained' (top row), 'Middle Constrained' (middle row), and 'Least Constrained' (bottom row) from our initial GALFIT test.

as:

$$\Sigma(R) = \Sigma(R_e) \exp[\kappa([R/R_e]^{1/n} - 1)], \tag{3.3}$$

parameterised by the effective radius R_e, the Sérsic index n (or concentration parameter), and the constant κ. R_e is where half the total light is contained within an isophotal ellipse.

GALFIT also solves for the total integrated flux $F_{\rm tot}$, in erg s^{-1}, for the Sèrsic component (where $R \to \infty$) is:

$$F_{\rm tot} = 2\pi R_e^2 \Sigma_e e^{\kappa} n \kappa^{-2n} \Gamma(2n) q, \tag{3.4}$$

where q is the axis ratio of the minor-to-major axes ($q = 0$–1). This description of $F_{\rm tot}$ is then used in conjunction with the Sèrsic function to integrate the total magnitude $m_{\rm tot}$, standardly defined as $m_{\rm tot} = -2.5 \log_{10} F_{\rm tot}+$ magnitude

zeropoint. This results in each Sérsic profile having seven parameters to be fit (or fixed): the centre (x_0, y_0), $m_{\rm tot}$, R_e, n, q, and the PA (position angle).

The de Vaucouleurs' profile is recovered from this more general form when the Sérsic $n = 4$, and $\kappa = -7.67$. The traditional disc-like exponential surface brightness profile is also a special case of the Sérsic profile where $n = 1$ and R_e is the scale radius, R_s (where $R_e = 1.678R_s$).

Those galaxies which yield unphysical solutions are re-fit with a single Sérsic profile component, where the Sérsic index (n) was allowed to vary. Such cases generally represent disc galaxies which are bulgeless and/or more clumpy and irregular than regular well-formed spirals. In the DEIMOS sample, ∼60% of our galaxies were adequately fit using a 1-component n-varying Sérsic profile fit, and ∼40% benefitted from a two-component bulge plus disc solution. In the LRIS sample, the percentages were ∼63% and ∼37%, respectively. This mixture gives some indication of the morphological distribution of our sample indicating that less than half are clearly well-formed spirals with a clear bulge (§3.1). Disc sizes, inclinations and PAs were taken from best-fit disc component if more than one component can be fit. To track possible biases in the disc-bulge decomposition we will later flag those galaxies for which significant bulge components were measured.

Before settling on this procedure, we experimented with various types of hard (fixed numbers) and soft (allowed ranges) constraints on the GALFIT parameter fits. Fitting a one component Sérsic profile (in addition to a sky fit) is by far the most stable fit, when varying the initial guess parameters. However a two-component Sérsic profile fit unsurprisingly has significantly better residuals, especially in galaxies with obvious bulge components. To better understand these scenarios, we ran three different GALFIT configurations on all galaxies:

1. An exponential disc and a de Vaucouleurs' profile component with n: 0.95 - 1.05, 3.95 - 4.05 (the 'Most Constrained' scenario),

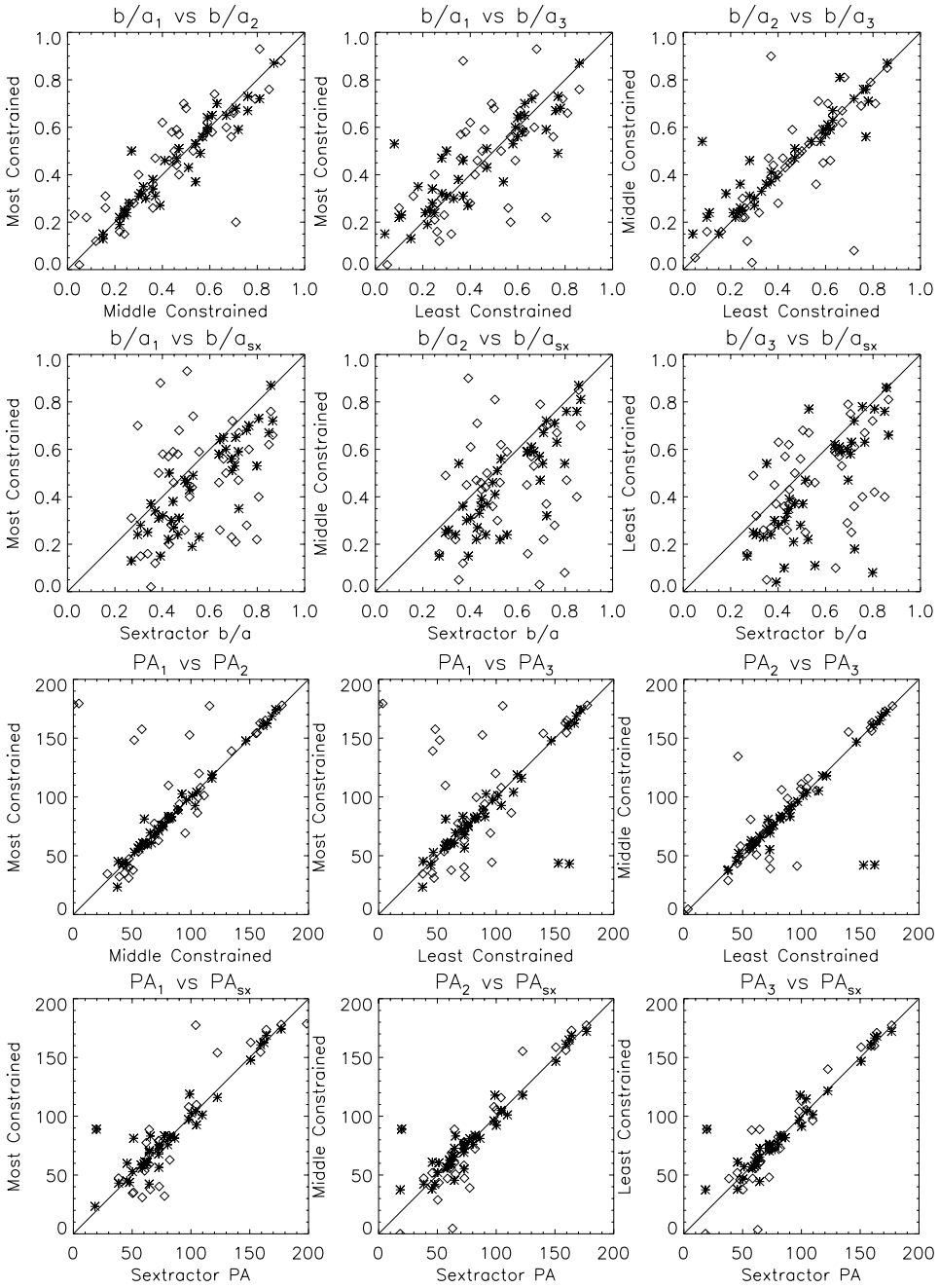

Figure 3.5 The **1st and 3rd rows** compare b/a and PA, respectively, between the Most Constrained (1), Middle Constrained (2) and Least Constrained (3) parameter fits in GALFIT to illustrate the relative difference between the method described §3.2.2. The **2nd and 4th rows** compare the 3 different GALFIT constraint runs to the original SExtractor values, which act as initial guess values for GALFIT. Asterisks are the disc components and diamonds are the bulge components, except for the 3rd (Least Constrained) run, which does not designate a bulge and disc components since the two constraint sets are the same.

2. Two somewhat constrained Sérsic profile components with n: 0.2 - 3.5, 3.5 - 8.0 (the 'Middle Constrained' scenario), and

3. Two relatively unconstrained Sérsic profile components with n: 0.2 - 8.0, 0.2 - 8.0 (the 'Least Constrained' scenario).

These are compared for each galaxy in Fig. 3.5. Other constraints for each run were that R_e must be within 0.3 and 80 pixels, the magnitude was within -2 to 2 magnitudes from the SExtractor (Bertin & Arnouts, 1996) catalog value of Giavalisco et al. (2004), and the centre x_0, y_0 coordinates of the two components had to be the same. This approach is well supported by the literature, e.g., the Häussler et al. (2007) paper on GEMS data.

With further experimentation on constraints, we ultimately removed the soft constraints (also confirmed by Peng, 2010), which showed that GALFIT runs most reliably with hard constraints or no constraints. As acceptable ranges for output parameters, soft constraints will unsurprisingly lead to results which do not converge well in the least-squares process under a Monte Carlo analysis. With appropriate masking of neighbours and bad pixels, GALFIT gave consistently reasonable results under the minimal hard constraints.

To ultimately achieve convergence on the GALFIT parameters and to assess any systematic uncertainty in the fitting technique, we ran a Monte Carlo analysis where we varied the initial guess of each parameter of the profiles, plus a value for the sky background, from those found by the SExtractor catalog results. While we adopted N=1000 for our Monte Carlo analysis, the distribution of results after N=250 was not significantly different from the final distribution. We found the parameter output distributions were much narrower than the input distributions without collecting at the edge of the allowed parameter space, so we are confident that we have probed an efficient range of input values for our analysis (see Fig. 3.6). Final parameter uncertainties from the Monte Carlo distributions are better than 5% on average, and we add these uncertainties in quadrature to the photometric errors from GALFIT.

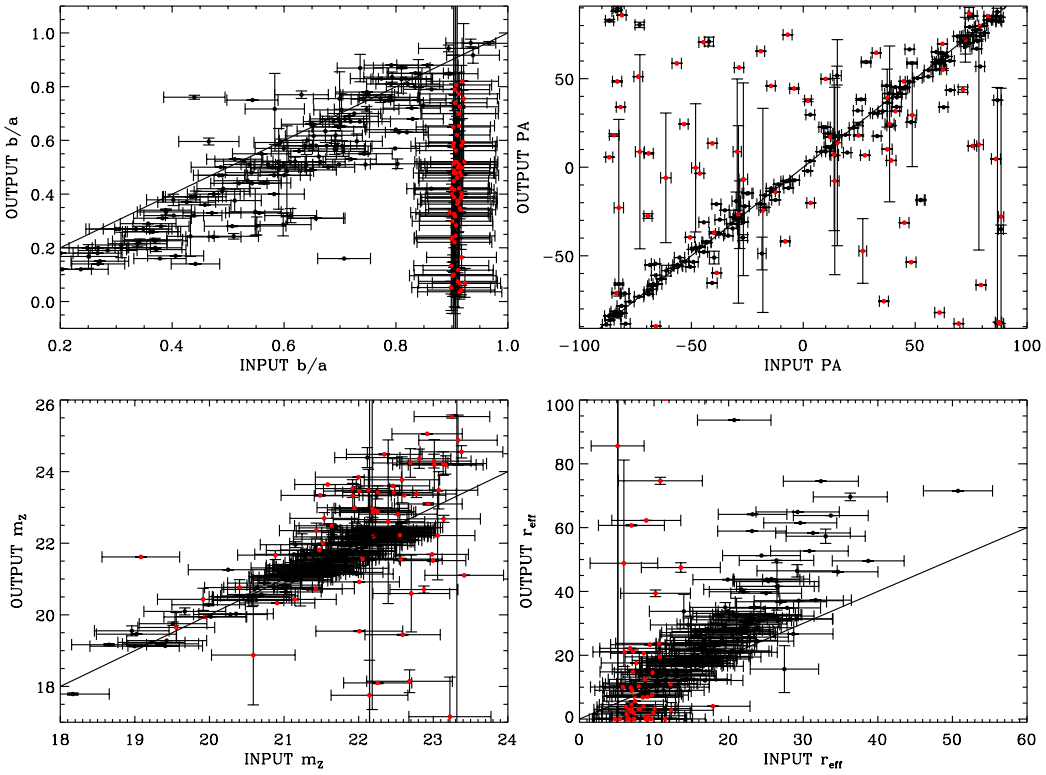

Figure 3.6 For the Monte Carlo GALFIT run, we plot the 1σ spread of input parameters with the corresponding spread in the output parameter distribution. Disc components are marked by a black point, while bulges are distinguished by an overlaying red point. The input distributions are based off of SExtractor results. In each panel we plot the one-to-one mapping with a solid black line. **In the top left panel**, the disc b/a (minor/major axis ratio) is guessed as the SExtractor value, while the bulge components are given a spread around 0.9 (nearly spherical). The output values for the discs correlate with a 0.05–0.1 scatter to their initial guesses, but the bulges show a nearly even spread across possible b/a values between 0 and 1 (although disfavour a b/a>0.8, suggesting a large number of bar component fits, confirmed by eye). **In the top right panel**, we observe that the PA (position angle) of the disc is strikingly similar to what is measured by SExtractor, although the bulge/bar component shows a wide variety of PAs. **In the bottom left panel**, the disc z_{F850LP} magnitudes, which dominate in most cases, are unsurprisingly similar to the SExtractor values, and the typically lesser bulge contribution weakens progressively towards the faintest galaxies. **In the bottom right panel**, we see clearly the effect that removing bulge contamination in disc light makes on size measurements (r_{eff}, effective radius, in this case, which encloses 50% of the component's light). A 1-component fit can under-estimate the disc size by a factor between 1 and 2.

We ran GALFIT using HST data in all four bands (B_{F435W}, V_{F606W}, i_{F775W}, and z_{F850LP}). The disc scale radii are consistent among the bands indicating no significant redshift-dependent bias within the sample (less than 5% in the DEIMOS sample and <10% for that of LRIS). In order to maximise the S/N, hereafter we used the GALFIT results from the reddest available filter (F814W or F850LP, as noted in Table 3.1 & 3.2).

Key measurements for the TF analysis which the GALFIT disc component-fitting provides, *i.e.* scale radius, position angle, and inclination, are typically measured better than 10%, except for 8% of cases. These uncertainties are propagated through to the relation parameters, resulting in larger error bars on the TF relation plots for those galaxies which are difficult to constrain.

3.3 Stellar mass estimates

Reliable stellar mass estimates were determined using a combination of infrared imaging, multi-band optical photometry, and redshift information, which was first utilised as a technique by Brinchmann & Ellis (2000). Measured magnitudes were in multiple bands were applied in a Bayesian code based on the precepts in Kauffmann et al. (2003). This work was initially presented in Bundy et al. (2005) as well as Bundy et al. (2009), and further details can be found in those papers since these estimates were not made explicitly by the author.

In summary, stellar masses are derived using a matched catalog of multi-band ACS data as well as available optical and ground-based NIR photometry (see Table 3.1 & 3.2 for ACS and infra-red availability per field). A Bayesian code fits the spectral energy distribution (SED) derived from $2''$ apertures, adopting the best spectroscopic redshift, and this SED is compared to a grid of 13440 synthetic SEDs from Bruzual & Charlot (2003). These models span a range of star formation histories (parameterized as an exponential), ages (restricted to less than the age of the universe at the observed redshift), dust

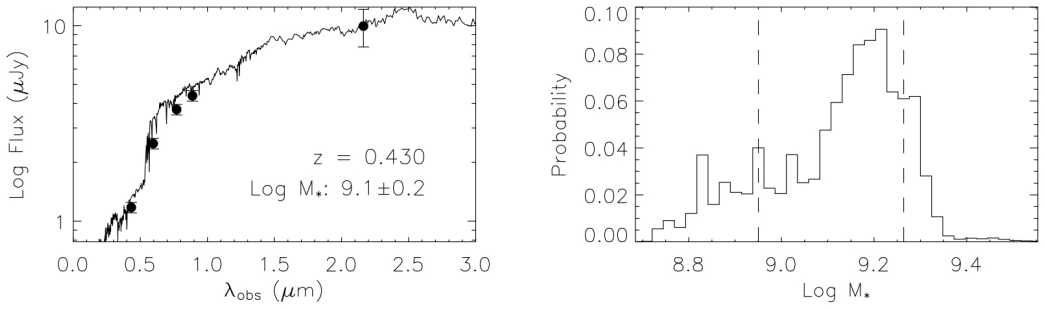

Figure 3.7 **Reproduced from Bundy et al. (2005):** the **left** panel shows an example of a spectral energy distribution (SED) of flux from 4 HST ACS bands, as well as the ground-based K-band flux. A best fitting SED from the synthetic grid of SEDs of Bruzual & Charlot (2003) is plotted along with the data points. In the **right** panel we see the posterior probability distribution of the likely stellar mass. The vertical dashed lines indicate the 1σ confidence interval in teh derived stellar mass, which is displayed in the left panel (9.1 ± 0.2 dex in $\log[M_*/M_\odot]$) for this $z = 0.43$ galaxy).

content, and metallicities. The stellar mass is estimated by multiplying the derived K-band mass-to-light ratio by the observed K-band luminosity derived from the `MAG_AUTO` total Kron magnitude determined by SExtractor (Kron, 1980). Assuming a Chabrier (2003) initial mass function (IMF), the probability for each fit is marginalised over the grid of models giving a stellar mass posterior distribution function, the median of which is the catalogued value.

In the DEIMOS sample, the final matched catalog is substantially complete to a limiting magnitude of K_{AB}=23.8, deeper than our spectroscopic limit. At the magnitudes probed, the uncertainties inferred from the width of these posterior functions is less than 0.1 dex. Including systematic errors (see Bundy et al. (2005) for a full discussion), we determine that the stellar masses are reliable to better than 0.2 dex, modulo uncertainties arising from the IMF normalisation and assuming the SED library accurately represents the objects under study.

For the LRIS sample, the uncertainties inferred from the median 68% equivalent width of these posterior functions is 0.174 dex. In order to determine the systematic uncertainties arising from combining different sets of photometry

for the LRIS part of our sample (see Table 3.2), we compare mass estimates for our sample in the different fields using different combinations of the available filters, *e.g.*,compare different mass estimates of galaxies from SSA22 using different combinations of the available photometry in EGS. The resulting dispersion in the distribution of stellar mass estimates ranges per galaxy from 0.005 to 0.1 in dex, with a median standard deviation of 0.052, which we add in quadrature to each galaxy's SED median posterior width. The combined stellar mass uncertainty is better than 0.2 dex for over 80% of our sample.

An attempt should also be made to understand systematic errors beyond what can be gleaned from the width of the probability distribution, which only includes the effects of mass degeneracies in the model parameter space (accounting for 0.1–0.2 dex of uncertainty), in addition to the photometric errors described above. Most likely, the largest systematic source of uncertainty is from the assumed Chabrier (2003) IMF. Masses derived assuming this IMF can be converted to other IMF assumptions by adding/subtracting a fraction of a dex from the final stellar mass estimate, *i.e.* for a Salpeter (1955) add 0.3 dex. The IMF may not be universal, but it is likely to be 'lighter,' in terms of M/L ratio, in spiral galaxies (Bell & de Jong, 2001; Cappellari et al., 2006; Brewer et al., 2012).

The choice of population synthesis models can introduce systematic uncertainties as well. For instance, Maraston et al. (2006) show that popular recipes such as those in Bruzual & Charlot (2003) do not accurately chart the evolution of thermally pulsing asymptotic giant branch stars. While we note this potential source of error, we do not explicitly correct for it in estimating stellar masses, since recent studies put into question the validity of the Maraston et al. (2006) results at the redshifts of interest (*i.e.* Kriek et al., 2010; Zibetti et al., 2012). Until our knowledge on the subject becomes more complete, we adopt the models of Bruzual & Charlot (2003).

In order to construct a self-consistent TF relation, we apply an aperture correction to the total stellar mass estimates (i.e., for a given fiducial radius,

an aperture stellar mass at that radius compared to the velocity measured at that fiducial radius). We extract equivalent Kron radius aperture fluxes on the z_{F850LP} band data to get the flux equivalent to that used in the total stellar mass estimates. We then take a scaled-down aperture flux within the given fiducial radius, and compare this to the Kron radii flux thus deriving a total-to-enclosed flux ratio. Assuming the z_{F850LP}-band and K-band are roughly equivalent stellar tracers, we can use this ratio to estimate the enclosed stellar mass. This approach maximizes the utility of the HST z_{F850LP} images which have much better resolution than our ground-based K-band data, thereby giving us the resolved mass distribution throughout the disc to match the detail seen in our rotation curves. The average reduction in stellar mass at $r_{2.2}$ is -0.187 dex compared to the total stellar mass estimates to the Kron radius.

3.4 Spectroscopic data

We now turn to the description of the spectroscopic dataset, which is in 2 parts: the pre-2008 DEIMOS campaign (§3.4.1), and the post-2008 LRIS campaign (§3.4.2). Because we are interested in the 2D segments of specific emission lines in the spectra, particular care was taken to separate the reductions of a given mask observed at different hour angles (and therefore different parallactic angles), taken on different runs, or observed under varying conditions. A scheme was developed to coadd 2D spectra of the same target from multiple observation sets prior to further analysis (§3.4.3).

3.4.1 DEIMOS observations

Over a number of seasons spectroscopic data was collected for this sample with the DEIMOS (DEep Imaging Multi-Object Spectrograph Faber et al., 2003) instrument on Keck II. In total, 236 galaxies were drawn from the target list discussed in §3.1 (17% of total sample), simply chosen to maximise the number of objects with best position angle alignment with that of the mask.

Slit masks were designed with position angles (PAs) within ±30° of the SExtractor catalog PAs in order to minimise tilt angle corrections in the reduction process. The 1200 l mm^{-1} grating blazed at 7500 Å was used with 1″slits (with the exception of 7 galaxies observed with the 600 l mm^{-1} grating blazed at 7500 Å). In this configuration a spectral resolution of 1.7 Å was achieved, corresponding to a velocity accuracy of 30 km sec^{-1}. All DEIMOS data were reduced by Kevin Bundy using the automated SPEC2D pipeline[1] developed by the DEEP2 survey (Newman et al., 2012; Cooper et al., 2012). The SPEC1D package[2] (Davis et al., 2003) was used to extract 1D spectra from the rectified 2D spectra produced by SPEC2D. The combination of 1D and 2D spectra were analysed using the ZSPEC software, also developed by DEEP2 (Coil et al., 2004), which fits a linear combination of galaxy, emission line, and stellar template spectra to each spectrum and allows the user to select the best-fitting template, thus determining the spectroscopic redshift. This redshift was used as the initial guess for the systematic velocity in our rotation curve models discussed below.

3.4.2 LRIS observations

For our $z > 1$ sample, exploit the sensitive region of LRIS (Low Resolution Imaging Spectrograph Oke et al., 1995) newly-installed red-side CCD, which has a greater efficiency over DEIMOS at ∼9000 Å (Rockosi et al., 2010) for which to target high $z > 1$ O[II]. From a prioritised list of typically 25 suitable targets per LRIS pointing discussed in §3.1, on average ∼10 of these were included per mask (20% of total sample). This was due to the requirement that slits must be suitably-oriented (all within ±45° of the mask PA) in addition to the accommodation of unrelated targets for simultaneous science campaigns. In designing multi-slit masks for LRIS, we aligned 1″ slitlets to the major axes of our targets as fit by SExtractor. The position angle (PA) of the mask was

[1]http://astro.berkeley.edu/∼cooper/deep/spec2d/
[2]Based on http://spectro.princeton.edu/idlspec2d_install.html

then selected to minimise slitlet tilts while maximising target count. We used the 600 l mm^{-1} grating blazed at 10000 Å, providing a instrumental velocity resolution of 58 km s^{-1} at 9000 Å. The spectroscopic LRIS data were reduced by Andrew B. Newman, using techniques described in detail by Newman et al. (2010) with the code developed by Kelson (2003). In this technique, sky modelling and subtraction is carried out with sub-pixel sampling of the background.

3.4.3 Co-additions

Because the exact positioning of an emission line can vary from one observation to the next (by $\sim$0.″2), $\approx$100 Å wavelength 'cutouts' were extracted around key emission lines of interest (the [OII] 3727 Å doublet, Hβ, the [OIII] 4959, 5007 Å doublet and Hα) for the co-addition of different reductions between varying observation runs on different nights.

Given a set of cutouts for the observation sets of a particular galaxy and emission line, optimally-weighted co-additions were conducted with weights based on the S/N and seeing full-width-half-max (FWHM) measured from alignment stars on the corresponding slit masks. Typically 5-6 alignment stars were included on each mask. Relatively sky-free windows (with $\Delta\lambda \lesssim 500$ Å) were selected on both the blue and red sides of each alignment star spectrum. The stellar flux in these windows was weighted by the inverse variance (as output from the reduction pipeline) and collapsed along the wavelength direction to obtain a stellar profile fitted with a Gaussian. The width and peak were used to estimate the S/N and FWHM for the blue and red components of each alignment star. The average FWHM across a mask and the average star-by-star ratio of S/N values provide the seeing FWHM and relative S/N for that observation set. The typical spread in FWHM among stars on a given mask is 0.03 arcsec. The weight of each observation set was then given by $w = s/f^2$, where s is S/N and f is the FWHM, and these were normalised by the weights of all the co-added masks.

Across all observing runs, the seeing varied from $0\farcs6$ to $1\farcs2$, so whenever measurements of the seeing are needed in the dynamical analysis, we adopt the weighted average value measured from the alignment stars in the final co-added observations. This measurement is preferred to the more standard acquisition of the seeing from the photometric images of the alignment stars during the alignment process. This way, we not only refer to seeing integrated over the entire exposure time of the spectra, but we also account for systematics in the observing, reduction, and co-addition process (which use different weights for different exposures).

All emission line cutouts were inspected by eye and occasionally rejected if the region extended beyond the detector area or if there was an artefact in the data that could interfere with the line of interest. To perform the co-addition, each 2D cutout was first rectified to a regular grid in wavelength and spatial position using the 2D wavelength solution output by the SPEC2D or Kelson (2003) pipeline for the DEIMOS and LRIS samples, respectively. We located the peak of the continuum along the spatial axis by collapsing the 2D cutout in the wavelength direction, initially masking out the emission feature. The collapsed profile was fit by a Gaussian with the resulting peak taken as the galaxy centre. In rare cases, the continuum was so weak that a position could not be determined without including flux from the emission line itself. The final centring of each cutout was verified by eye, and the cutouts were co-added with appropriate weighting after alignment in both wavelength and central continuum position.

Table 3.1: Summary of DEIMOS Observations and Data

Field	N_{msk}[1]	N_{obj}[2]	t_{exp}[3]	obs. date[4]	seeing	HST filters[5]	Ground IR Phot[6]	Catalog[7]
GOODS N	6	168(44,36)	21.6–28.8 ks	Mar 2004–Apr 2008	0.″97	*F435W, F606W* *F775W, F850LP*	MOIRCS (K_s) on Subaru	Bundy et al. (2009)
GOODS S	3	70(15,12)	21.6–28.8 ks	Mar 2004–Apr 2008	0.″99	*F435W, F606W* *F775W, F850LP*	ISAAC (K_s) on ESO VLT	Retzlaff et al. (2010)

Table 3.2: Summary of LRIS Observations and Data

Field	N_{msk}[1]	N_{obj}[2]	t_{exp}[3]	obs. date[4]	seeing	HST filters[5]	Ground IR Phot[6]	Catalog[7]
EGS	2	11(3,3)	30.0 ks	26–28 Jun 2009	1.″05	*F606W, F814W*	Palomar (JK_s)	Bundy et al. (2006)
		12(2,2)	14.4 ks	”	0.″93			
SSA22	2	13(3,3)	22.5 ks	”	0.″78	*F814W*	UH 2.2m (JHK_s)	Capak et al. (2004)
		12(2,1)	12.0 ks	”	0.″89			
GOODS N	1	8(1,3)	34.8 ks	5–6 Apr 2010	0.″86	*F435W, F606W* *F775W, F850LP*	MOIRCS (K_s) on Subaru	Bundy et al. (2009)
COSMOS	1	9(2,1)	28.8 ks	7 & 10 Jan 2011	0.″82	*F814W*	WIRCam (K_s) on CFHT	McCracken et al. (2010)
GOODS S	1	5(1,1)	25.2 ks	28 Feb 2011	0.″98	*F435W, F606W* *F775W, F850LP*	ISAAC (K_s) on ESO VLT	Retzlaff et al. (2010)

[1]number of masks per field
[2]number per mask and those of which are (compact, passive), see §**??**
[3]total integrated exposure time per mask
[4]dates observations were taken
[5]filters of HST ACS imaging available for size measures
[6]Ground-based infra-red photometry available for SED fitting, in addition to further optical filters (not shown)
[7]Reference to photometry matching catalog

3.5 Spectroscopic classifications: extended, compact, and passive

In this study, we have avoided quality culls of the data, which can be arbitrary and bias results in unintended ways. Even if the emission in a galaxy is not perfectly symmetric, a model should still be attempted (with its potentially broader errors quantified) so that a full census of rotationally supported galaxies are accounted for in scaling relations. We must therefore ensure that the emission being modelled is resolved in order to not bias our results in forcing fits to spectra which reveal no intrinsic information about the galaxy dynamics. There are two situations in which this resolution criterion may not occur: (1) when the angular extent of the galaxy is insufficient compared to the seeing and spatial sampling of the instrument, and (2) when the galaxy may be sufficiently extended in broad band imaging but the spectroscopic emission remains unresolved. Our morphological selection, which avoids compact objects, has effectively de-selected the first category, so we now address the second.

Ideally, the line emission must extend beyond the seeing-dispersion beam. This is effectively the point-spread-function of a spectra, represented by a 2D Gaussian, where a point source would be blurred by the seeing in the spatial direction and the instrumental dispersion in the spectral direction. Emission must extend past this point-spread beam in order to robustly model the dynamics with the arctan function, and we have generally found that this corresponds to emission extended past one disc scale radius at the redshifts of interest in this study.

In testing the performance of the modelling code with simulated data of varying emission extents at the resolution of DEIMOS, too many possible models are consistent with the data if this simple criterion regarding the emission line extent is not met (see Fig. 3.8). By removing flux from the outer disc emission in the data progressively and re-fitting the model, the simulations are

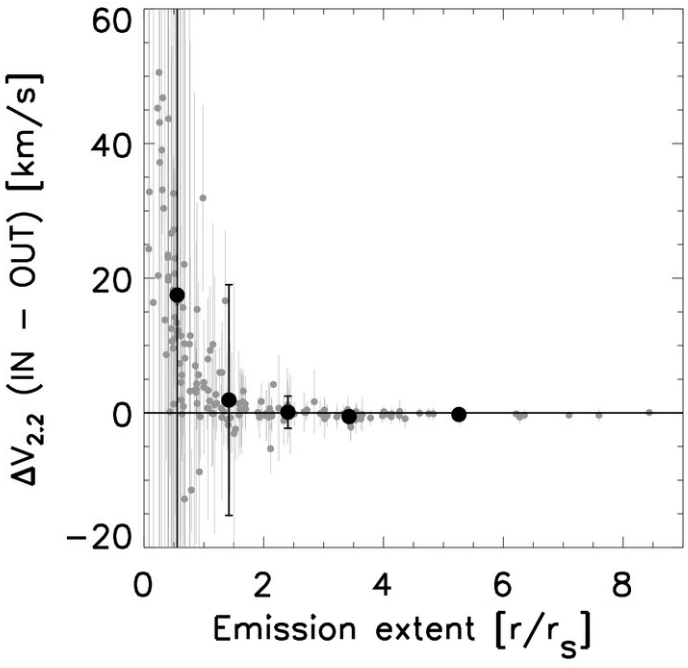

Figure 3.8 Recovery of velocities extracted at 2.2 scale radii from modelled rotation curves of simulations of varying turnover radii and asymptotic velocities with distributions similar to what is found in our dataset. When emission extends past 1 scale radius, the effect is dramatic and velocities are typically known within 5%. This typically corresponds to emission extending past the seeing-dispersion beam of the spectrum.

confirmed in the data: that $V_{2.2}$ cannot be successfully recovered (better than 5%) when emission does not extended past one disc scale radius.

We thus apply this criterion to define that subset of our sample for which emission line data can be appropriately modelled, marking the difference between spectroscopically **compact** and **extended** discs. Studies which do attempt to dynamically model compact, unresolved kinematics in emission will very likely introduce scatter into their scaling relations. Unresolved rotational velocity gradients, in both IFU and multi-slit datasets, will propagate through the instrument as increased dispersion, degenerate with the intrinsic velocity dispersion in the optical and NIR -emitting gas of the galaxy. Especially if the unresolved velocity gradient of the inner solid body rotation is the only part of the galaxy with sufficient S/N, fitting a model such as the arctan function

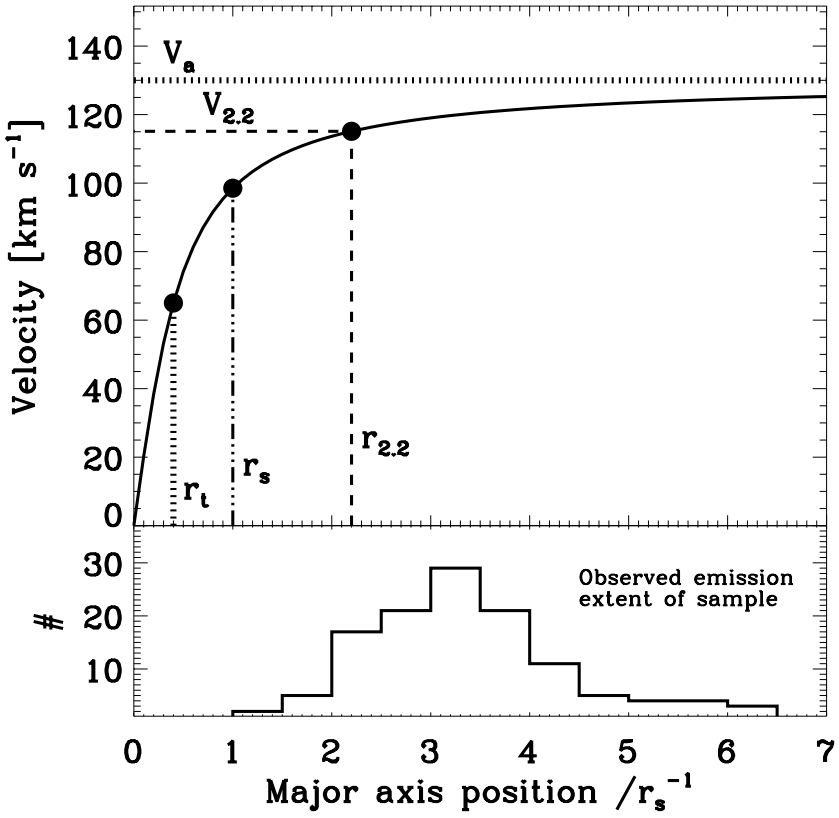

Figure 3.9 A functional arctan rotation curve with various characteristic radii (from Ch. 2, §2.2.1) shown as dimensionless factors of the disc scale length (r_s^{-1}). The histogram below shows the extent to which we can reliably trace emission lines in the *extended* sub-sample of the DEIMOS sample. In our TF relations, we have opted to use $V_{2.2}$, the velocity at $r_{2.2}$, and since ∼90% of these galaxies are traced to $2.2r_s$ (and all to at least the r_s, by design), this helps to minimise uncertainties arising from extrapolation.

in Eq. 2.3 will result in poorly constrained extrapolated velocities toward the outer disc, e.g. any velocity which is meant to sample the flat part of the rotation curve for a Tully-Fisher study (Courteau, 1997; Miller et al., 2011, 2012).

Of the 236 DEIMOS spectra, 129 show at least one emission line that would classify as extended, 59 have only compact emission lines that sample the unresolved central region, and 48 are **passive**, which show no significantly detected emission lines across the 2D spectrum, although weak lines may be recovered in the integrated spectrum (Fig. 3.10, Table 3.3).

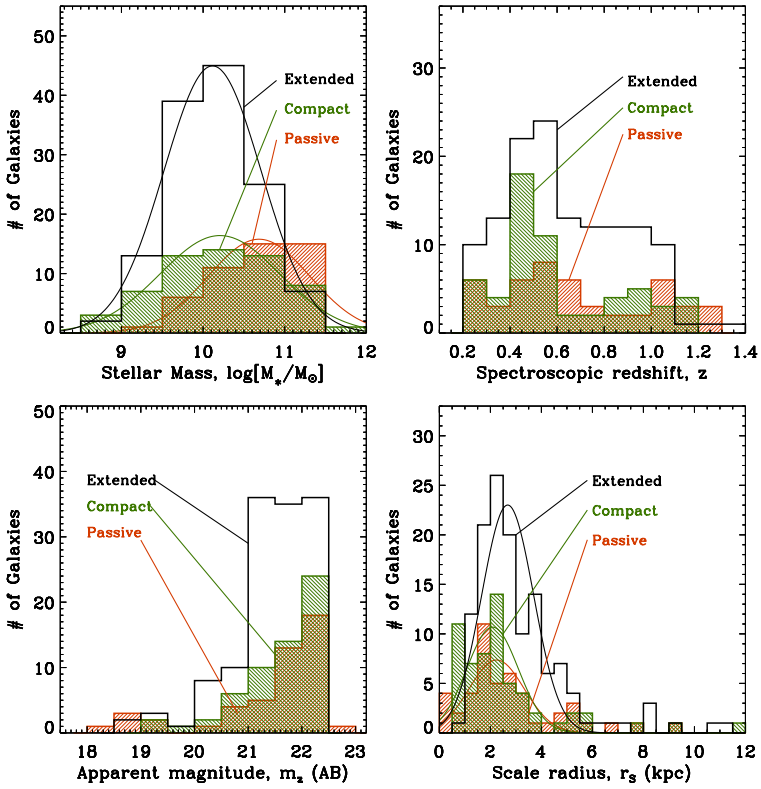

Figure 3.10 The properties of galaxies in our DEIMOS sample in terms of the distributions of stellar mass estimates, spectroscopic redshifts, z_{F850LP} apparent magnitudes, and disc scale radii. Each histogram is partitioned into the 3 spectral categories: extended emission lines (black, N=129), passive spectra with no emission (orange, N=49) and spectrally compact sources where emission does not extend beyond the central-most regions of their discs (green, N=59) (see §3.5 and Table 3.3 below).

Table 3.3: DEIMOS Sample Best Gaussian Fits of Stellar Mass and Scale Radii Distribution

Emission Classification	N	$\langle \log M_* \rangle$[1]	σ_{M_*}[2]	$\langle r_s \rangle$[3]	σ_{r_s}[4]
Extended	129	10.11±0.05	0.60	2.68±0.09	1.02
Compact	59	10.21±0.10	0.73	2.09±0.13	1.01
Passive	48	10.69±0.09	0.62	2.24±0.16	1.08
TOTAL	236				

[1]best-fit gaussian centroid of log stellar mass
[2]*FWHM* of best-fit Gaussian of log stellar mass
[3]best-fit gaussian centroid of scale radii in kpc
[4]*FWHM* of best-fit Gaussian of scale radii in kpc

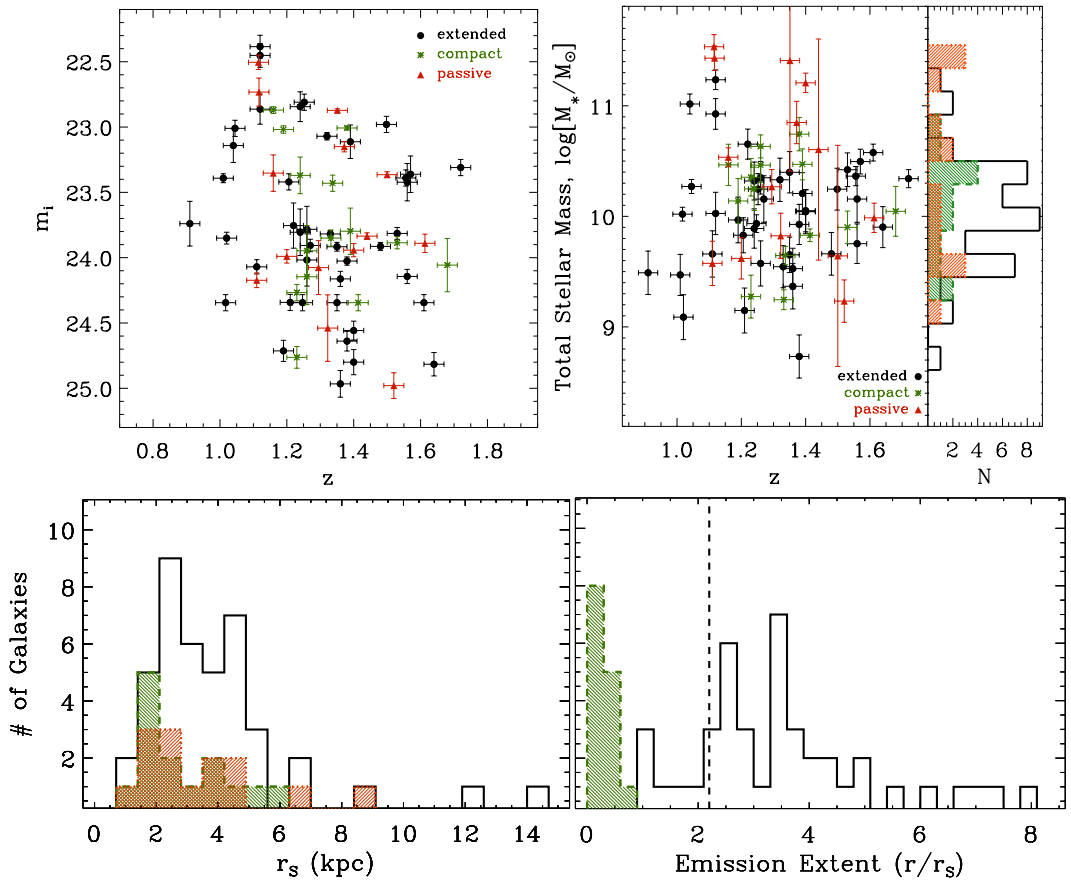

Figure 3.11 For our LRIS sample, distributions of redshift, stellar mass, exponential disc scale radius (r_s), and the extent of [O II] line emission (measured in terms of the disc scale radius, r_s). The equivalent emission extent distribution for the DEIMOS sample is in Fig. 3.9. As with the DEIMOS sample in Fig. 3.10, we partition this sample into the three spectral categories discussed: extended line emission (black line, N=42), compact line emission (green dashed line, N=14), and passive sources (orange dotted line, N=14). In the last panel, the fiducial radius of 2.2 times the disc scale radius, $r_{2.2}$ (§2.2.2), is plotted with the vertical black dashed line.

Of the 70 LRIS spectra, 42 show sufficiently extended emission, 14 have compact emission lines, and 14 are passive in emission in the 2D spectrum (see Table 3.3). In terms of percentages, this 60/20/20 composition of extended, compact, and passive spectral emission respectively, is similar to the equivalent mix (55/25/20) seen in the DEIMOS sample.

The bulk of our analysis is thus based on the combined 171 galaxies with extended line emission from both the DEIMOS and LRIS datasets. While

this subsample makes up only 56% of our initially targeted sample, the three spectrally classified subsets are not statistically drawn from different distributions in either redshift or apparent magnitude (Fig. 3.10 & Fig. 3.11). The only differences amongst the 3 subsamples concerns their disc sizes and stellar masses, yet these differences are not statistically strong (see Table 3.3). Discs with extended line emission have larger scale radii than those of the compact and passive subsamples, and passive galaxies are largely drawn from the upper end of the total stellar mass distribution. The spectrally compact objects as well as the spectrally passive objects have larger stellar masses by 0.2 dex than discs with extended emission. Spectrally passive discs have only slightly redder $I - K$ colours (again by $< 1\sigma$) than the distribution width of extended emission galaxies. These differences are not surprising given the hierarchical paradigm of galaxy formation and evolution and do not lead us to suspect that our combined working sample of 171 disc galaxies is biased in its range of physical properties compared to the original parent selection for a comprehensive TF study.

3.6 Extracting intrinsic disc velocities

We have described two distinct samples of galaxies that together comprise the disc galaxy sample of this thesis, defined primarily by their redshift range (intermediate vs. high redshift) and the Keck instrument with which they were targeted (DEIMOS vs. LRIS). We have also discussed the major spectroscopic classifications of the observed sample, which are kept as simple as possible to avoid unnecessary exclusion of any type of rotationally supported galaxy in the universe above the magnitude/mass limits. Our aim is to reduce biases in Tully-Fisher analysis brought about by quality culling of the data.

However, galaxies with unresolved emission must be removed from the rotation curve fitting sample, or else the resulting Tully-Fisher relation would be plagued with irrelevant velocity measurements. Thus we extract the intrinsic

rotation curves from the spectroscopically extended sub-sample. In this sub-sample, we robustly trace the rotation curve with at least one optical emission line to $r_{2.2}$ for $\sim$90% of our **extended** galaxies (Fig. 3.9).

We use the method described in §2.3, and all the observed emission lines in a given spectrum are treated independently by the CURVATION code (although only [O II] is visible for galaxies above z$\sim$0.9). All traces are visually inspected to ensure that spurious reduction artefacts do not interfere with the fit, such as a sub-optimally subtracted sky line. Examples of our spectral data and respective best-fit model rotation curves can be found in Fig. 3.12 and Fig. 3.13 for the DEIMOS sample and Fig. 3.18 for the LRIS sample.

The velocity at $r_{2.2}$ is calculated from the best-fit arctan mode, where $r_{2.2}$ is measured from the z_{F850LP} band HST data (see §3.2). For the $\sim$10% of the extended sub-sample that does not directly probe $r_{2.2}$, we must infer $V_{2.2}$ by extrapolating beyond the point of maximum emission extent in the best-fit rotation curve. However, we are confident in these extrapolations, since by design, all of the rotation curves in this sub-sample were constrained from galaxies where emission extends to at least the scale radius (§3.5, Fig. 3.8, and §2.3).

Each emission line is fit independently with separate $V_{2.2}$ extractions which are found to be consistent to 1σ in $> 90\%$ of our galaxies. We combine the emission line fits for the same galaxy into a final weighted average of $V_{2.2}$ and propagate the error in $r_{2.2}$ into the final uncertainty.

Because the slitlets were determined by the SExtractor catalog position angles (PAs), and this measurement was subsequently refined by the GALFIT bulge-disc decomposition, the extracted $V_{2.2}$ measurements must be corrected for the effect due to any the misalignment between the PA of the DEIMOS slit and the major axis of the galaxy as determined from GALFIT (no significant PA offsets exist in the LRIS dataset). The extracted velocities must also be deprojected for effects of inclination. Not having observations perpendicular

to the major axis is the central disadvantage of slit spectra compared to IFU spectra, since the full velocity field allows for a better characterisation of the kinematic axis. Even if the DEIMOS observations in particular offer a factor of 2-3 improvement in spectral and spatial resolution compared to IFUs like the FLAMES/GIRAFFE instrument on the VLT, we must still attempt to quantify the effects of inclination uncertainty. We propagate the spread in likely inclination resulting from the Monte-Carlo analysis of the GALFIT runs (described in §3.2), which results in large uncertainties in the few examples where inclination is not well constrained, but most uncertainties are mild (<5%) to moderate (<10%).

Adopting the simple geometrical convention $i = 0°$ for face-on and $i = 90°$ for edge-on discs, the inclination correction is:

$$V_{corr} = \frac{V_{obs}}{(\sin i)}, \tag{3.5}$$

$$i = \cos^{-1}\sqrt{\frac{(b/a)^2 - q_0^2}{1 - q_0^2}}, \tag{3.6}$$

where $q_0 \simeq 0.1$-0.2 represents the intrinsic flattening ratio of an edge-on galaxy (Holmberg, 1958; Haynes & Giovanelli, 1984; Courteau, 1996; Tully et al., 1998). Although the precise value depends on morphology, the uncertainty leads to changes in the final velocity measurement on the order of 1 $\mathrm{km\,s^{-1}}$ (Pizagno et al., 2005; Haynes & Giovanelli, 1984). We assumed $q_0 = 0.19$ for all systems, similar to Pizagno et al. (2005).

For the PA offset, we determine a correction:

$$V_{corr} = \frac{V_{obs}}{\cos(\Delta PA)}. \tag{3.7}$$

again from simple geometrical assumptions, and accounting only for the misaligned slit component of the true major axis. Only 10 galaxies in our extended sample have velocity corrections arising from a PA offset greater than 10%, and no PA offset exceeds 45°.

We apply these two corrections to produce a catalog of corrected $V_{2.2}$ measurements, where the effects of seeing, velocity dispersion and the emission line brightness profile are accounted for in the model (see Table 3.4 for the DEIMOS sample). As explained in §3.3, to compare like with like in our TF relations, we match $V_{2.2}$ to an estimate of the stellar mass within $r_{2.2}$. In the DEIMOS sample, in order to compare this *enclosed* relation to a more familiar construction of the TF relation used in previous studies, we also consider a *total* mass relation, which compares the stellar mass estimated from the Kron radius with the velocity associated with the optical radius $r_{\rm opt}$, defined for an exponential profile as one enclosing ∼83% of the light, or $3.2r_s$. While this measurement of $V_{\rm opt}$ is marginally comparable to the V_{circ} or V_{max} of many previous intermediate-redshift studies, $r_{\rm opt}$ is much more consistent between discs than the r_{max} or asymptotic limi used in those studies (more details in §2.2.2). We compare the effect on the TF relation of these various fiducial velocity choices in Chapter 4.

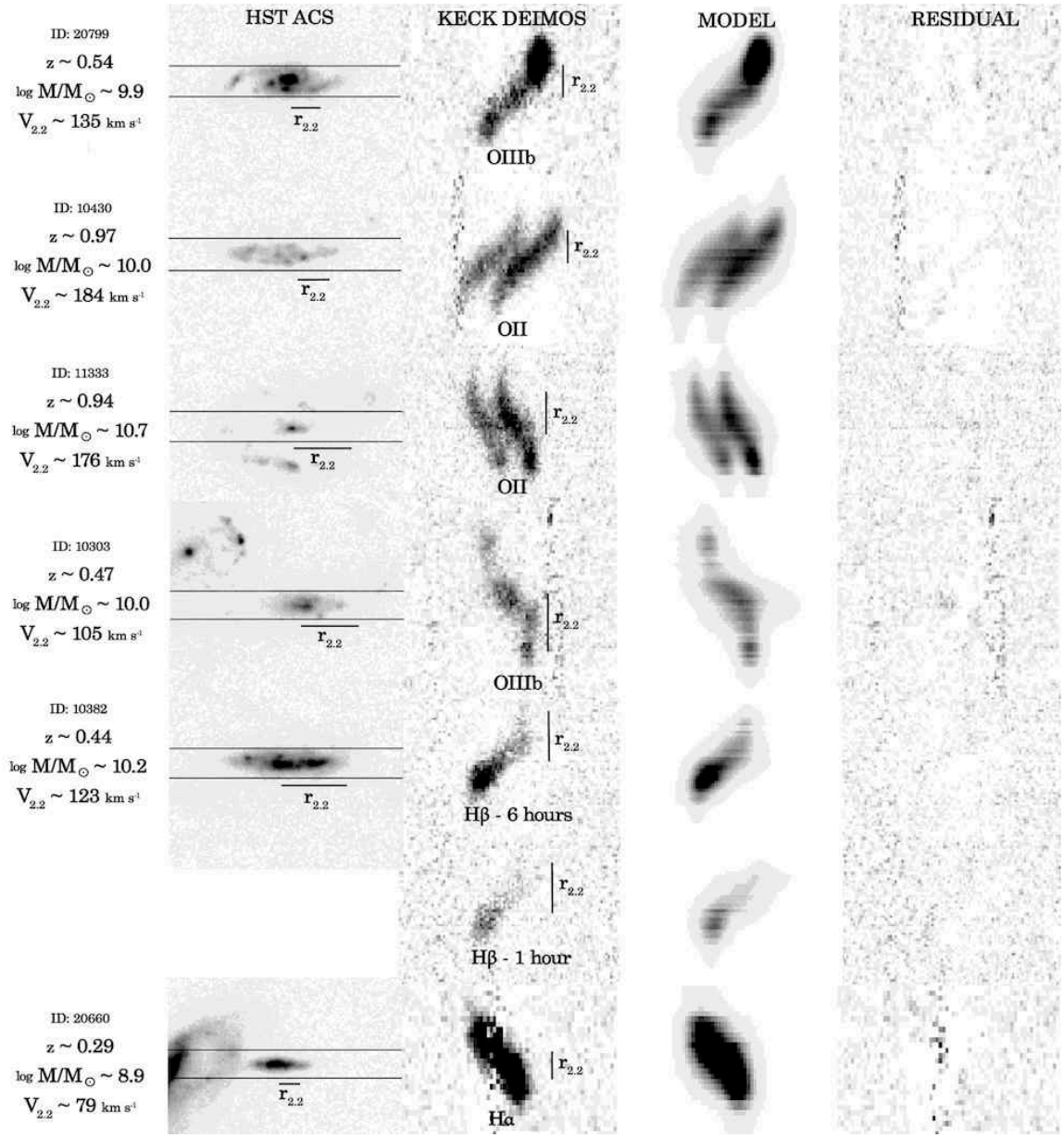

Figure 3.12 Examples of data from the DEIMOS survey. For each source we show an HST ACS composite (B, V, i, z) photometry postage stamp rotated for convenience so the overlaid $1''$ slit level is horizontal, the Keck DEIMOS 2D emission line cutout, the corresponding best model and residual of model minus data. The extent of $r_{2.2}$, where $V_{2.2}$ is measured is also overlaid. The triptych second to the bottom shows the same emission line as the one above but with only 1 hour spectroscopic integration.

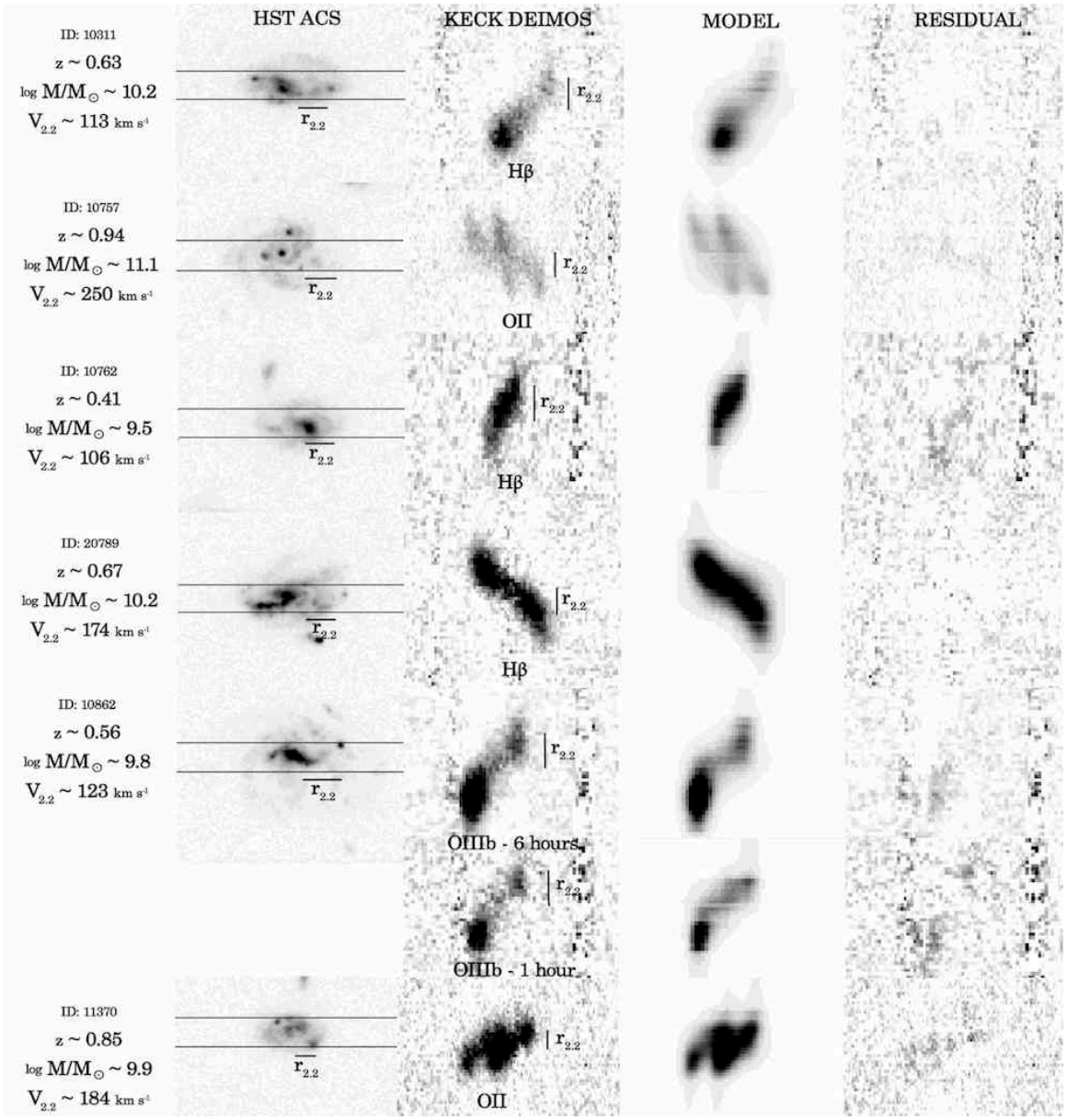

Figure 3.13 As Figure 3.12 but for more disturbed, visually asymmetric discs, some of which appear to be undergoing minor mergers. Although the morphologies are more irregular, we usually succeed in fitting an appropriate arctan-based model.

Table 3.4: Table of Observed and Derived Measurements from DEIMOS Extended Sample

R.A.	Dec.	z	m_z	PA_{slit} [1]	PA_{off} [2]	$\sin(i)$ [3]	$r_{2.2}$ [4]	r_t [5]	$M_*(r_{2.2})$ [6]	M_B [7]	M_{K_s} [8]	$V_{2.2}$ [9]	V_{slit} [10]	Lo M_{dyn} [11]	Up M_{dyn} [12]
189.28400	62.204340	0.59	22.22	36.10	0.00	0.97	3.92±0.22	0.60±0.08	9.53±0.17	-19.83±-0.56	-22.76±-0.64	69.54±10.33	29.92	9.52±0.11	9.96±0.11
189.34309	62.196030	0.53	21.97	81.30	0.73	0.96	7.17±0.19	0.41±0.04	9.38±0.14	-19.76±-0.48	-22.41±-0.54	66.84±6.39	16.26	9.75±0.06	10.06±0.06
189.32520	62.213470	0.91	22.17	36.70	0.02	0.96	14.63±0.70	9.82±1.58	10.89±0.03	-20.82±-0.10	-24.97±-0.10	268.61±46.83	10.26	11.26±0.13	11.42±0.13
189.38380	62.212980	1.02	21.22	76.40	0.02	0.79	18.87±0.25	4.39±0.87	11.44±0.12	-22.17±-0.36	-26.23±-0.43	276.55±55.10	12.74	11.40±0.14	11.56±0.14
189.33160	62.215710	0.91	22.47	54.30	0.00	0.86	4.96±0.23	0.19±0.10	10.69±0.04	-20.66±-0.13	-24.62±-0.13	131.03±70.47	34.05	10.17±0.62	10.50±0.62
189.40388	62.242610	0.63	21.39	66.00	0.09	0.93	11.33±0.21	0.93±0.05	10.16±0.18	-20.64±-0.57	-23.49±-0.65	101.71±6.33	13.82	10.31±0.04	10.55±0.04
189.44249	62.244660	0.64	21.49	72.30	0.04	0.84	4.53±0.21	4.26±0.22	10.57±0.04	-20.55±-0.12	-24.38±-0.15	216.03±17.73	33.86	10.57±0.06	10.82±0.06
189.30710	62.253220	0.52	21.03	43.80	0.00	0.88	5.78±0.19	2.48±0.39	10.48±0.06	-20.29±-0.18	-24.13±-0.21	203.20±33.31	28.62	10.62±0.12	10.86±0.12
189.33580	62.274980	0.84	21.59	72.20	0.03	0.88	11.21±0.23	3.38±0.03	10.24±0.18	-21.28±-0.58	-24.09±-0.65	179.98±4.93	18.26	10.80±0.02	11.01±0.02
189.21300	62.175340	0.41	19.94	36.10	0.18	0.56	5.51±0.16	1.21±0.06	10.85±0.06	-20.46±-0.18	-24.70±-0.22	180.18±11.31	27.67	10.49±0.04	10.74±0.04
189.17271	62.181010	0.94	22.47	73.50	0.12	0.96	7.47±0.24	7.62±1.91	10.52±0.06	-20.65±-0.19	-23.74±-0.20	213.43±54.27	20.06	10.77±0.19	10.98±0.19
189.22171	62.188090	0.94	21.27	73.40	0.22	0.64	10.86±0.24	10.38±1.53	11.08±0.05	-21.72±-0.16	-25.64±-0.19	282.52±42.61	21.64	11.18±0.10	11.37±0.10
189.29829	62.190790	0.41	21.81	26.20	0.06	0.84	7.68±0.48	2.63±0.18	9.47±0.10	-19.01±-0.33	-21.57±-0.37	92.16±5.03	20.20	10.06±0.05	10.35±0.05
189.27409	62.257080	0.50	21.86	58.90	0.04	0.76	7.95±0.18	0.56±0.08	9.81±0.09	-19.51±-0.28	-22.40±-0.32	118.67±17.55	23.41	10.29±0.10	10.57±0.10
189.06029	62.121890	0.97	21.25	79.70	0.15	0.50	14.82±0.24	3.76±0.12	11.13±0.03	-22.24±-0.11	-25.20±-0.12	252.24±9.84	14.03	11.22±0.03	11.39±0.03
189.15370	62.126510	1.00	22.10	79.00	0.00	0.61	9.00±0.24	0.55±0.21	10.45±0.19	-21.90±-0.64	-24.80±-0.73	172.24±66.93	26.13	10.67±0.35	10.92±0.35
189.05609	62.153080	0.41	20.59	64.90	0.02	0.80	8.17±0.22	2.42±0.14	10.22±0.06	-20.21±-0.20	-23.20±-0.23	131.34±9.13	19.79	10.39±0.05	10.64±0.05
189.02771	62.164350	1.20	21.07	45.20	0.02	0.99	33.16±0.25	4.39±0.79	11.11±0.03	-20.66±-0.11	-25.25±-0.11	226.67±40.95	1.78	11.47±0.13	11.60±0.13
189.11980	62.173260	0.94	21.88	37.70	0.38	0.82	24.22±0.97	6.79±0.16	10.70±0.05	-21.27±-0.17	-24.44±-0.20	180.29±9.34	9.51	11.14±0.04	11.31±0.04
189.15421	62.199970	0.78	21.38	79.50	0.06	0.65	12.50±0.22	0.80±0.07	10.44±0.17	-21.24±-0.55	-24.09±-0.62	144.28±12.42	17.87	10.66±0.06	10.88±0.06
189.34558	62.238910	1.02	22.25	77.70	0.67	0.99	27.69±0.25	2.62±0.54	10.90±0.04	-21.11±-0.13	-25.13±-0.14	228.05±47.23	2.77	11.40±0.15	11.54±0.15
189.32971	62.192100	0.56	20.06	21.30	0.26	0.50	32.39±0.19	0.28±0.02	10.88±0.06	-21.14±-0.18	-25.06±-0.21	286.45±23.64	5.20	11.67±0.05	11.81±0.05
189.06290	62.164470	0.45	21.98	81.30	0.24	0.95	5.55±0.17	0.72±0.04	9.57±0.11	-19.26±-0.36	-21.81±-0.41	107.01±7.50	21.41	10.04±0.05	10.33±0.05
189.50929	62.260080	0.46	21.18	76.30	0.07	0.83	7.15±0.17	2.35±0.07	9.61±0.11	-20.42±-0.37	-22.72±-0.41	138.94±2.87	23.48	10.38±0.02	10.64±0.02
189.39801	62.301540	0.84	20.54	61.30	0.07	0.88	25.15±0.23	13.37±0.14	11.41±0.13	-22.03±-0.40	-25.92±-0.47	344.49±2.53	8.13	11.72±0.01	11.86±0.01
189.32159	62.301370	0.97	22.32	41.60	0.00	1.00	13.27±0.24	7.55±0.35	10.03±0.20	-21.03±-0.67	-23.94±-0.76	206.60±10.93	7.17	10.99±0.03	11.15±0.03
189.36980	62.311000	0.52	22.48	19.10	0.03	1.00	5.17±0.19	0.16±0.10	9.73±0.07	-19.03±-0.22	-22.11±-0.25	73.80±47.40	14.42	9.69±1.04	9.97±1.04
189.17931	62.175180	0.55	21.83	65.10	0.07	0.90	5.14±0.19	0.57±0.02	9.71±0.17	-19.96±-0.55	-22.95±-0.63	114.71±6.98	31.62	10.07±0.04	10.41±0.04
189.17041	62.181960	0.87	22.26	47.20	0.25	0.53	3.25±0.23	1.83±0.18	9.80±0.05	-20.74±-0.18	-23.56±-0.20	136.10±3.73	50.15	10.02±0.04	10.42±0.04
189.15950	62.197540	0.84	22.04	18.60	0.00	0.83	7.11±0.23	6.34±1.28	10.74±0.05	-20.65±-0.18	-24.72±-0.20	282.82±58.58	31.01	11.00±0.15	11.21±0.15
189.16029	62.220390	0.63	22.38	58.00	0.03	0.88	7.33±0.21	3.15±0.07	9.42±0.17	-19.91±-0.56	-22.59±-0.63	118.84±3.95	25.08	10.26±0.02	10.55±0.02
189.22540	62.231870	0.85	22.26	59.00	0.02	0.76	6.09±0.23	0.82±0.07	9.93±0.16	-20.65±-0.53	-23.74±-0.60	158.17±16.24	29.74	10.42±0.07	10.70±0.07
189.24078	62.248690	0.85	21.66	41.70	0.01	0.83	8.81±0.23	2.64±0.14	10.74±0.10	-21.01±-0.32	-24.99±-0.37	201.34±12.81	25.09	10.79±0.04	11.02±0.04
189.26770	62.273660	0.47	21.48	71.30	0.00	0.99	13.22±0.18	6.97±0.05	10.20±0.06	-19.65±-0.19	-23.46±-0.22	170.63±3.47	3.19	10.83±0.01	10.97±0.01
189.20830	62.277070	0.50	21.31	49.70	0.02	0.93	7.85±0.18	3.59±0.15	10.11±0.12	-20.00±-0.36	-23.39±-0.42	148.70±7.82	17.49	10.48±0.04	10.70±0.04
189.04440	62.187090	0.85	22.08	67.80	0.18	0.84	7.80±0.23	2.83±0.11	9.97±0.20	-20.92±-0.65	-23.74±-0.74	173.67±9.89	27.82	10.61±0.04	10.87±0.04
189.11090	62.214560	0.56	20.59	21.80	0.01	0.60	10.87±0.19	3.35±0.06	10.48±0.12	-21.04±-0.37	-24.08±-0.43	174.61±2.93	17.22	10.76±0.01	10.97±0.01
188.98679	62.164390	0.46	22.36	59.20	0.00	0.98	6.96±0.18	2.49±0.27	9.47±0.15	-17.72±-0.46	-20.15±-0.53	74.71±8.53	12.88	9.83±0.08	10.09±0.08
189.26929	62.281140	0.38	20.18	30.80	1.33	0.71	9.19±0.16	1.52±0.05	10.36±0.08	-20.38±-0.26	-23.59±-0.30	118.11±4.93	17.19	10.35±0.03	10.59±0.03
189.24979	62.287780	0.36	19.39	75.50	0.27	0.88	11.56±0.15	1.26±0.15	10.78±0.10	-20.69±-0.30	-24.58±-0.36	265.33±32.89	11.41	11.15±0.08	11.31±0.08
189.05009	62.194220	0.28	18.84	30.20	0.14	0.71	7.38±0.13	0.88±0.07	10.72±0.10	-20.62±-0.31	-24.32±-0.37	271.94±23.41	17.36	10.98±0.06	11.16±0.06
189.06628	62.210490	0.29	19.34	20.90	0.00	0.75	11.44±0.13	7.53±0.26	10.32±0.07	-20.50±-0.20	-23.53±-0.24	155.83±5.92	11.46	10.68±0.02	10.87±0.02
189.33360	62.275660	0.44	21.02	15.50	0.16	0.54	5.03±0.17	0.67±0.06	10.22±0.06	-19.99±-0.20	-23.15±-0.23	138.69±13.63	30.94	10.23±0.07	10.53±0.07
189.36060	62.307400	0.44	20.46	75.50	0.67	0.85	9.35±0.17	0.16±0.06	10.50±0.06	-20.37±-0.18	-23.77±-0.21	175.15±63.22	17.02	10.70±0.31	10.90±0.31
189.09290	62.211670	0.46	20.60	75.50	0.38	0.98	16.43±0.17	1.76±0.15	10.51±0.07	-20.06±-0.20	-24.05±-0.24	160.89±13.61	5.62	10.87±0.06	11.03±0.06
189.31931	62.253230	0.23	20.50	27.00	0.56	0.66	13.79±0.26	2.58±0.01	9.57±0.13	-21.01±-0.44	-23.65±-0.50	153.98±4.02	8.07	10.76±0.02	10.93±0.02
189.38620	62.345700	0.32	22.31	75.50	0.08	0.99	6.47±0.14	4.11±0.63	9.18±0.08	-18.07±-0.25	-20.75±-0.29	107.90±16.73	5.98	10.12±0.11	10.29±0.11
189.36340	62.352230	0.28	20.41	45.60	0.00	0.99	9.82±1.22	2.44±0.37	10.28±0.05	-19.17±-0.16	-23.33±-0.19	154.63±13.96	3.93	10.61±0.09	10.76±0.09
189.18231	62.232530	0.20	20.81	71.40	0.01	1.00	7.78±0.10	4.78±0.38	9.28±0.09	-18.46±-0.29	-21.06±-0.33	102.18±8.29	4.86	10.15±0.05	10.32±0.05
189.26669	62.256550	0.38	21.85	40.90	0.09	0.93	2.77±0.16	0.36±0.01	9.59±0.07	-18.77±-0.22	-21.73±-0.25	67.99±4.72	32.48	9.35±0.05	9.81±0.05
189.05879	62.196500	0.29	20.24	75.50	0.69	0.73	10.66±0.13	0.12±0.04	9.92±0.07	-19.72±-0.22	-22.57±-0.26	80.56±25.47	12.34	10.08±0.26	10.33±0.26
189.37871	62.224510	0.89	22.18	96.30	0.30	0.76	3.56±0.23	6.33±0.94	10.26±0.17	-20.93±-0.55	-24.17±-0.63	151.95±26.67	51.55	10.16±0.13	10.54±0.13

Continued on Next Page...

Table of Observed and Derived Measurements from DEIMOS Extended Sample – Continued

R.A.	Dec.	z	m_z	PA_{slit}[1]	PA_{off}[2]	$\sin(i)$[3]	$r_{2.2}$[4]	r_t[5]	$M_*(r_{2.2})$[6]	M_B[7]	M_{K_s}[8]	$V_{2.2}$[9]	V_{slit}[10]	Lo M_{dyn}[11]	Up M_{dyn}[12]
189.30780	62.226520	0.78	21.42	113.80	0.04	0.65	9.84±0.22	3.06±0.07	10.46±0.13	-21.12±-0.42	-24.47±-0.48	220.65±8.76	22.70	10.92±0.03	11.13±0.03
189.32401	62.244340	0.41	21.00	94.90	0.02	0.87	5.51±0.18	0.84±0.01	10.21±0.10	-19.73±-0.30	-23.21±-0.35	151.98±7.55	26.88	10.35±0.04	10.61±0.04
189.41330	62.248570	0.82	21.17	115.10	0.01	0.90	5.04±0.23	1.34±0.06	10.74±0.07	-21.73±-0.22	-25.14±-0.25	116.43±5.53	29.65	10.08±0.04	10.40±0.04
189.43120	62.275560	0.44	21.18	110.10	0.00	1.00	10.46±0.49	5.07±0.26	10.16±0.07	-19.73±-0.22	-23.37±-0.26	134.73±5.54	6.25	10.52±0.03	10.68±0.03
189.34360	62.281020	0.84	22.40	87.10	0.14	0.79	5.74±0.68	0.67±0.08	10.43±0.10	-20.51±-0.33	-23.86±-0.37	150.03±31.12	30.88	10.35±0.16	10.64±0.16
189.27588	62.225870	0.75	21.60	114.90	0.01	0.90	12.89±0.22	2.61±0.85	10.42±0.09	-20.77±-0.28	-24.32±-0.32	195.58±63.52	14.45	10.93±0.27	11.12±0.27
189.30460	62.226140	0.84	22.09	100.00	0.00	0.96	7.12±0.97	3.05±0.49	10.06±0.13	-20.61±-0.43	-23.72±-0.50	119.50±12.86	20.13	10.25±0.10	10.51±0.10
189.26041	62.228430	0.56	21.55	98.00	0.56	0.88	14.10±0.19	2.65±0.10	9.79±0.17	-20.27±-0.57	-22.84±-0.64	113.94±4.98	12.30	10.50±0.03	10.72±0.03
189.18930	62.256530	0.68	22.24	78.20	0.09	0.99	4.02±0.21	0.34±0.03	9.38±0.05	-20.15±-0.18	-22.71±-0.21	88.10±10.54	25.24	9.73±0.08	10.08±0.08
189.18130	62.259070	0.85	22.40	87.70	0.06	0.83	5.56±0.23	0.95±0.04	9.88±0.17	-20.53±-0.55	-23.59±-0.63	110.24±8.33	30.89	10.07±0.05	10.41±0.05
189.20779	62.261720	0.94	22.37	99.20	0.01	0.76	5.89±0.24	4.22±0.48	10.63±0.05	-20.74±-0.16	-24.56±-0.18	215.59±27.53	31.64	10.68±0.09	10.92±0.09
189.19301	62.270830	0.50	21.64	77.70	0.00	0.91	5.85±0.18	0.79±0.24	10.16±0.06	-19.55±-0.20	-23.35±-0.23	136.26±41.40	25.26	10.28±0.24	10.55±0.24
189.08980	62.216840	0.69	20.92	88.40	0.13	0.77	13.99±0.21	3.55±0.13	10.71±0.11	-21.19±-0.35	-24.63±-0.41	170.49±7.39	15.31	10.85±0.03	11.05±0.03
189.12860	62.242740	0.44	21.12	83.40	0.01	0.88	6.58±0.17	6.77±3.15	10.13±0.09	-19.76±-0.29	-23.23±-0.34	154.83±72.23	22.80	10.44±0.47	10.68±0.47
189.07790	62.246300	0.78	21.98	95.80	0.01	0.99	15.04±0.38	6.13±0.56	10.56±0.05	-20.40±-0.16	-24.33±-0.18	213.67±21.08	6.59	11.08±0.07	11.23±0.07
189.06129	62.248460	1.02	22.30	115.50	0.11	0.87	5.94±0.24	9.53±1.59	10.20±0.16	-21.18±-0.53	-24.31±-0.60	162.41±28.64	28.61	10.44±0.13	10.70±0.13
188.99889	62.246390	0.53	21.96	88.30	0.05	0.67	4.24±0.19	0.67±0.02	9.92±0.07	-19.51±-0.21	-22.57±-0.24	124.70±7.25	35.01	10.06±0.04	10.40±0.04
189.42209	62.246210	0.42	21.11	91.00	0.00	1.00	12.78±0.17	6.56±0.19	10.02±0.09	-19.51±-0.28	-23.01±-0.33	165.35±5.60	5.18	10.78±0.02	10.94±0.02
189.46970	62.274590	0.31	18.63	60.00	0.28	0.65	6.72±0.23	1.88±0.07	10.63±0.06	-21.51±-0.18	-24.73±-0.21	187.59±5.59	20.17	10.61±0.02	10.83±0.02
189.34779	62.246850	0.25	19.27	60.00	0.51	0.81	7.85±0.12	0.11±0.04	10.41±0.10	-19.97±-0.32	-23.67±-0.38	188.74±72.53	14.74	10.69±0.34	10.88±0.34
189.16541	62.257410	0.38	20.22	120.00	0.07	0.97	11.09±0.16	3.93±0.06	10.42±0.06	-19.90±-0.18	-23.83±-0.22	180.08±2.36	8.41	10.80±0.01	10.96±0.01
189.26430	62.275380	0.36	21.08	120.00	0.74	0.67	7.69±0.15	0.14±0.01	9.81±0.08	-19.59±-0.25	-22.37±-0.29	105.12±9.78	19.74	10.17±0.06	10.45±0.06
189.51790	62.278490	0.48	21.29	61.80	0.04	0.96	7.41±0.18	1.34±0.19	10.10±0.10	-19.82±-0.30	-23.34±-0.36	155.72±22.89	15.00	10.50±0.10	10.70±0.10
189.44400	62.237440	0.51	21.44	91.10	0.15	1.00	21.50±0.19	1.94±0.13	10.02±0.09	-19.53±-0.29	-23.12±-0.34	104.47±7.00	3.44	10.61±0.04	10.77±0.04
189.01889	62.261910	0.46	21.21	85.80	0.05	0.98	8.82±0.17	3.32±0.06	10.33±0.11	-18.65±-0.31	-23.09±-0.39	138.06±4.70	10.49	10.47±0.02	10.66±0.02
189.47899	62.279210	0.31	21.42	120.00	0.08	0.99	5.69±0.14	1.43±0.08	9.60±0.07	-18.78±-0.22	-21.76±-0.25	85.42±5.68	10.65	9.86±0.04	10.09±0.04
189.21719	62.249330	0.36	21.81	60.00	0.32	0.95	7.48±0.15	0.95±0.07	9.35±0.12	-19.22±-0.39	-21.56±-0.44	76.55±6.31	14.06	9.88±0.05	10.15±0.05
189.00650	62.253800	0.30	21.33	94.10	0.01	0.87	7.56±0.13	3.68±0.31	9.63±0.09	-18.48±-0.64	-21.62±-0.31	122.81±10.86	15.99	10.30±0.06	10.53±0.06
53.073419	-27.715956	0.65	22.11	139.70	0.21	0.88	3.33±0.55	0.98±0.20	9.97±0.19	-20.11±-0.60	-21.21±-0.63	116.95±12.82	43.31	9.90±0.11	10.30±0.11
53.086315	-27.748247	0.97	20.94	135.40	0.03	0.75	15.89±0.24	2.01±0.10	11.05±0.17	-22.12±-0.53	-23.55±-0.57	279.56±15.74	15.24	11.33±0.04	11.51±0.04
53.097517	-27.721268	0.61	20.48	136.60	0.16	0.67	8.46±0.20	0.19±0.01	10.90±0.14	-21.34±-0.44	-23.05±-0.47	201.00±15.13	24.21	10.77±0.05	11.00±0.05
53.102506	-27.741145	0.54	21.89	160.00	0.05	0.86	6.74±0.19	5.51±0.38	9.46±0.09	-19.93±-0.31	-20.29±-0.32	127.84±10.10	25.84	10.28±0.05	10.57±0.05
53.103982	-27.663578	0.67	22.06	7.60	0.02	0.98	9.26±0.21	2.27±0.21	10.36±0.10	-19.92±-0.30	-21.88±-0.33	219.07±21.41	12.02	10.89±0.07	11.06±0.07
53.108303	-27.879445	0.53	21.17	146.90	0.02	0.98	13.34±0.19	2.46±0.11	10.32±0.06	-19.87±-0.18	-21.42±-0.19	155.40±7.72	7.51	10.75±0.03	10.92±0.03
53.109717	-27.699478	0.74	21.80	9.30	0.23	0.77	10.00±0.22	0.39±0.04	9.95±0.12	-20.67±-0.39	-21.38±-0.40	139.76±15.22	22.02	10.53±0.07	10.78±0.07
53.124394	-27.755701	0.95	21.01	152.90	0.24	0.57	19.72±0.80	0.77±0.07	10.99±0.17	-22.01±-0.52	-23.53±-0.56	260.33±27.55	11.41	11.37±0.07	11.53±0.07
53.128348	-27.667814	0.77	21.94	160.00	0.00	0.90	7.87±0.22	1.92±0.06	10.10±0.12	-20.66±-0.39	-21.49±-0.40	186.58±3.96	23.83	10.68±0.02	10.91±0.02
53.129910	-27.671529	0.56	20.50	171.80	0.01	0.96	15.25±0.20	8.32±0.31	10.79±0.06	-20.88±-0.19	-22.70±-0.20	246.19±10.13	8.30	11.21±0.03	11.36±0.03
53.130652	-27.790271	0.67	21.01	155.10	0.16	0.86	11.19±0.21	2.69±0.04	10.16±0.11	-21.23±-0.36	-22.05±-0.38	166.03±3.78	17.20	10.73±0.02	10.94±0.02
53.131569	-27.834610	0.54	21.52	175.90	0.04	0.94	8.94±0.19	4.19±0.23	9.90±0.06	-19.92±-0.20	-20.78±-0.21	137.19±8.64	15.16	10.47±0.04	10.68±0.04
53.132594	-27.884840	0.57	22.04	12.30	0.07	0.91	3.90±0.20	0.23±0.03	9.55±0.11	-19.79±-0.36	-20.35±-0.37	86.92±11.79	31.49	9.71±0.10	10.10±0.10
53.150125	-27.739944	1.04	21.98	150.90	0.13	0.84	10.36±0.80	2.17±0.20	9.93±0.04	-21.45±-0.15	-22.33±-0.16	108.38±6.15	22.23	10.33±0.05	10.61±0.05
53.161898	-27.845847	1.02	21.18	155.40	0.09	0.70	25.14±0.24	2.71±0.13	11.00±0.10	-21.99±-0.31	-23.38±-0.33	246.03±11.88	9.75	11.42±0.03	11.58±0.03
53.165209	-27.873944	1.10	22.36	11.70	2.74	0.84	7.41±0.25	0.29±0.10	9.75±0.03	-21.29±-0.09	-21.58±-0.10	106.96±36.52	31.55	10.17±0.29	10.52±0.29
53.166178	-27.787519	1.09	21.42	13.80	0.10	0.62	10.70±0.24	9.22±1.09	10.32±0.02	-22.11±-0.06	-23.26±-0.06	237.22±29.18	22.59	11.02±0.08	11.23±0.08
53.175611	-27.838532	0.46	21.74	150.70	0.00	0.99	8.55±0.17	3.44±0.08	9.69±0.06	-19.71±-0.19	-19.80±-0.19	133.50±2.11	6.07	10.42±0.01	10.59±0.01
53.114940	-27.828123	0.29	22.43	172.80	0.01	0.99	4.27±0.13	1.35±0.17	8.99±0.08	-17.53±-0.24	-18.41±-0.26	74.81±10.09	9.76	9.62±0.09	9.85±0.09
53.125279	-27.721939	1.10	21.59	164.10	0.13	0.83	5.30±0.25	0.87±0.09	10.75±0.09	-22.02±-0.28	-23.73±-0.30	167.82±20.87	34.60	10.41±0.09	10.70±0.09
53.107433	-27.817121	0.74	22.35	147.20	0.07	0.94	6.59±0.22	1.40±0.35	9.70±0.12	-19.91±-0.38	-20.70±-0.39	150.76±38.29	24.27	10.42±0.19	10.67±0.19
53.028759	-27.726879	0.68	22.32	125.00	0.20	0.91	8.26±0.26	3.37±2.24	9.85±0.23	-20.05±-0.73	-20.37±-0.74	101.01±67.34	20.66	10.17±1.25	10.45±1.25
53.029840	-27.732207	1.21	21.92	125.00	0.26	0.71	13.53±0.25	4.12±0.16	10.92±0.08	-21.80±-0.27	-22.84±-0.28	255.74±11.92	18.75	11.19±0.03	11.38±0.03
53.051258	-27.753631	0.65	21.38	152.40	0.11	0.57	6.68±0.21	0.80±0.08	10.23±0.07	-20.73±-0.22	-21.84±-0.23	155.32±17.92	29.24	10.45±0.08	10.72±0.08
53.086036	-27.788086	0.73	21.14	119.80	0.04	0.82	11.24±0.26	3.07±0.18	10.42±0.08	-21.36±-0.26	-22.21±-0.27	187.63±12.58	18.88	10.84±0.04	11.05±0.04

Continued on Next Page...

Table of Observed and Derived Measurements from DEIMOS Extended Sample – Continued

R.A.	Dec.	z	m_z	PA_{slit}[1]	PA_{off}[2]	$\sin(i)$[3]	$r_{2.2}$[4]	r_t[5]	$M_*(r_{2.2})$[6]	M_B[7]	M_{K_s}[8]	$V_{2.2}$[9]	V_{slit}[10]	Lo M_{dyn}[11]	Up M_{dyn}[12]
53.087338	-27.743006	0.52	21.68	110.90	0.05	0.95	6.01±0.22	3.60±0.25	9.75±0.14	-20.05±-0.45	-20.88±-0.46	115.53±10.13	21.53	10.15±0.06	10.42±0.06
53.101451	-27.790275	0.52	21.83	121.60	0.01	0.74	4.55±0.19	0.16±0.07	9.82±0.06	-19.70±-0.19	-20.52±-0.20	122.99±53.28	32.64	10.08±0.41	10.41±0.41
53.149888	-27.814002	1.31	21.63	105.30	0.45	0.87	5.07±0.50	4.24±1.79	10.27±0.05	-22.65±-0.16	-22.75±-0.16	112.33±49.97	34.67	10.05±0.44	10.41±0.44
53.186875	-27.841166	0.78	21.78	101.70	0.21	0.97	4.45±0.22	2.61±0.06	9.75±0.20	-21.05±-0.68	-21.22±-0.68	89.09±5.97	30.18	9.79±0.05	10.17±0.05
53.251739	-27.874499	1.09	21.79	142.10	0.16	0.89	14.30±0.24	1.06±0.42	11.04±0.06	-22.13±-0.21	-1.00±-1.00	191.24±76.15	14.67	10.96±0.36	11.15±0.36
53.040721	-27.758156	0.61	22.42	100.00	0.01	1.00	3.86±0.20	3.16±0.75	9.56±0.24	-19.73±-0.77	-20.28±-0.80	131.40±32.80	41.47	10.06±0.19	10.43±0.19
53.176342	-27.830645	0.46	20.33	100.00	0.48	0.87	10.89±0.19	2.45±1.04	10.45±0.06	-20.63±-0.18	-21.81±-0.19	128.63±54.59	14.50	10.50±0.40	10.71±0.40
53.232835	-27.891105	0.98	21.48	102.80	0.04	0.83	11.66±0.24	9.36±1.09	10.41±0.02	-21.73±-0.07	-23.14±-0.07	271.50±32.70	19.74	11.18±0.08	11.36±0.08
53.114878	-27.725393	0.74	22.43	145.90	0.09	0.96	8.02±0.22	3.19±0.25	9.58±0.11	-19.82±-0.36	-20.34±-0.38	108.26±9.60	17.32	10.21±0.06	10.47±0.06
53.112810	-27.734626	0.74	22.24	153.80	0.01	0.99	7.20±0.22	1.15±0.12	9.61±0.05	-20.68±-0.18	-21.04±-0.18	103.67±11.69	8.44	10.13±0.08	10.32±0.08
53.072847	-27.737606	0.40	22.13	150.60	0.04	0.92	4.80±0.16	3.28±1.21	9.59±0.07	-18.91±-0.22	-19.35±-0.22	97.67±36.35	26.07	9.90±0.33	10.23±0.33
53.051258	-27.753631	0.65	21.38	152.40	0.11	0.57	6.68±0.21	0.18±0.03	10.23±0.07	-20.73±-0.22	-21.84±-0.23	143.93±23.36	29.24	10.38±0.11	10.67±0.11
53.064826	-27.716624	0.25	21.85	136.30	0.03	0.97	6.20±0.12	1.29±0.02	9.11±0.20	-17.45±-0.61	-17.95±-0.63	72.48±2.26	10.61	9.75±0.02	10.00±0.02
53.140968	-27.796648	0.34	21.72	130.40	0.00	0.87	4.60±0.15	1.06±0.09	9.45±0.15	-18.68±-0.46	-19.47±-0.48	88.47±8.32	28.79	9.80±0.06	10.17±0.06
53.159058	-27.832622	0.51	21.89	133.10	0.05	0.54	16.96±0.19	1.20±0.01	9.42±0.11	-19.65±-0.37	-20.09±-0.38	166.07±3.10	9.96	10.91±0.01	11.09±0.01
53.186875	-27.841166	0.78	21.78	101.70	0.21	0.97	4.45±0.22	5.96±0.34	9.75±0.20	-21.05±-0.68	-21.22±-0.68	70.86±2.99	30.18	9.59±0.04	10.02±0.04
53.203502	-27.872829	0.33	20.74	142.10	0.00	0.98	7.25±0.14	1.71±0.03	9.92±0.07	-19.57±-0.22	-20.72±-0.24	129.19±4.34	10.84	10.32±0.02	10.52±0.02
53.033360	-27.729494	0.47	21.59	106.20	0.02	0.99	8.59±0.26	1.63±0.09	10.06±0.05	-19.37±-0.14	-20.95±-0.15	145.36±10.35	8.81	10.50±0.05	10.68±0.05
189.20709	62.220390	0.47	21.28	84.30	0.02	0.98	9.40±0.18	0.94±0.14	10.45±0.04	-19.73±-0.13	-23.79±-0.16	113.63±17.16	9.69	10.32±0.10	10.52±0.10
189.35570	62.268900	0.57	22.37	174.00	0.09	0.99	8.16±0.20	4.08±0.04	9.47±0.15	-19.74±-0.49	-22.04±-0.55	120.70±3.90	10.94	10.32±0.02	10.52±0.02
189.33760	62.246220	0.50	21.46	165.80	0.04	0.94	10.59±0.18	2.94±0.38	10.11±0.08	-20.02±-0.25	-23.07±-0.28	157.62±20.75	12.73	10.66±0.09	10.85±0.09
189.24030	62.357420	0.53	21.72	151.20	0.02	0.99	6.62±0.52	3.05±0.30	10.29±0.05	-19.81±-0.16	-23.65±-0.19	130.45±6.52	12.46	10.29±0.05	10.50±0.05
189.28380	62.330050	0.32	21.60	10.80	0.01	1.00	7.38±0.14	1.09±0.10	9.62±0.08	-18.31±-0.23	-21.98±-0.28	87.94±8.66	6.79	10.00±0.07	10.19±0.07
189.25519	62.306520	0.94	22.38	159.40	0.01	0.79	9.01±0.24	2.11±0.02	9.88±0.08	-21.36±-0.29	-23.97±-0.32	121.55±4.35	26.17	10.37±0.03	10.66±0.03

[1] in degrees
[2] in radians
[3] sin of inclination
[4] 2.2 × scale radius in kpc
[5] model turnover radius in kpc
[6] enclosed stellar mass in log $M_*/M_\odot$ dex
[7] total absolute B-magnitude in mags
[8] total absolute K-magnitude in mags
[9] best modeled velocity at $r_{2.2}$ in kms^{-1}
[10] estimate of upper limit of velocity broadening of slit, in kms^{-1}
[11] enclosed dynamical mass in log $M_*/M_\odot$ dex, lower limit (without slit effects correction, assuming an oblated potential where q=0.4)
[12] enclosed dynamical mass in log $M_*/M_\odot$ dex, upper limit (with slit effects correction, assuming a spherical potential)

3.7 Verifying models of DEIMOS spectra

As previously discussed, a major advance in our survey is the use of extended integration times (typically 6-8 hours). Previous analysis on sources with similar apparent magnitudes ($m_{z_{F850LP}} \lesssim 24$) have typically been observed for $\sim$1 hour on similar instruments (Vogt et al., 1997; Conselice et al., 2005; Weiner et al., 2006b; Kassin et al., 2007). In addition to ensuring our emission lines are traced to $r_{2.2}$ (Figure 2.2), this leads to improved S/N (of factors of 2–3) at all radii. We can demonstrate the effect this has on our derived velocities by using our model fitting code on a subset of our data taken with a 1 hour integration time. Comparing the results with the 6 hour integrations in Figure 3.14, we can draw two important conclusions.

Firstly, while most $V_{2.2}$ measurements are consistent given the error bars, the 1 hour data has significantly larger error bars and there is a systematic offset whereby the 1 hour analysis produces on average a 13% higher measurement of $V_{2.2}$ than the 6 hour data. This suggests that if errors are not properly accounted for, studies using a similar modelling procedure but with less integration time may falsely detect evolutionary signals as a result of over-estimated velocities due to the decline in S/N.

Secondly, as expected, the 6 hour data enables us to probe largely beyond $r_{2.2}$, whereas this is not the case for the 1 hour subset. The right hand panel in Fig. 3.14 shows the gains made in detected emission extent in factors of scale radius. We trace, on average, 30% further along the disc with the 6 hour data than the 1 hour data. We find that with only 1 hour of data, 1/6 of the sample would have been in our spectrally compact category and 1/3 of the sample would have been considered passive in emission, i.e., not detected at all by DEIMOS. That means over half of the sample that we include in our Tully-Fisher relations would be prematurely excluded based on an emission cut after only $\sim$1 hour. A recent study which has done precisely that is the MASSIV survey sample, which used [OII] emission criteria from a VLT survey

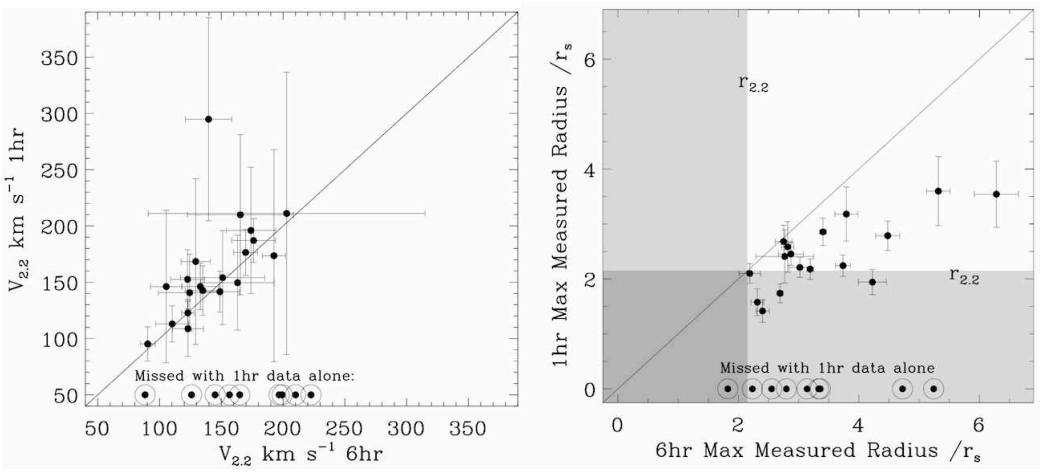

Figure 3.14 A comparison of the modelled $V_{2.2}$ values and maximum measured emission line extent as derived from our total exposure time (6 hours in these examples) to those derived from a 1 hour exposure extracted as a subset of our data. Left: the agreement between $V_{2.2}$ values is reasonable given the errors, however there is a systematic offset and the errors are significantly larger for the 1 hour subset. Right: almost every galaxy reveals significantly more extended emission in the 6 hr data. The shading marks the $r < r_{2.2}$ region; if the emission does not extend beyond this region, $V_{2.2}$ must be extrapolated, as is the case for several 1hr galaxies. Note also that a third of the rotation curves cannot be adequately traced with only 1 hour of integration (circled points).

with integration time <1 hour to screen for IFU targets (Contini et al., 2012; Vergani et al., 2012).

However, this analysis uses the CURVATION code presented here, so it is interesting to compare to velocities for the same galaxies derived using alternative techniques. Indeed we find much more scatter in the comparison between our results and modelling methods which adopt a different formalism. The greatest sample overlap can be found in the TKRS/GOODS study (Wirth et al., 2004; Giavalisco et al., 2004), which fortunately uses the same instrument (DEIMOS) and telescope (Keck), so that the only differences between the measurements are the velocity extraction procedure and the integration time. Figure 3.15 shows 35 of our galaxies in common with in the TKRS/GOODS sample for which there are 2D spectral fits for V_{rot} (equivalent to V_a and does not include a correction for inclination), and all of our sample overlaps with their 1D line

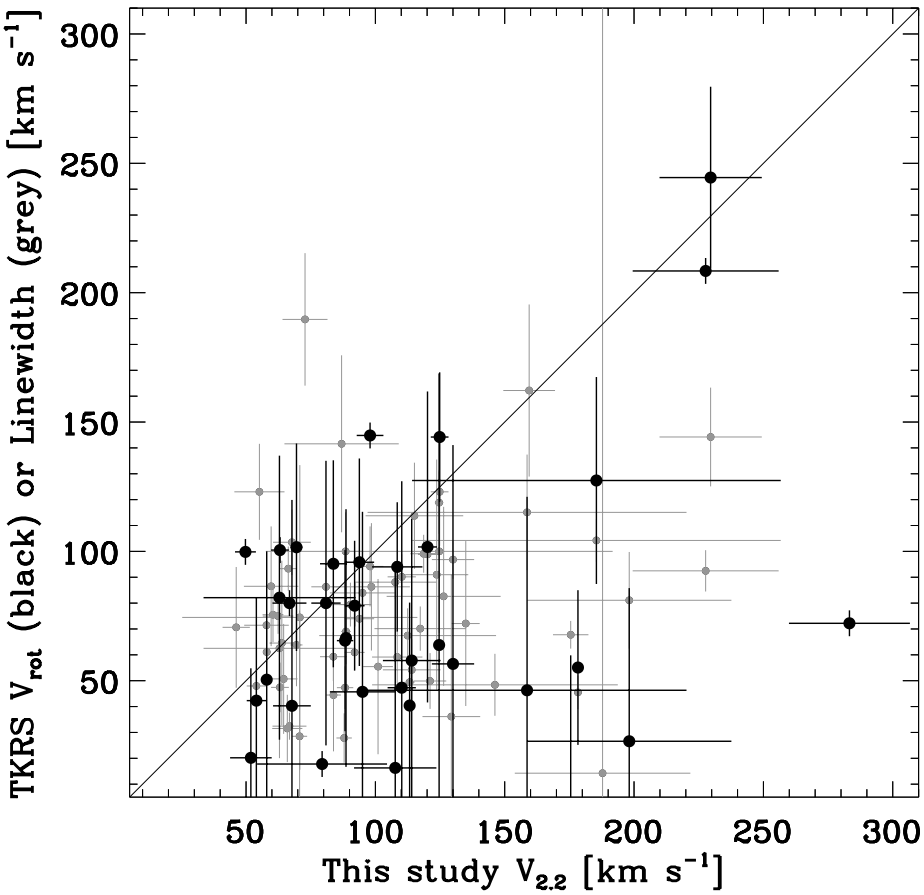

Figure 3.15 A comparison of the velocities for 35 galaxies that overlap between this study and the TKRS/GOODS study of Wirth et al. (2004) & Giavalisco et al. (2004). In black are shown the The TKRS/GOODS 2D spectral fits for V_{rot} (equivalent to V_a), and in grey are the TKRS/GOODS 1D line width measurements. Inclination corrections are not applied to any of the velocity measurements plotted here.

width measurements (Weiner et al., 2006a,b). We compare the velocities we measure for these galaxies without the inclination correction applied for a most direct comparison.

On average, the mean V_{rot} for the TKRS 2D data is 68% of the mean $V_{2.2}$ for our study. For the 1D linewidth data, the TKRS measurements have a mean that is 75% of the $V_{2.2}$ mean in our study. Our current data have significantly smaller error-bars as would be expected given the longer integration times: the median fractional error bar is 8.6% for this study, and 59.1% for TKRS. As-

suming our velocity measurements are more precise, given that the data have a higher S/N and that we have taken extra steps (as described in Ch. 2) to increase the precision of our measurements, we could conclude from this comparison that a fair amount of scatter is induced in the TF relations of Weiner et al. (2006a) and Kassin et al. (2007) studies from the velocity measurements alone, and velocities are down-scattered at least 25%, on average. This could also be taken as further evidence against the adoption of the arctan V_a value as the fiducial TF velocity.

The three galaxies in common with the IMAGES sample of Flores et al. (2006); Puech et al. (2008) have consistent velocity measurements within the error bars when comparing only the equivalent slit area from our study to their modelled IFU data. One galaxy has an inconsistent TF velocity measurement since a higher V_{max} is found on either side of the slit area on the full modelled IFU velocity field. Little can be concluded from a comparison of three objects, however in terms of sample selection, it is encouraging that the three shared objects between our studies all belong to the sub-class of 'Complex Kinematics' in the Flores et al. (2006) kinematical classification scheme, consisting of objects with the most irregular, peculiar observed kinematics.

Even with 6-8 hours of observation it is possible that systematic offsets can dominate the signal which one wishes to be sensitive to in a TF study. We have seen some evidence of this in the tests presented so far, and we will explore this further still in Chapter 4.

3.8 Applying the method to high-z LRIS data

There are several observational challenges in pursuing the rotation curves beyond $z \simeq 1$. The angular diameter distance is at its relative minimum according to ΛCDM cosmology, so that the physical scale being probed is comparable to just a few times the average seeing. A typical emission extent of $5r_s$ in diameter at z$\simeq$1.6 corresponds to $\simeq$2.5″, and a typical scale radius of 4 kpc is

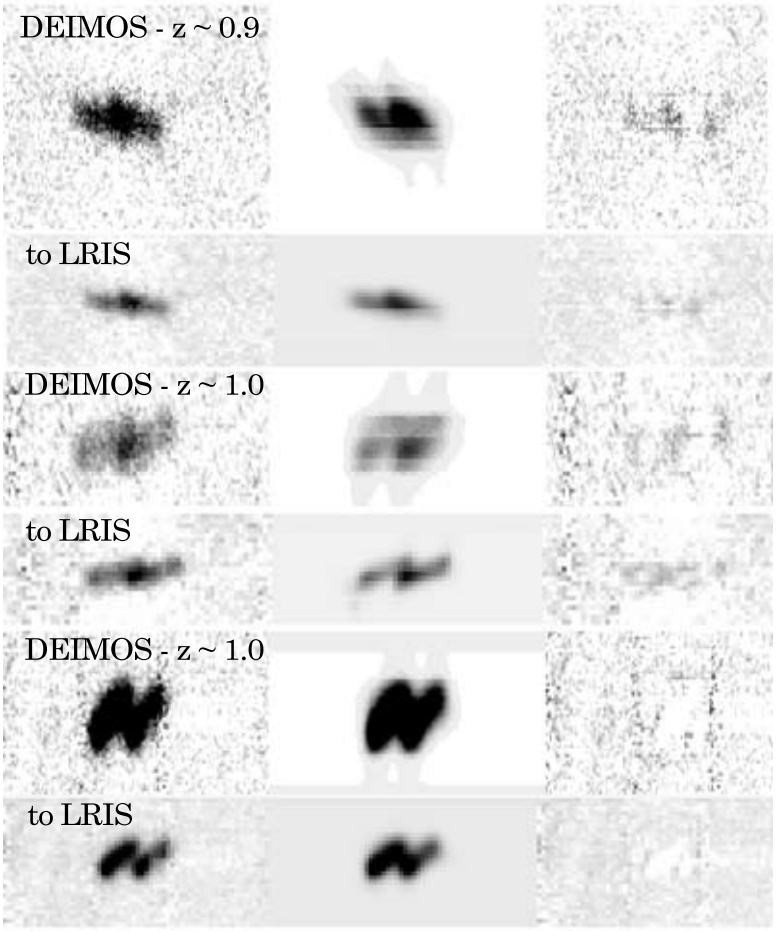

Figure 3.16 Three of the least-extended galaxies at $z \sim 0.9 - 1.0$ observed with DEIMOS, compared to a simulated observation at the different spatial and spectral resolution of the LRIS instrument directly below. From left to right, the columns show (i) the spectral data, (ii) the best-fit model, and (iii) the residual of the data from the model.

only $\sim 0.5''$, so seeing compounded by the instrumental dispersion blur much of the detail in our LRIS spectra. Because it is not always clear by eye that an intrinsic rotation curve with a characteristic turnover point is extractable from this data (Fig. 3.18), it is necessary to demonstrate the reliability and precision of our analysis method and the appropriateness of its application to the high-z LRIS data.

To facilitate this, we selected galaxies in the redshift range $0.85 < z < 1.3$ studied with DEIMOS and re-sampled these data to the spatial and spectral resolution of the LRIS data. With the cosmology assumed, the average angu-

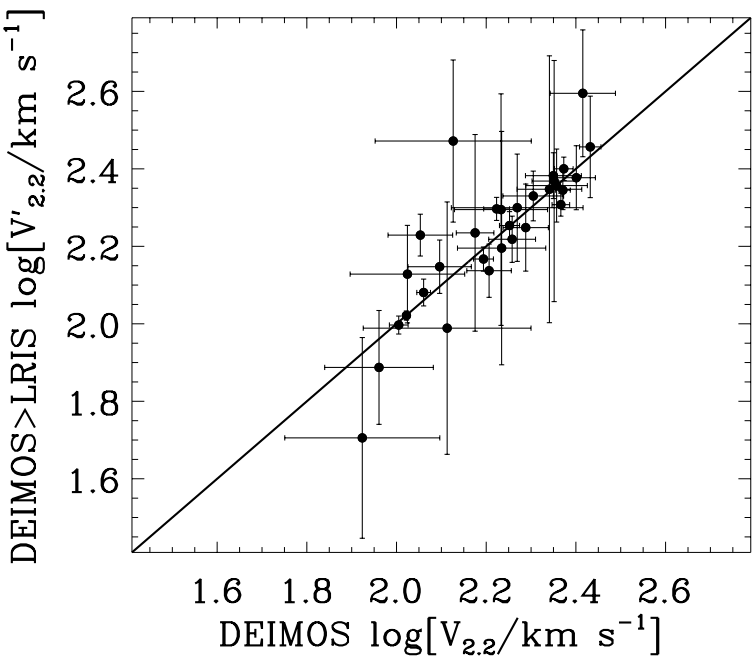

Figure 3.17 Testing the method: For a subset of galaxies from the DEIMOS sample in the redshift interval $0.85 < z < 1.3$ we re-sample their original DEIMOS spectra to the spatial and instrument resolution of LRIS and compare the derived $V_{2.2}$ with the original measures (see text for details).

lar scale of the LRIS galaxies (at $\langle z \rangle$=1.31) is 8% smaller than that for our chosen DEIMOS sample (at $\langle z \rangle$=0.98). To account for differences between the DEIMOS survey and the sample sought from LRIS, we resample for the different spatial pixel scales (0.″1185 with DEIMOS to 0.″27 with LRIS) and match the LRIS spectral dispersions (58 km s^{-1} at 9000 Å with 27.9 km s^{-1} for each pixel). We then analysed the resampled DEIMOS data using the same rotation curve fitting procedure described above, and the results can be seen in Figs. 3.16 & 3.17. Encouragingly, when we subtract the recovered $V_{2.2}$ of the resampled DEIMOS data from that of the original data, we find a weighted mean of less than 0.002±0.009 dex, and the scatter in the relation between the two is 0.098 dex, which is similar to the rms scatter found in the Tully-Fisher relation established locally (and in our DEIMOS results, presented in Ch. 4; Miller et al., 2011). Re-sampling objects at $z \sim 1.0$ to the angular diameter distance of that found at $z \sim 1.3$ did not make significant changes in the recov-

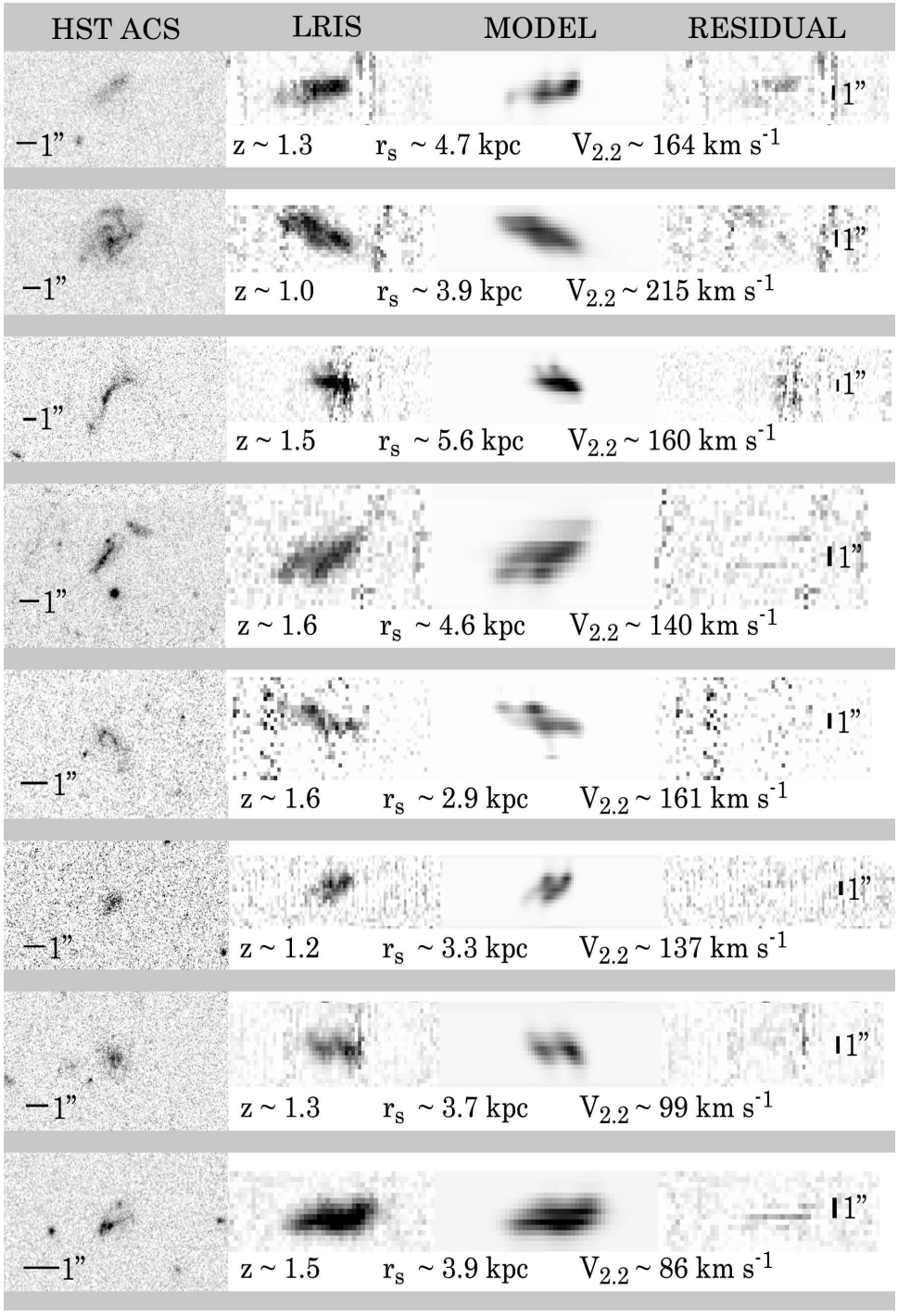

Figure 3.18 Examples of our kinematic analysis: (from left to right) the HST image of the galaxy in ACS *F850LP* or *F814W* filter; the 2D [O II] data in the reduced LRIS spectra; the best-fit model produced from the CURVATION modelling code; the residual obtained by differencing the data and model flux maps.

ered $V_{2.2}$, which is unsurprising given this corresponds to only an 8% reduction in the angular scale. Examples from the LRIS dataset modelling can be seen in Fig. 3.18.

We also tested the data with models simpler than one assuming an arctan function. This addresses a possible concern that we could 'over-fit' the data given the apparent lack of resolved detail at this somewhat higher redshift. By assuming a linear fit to the emission at LRIS resolution, the scatter in the resulting estimated $V_{2.2}$ was as large as 1 dex in log[V/km s^{-1}] compared to that of the arctan-based fits at DEIMOS resolution. We also tested whether we could recover $V_{2.2}$ by measuring dV/dr at intervals of 0.1 scale radii along the discs, but the scatter in the estimated $V_{2.2}$ was on average 0.5 dex, depending on the radial extent of the emission. Thus while the signal is marginal and difficult to determine by eye, we are likely resolving some characteristic turnover in the emission lines of our LRIS data.

3.9 Summary of Chapter 3

In this chapter we have presented 2 distinct datasets with which we will conduct our Tully-Fisher analysis, distinguished by the instrument which was used to procure their spectroscopic data:

1. the DEIMOS dataset, which covers $0.2 < z < 1.3$, and
2. the LRIS dataset, which covers $1 \lesssim z < 1.7$.

The samples were collected specifically to avoid unnecessary culls of the data based on disc regularity and symmetry. Only compact, unresolved objects have been avoided in the selection, and our sample includes irregular galaxies, mergers, chains, and peculiar galaxies, as well as more regular spirals and discs with bulges of all types.

We conduct a bulge-to-disc decomposition with Monte-Carlo GALFIT analysis, finding that 60/63% of galaxies in the DEIMOS/LRIS samples were better

described by 1 disc component than a bulge+disk. This analysis produces a number of measurements needed for the extraction of our fiducial velocities, such as the disc scale length, the inclination, and the position angle offset between the disc major axis and the slitlet of the spectroscopic mask.

We also describe the method by which our stellar masses have been estimated, where multi-band photometry, including ground-based infra-red data, is employed in a SED fitting analysis.

We then describe the spectroscopic observations made using the Keck DEIMOS and LRIS instruments, as well as the reduction and co-addition methods. This leads to the spectroscopic description of the sample, including three subsamples: **passive**, **compact**, and **extended**, only the latter of which can be applied in a rotation curve fitting analysis.

The CURVATION code provides the rotation curve models, and the disc velocities are extracted and deprojected with the measurements described earlier in the Chapter. We verify these velocity extractions via a number of tests, quantifying what gains were made with the extended integration times, as well as comparing to the results from studies using other extraction methods but similar instruments.

Finally, we discuss extra considerations made in applying the CURVATION code to the higher-redshift LRIS data, and find that the intrinsic velocities are possible to procure. We show that while the uncertainties are larger and the scatter in the relation will likely increase, the velocities should not be systematically biased with respect to the DEIMOS measurements.

With fiducial values of disc velocities, magnitudes, and masses secured from a dataset of well-resolved Keck and HST data, we now turn in the next chapter to the primary observational goal of this thesis: the Tully-Fisher analysis and any evolution thereof from intermediate to high redshift.

Chapter 4

The Evolution of the Tully-Fisher Relation

We now reach the primary aim of this thesis: to present the redshift-dependent stellar mass Tully-Fisher (M_*-TF) relation over $0.2 < z < 1.7$. In the Introduction chapter of this thesis, we reviewed the development of the Tully-Fisher (TF) relation as an important tool in the local universe, as well as previous work on the evolution of the relation from high redshift.

In this chapter, we begin by highlighting key issues and remaining questions in TF relation after several decades of study (§4.1). We then present our results (§4.2) of the M_*-TF relation, exploring the quantitative improvement which our extended integrations and subsequent rotation curve models have made. We make the comparisons with respect to earlier work in a number of ways, but the intrinsic scatter around the relations provides the foremost indication of our progress. We examine relations using masses derived within our chosen fiducial $r_{2.2}$ radius, the so-called 'enclosed' relations, alongside those for the more traditional 'total' relations (introduced in Ch. 2 & §3.3). We also examine and discuss the classic B-band TF relation from our survey since the literature contains many estimates of this scaling relation and previous studies have claimed evolution, despite large scatter and possible incompleteness biases (§4.3). In this Chapter we present the TF results from $0.2 < z < 1.7$ within a basic context, so that in Chapter 5 we may explore various modes of more

detailed interpretations of our results.

4.1 Key issues in TF relation studies

We begin with a summary on our understanding of the TF relation, as articulated in a set of final questions[1] by the Scientific Organising Committee of the 'Tully-Fisher at 35' Green Bank workshop. These highlight the motivation behind the primary results of this thesis that we present in the following sections of this chapter. The questions are followed by brief explanations as to why these issues remain after decades of hard work, which will be addressed in the following analysis, and discussed further in Chapter 5.

1. **What is the intrinsic scatter of the TF relation?** The debate in the literature over the answer to this question is greatly informed by the context of the two predominant frameworks in which it is posed: those who use the TF relation for distance measurements, and those who apply the relation to understanding galaxy evolution. For those measuring distances, a TF relation with minimal scatter is preferable as it makes the TF relation one of the most powerful distance tools (as well as one of the most precise ways to measure H_0, *e.g.*, Freedman et al., 2011; Courtois et al., 2012). In this sense, hand-selecting ideal samples where measurements are most precise and scatter in the relation is effectively non-existent simply sharpens the distance-measuring properties of the tool (Verheijen, 2001; McGaugh, 2005).

[1]Not included are the 2 questions posed which pertain only to HI studies, and so not immediately pertinent to this work: 'Does cold HI trace molecular gas?' — an interesting question posed by Robert Minchin, but beyond the scope of this thesis, and '10^{19}, $\sim 2\times10^{18}$, 10^{17}?' posed by Felix J. Lockman, essentially asking how low will we be able to detect HI emission in column density for the coming years. Two additional 'tongue-in-cheek' questions were posed: 'What happened to 35 years?' and 'Are we still going to be asking these questions in 20 or 30 years?', but perhaps the most poignant question, posed by Rick Fisher himself, was 'Why are we only looking under 1 rock?' In many ways this last question deserves the most serious consideration of all, and one I hope to address in future work.

However, for understanding galaxy evolution, the intrinsic scatter of the TF relation reveals a fundamental connection between baryons and dark matter, *i.e.* whether stars assemble homologously within their dark matter haloes. To this purpose, it is vitally important that a complete sample of rotationally supported galaxies be examined, so that what is evaluated is precisely how much intrinsic scatter there is for a fully representative sample.

While the observed scatter of the local stellar mass TF relation is typically $\sim$0.2 dex, a potentially critical problem for ΛCDM is that the intrinsic scatter of the observed baryonic TF relation is $<$0.15 dex in baryon mass (Verheijen, 2001; Stark et al., 2009; McGaugh, 2011). If the measurement-dominated error of the TF scatter continues to decrease, as it has over the past several decades, then eventually the scatter of the observed relation will be less than that predicted by ΛCDM models (which at $\sim$0.15 dex is only just consistent with observations: McGaugh, 2011, 2012; Dutton, 2012).

Because of this emphasis on scatter and its sensitivity to the fundamental interactions between baryons and dark matter in standard ΛCDM theory, we draw particular attention to scatter in our TF relations as we probe to high redshifts.

2. **Why is there a TF relation?** It is remarkable that after decades of study, the underlying driver(s) of the TF relation, including its unparalleled low scatter amongst galaxy scaling relations, remains a mystery.

   Starting from the virial theorem, Aaronson et al. (1979) showed that $V_{\rm max}^4 \propto \mu_0 M$, where μ_0 is the central surface density (crediting Paul Schechter for the original demonstration). Celebrated at the time as the simplest explanation for the TF relation, decades of work thereafter would reveal that the predicted dependancy on surface density is mysteriously

absent (Sprayberry et al., 1995; Zwaan et al., 1995; Courteau & Rix, 1999b; McGaugh, 2005). The galaxy scale dependancy which further reduces the residuals of the relation between luminosity and dynamics in the Fundamental Plane (Djorgovski & Davis, 1987) does not occur for disc galaxies— in a sense the TF relation is already the optimal projection of the plane (McGaugh, 2012).

Furthermore, ΛCDM struggles to explain the TF relation in a straightforward way. The precisely constrained baryon fraction ($f_{\rm bar} = 0.167 \pm 0.004$ Komatsu et al., 2011) combined with the well-known scaling of the virial masses and rotation velocities of dark matter haloes ($M_{\rm vir} \propto V_{\rm vir}^3$: Mo et al., 1998) results in a predicted TF relation that is over an order of magnitude offset in normalisation and slope from that observed. This large offset is a key exemplar of the 'Missing Baryon Problem' (Bell et al., 2003; Fukugita & Peebles, 2004; Read & Trentham, 2005), and requires that feedback act in a way that most affects lower mass galaxies, which undergo the least efficient star-formation.

While the nature of the required feedback is counter-intuitive, it should not immediately discount ΛCDM without further investigation, which we develop further in Ch. 5. Tightly tracking the evolution in the TF relation has significant potential to inform this most fundamental question regarding disc galaxies, and can be considered as one of the major motivations of this work.

3. **Why does the TF relation evolve (or not)?** As introduced in the first chapter of this thesis, the TF results at high redshift have been varied— even contradictory. However, there has been one point of consistency between the previous works at high redshift, which is the scatter of the TF relation appears to increase significantly. What has not been clear is whether this increase in the scatter is intrinsic, or merely a consequence of the increasing challenge of precision measurements of galaxy

kinematics as redshift increases. Until we know more precisely the nature of intermediate and high redshift TF scatter, it will be impossible to gauge whether evolution is occurring in the relation.

This is what we have attempted to achieve in this thesis, and now that sufficient context has been aggregated in which to place our results, we present a new offering to the understanding of how disc galaxies assemble and evolve via the Tully-Fisher relation across two-thirds of the age of the universe.

4.2 The stellar mass TF relation to $z\sim1$ and beyond

We consider the case for evolution in the stellar mass (M_*)-TF relation for the galaxy dataset of this thesis. Relations are fit separately between the DEIMOS and LRIS datasets (in §4.2.1 and §4.2.2, respectively), to examine both potential systematic offsets as well as intrinsic differences between the two. We then combine the two sets of analyses (§4.2.3) to infer the nature of the evolution of the M_*-TF relation over the whole redshift range ($0.2 < z < 1.7$).

4.2.1 DEIMOS: $0.2 < z \lesssim 1$

We begin with the TF relations of the DEIMOS sample, and the results are illustrated in Fig. 4.1 and listed in Table 4.1. Redshift bins were selected to ensure nearly uniform samples over the redshift range of the sample. Shifting the boundaries of these bins by modest amounts (±0.2) does not change the overall conclusions we present below.

To fit a linear regression to our data we adopt a least-squares approach that incorporates a measurement of the intrinsic scatter $\sigma_{\rm int}$, which is added in quadrature to the velocity uncertainty and adjusted so that the value of χ^2 per degree of freedom is unity (similar to Tremaine et al., 2002). We fit a line which

is zero-pointed (M_0) within the data range, which allows us to more sensitively gauge the errors:

$$\log\left(\frac{M_*}{M_\odot}\right) = a + b\ \log\left(\frac{V_{2.2}}{\mathrm{km\ s^{-1}}}\right) - \log\left(\frac{M_0}{M_\odot}\right), \tag{4.1}$$

where $M_0 = 10^{10} M_\odot$, and while we plot the relation in the familiar way with velocity on the x-axis and a y-intercept given in terms of stellar mass, we treat velocity as the dependent variable in the linear regression. Fitting linear regressions with stellar mass as the dependent variable leads to fits which suffer much more from the effects of incompleteness bias (Bamford et al., 2006; Weiner et al., 2006a).

For fitting the linear regression with Eq. 4.1, we adapted an IDL code which takes into account errors in both the ordinate and abscissa. We first fit an unrestricted slope to the entire data set (all redshifts), and then fit the individual redshift-binned relations with a distribution of slopes drawn from a Monte Carlo (N=100) Gaussian distribution centred on the slope from the full sample. We do this for both the *enclosed* mass (i.e. that associated with our fiducial radius, $r_{2.2}$), and the *total* mass. We also experimented with simpler approaches to linear regressions, with well-known IDL codes like FITEXY.PRO and the Bayesian LINMIX_ERR.PRO (Kelly, 2007), which result in similar trends (typically within 1-2 %) but with naively smaller errors, so we present here our most robust results with the broadest consideration of the uncertainties using the Monte Carlo approach.

When we fit free slopes to each of the redshift bins, the error bars are several times larger in each case, so while the slopes are consistent with each other and with the free slope from the total relation, we cannot determine any potential difference in the normalisation of the TF relation in each bin.

For a local comparison, we consider the M_*-TF relation derived from K-band luminosities published by Bell & de Jong (2001) and the M_*-TF relation from Pizagno et al. (2005), the latter of which is based on velocities from $r_{2.2}$ as presented in the enclosed relation of this study.

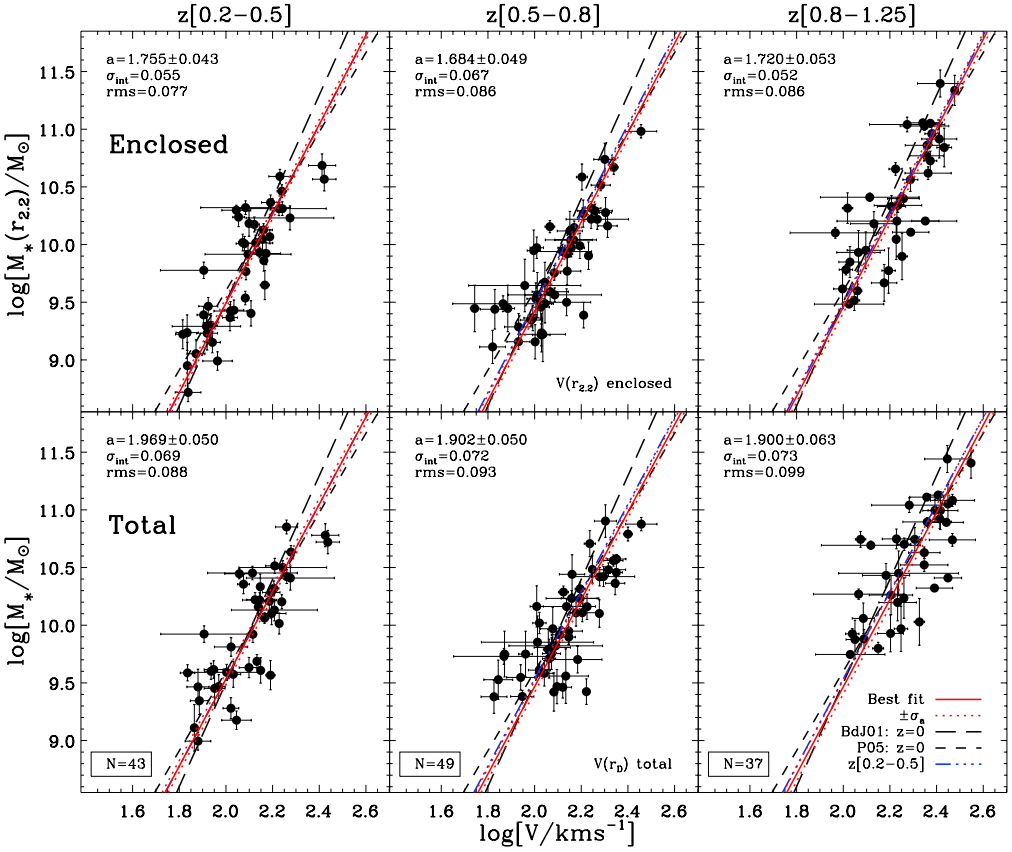

Figure 4.1 Redshift-dependent stellar mass Tully-Fisher (M_*-TF) relations using the enclosed (top panels) and total (bottom panels) mass estimates. Dashed lines refer to the local relations of Bell & de Jong (2001) and Pizagno et al. (2005). Dot-dashed lines refer to the fit to the lowest redshift bin in the current dataset. To fit fixed slopes between redshift bins, we fit relations using a Monte Carlo distribution of slopes from the best-fit free slope of the entire sample. The resulting mean slope is shown as a solid red line with red dotted lines showing the 1σ error in the zero-point (in $M_*/M_\odot$ dex). Using the velocity and enclosed mass at the $r_{2.2}$ aperture reduces both the intrinsic scatter ($\sigma_{\rm int}$) and the rms of the relationship in each redshift bin. The uncertainty of the determination of $\sigma_{\rm int}$ is ±0.015 dex. (in velocity).

Table 4.1: Stellar mass TF relations from DEIMOS sample

z range	$\langle z \rangle$	N	a[1]	b[2]	$\sigma_{int,V}$[3]	med σ_V[4]	rms_V[5]	$\sigma_{int,M}$[6]	med σ_M[7]	rms$_M$[8]
Enclosed: $M_*(r_{2.2})$ vs. $V(r_{2.2})$:										
0.2<z≤1.3	**0.64**	**129**	**1.718±0.415**	**3.869±0.193**	**0.058**	**0.022**	**0.083**	**0.224**	**0.091**	**0.323**
0.2<z≤0.5	0.37	43	1.755±0.043	” fixed	0.055	0.035	0.077	0.211	0.081	0.297
0.5<z≤0.8	0.62	49	1.684±0.049	” fixed	0.067	0.045	0.086	0.257	0.118	0.334
0.8<z≤1.3	0.96	37	1.720±0.053	” fixed	0.052	0.062	0.086	0.202	0.098	0.331
Total: M_* vs. $V(r_{\rm opt})$										
0.2<z≤1.3	**0.64**	**129**	**1.926±0.476**	**3.783±0.223**	**0.070**	**0.023**	**0.093**	**0.266**	**0.087**	**0.353**
0.2<z≤0.5	0.37	43	1.969±0.050	” fixed	0.069	0.037	0.088	0.262	0.083	0.332
0.5<z≤0.8	0.62	49	1.902±0.050	” fixed	0.072	0.057	0.093	0.272	0.110	0.351
0.8<z≤1.3	0.96	37	1.900±0.063	” fixed	0.073	0.064	0.099	0.277	0.084	0.375

[1]For Eq. 4.1, the best-fit y-intercept in $M_*/M_\odot$ dex assuming scatter in V/kms^{-1} dex
[2]slope assuming scatter in V/kms^{-1} dex
[3]internal scatter in V/kms^{-1} dex
[4]median velocity error in V/kms^{-1} dex
[5]total scatter in V/kms^{-1} dex
[6]internal scatter in $M_*/M_\odot$ dex
[7]median stellar mass error in $M_*/M_\odot$ dex
[8]total scatter in $M_*/M_\odot$ dex

Before discussing possible evolution, we consider the derived scatter around the relations since this is a valuable indication of our gains in precision. Satisfactorily, we find intrinsic scatters in the fits of 0.055, 0.067, 0.052 (dex of V km s^{-1}, with an uncertainty of 0.015 dex) at $\langle z \rangle$=0.37, 0.62, 0.96, which are comparable to that seen in local TF relations (i.e., ∼0.049 in Pizagno et al. (2005)). Our analysis therefore represents a significant improvement on the scatter seen in earlier intermediate-redshift studies, for example an improvement of a factor of 2-3 over the study of Conselice et al. (2005). We also achieve a scatter less than that found in the M_*-$S_{0.5}$ relation of Kassin et al. (2007, between 0.08 and 0.11 dex), despite the fact that they introduce an additional scaling parameter in $S_{0.5}$, which significantly tightens the relation from their log V - M_* relation (discussed in §1.3).

Table 4.1 shows that with our increased precision, there is little room for evolution in the M_*-TF relation. Fitting a straight line through the zero-points between redshift bins, we detect a modest but statistically insignificant trend for a larger stellar mass at fixed velocity at lower redshift: ΔM_*∼0.037 ± 0.065 dex (1σ) from $\langle z \rangle$∼1.0 to 0.3. Fitting a straight line through zero-points between redshift bins in the Conselice et al. (2005) study, we find a ΔM_*∼$0.07 \pm$ 0.19 dex (1σ) from $\langle z \rangle$∼1.0 to 0.3, consistent with our result, yet more uncertain. Interestingly, our 1-sigma limit for evolution is consistent with the modest $\Delta \log M_*/M_\odot$ predicted by Portinari & Sommer-Larsen (2007) ($\Delta M_* \sim 0.1$), Somerville et al. (2008) (10% decrease in V at fixed M_* with time), and consistent with Dutton et al. (2011a) ($\Delta M_* \sim 0.2$) over a similar redshift range only at the 2-sigma level. Importantly, the lack of clear evolution is robust to the inclusion of the local data for both the 'enclosed' and 'total' relations.

We note that the scatter in the total M_*-TF relations is increased somewhat compared to that in our preferred enclosed relations, most likely due to the effect of the increased number of extrapolated velocity measurements (discussed in Ch. 2 & 3). We trace spectroscopic emission beyond $r_{\rm opt}$ on ∼60% of our disks as opposed to ∼90% beyond $r_{2.2}$.

4.2.2 LRIS: $1 \lesssim z < 1.7$

We now turn to the M_*-TF relation for the high redshift ($1 < z < 1.7$) LRIS sample, shown in Fig. 4.2. As with the DEIMOS sample, we plot the enclosed stellar mass within $r_{2.2}$ against the de-projected rotational velocity $V_{2.2}$, and inversely fit a linear regression using a least-squares method incorporating the intrinsic scatter (σ_{int}) added in quadrature to that of the velocity, accounting for errors in both the ordinate and abscissa.

Due to the increased uncertainty in the velocity measurements, we fix the slope b=3.869 as that derived for the total DEIMOS sample, and we find a=1.692±0.060, σ_{int}=0.080 dex in $\log[V/\mathrm{km\ s^{-1}}]$. We find a total rms of 0.117 dex, which is reasonable considering the median error is 0.102 dex. In stellar mass, this corresponds to σ_{int}=0.310 dex in $\log[M_*/M_\odot]$ and an rms of 0.452 dex (where the median error is 0.186 dex). When we fix the slope to that of the local relation (Reyes et al., 2011b), there is no substantial change in the result (right panel of Fig. 4.2), and when we fit a free slope, the results remain consistent, although the uncertainty is several times larger which would obscure any potential change in the TF normalisation.

While we recover a zero-point for the fixed-slope M_*-TF relation similar to that found in the DEIMOS sample for $0.2 < z < 1.3$, the scatter in the relation has apparently increased as much as 60% as compared to the local relation. Part of this increased scatter could be attributed to the more challenging observations undertaken with LRIS. We note, for example, that the additional scatter introduced by using LRIS *c.f.* DEIMOS as described earlier in §3.8 (∼0.098 dex in $\log[\mathrm{V/km\ s^{-1}}]$), implies the intrinsic scatter could be as low as 0.063 dex. Given the uncertainty in the scatter is about 0.01 dex, this value is not significantly different than that found in DEIMOS (0.058 dex, Miller et al., 2011). So while it is possible that the relation is less well-defined by a broadening of up to 60% compared to $z \sim 0$, where average scatter is found to be ∼0.05 dex (i.e., Pizagno et al., 2005; Reyes et al., 2011b), we cannot rule

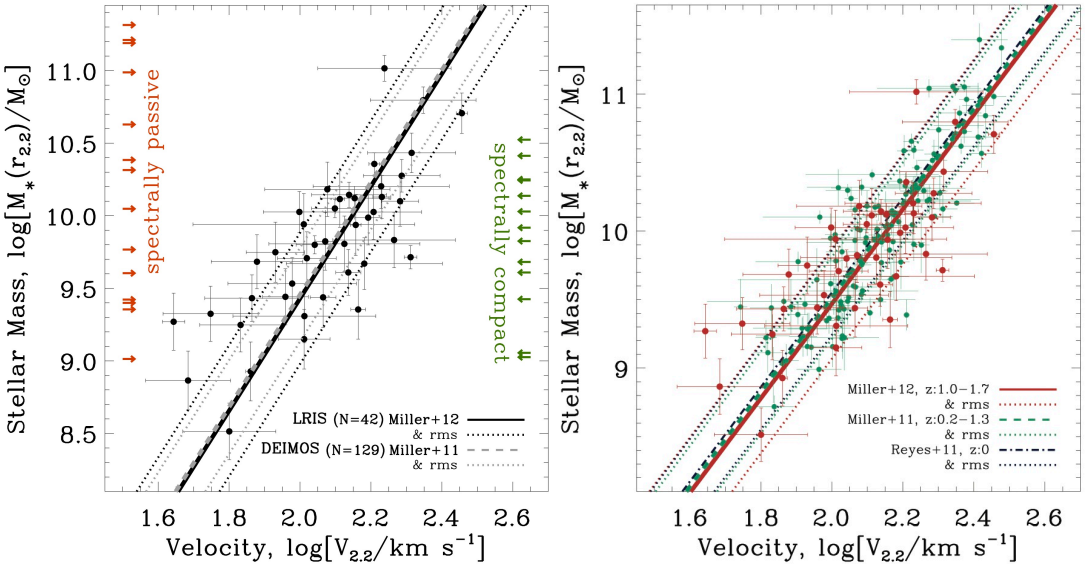

Figure 4.2 **Left:** The M_*-TF relation derived for 42 suitable galaxies in the redshift interval $1 \lesssim z < 1.7$. The best inverse fit relation, with the slope fixed to that of the DEIMOS relation, is shown as a solid black line and the rms scatter is displayed as a pair of dotted lines. The slope is fixed to the best-fit M_*-TF relation found from the DEIMOS sample ($z \sim 0.2$ to $z \sim 1$), shown as the dashed grey line (which is nearly coincident with the results of this study). The rms scatter around the DEIMOS sample fit is shown the pair of grey dotted lines. Although the zero point has not changed in the intervening 2 Gyr, the *apparent* scatter has increased (although perhaps not the intrinsic scatter—see text). We also show with arrows the stellar masses of two categories of galaxies for which we cannot extract measurements of $V_{2.2}$ (see Ch. 3, §3.5 for details). **Right:** The M_*-TF relation from both DEIMOS and LRIS samples plotted together, where the slope has been fixed to the local relation of Reyes et al. (2011b, slightly shallower but consistent within 1σ of the DEIMOS slope used in the figure to the left). With the relations plotted in this way, the 60% increase in scatter of the LRIS ($1 \lesssim z < 1.7$) is apparent, noting well that the increase appears to be to the 'faster' or 'less massive' side of the relation. Why this may be so will be explored further in Ch. 5).

out the possibility that the tightness of the relation in this study is the same as that found locally.

We also show in Fig. 4.2 the stellar masses for two important subsets of the originally-targeted sample whose resolved dynamics cannot be determined (details in Ch. 3, §3.5). The first category are the 14 spectrally 'passive' objects which are clearly some of the most massive galaxies in the sample. It is possible

that these passive galaxies are evolving off the TF relation and transitioning onto the red sequence. On the other hand, the stellar masses of the spectrally 'compact' objects do not significantly differ from that for main sample displaying suitably extended emission. While mass is unlikely to be the main driver of galaxies transitioning from the blue to the red sequence, there is a clear mass dependence between the two. In this respect it is interesting we see no such difference in the spectrally extended and compact objects of this study (although it would be interesting if this were still the case with an even larger sample size). Most spectrally compact galaxies appear to have extended disks in the HST ACS images, although star formation appears to have largely shut off in their outer disks as evidenced by their spectrally compact nature. Conceivably, these galaxies could comprise systems with actively forming bulges, up to a few times 10^{10} $M_{\odot}$ in stellar mass. However, this would beg the question as to what is feeding this behaviour, which we will discuss further in Ch. 5.

During the completion of this thesis, a study appeared on arXiv.org [astro-ph] pre-print service, (Vergani et al., 2012), which plots 23 galaxies from the MASSIV survey onto a stellar mass TF relation with similar or larger scatter as that found in our relation (σ_{int}=0.32 or 0.52 and rms=0.48 or 0.72) and little to some evolution in the stellar mass zero-point (-0.05 $\pm$ 0.16 dex or -0.36 $\pm$ 0.11), depending on the Bell & de Jong (2001) or Pizagno et al. (2007) slope adopted, respectively. While the kinematics data was obtained on the SINFONI IFU, only 5 of these objects were observed using AO (and only 2 in the sub-sample used to plot the stellar mass TF relation). In their TF constraints, they exclude over half of their sample where significant emission was detected, not only when the emission is unresolved, as in our study, but also when their velocity field is not well described by a symmetrically rotating disc, the kinematic position angle differs significantly from the morphologically derived major axis, or when their measured $v/\sigma < 1$ (all criteria which are not included in our study). The addition of the modelled velocities in these excluded galaxies adds considerably to the apparent scatter in the Vergani et al. (2012) stellar mass Tully-Fisher

relation, whereas our inclusion of merger-like systems or galaxies where rotation curve centres appear offset to the HST-derived centres do not appear to result in the same large scatter. This may be due to their use of V_{max}, described in Ch. 2 as potentially leading to an inaccurate representation of the true intrinsic maximal rotation velocity because of its dependancy on the distribution of emitting gas in the disc and inconsistency between galaxies in a diverse sample such as theirs and ours. Also a potential problem for their results, we find in Ch. 2 that assuming an intrinsic emission distribution based on broad-band optical or NIR HST imaging can often lead to systematic offsets in χ^2 minimisation dynamical modelling, amplified by the scale of seeing and dispersion in the spectral data. If this effect is significant for slit-based modelling, then it would be just as damaging if not more so in 2-D IFU-based modelling. The zero-point evolution of the TF relation from this study is plotted on the left side of Fig. 4.2.

4.2.3 Evidence for TF evolution from $0.2 < z < 1.7$

Finally, to place our M_*-TF relation results across the entire redshift range of interest in the context of earlier work, Fig. 4.3 summarises recent results over $0<z<3$. Notwithstanding possible selection biases discussed further in Ch. 5, it is illustrative to consider this figure. Evolution in the M_*-TF relation zero-point can be normalised with respect to the local study of Reyes et al. (2011b), calibrated from the SDSS parent sample and also adopting the same $V_{2.2}$ parameterisation used in this work. To ensure an adequate comparison, we re-fit our data using the Reyes et al. (2011b) slope (right side of Fig. 4.2), which we note is not significantly different from the slope we find in the DEIMOS dataset. Because Reyes et al. (2011b) use the total mass rather than that enclosed at $r_{2.2}$, we move their zero-point by -0.187 dex in stellar mass to account for the difference in the enclosed mass as compared to the total stellar mass. We make a further correction to account for the different IMF assumed, since Reyes et al. (2011b) adopted a Kroupa (2002) IMF, which both sets

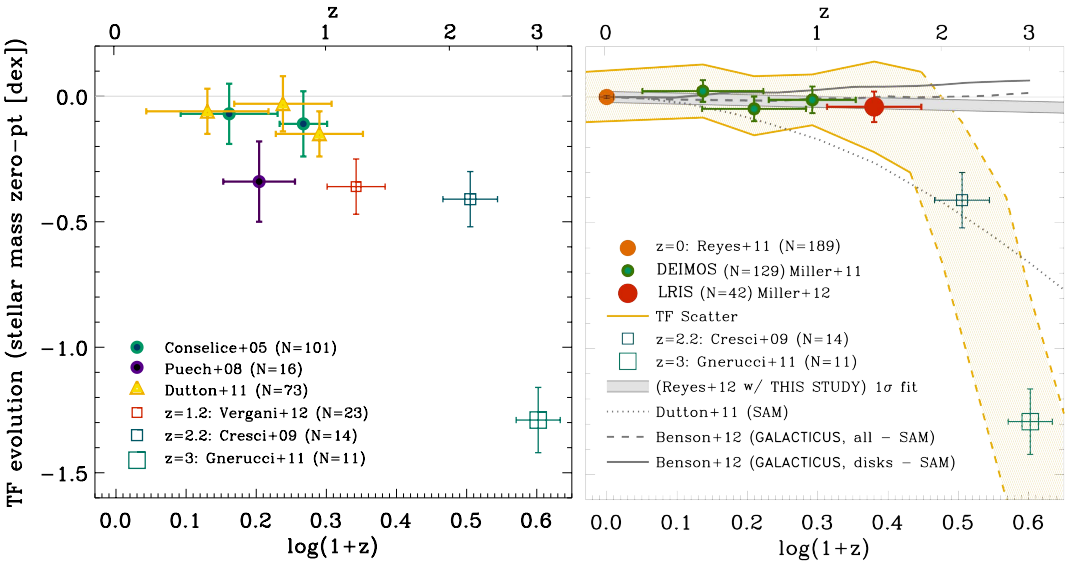

Figure 4.3 **Left:** shows the progress in constraining the evolution of the M_*-TFR zero-point (Conselice et al., 2005; Puech et al., 2008; Dutton et al., 2011a) before the completion of this thesis and its corresponding papers (Miller et al., 2011, 2012), with exception of Vergani et al. (2012), which appeared on the arXiv during the final stages of the completion of this thesis. We note that all of the IFU studies (Puech et al., 2008; Vergani et al., 2012; Cresci et al., 2009) lie suggestively offset from the local relation at the same interval in dex, with exception of the highest redshift study done at present (Gnerucci et al., 2011). **Right:** shows the improvement of our results, showing both the redshift dependent M_*-TFR scatter and zero-point, assuming a fixed slope as determined by Reyes et al. (2011b) at z∼0 (orange circle). We compare the results from LRIS (red circle) and DEIMOS (green circles) to those at even higher redshift (Cresci et al., 2009; Gnerucci et al., 2011). We also compare semi-analytic models (SAM) from Dutton et al. (2011a) and Benson (GALACTICUS, 2012) For a full discussion of this plot, please see both §4.2.3 and Ch. 5.

of authors agree accounts for a 0.05 dex decrease compared to our assumed Chabrier (2003). In total, this is a -0.137 dex calibration between the Reyes et al. (2011b) study and our work, resulting in only a marginal change in the M_*-TFR zero-point since $z \simeq 1.7$. Formally, the linear regression shown in Fig. 4.3 yields a stellar mass zero-point change of only 0.02±0.02 dex over the last 9.8 billion years (over two-thirds the age of the universe).

We also include results at $z \sim 2.2$ and $z \sim 3$ from Cresci et al. (2009) and Gnerucci et al. (2011), respectively, which suggest a surprisingly rapid and significant evolution beyond $z \sim 1.7$. However, the average stellar mass in the

Cresci et al. (2009) sample is 6.3×10^{10} $M_{\odot}$, and range from 0.62–31.6 $\times10^{10}$ $M_{\odot}$, whereas our sample average is 1.3×10^{10} $M_{\odot}$, and ranges from 0.05–17.2×10^{10} $M_{\odot}$ (both using a Chabrier IMF). As suggested earlier, we will discuss possible causes, including sample differences, which could account for this dramatic shift in the zero-point in Ch. 5.

As a theoretical comparison we present preliminary M_*-TF relation evolution results computed using GALACTICUS v0.9.1 r631[2] (Benson, 2012), which includes various modules for star formation and AGN feedback as well as state-of-the-art theoretical predictions for baryon-halo evolution. Shown in Fig. 4.3 are GALACTICUS models for both disk-dominated galaxies (bulge-to-total mass fraction < 0.3) and all galaxies. In each case, the mean zero-points correspond to galaxies with stellar masses between 0.5 and 2×10^{10} $M_{\odot}$. Interestingly, the results from models of all galaxies shows a similar, non-evolving trend in the M_*-TFR zero-point, whereas the the disk-only sub-sample of the models depart in evolution to the slow side of the observed relation as redshift increases, but never more than 0.1 dex — even to $z\sim3$. In this figure we also include the semi-analytical model of Dutton et al. (2011a), which is consistent with a sample subset of the results originally presented in Weiner et al. (2006b) and Kassin et al. (2007, N=73 from 544 galaxies). Their projected evolution departs from the results of this work at $z \sim 1$ and beyond. We will explore possible reasons for this in Ch. 5.

4.3 Evolution in the B-band TF relation

We undertake a similar analysis as that in §4.2.1 for the absolute B magnitude (M_B) TF relation, where M_B measurements come from the best-fit SEDs (described in §3.3), and are aperture corrected in the same way as the stellar mass estimates. The TF relations are shown in Fig. 4.4 for both total and enclosed luminosities and the results are listed in Table 4.2. Any difference in

[2]computed with an input parameter file which is available from http://sites.google.com/site/galacticusmodel/downloads/parameter-sets

the redshift-dependent trends compared to that for stellar mass relation would indicate changes in the star formation rate per unit stellar mass. Some workers have claimed to see evolution in the M_B-TF relation (Weiner et al., 2006a; Fernández Lorenzo et al., 2010) and we aim to verify or otherwise these trends with our improved dataset. As before, we use the local relations of Pierce & Tully (1992) and the $\langle z \rangle \sim 0.3$ study of Bamford et al. (2006) as comparison datasets.

Once again, the intrinsic scatter around our redshift-dependent M_B-TF relations, 0.424, 0.641, 0.670 in mag, at $\langle z \rangle$=0.37, 0.62, 0.96, are comparable to those seen in the local relations: $\sim$0.4 mag in Pierce & Tully (1992), and 0.3-0.5 in Verheijen (2001). We note a considerable improvement over previous intermediate-redshift studies. The $\langle z \rangle \sim 0.3$ study of Bamford et al. (2006) and the $\langle z \rangle \sim 0.85$ study of Chiu et al. (2007) have scatters twice as large ($\sim$0.9 in mag), and those of Weiner et al. (2006b) to z$\sim$1.2 and Fernández Lorenzo et al. (2010) to z$\sim$1.4 have scatters $\simeq$2-3 times as large ($\sim$1.5 mag and $\sim$1.2 mag, respectively).

Even though the M_B-TF relation is not as tight as our M_*-TF relation, there is evidence for a stronger evolution in the M_B-TF relation than in the M_*-TF relation, as expected from the well-established increase in disk star formation rate to $z \sim 1$ (Lilly et al., 1996; Madau et al., 1996). Fitting a linear regression through the zero-points between redshift bins of the enclosed M_B-TF relation we find $\Delta M_B \sim 0.85 \pm 0.28$ mag evolution in the relation from $\langle z \rangle \sim 1.0$ to 0.3. We can check if this result is affected by a Malmquist bias (given the distribution of luminosities is significantly different between redshift intervals), by comparing subsets with similar luminosities and stellar masses, and the trends do not substantially change. Weiner et al. (2006b) find a consistent trend of $\sim$1.0-1.5 mag evolution from a similar redshift range of $\langle z \rangle \sim 1.2$ to 0.4, but with more uncertainty. Our results are consistent with the evolution shown in the models of Portinari & Sommer-Larsen (2007): $\Delta M_B \sim 0.85$ from $z \sim 1$. We can understand the different evolutionary trends in the M_B-TF and

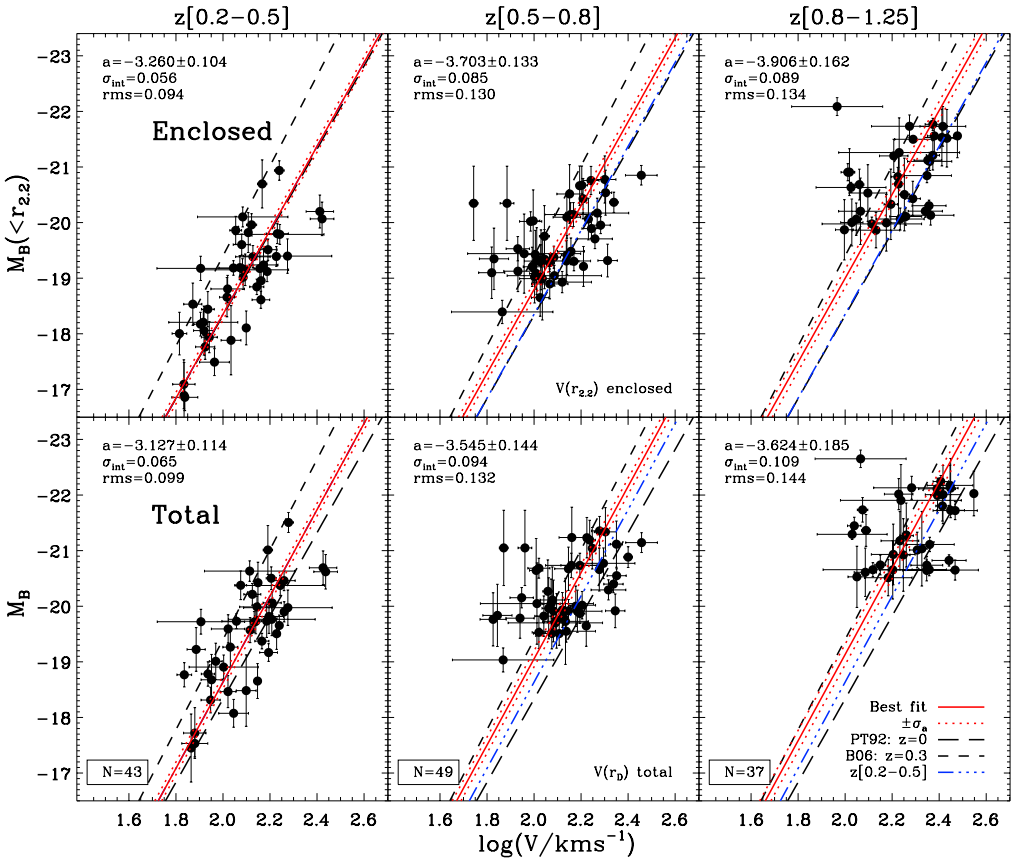

Figure 4.4 As Fig. 4.1 but for the absolute B-band magnitude (M_B) Tully-Fisher relation. For comparison purposes, we show the local relation of Pierce & Tully (1992) and the $z \sim \langle 0.3 \rangle$ relation of Bamford et al. (2006) as dashed lines. Other lines are as in Fig. 4.1.

M_*-TF relations by examining the redshift-dependent correlation between M_B and M_*. To first order, as expected, the difference is explained by the increase in the B band luminosity per unit stellar mass with redshift (Bundy et al., 2005).

Table 4.2: Absolute B-band magnitude TF relations from DEIMOS sample

z range	$\langle z \rangle$	N	a[1]	b[2]	$\sigma_{int,V}$[3]	med σ_V[4]	rms_V[5]	$\sigma_{int,M}$[6]	med σ_M[7]	rms$_M$[8]
Enclosed: $M_B(r_{2.2})$ vs. $V(r_{2.2})$:										
0.2<z≤1.3	**0.64**	**129**	**-3.589±0.893**	**-7.546±0.578**	**0.081**	**0.022**	**0.127**	**0.612**	**0.291**	**0.956**
0.2<z≤0.5	0.37	43	-3.260±0.104	” fixed	0.056	0.035	0.094	0.425	0.245	0.711
0.5<z≤0.8	0.62	49	-3.703±0.133	” fixed	0.085	0.045	0.130	0.641	0.364	0.979
0.8<z≤1.3	0.96	37	-3.906±0.162	” fixed	0.089	0.062	0.134	0.670	0.299	1.011
Total: M_B vs. $V(r_{\rm opt})$										
0.2<z≤1.3	**0.64**	**129**	**-3.413±1.037**	**-7.754±0.657**	**0.091**	**0.023**	**0.130**	**0.706**	**0.250**	**1.008**
0.2<z≤0.5	0.37	43	-3.127±0.114	” fixed	0.065	0.037	0.099	0.505	0.258	0.771
0.5<z≤0.8	0.62	49	-3.545±0.144	” fixed	0.094	0.057	0.132	0.731	0.364	1.027
0.8<z≤1.3	0.96	37	-3.624±0.185	” fixed	0.109	0.064	0.144	0.845	0.272	1.114

[1]best-fit y-intercept in mag assuming scatter in V/kms^{-1} dex
[2]slope assuming scatter in V/kms^{-1} dex
[3]internal scatter in V/kms^{-1} dex
[4]median velocity error in V/kms^{-1} dex
[5]total scatter in V/kms^{-1} dex
[6]internal scatter in mag
[7]median stellar mass error in mag
[8]total scatter in mag

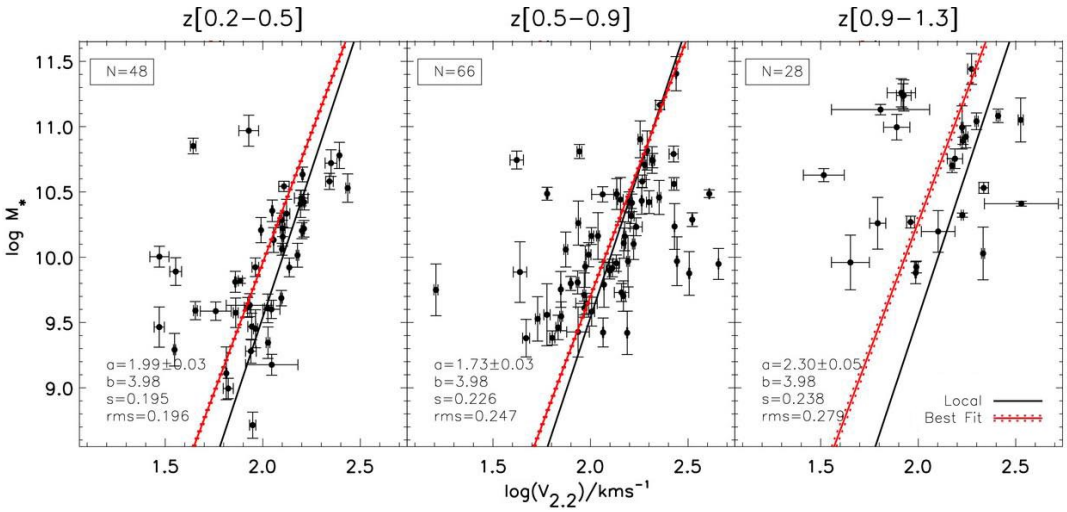

Figure 4.5 The M_*-TF relation in three redshift bins, where velocities have been extracted from a rotation curve modelling code which assumes the line profile in individual spatial bins to be Gaussian, rather than the 2 half-Gaussian trace of CURVATION. Small offsets in the trace can propagate (here in ∼25% of galaxies) to large velocity offsets in the extracted fiducial velocities, even at $r_{2.2}$.

4.4 The effect of adopting previous rotation curve methodologies

Before moving forward to the interpretation of these results in Ch. 5, we take a moment to demonstrate the critical nature of a few measurement and analysis choices, given the challenge of disc dynamics at intermediate to high redshifts. This demonstration relies on the assumption that by implementing some feature of a velocity extraction code which decreases the scatter of the TF relation, we are likely extracting more *accurate* results, rather than simply more *precise* measurements (demonstrated in Ch. 2 & 3).

Firstly, we demonstrate the difference which is made by a feature as simple as the assumed shape of the emission line in each spatial bin. A tracing code which does not implement the 2 half-Gaussian feature of our preferred procedure, CURVATION, was demonstrated in Ch. 2, Fig. 2.5. Visually, the traces appear acceptable, but the subtle biases propagate through the modelling process, compounding in major offsets from the final relation for 25%

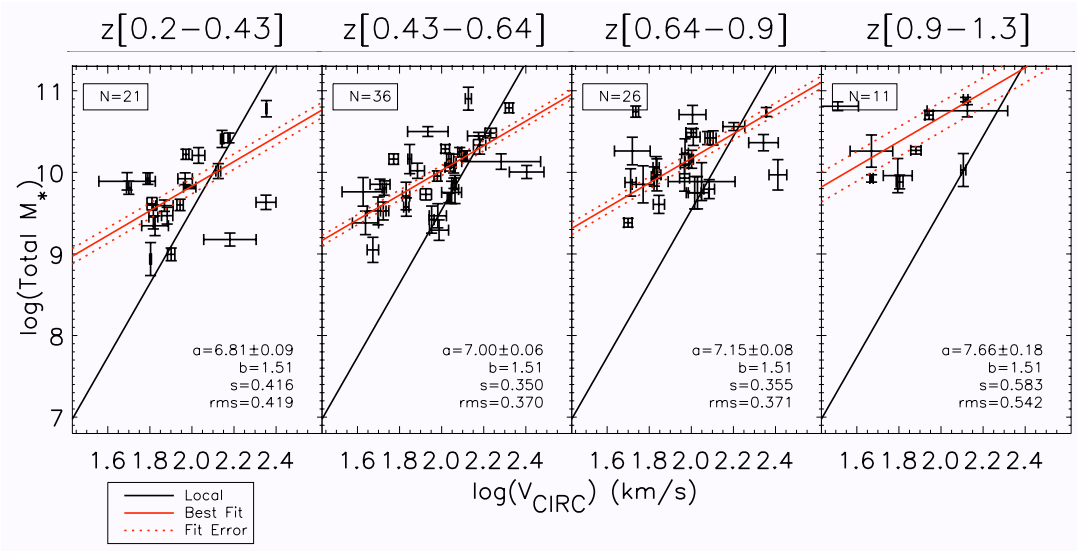

Figure 4.6 The M_*-TF relation results from velocity extraction procedures where the asymptotic velocity (V_a) is assumed to be equivalent to $V_{\rm circ}$ (and corrected for inclination). The code used here is constructed similarly to previous studies, such as Metevier et al. (2006); Weiner et al. (2006a); Kassin et al. (2007); Vogt et al. (1996). The points with the highest residuals from the local relation (black line) were typically the galaxies with the least extended emission lines. They also were typically the galaxies where the emission surface brightness profile in the observed spectra were most unlike the exponential surface brightness profile assumed in most models. Naively, this is not a bad assumption based on the ubiquity of exponential discs. However, in practice the emission brightness profile is rarely exponential, and does not often follow the measured profile from broad-band HST imaging most appropriate for the emission line of interest. Relatively small errors fit to the inner rotation curve compound, leading to a large induced velocity axis scatter in the resulting Tully-Fisher relation. Fortunately, this induced scatter can be largely avoided with a few detail-oriented implementations of the modelling scheme (explained further in Ch.2, §2.3).

of final velocity extractions (Fig. 4.5). This accounts for an increase of TF relation scatter of 3-4× what is recovered using the CURVATION code. This is especially remarkable given that we velocities are extracted at $r_{2.2}$ in this demonstration, which has been shown to truncate false extrapolations (Ch. 2).

Secondly, we have experimented with the assumption of $V_{\rm circ} \simeq V_a$, which has been cited and demonstrated as a scatter inducing assumption in Chapters

2 & 3. To show the full affect of an assumption such as this, even given the quality of data with which we are working with, Fig 4.6 shows the results of an code we developed which is similar to that of Vogt et al. (1996); Metevier et al. (2006); Weiner et al. (2006a); Kassin et al. (2007).

We found that the $V_{\rm circ}$ extractions (effectively V_a), tend to be dominated by systematic offset effects when the inner rotation curves are not precisely constrained, leading to relations where the TF scatter is anywhere from 7–10$\times$ what was extracted with CURVATION at $V_{2.2}$. The scatter in Fig 4.6 also appears to be consistent with the scatter found in the M_*-TF relation presented in Kassin et al. (2007) as well (top panels in Fig. 1.8). While they do not publish these figures directly, by attempting to pull the data from the plots presented, a rough analysis shows that the scatter in velocity appears to be at least 0.4 dex in km s^{-1} in each redshift bin.

This version of the code also assumes a standard exponential surface brightness profile for the intrinsic emission profile across the disc. That is to say, we do not implement the CURVATION feature which takes the emission brightness profile directly from the trace of the emission line, because this is not a feature of the procedures we wish to emulate in this demonstration (Vogt et al., 1996; Metevier et al., 2006; Weiner et al., 2006a; Kassin et al., 2007).

It is remarkable how that, even with an exemplary spectroscopic dataset such as that presented in Ch. 3, choices like the extraction velocity, and something apparently as simple as the emission brightness profile assumption, can dramatically change whether the TF relation is sufficiently dominated by measurement error that evolutionary signals are impossible to constrain.

4.5 Summary of Chapter 4

In Chapter 4, we have presented the following:

- The stellar mass (M_*)-TF relations from $0.2 < z < 1.7$ with intrinsic scatters that are consistent with the local relation, which is 2-3 times less

than that of earlier work at similar redshifts, including the $S_{0.5}$ relation of Kassin et al. (2007). However, there is evidence that the scatter could increase up to 60% in the highest redshift range of this study ($1.0 \lesssim z < 1.7$) with respect to the local relation, but the results are consistent with no increase as well.

- Little evidence for evolution in the M_*-TF relation across $0.2 < z < 1.7$, less than 0.04 dex (1σ) in stellar mass for the zero-point shift (normalisation of the relation).

- The modest evolution seen in the M_*-TF relation over $0 < z < 1.7$ contrasts markedly with results emerging at $z > 2$. However, systematic offsets due to sample difference and other effects could be driving such a dramatic shift, and this is explored further in Ch. 5.

- The classic B-band absolute magnitude (M_B)-TF relation with scatter similar to the local relation in the lowest redshift bin $0.2 < z < 0.5$, which appears to increase significantly with look-back time.

- Even with the increase scatter of the M_B-TF relation at higher redshift, we detect a marginal (just over 3σ) decline in luminosity with cosmic time of 0.85 ± 0.28 mag from $\langle z \rangle \simeq 1$ to $\langle z \rangle \simeq 0.3$, consistent with the known decreasing disc galaxy star formation rate at a given mass since $z \sim 1$.

- Overwhelming evidence that the stellar mass Tully-Fisher relation is a more fundamental relation than the B-band relation over a major fraction of the age of the universe in describing disc galaxy assembly.

- Further demonstration via the TF relation scatter that our modelling procedure results are not only more precise velocity extractions than previous similar work (demonstrated in Ch. 2 & 3), but more accurate velocities as well.

Already 2 of the 3 questions posed in §4.1 have begun to be addressed before attempting to reintegrate these quantitative descriptions back into the popular theoretical frameworks which ultimately inform the data analysis. We have attempted at each turn to base the analysis on purely phenomenological methods, such as the adoption of the arctan function, however certain theory/model-laden methods were practically unavoidable, *e.g.*, ΛCDM-based distance moduli for the absolute magnitudes and Chabrier IMF adoptions for the stellar mass estimates. With attention to these analytical and methodological assumptions, our results are now applied in an interpretive set of analyses in the following chapter.

Chapter 5

Interpretations for Disc Galaxy Evolution and Dark Matter

We now seek to further understand and interpret the physical significance of the results presented in Chapter 4, in the context of current models of disc galaxy assembly. We begin by estimating where and how the gas and dark matter is distributed in the galaxies of our sample (§5.1), to aid in our interpretive analysis. We then discuss the results of the Tully-Fisher relations in a wider context (§5.2) including comparisons to pioneering work at higher redshift, as well as some of the latest semi-analytical models which examine the evolution of the Tully-Fisher relation. In the last section (§5.3) we explore potential drivers of disc assembly, by presenting results of the morphological analysis of the Ch. 4 results, and then discuss various implications and hypotheses from this work to be tested, also drawing on a wide context.

5.1 Estimating the dark matter content of disc galaxies

For this exercise in determining the dark matter distributions of the galaxies in our sample, we first discuss various procedures for estimating dynamical masses from our rotation curve data (§5.1.1) and what corrections may be necessary to account for possible underestimation of the dynamical masses (§5.1.2). Because we do not have a direct means of estimating the gas content in these galaxies,

we indirectly derive estimates of the total baryonic mass (§5.1.3). We combine these baryonic and dynamical mass estimates to evaluate the relative role dark matter out to the observable radii probed with our deep exposures (§5.1.4).

Because of the uncertainties, we conduct this exercise only with the better-resolved DEIMOS dataset. Although there are some uncertainties in what follows, our intent at this stage is to illustrate the possibilities that will arise when gas masses can be determined for samples such as ours so that the total baryonic components would be accurately measured and their role in the Tully-Fisher relation established.

5.1.1 Dynamical mass estimates

The physical basis of our interest in the Tully-Fisher relation is that the dynamical mass is expected to be strongly correlated with the luminous and stellar mass components, and by analysing empirical constraints, we can gain an understanding of the relative assembly histories of dark and baryonic matter. We thus seek to use our data to estimate both the dynamical masses (i.e., the total mass, including dark and baryonic) as well as that of the stars and gas. Previous studies of this nature at low redshift (Pizagno et al., 2005; Gnedin et al., 2007; Williams et al., 2010) derived dynamical masses from kinematic data that probe sufficiently far in radius to detect the dark halo by revealing a deficit of baryons when dynamic masses are compared to stellar masses.

However, our method of using emission line velocities to estimate the mass within a given radius, such as $r_{2.2}$, depends sensitively on the assumed shape of the underlying gravitational potential, and hence the distribution of mass throughout the disc. For a given ellipsoid potential, the velocity can be most simply approximated as:

$$V_c(r)^2 \approx \xi \frac{GM(r)}{r}, \tag{5.1}$$

where ξ=1 in the case of spherical symmetry. Assuming a **spherical potential** will likely overestimate the disc mass unless a spherical dark matter halo

dominates the density distribution within the relevant radius. As such it supplies an effective upper limit for a given mass of an ellipsoid calculated from the observed circular velocity. Traditionally, dynamical disc masses have been calculated with an **exponential 'Freeman' potential**, solved with modified Bessel functions by assuming a constant mass-to-light ratio and an infinitely-thin disc of infinite size (Freeman, 1970). This ignores the presence of the bulge and halo, known to be important even at the scales considered here (e.g., Trott et al., 2010; Dutton et al., 2011b). Therefore, as an alternative method of estimating a lower limit, we adopt an **oblate potential**, characterised by a flattening factor q, which is the ratio of the scale length normal to the disc over the scale length of the disc. As shown in Binney & Tremaine (1987), the velocity for an oblate sphere can then be considered as:

$$V_c(r)^2 \approx 4\pi G q \int_0^r \frac{\rho(m^2)m^2 dm}{\sqrt{r^2 - m^2(1-q^2)}}, \tag{5.2}$$

where $m^2 = r^2 + r_s^2$, and ρ is the assumed density function. More realistically, the exact shape of the potential will depend on the relative contributions of luminous and dark matter, as well as on the triaxial shape of each component. Although halos are believed to be prolate on large scales, their shape is less clear on the scales considered here. Lensing and dynamical studies of individual systems (Dutton et al., 2011b) suggest that they could be considerably rounder. Furthermore, the presence of a bulge generally implies that the stellar density distribution is significantly steeper than that of a pure disc. We adopt $q = 0.4$ and an exponential density function for ρ in Eq. 5.2 as representative of the maximum oblateness, equivalent to $\xi \approx 0.752$ for Eq.5.1. If we were to use a de Vaucouleurs profile (Sérsic profile where $n = 4$) instead of an exponential density profile, ξ would be ≈ 0.833, resulting in a less than 10% change in the dynamical mass calculation. In the following we will consider the $q = 1$ spherical case and the $q = 0.4$ oblate case as indicative of the range we can expect in the shape of the total potential. Additional systematic uncertainties include the effects of non-streaming motions, warps and non-gravitational

forces, as discussed in the well-established literature on the interpretation of local rotation curves (see Binney & Tremaine, 1987, and references therein). Also, in the following section, we consider possible biases arising from spectroscopic effects by estimating their maximal limits propagated to the dynamical mass estimates.

5.1.2 Slit-effect correction

Recent progress with integral field unit (IFU) spectrographs has illustrated some limitations of traditional long-slit and multi-slit techniques in determining the internal dynamics of intermediate redshift galaxies. This slit-effect is similar to beam smearing in radio astronomy, where the range of velocities from incoming light are averaged over the width of the slit, resulting in a broadening of Doppler shifted lines and an average reduction of the rotational velocity. The magnitude of this effect has been considered by Kapferer et al. (2006), and was used by Flores et al. (2006) to compare IFU-derived rotational velocities to those determined with a multi-slit instrument. Kapferer et al. (2006) systematically investigated the effects of various slit widths in combination with inclination, spatial binning and position angle offsets on measured disc velocities using N-body/SPH simulations. We can use these results to consider the effect our slit size and placement might have in affecting our velocities taking into account the galaxy sizes and shapes relative to the DEIMOS slits. The aim is to provide an upper-limit to the correction to the velocity $V_{2.2}$. The effect of the slit width is dependent on scale radius (r_s) of each galaxy according to its axis ratio (b/a), for a given inclination i. Kapferer et al. find no systematic bias due to the effects of binning or position angle offset (beyond the correction we have already made, §2.3). Derived from Figs 9 & 10 of Kapferer et al. (2006), the correction is:

$$V_{corr} = V_{obs} + V_{beam} \frac{1}{(b/a)} \frac{r_{slit}}{r_s} \sin i, \tag{5.3}$$

where $V_{beam} \sim 20$ km s^{-1}. We find correlations in the correction with respect to scale radius and inclination, but none with mass, redshift, position angle or observed velocity. The correction added to $V_{2.2}$ ranges from 2 km s^{-1} to 52 km s^{-1}, with a mean of 20 km s^{-1}. These corrections can be found in our catalog.

Because of the imprecise nature of these corrections, arising from the fact that the Kapferer et al. result assumes a symmetric Gaussian to the spectral line profile (while we fit for two half-Gaussians to account for much of the blending between the seeing and dispersion), the Kapferer et al. correction remains an upper limit. Thus we did not include them in our precisely measured Tully-Fisher relations in §4. However, we consider it important to apply them to our dynamical mass calculation in order to not over-estimate the dominance of the stellar mass compared to the dark matter. The effect can be seen in Fig. 5.2.

5.1.3 Baryonic mass estimates

In order to examine the redshift-dependent fraction of baryonic mass within $r_{2.2}$ we need to obtain an estimate of the total baryonic mass. In addition to stellar masses, discussed in § 3.3, we need to account for the presence of gas.

Accurate gas masses are not yet available for intermediate redshift galaxies, although masses derived with the rotational transition lines in carbon monoxide (CO) have begun to appear for some systems at z>, e.g., with the Plateau de Bure Interferometer (PdBI) (Tacconi et al., 2010; Daddi et al., 2010). Nonetheless the situation will improve significantly through upcoming facilities such as the Atacama Large Millimetre Array (ALMA), as well as for HI with the Meer Karoo Array Telescope (MeerKAT) and eventually with the Square Kilometre Array (SKA). Although what follows is somewhat speculative, it provides a reasonable illustration of what will soon be possible. To make progress, we estimated gas masses (M_g) for our sample using the local stellar-to-gas mass (M_*-to-M_g) ratio as a function of M_*, recently parameterised by Peeples & Shankar (2010) based on H I measures from The H I Nearby Galaxy Survey

(THINGS) and helium-corrected, CO-derived H_2 masses from the HERA CO-Line EXtragalactic Survey (HERACLES) and the Berkeley-Illinois-Maryland Association Survey of Nearby Galaxies (BIMA SONG) (Leroy et al., 2008).

According to the parameterisation by Peeples & Shankar (2010):

$$\frac{M_g}{M_*} = K_f M_*^{-\gamma} \tag{5.4}$$

where $K_f = 316228$, γ=0.57, and M_* is measured in units of solar masses.

Until precision gas masses become available we cannot be certain that the Peeples & Shankar (2010) formalism can be applied in this manner at intermediate redshift. However, locally-measured gas-to-stellar mass ratios will underestimate the gas mass for intermediate-redshift galaxies since many stars have subsequently formed. To correct for this, we consider the observed evolution in the specific star-formation rate (sSFR) for blue galaxies to z$\sim$2 as measured by Oliver et al. (2010). To determine the correction for each galaxy, we integrate the best-fit sSFR relation out to the relevant redshift. Oliver et al. (2010) find:

$$\mathrm{sSFR} = X(1+z)^{\alpha} \tag{5.5}$$

where $\log_{10} X/Gyr^{-1} = -1.36 \pm 0.41$ and $\alpha = -3.4 \pm 0.3$. We temper this correction by the gas recycling rate (e.g., Kennicutt et al., 1994; Madau et al., 1998; Cole et al., 2001), estimated to be $\sim$40% for a Chabrier (2003) initial mass function from z$\sim$1 to present. This scenario is not strictly a closed-box model, where a galaxy sits in a huge reservoir of gas and simply converts that gas to stars over time. For instance, we include the substantial Chabrier recycling rate consistent with the IMF we assume in our stellar mass estimates.

Moreover, the scenario we present here is also consistent with roughly equal inflow and outflow since $z \sim 1$. The fraction of feedback driven material that exceeds the escape velocity of the galaxy's potential well, and also the typical redshifts at which the filaments that feed galaxies evaporate, are still largely unknown. We find that this method predicts up to 50% more mass than that determined by inverting the Kennicut-Schmidt relation (Kennicutt, 1998),

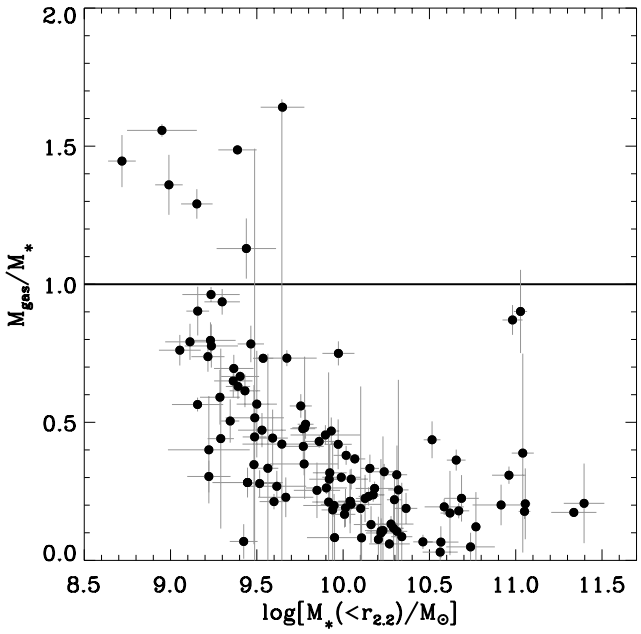

Figure 5.1 The gas-to-stellar mass ratios for our sample as a function of the enclosed stellar mass. The gas mass estimates are dependent on stellar mass (accounting for the general trend seen here in this figure), and redshift, (accounting for the scatter in the general trend).

using our absolute B-magnitudes to estimate star-formation surface density and thus the gas surface density in our galaxies. On average we are estimating a third more gas, so this should considered in the following results. The gas mass estimates are on average 30% of the total stellar mass estimates (Fig. 5.1), and exceed that of the stellar mass in a few of the lowest mass objects. Therefore, we claim that our gas mass estimates are not the main drivers of our conclusions, and each galaxy's stellar mass and redshift essentially determine the gas mass estimate for this scenario.

5.1.4 Comparison of baryonic and dynamical masses

We finally turn to our comparison of the dynamical mass with the stellar and baryonic mass. The results of this comparison are given in Figure 5.2. The top panels show the stellar-to-dynamical mass ratio for a spherical and oblate potential. Across our redshift range we find our stellar-to-dynamical mass

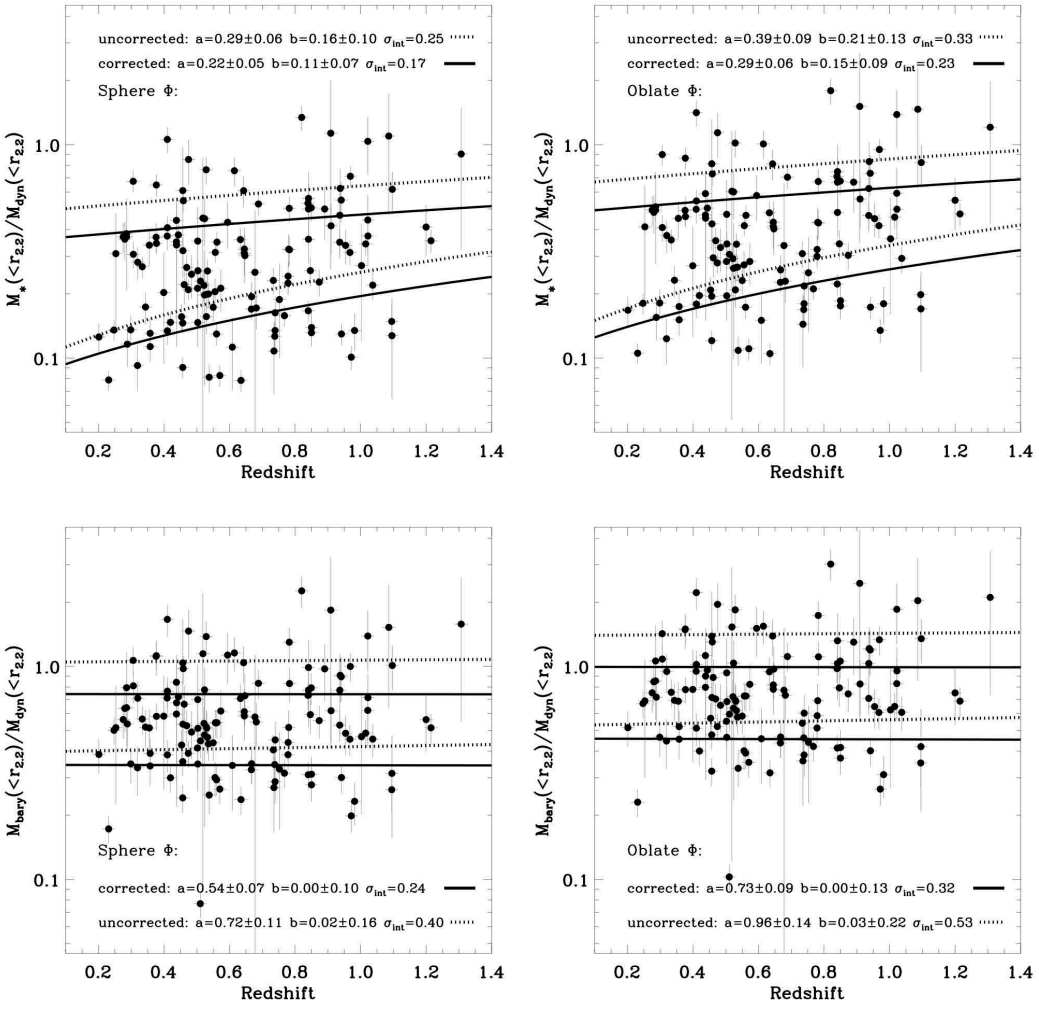

Figure 5.2 **Top panels:** stellar-to-dynamical mass ratio within our fiducial $r_{2.2}$ aperture as a function of redshift, assuming a spherical potential **(left)** and an oblate potential **(right)**. Curves indicate 3σ variations around the best-fit linear relation, with slope b and intercept a. The solid lines are derived from dynamical masses including the slit-effect correction, and the dotted lines are derived from the uncorrected dynamical masses. The scatter around the best fit relation is also given in each plot. **Bottom panels:** same as the top panels for baryonic (stellar plus gas) mass.

fractions are ~ 0.3 for a spherical potential and ~ 0.4 for an oblate potential, with considerable scatter. The dynamical mass estimates for the points plotted include the slit-effect correction (§5.1.2), representing an upper-limit for the dynamical masses, and thus a lower limit for the stellar-to-dynamic mass fraction. For comparison, the dotted lines are derived from the uncorrected data, and represent a lower limit to the dynamical masses, given an assumed potential shape (spheroid or oblate in our example), and 3σ best-fit contours are plotted for the uncorrected data. In a few cases, the stellar-to-dynamical fractions are as high as unity, suggesting that baryons play a significant role in driving the TF relation. A dominant baryon fraction is broadly consistent with earlier results by Conselice et al. (2005), Gnedin et al. (2007), Dutton & van den Bosch (2009) and Dutton et al. (2010a), especially considering the many uncertainties involved in both mass estimates, including the stellar initial mass function (IMF).

The hypothesis that baryonic mass primarily governs the slow redshift-dependent trends in our observed TF relations is supported further when we attempt to add estimates for the missing gaseous components to our stellar masses. We then find that our baryonic mass estimates within $r_{2.2}$ approach those determined dynamically, with no redshift dependence (bottom panels of Figure 5.2). The average baryonic-to-dynamical mass ratio is $\sim 50\%$ and ~ 70 % respectively for spherical and oblate potentials (including slit-effect corrections). It must be remembered this baryonic estimate does not include any ionised gas.

Next we explore the radially dependent profile of the dynamical mass as calculated from the rotation curve, to compare to the baryonic component mass profile. At each tenth of a scale radius along the profile, we compute the dynamical mass given the best modelled velocity at that radius, and compare that to the enclosed baryonic mass. The baryonic mass is assumed to follow the stellar mass profile, which we approximate to follow the distribution of light found in the reddest HST F850LP filter (see §3.3). The enclosed light at each

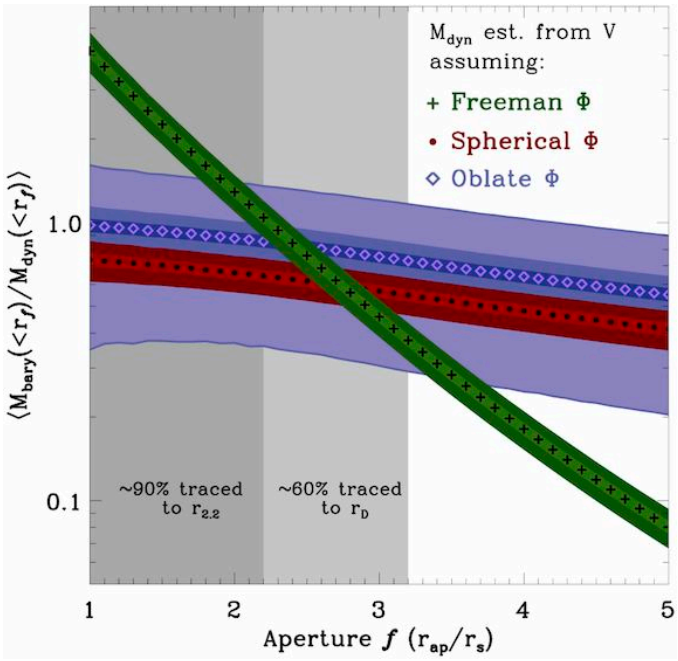

Figure 5.3 Estimates of the mean baryonic-to-dynamical mass fraction over all redshifts as a function of relative aperture ($f = r/r_s$). Shaded regions show the percentage of discs traced to f=2.2 and 3.2 (r_D); our Keck survey adequately samples the rotational velocities to $f \simeq 3.5$. Different curves relate to different determinations of the dynamic mass (see text for details) and the tight contours show the 1 and 3 times the standard error on the mean. Light shading around the results assuming an oblate potential indicate the aperture-dependent region containing 68% of the individual fractions for our discs. These regions are not shown for the other two potentials, but are of similar size to that of the oblate potential.

tenth of a scale radius is compared to the total light, stepping out in elliptical apertures from the photometry, and the aperture mass is calculated from these ratios.

Although past studies of rotation curves and the TF relation were often motivated as a means of tracing the influence of dark matter on the baryonic assembly of galaxies, (e.g., Rubin et al., 1980; Vogt et al., 1997; Pizagno et al., 2005; Conselice et al., 2005), it has been suggested in local TF studies that the role of dark matter is minimal in the optical disc (e.g., Courteau & Rix, 1999b; Palunas & Williams, 2000; Bell & de Jong, 2001; Kassin et al., 2006). Figure 5.3 shows that, irrespective of the aperture f, defined in terms of the

scale radius (i.e. f=2.2 for $r_{2.2}$), out to the furthest observable extent in our discs, the mean baryonic-to-dynamical fraction is consistent with unity when using an oblate potential for our dynamical mass estimates. However, for a spherical potential, we find our results permit an equal contribution from dark and baryonic matter by $r_{2.2}$, consistent as we noted above with Portinari & Sommer-Larsen (2007) and Dutton et al. (2010b).

We also show the baryonic-to-dynamical fraction with respect to aperture for a Freeman (1970) potential. The unphysical and sharp rise above unity for small radii shows that the dynamical mass is likely underestimated for the central-most part of the galaxy using this potential. If used in a maximal disc fit, which would re-normalise the sharply rising peak down to unity, the fit would likely result in an underestimate of the overall dynamical contribution of the baryons for what is nominally the scenario where baryons are maximally contributing to the potential. This suggests that the Freeman potential, which assumes a constant mass-to-light ratio for an infinitely-thin exponential disc, may not be the best approximation in maximal/minimal fit applications for a disc of a finite thickness and size.

We thus conclude that the contribution by baryons to the total mass within the radial range probed by our observations could be as high as 50% to 100%. Baryons therefore appear to be the most important component within 2.2 scale radii, and perhaps to larger radii, depending on the uncertain conversion from circular velocity to stellar mass. In addition, such a high fraction of baryons is expected to influence significantly the overall profile of the dark matter halo at these scales through gravitational interactions (see, e.g., Noordermeer et al., 2007, and references therein for a discussion of this topic in the local universe). Therefore even if dark matter is present in equal amount, it will be tightly coupled to the baryonic content.

5.2 Understanding the TF results in context

Our major goal in seeking a second dataset with LRIS at higher redshift was to determine if the the TF relation was being formed between $z \sim 1$–2. Figure 4.3 (the right-side of which is reproduced in Fig. 5.4 for convenience) presents a puzzling discontinuity in behaviour over a relatively narrow period of cosmic history. A key uncertainty in the interpretation of this figure, however, is that some of our sample does not satisfy our criterion of providing a reliable estimate of $V_{2.2}$. Although we have maintained continuity in our morphological selection techniques from DEIMOS to that in LRIS, similar criteria of morphological appearance or extended emission lines are difficult to usefully apply to the star-forming galaxies being studied beyond $z \simeq 2$. As redshift increases in Fig. 4.3, some subset of a mass-selected or a star formation rate (SFR)-limited population is likely not included in the TF analysis.

Such a selection bias may be more or less important depending on the physical model we wish to test. If discs grew from chaotic beginnings, where clumps collide at the centres of dark halos (van den Bergh et al., 1996; Abraham et al., 1997; Elmegreen & Elmegreen, 2005), then the TF relation will continue to evolve as the chaotic behaviour and mergers (Hammer et al., 2005) transitions into more regular accretion onto well-formed discs. In this scenario, we could interpret the lack of observed evolution as the result of a bias towards 'mature' systems at all redshifts. However, since we expect high SFRs in this violent phase, these less mature systems are more likely to be included in our analysis, unless dust obscuration or possible nuclear concentration of star formation makes extended emission lines difficult to detect (*i.e.* our spectrally compact and passive targets).

Alternatively if discs form predominantly via smooth accretion over time, they could easily evolve along self-similar dynamical relations, making selection effects much less important in understanding the lack of evolution. How then could we interpret the more drastic offsets implied by Fig. 4.3? Even

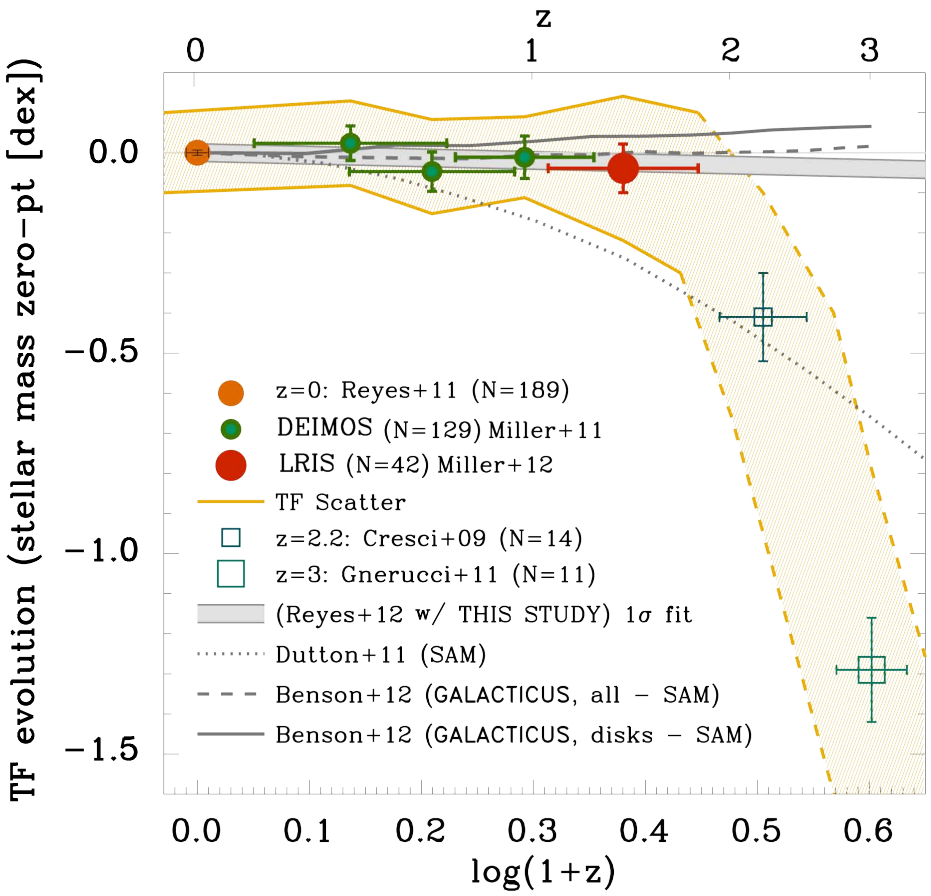

Figure 5.4 **Reproduced from right side of Fig. 4.3 for convenience:** we show the redshift dependent M_*-TF relation scatter and zero-point, assuming a fixed slope as determined by Reyes et al. (2011b) at z∼0 (orange circle). We compare the results from LRIS (red circle) and DEIMOS (green circles) to those at even higher redshift (Cresci et al., 2009; Gnerucci et al., 2011). We also compare semi-analytic models (SAM) from Dutton et al. (2011a) and Benson (GALACTICUS, 2012) This plot is introduced in §4.2.3 and discussed further here in Ch. 5.

with smooth, cold accretion (e.g., Dekel & Birnboim, 2006), if galaxies formed stars more vigorously and erratically from z∼2–4 than at present times (e.g., Förster Schreiber et al., 2006; Genzel et al., 2008), then a tight M_*-TF relation would be delayed until disc properties are homogenised across the observed populations— similarly for a transition from dynamically hot objects to discs which are primarily rotationally supported. Any inhomogeneity, including differences or changes in:

- rotational versus dispersion support,
- baryonic mass-to-light ratio across the disc,
- baryonic versus dark matter fraction,
- specific star formation rate, and
- gas fraction or gas reservoir size and distribution

across redshift bins should lead to an evolution in the M_*-TF relation. While various combinations of the above characteristics are likely correlated, they may not evolve in tight lock-step. Thus the emergence of a recognisable M_*-TF relation at $z\simeq1.5$ is already a result of significance — even if it only applies to some subset of the star-forming population.

At $z\sim3$, Gnerucci et al. (2011) argue that the nascent TF relation has a scatter of over an order of magnitude larger than what we observe at $z\simeq1$. Given that the angular momentum properties are shown to be similar to those at $z<1$ (Bouché et al., 2007), if the sources targeted by Cresci et al. (2009) were less efficient star-formers than those studied here, perhaps this could explain the marked stellar mass deficiency indicated in Fig 4.3. However, the earlier systems display **higher** gas fractions and star-formation rates (Tacconi et al., 2010), and considering that they may have additional dynamical mass supported by higher velocity dispersions only makes this discrepancy worse. Studies of less massive sources at $z \sim 2$ and beyond as well as better constraints on the physical sizes of these components will be valuable in resolving this possible discrepancy.

Cresci et al. (2009) and Gnerucci et al. (2011) note the increasingly dispersion-dominated behaviour at $z \sim 2$, as shown also in Förster Schreiber et al. (2009), is key to explaining the observed M_*-TF relation evolution. However this picture, which posits a greater degree of turbulent support in thicker discs at high redshift, should result in **less** rotational motion per unit stellar mass at earlier

times, in contrast to the trend shown in Fig. 5.4. Given the negative M_* zero-point evolution observed, a reduced V/σ at higher redshift would thus imply a substantial evolution in the gas fraction. Simultaneous changes in the dark matter fractions, baryonic mass-to-light ratios, and disc geometries may lead to a less severe evolution in gas fraction. Understanding how these characteristics could conspire to keep the M_*-TF relation from more dramatic changes can be addressed by more sophisticated tools.

Comparing the relative evolution in our study to that of semi-analytical models can thus provide interesting interpretations as to the predicted interplay between baryons and dark matter over these epochs. We note that the model of Dutton et al. (2011a) departs significantly from the observed trends before $z{\sim}1$, whereas the Benson (2012) GALACTICUS models with several more forms of baryonic feedback are a closer match. This suggests that understanding the subtleties in the baryonic physics of galaxies is vitally important to our understanding galaxy assembly via tools like the Tully-Fisher relation.

In fact, Dutton et al. (2011a) see much less evolution in their baryonic Tully-Fisher relation over the same redshift range, signalling the effect of evolving gas fractions in conjunction with their stellar components. Since the evolution of the dark halo drives the self-similar evolution in disc circular velocity in their model, the evolution present in both their baryonic and M_*-TF relations is being driven by dark matter, similar to the results of Somerville et al. (2008). However, we find in §5.1 that baryons may be the dominant driver of dynamics within $r_{2.2}$, and furthermore, the dominance of dark matter would stabilise the disc against the intense star formation which is observed (Genzel et al., 2008).

Because the role of gas in disc galaxies throughout their formation is not adequately understood across a wide range of masses and environments at high redshift, it is likely that further work and exploration of the evolution of the baryonic Tully-Fisher relation will help explain why we see so little evolution in the M_*-TF relation since $z \sim 1.7$. This would especially help to clarify 'conspiracies' implied by the lack of evolution, since gas fractions appear to

evolve with time (Tacconi et al., 2010), as well as the dark halo response to baryonic matter in standard ΛCDM models (Dutton et al., 2011a).

If the increased scatter we find in the TF relation in this study from $1 < z < 1.7$ is truly intrinsic, then we should be able to determine the specific characteristics of those systems which have not yet arrived on the 'mature' TF relation, if an immature form of the relation does in fact exist. In §5.3, we will more closely examine the various characteristics of disc galaxies in our samples from $0.2 < z < 1.7$: their estimated mass components, their dynamics, and their bulge-to-disc morphology. For example, it has been postulated (i.e., Bournaud et al., 2007) that the development of a central bulge through inspiraling, unstable clumps is key to stabilising the disc. Alternatively, morphology could be driven by halo accretion type (hot versus cold), in which the circular velocity shows little dependency on morphology in the recent work by Sales et al. (2011). By examining the M_*-TF relation as a function of the bulge-to-disc ratio and morphology, such hypotheses can be directly tested.

5.3 Exploring drivers of disc assembly

We began in the introduction of this thesis with 2 fundamental questions asked by Roberts (1969) on the integral properties of spiral and irregular galaxies, and have thus far made significant progress on his second question regarding their evolutionary history. The pursuit of this inquiry has led to new questions, such as how to explain the surprising rapid evolution of the TF relation zero-point between $z \sim 1.5$ and $z \sim 2$ (Fig 5.4). If this dramatic shift between our study and those at higher redshifts is real, then in only ∼1–2 Gyr, morphologically-irregular and dispersion-dominated star-forming galaxies (Förster Schreiber et al., 2006; Law et al., 2007; Förster Schreiber et al., 2009), emerge at $z \sim 1$ with well-ordered star formation taking place at a lower rate in molecular clouds several orders of magnitude less massive (Aumer & Binney, 2009). As discussed in the previous section, the dramatic evolution could be

exaggerated by intrinsic differences between the samples. However reconciling the nature of the differences is challenging given that we see less stellar mass at a given velocity for more massive galaxies at higher redshift, which is counter-intuitive to the hierarchical-yet-'downsizing' paradigm.

To address this challenge, we return to Roberts' first question, 'Why are there different types of galaxies?' Since we have achieved similar precision in our z-dependent TF studies as that of the local relation, we can ask whether the relations show signs of assembling between $1<z<2$ by examining individual galaxies within the relations, and ultimately seek to learn more about the existence of the Hubble sequence in return.

5.3.1 Renegade bulgeless discs at $z \sim 1$

Bulgeless disc galaxies are an interesting feature of the universe for a variety of reasons. Their mere presence in numbers greater than $> 15\%$ of the population in the local universe (Kormendy et al., 2010) has provided an interesting challenge for hierarchical galaxy formation models in the ΛCDM paradigm, which without substantial feedback will lead to inevitable bulge growth (Robertson et al., 2006; Governato et al., 2010). Because of their more secular formation history, they provide an interesting laboratory in which to explore the assembly of galaxies which have likely not undergone a major merger event, and are thus supposedly in a more pure dynamical form.

When revisiting the M_*-TF relation with an eye to bulgeless discs, we find an intriguing result, which gives a possible indication of how a transformation in disc galaxies may occur. At the significance of 4.16σ, we see an offset in the zero-point of the M_*-TF relation of bulgeless discs at high redshifts ($z < 0.8$) compared to the rest of the galaxies in the DEIMOS dataset (Fig. 5.5). By separating our sample according to the HST-derived GALFIT results into galaxies with prominent bulges and those without (bulgeless defined as bulge-to-total ratio, B/T, < 0.1), we find bulgeless galaxies are offset from the local TF relation in the highest redshift bin at -0.5 dex in stellar mass. The presence

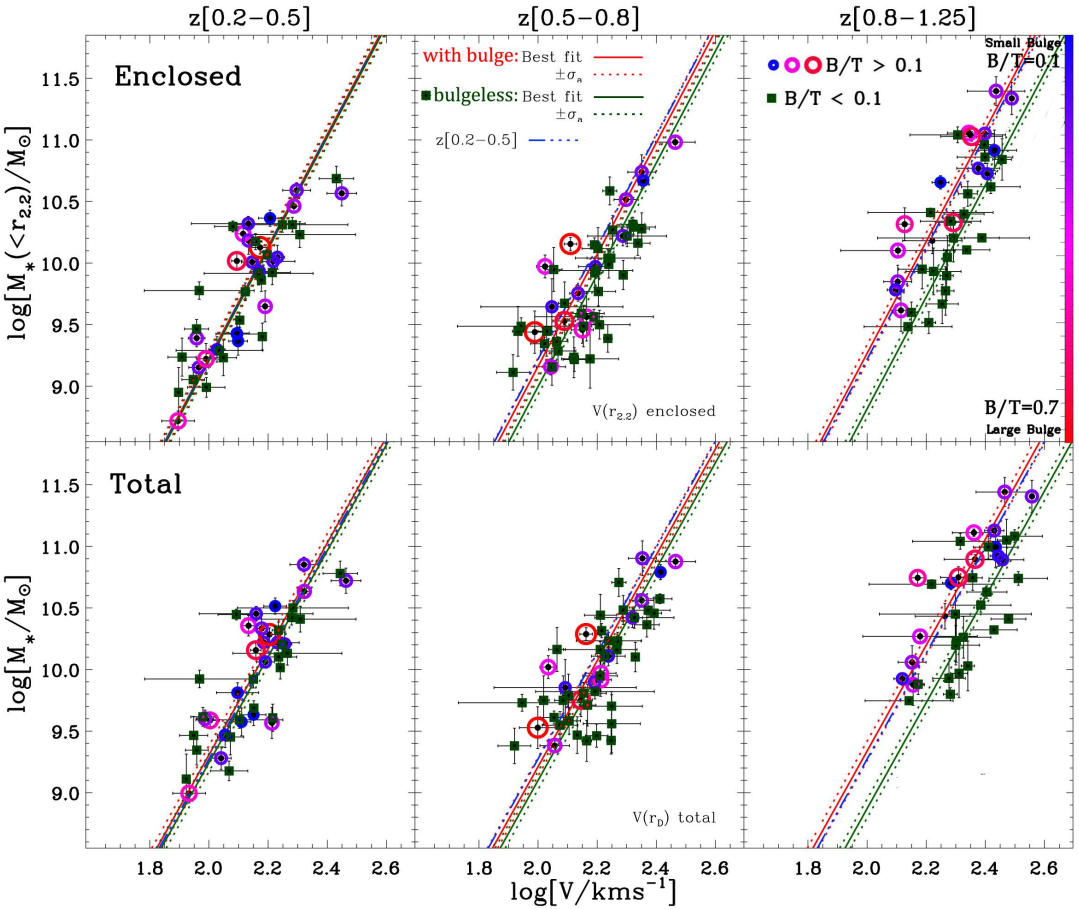

Figure 5.5 The **enclosed (top)** and **total (bottom)** stellar mass TF relations in three redshift bins from the DEIMOS sample, similar to Fig. 4.1, however we denote morphology here. Galaxies with bulges are circled in blue-fuchsia-red depending on the size of the bulge, small (B/T=0.1) to large (B/T=1) according to the colour bar key, and fit with a red line. These galaxies lie along the local relation up to z $\sim$ 1, whereas as z increases, galaxies without bulges (green squares and green line) are increasingly offset from both galaxies with bulges and the local M_*-TF relation. To aid the eye, we include a blue dot-dashed line in the middle and high redshift bins which reproduces the total trend of the lowest redshift bin. The trends in this figure suggest a different evolutionary path emerging from the bulgeless discs assembling at high redshift.

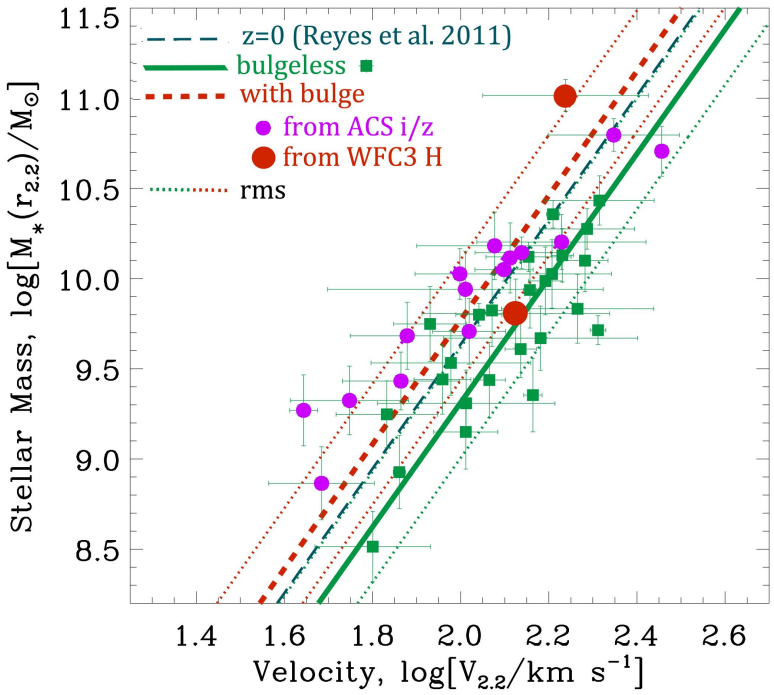

Figure 5.6 The LRIS M_*-TF relation separated in two subsamples of discs with bulges (fuchsia circles) and bulgeless discs (green squares). We see a similar trend as that seen at high redshift in Fig. 5.5 in the LRIS data at even higher average redshift, although with less significance due to the increased uncertainty. Two galaxies which are effectively bulgeless in the ACS data but show significant bulge components in the WFC3 F160W data are denoted by two large red circles (see Fig. 5.9). The local relation of Reyes et al. (2011b) is plotted with a blue dashed line, which is the slope adopted in both of the LRIS subsets to measure their zero-point offset ($\sim 2\sigma$).

of a bulge appears to secure a disc galaxy's 'place' on the stellar mass TF relation, however bulgeless discs also arrive onto the TF relation by the latter half of the age of the universe. In fact, the insignificant increase in the M_*-TF zero-point with redshift arises largely from the evolution of the bulgeless disc galaxies towards the local relation.

This is especially interesting since the total scatter across the DEIMOS relations (including both galaxies with and without bulges) does not significantly evolve, meaning that the bulge-separated relations in the highest redshift bin have tighter scatters than when samples are combined in all redshift bins. This is likely an effect due to the lack of lower mass galaxies in the highest red-

shift bin, which tend to produce more scatter than the higher mass galaxies (*i.e.* Begum et al., 2008). However, the LRIS sample does not suffer from this same incompleteness to higher redshift as the DEIMOS sample. Furthermore, as stated in the previous chapter, the LRIS sample intriguingly shows up to 60% increase of scatter, which is in the same direction as the bulgeless discs trend in the DEIMOS sample, so we investigate the bulge-dependence of the TF relation with the higher redshift LRIS sample as well (Fig. 5.6).

Remarkably, we do see a possible continuation of this trend in the bulgeless discs of the LRIS data, however because of the lesser precision of the measurements as compared to the DEIMOS data, the significance of the offset is only at the 2σ level, and the bulgeless discs lie at one length of the rms from the local relation to the fast-V/low-mass side (Fig. 5.6). Besides the larger errors, another difficulty in this determination is the small numbers– there are only 15 galaxies (36% of the sample) with significant bulges in the LRIS-derived relation (see Fig. 5.7).

To demonstrate whether or not we should clearly see the same trend found in DEIMOS in our LRIS data, we simulate 100 random realisations according to the Gaussian distributions of uncertainty in the best-fit DEIMOS $z<0.8$ trend. We include 2 sub-samples (*i.e.* with bulge & bulgeless) of N=10, 15, 20, 25, & 30 each, and we find that subsamples of N=20 consistently recovered a $+3\sigma$ determination, whereas subsamples of N=10 & 15 would recover the trend in fewer than half of their realisations (Fig. 5.8). Since it is standard to adopt a 3σ significance in galaxy scaling relation studies, we find that even if the bulgeless discs trend persists at this redshift in the LRIS data, we would not expect to clearly see the trend without a larger subsample of discs with significant bulge components.

A final and crucial issue to be addressed affects both LRIS and DEIMOS datasets, which is the effect of morphological band-pass shifting. This is the change in morphology seen when the rest-frame wavelength shifts from redder to bluer light as the systematic redshift of the galaxy increases. This can

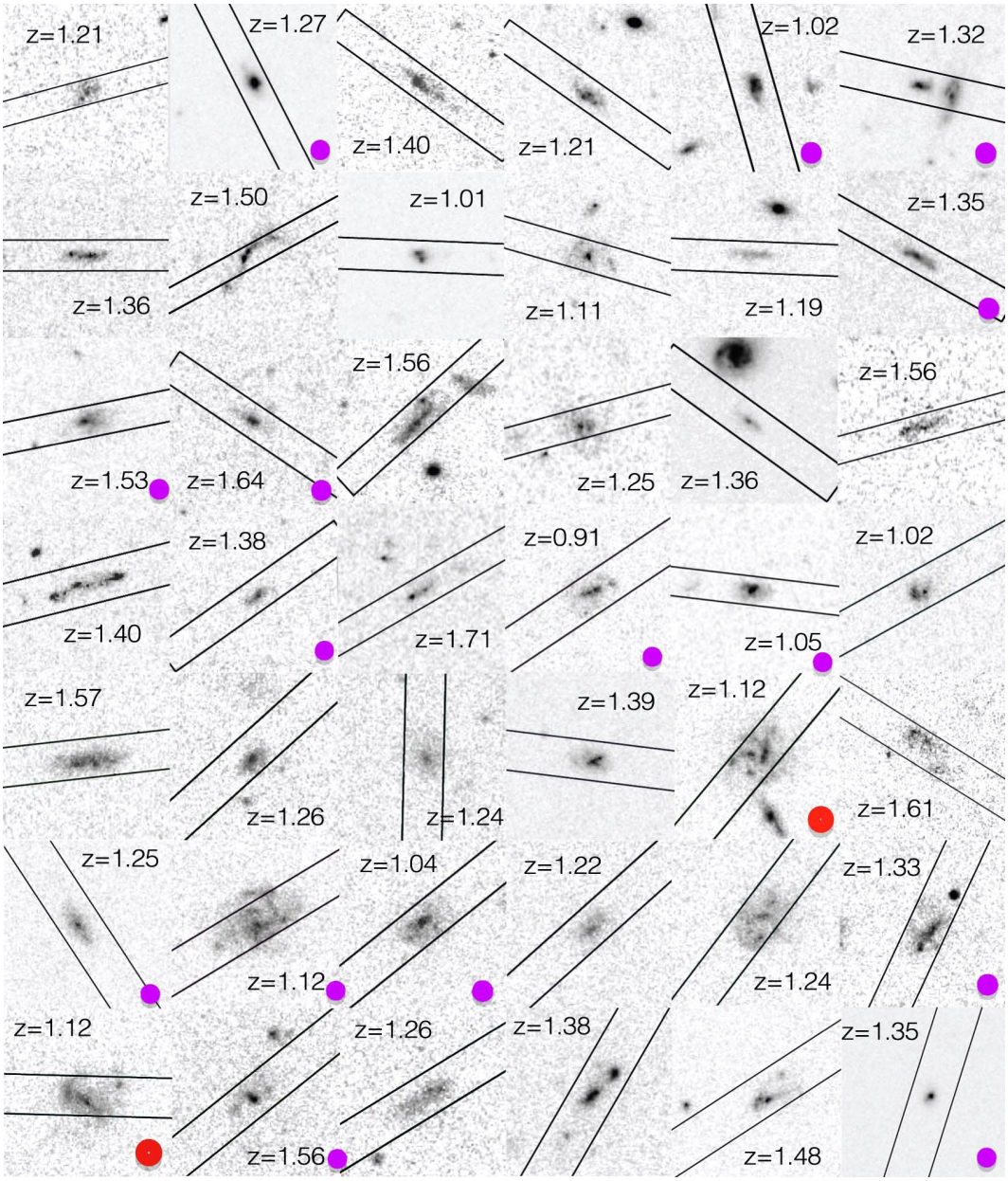

Figure 5.7 Images of the galaxies in our TF sample, with either the HST F814W or F850LP (whichever is available according to Table 3.2) and their 1″ slits overlaid. We include the redshift of each target, and denote whether the galaxy was determined to have a bulge component according to our GALFIT algorithm (§3.2) with a fuchsia circle. The larger 2 red circles denote galaxies which do not appear to have a bulge component in the ACS filters, but do however show significant bulge components when redder imaging in the rest-frame optical filter is available with the HST WFC3 F160W.

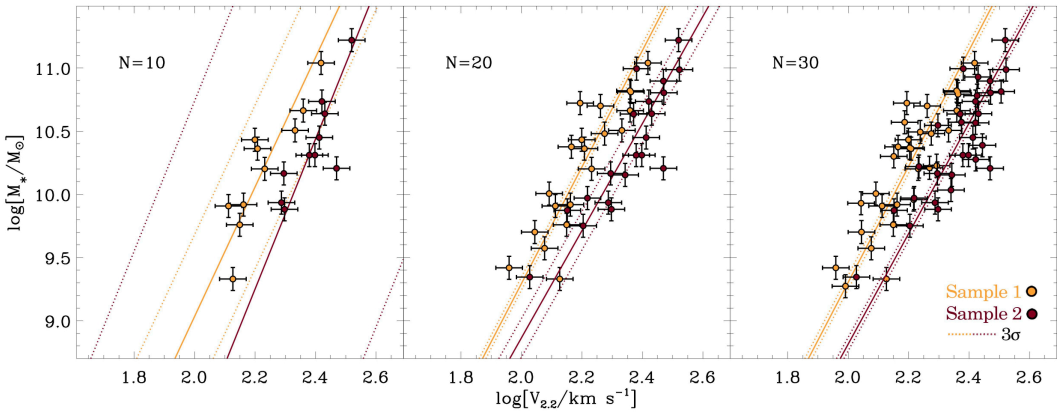

Figure 5.8 Simulated realisations of 2 offset TF relations with subsample sizes of N=10, 20, and 30 objects per bin (from left to right). The offset is reproduced to be that measured between discs with and without bulges in the DEIMOS z<0.8 data. Each panel shows one of 100 realisations of randomly generated data points, selected from the expected Gaussian distributions of sample characteristics based on the DEIMOS data and best-fits. Each fitted relation is shown as a solid line, with the 3σ uncertainties shown as dotted lines. We find that subsamples of at least N=20 galaxies are optimal in consistently recovering 3σ offsets of the nature we find in the high redshift bulgeless discs of the DEIMOS data.

become a major problem in our dataset around z>1 where the rest-frame light of the F814W and F850LP filters shift blue-ward from the rest-frame optical, sensitive to the older and redder populations that dominate the stellar mass and constitute the bulk of any classical bulge component. Without tracing rest-frame optical light, bulge components can disappear, as exemplified by Fig. 5.9. Furthermore, it is important to be able to distinguish between galaxies which have bright, star-forming nuclear clusters (which appear when these filters trace rest-frame blue and UV light) and those with true bulge components traced with redder light. If the central components are small and the light profiles not well resolved by GALFIT, central star-burst clusters could be confused with bulges when the image is rest-frame blue light. It can be difficult in these cases to distinguish between steeper bulge profiles and flatter star-bursting nuclear discs or rings, which may exist in our sample (Fig. 5.7).

For tracing rest-frame optical at $1 < z < 2$, the HST Wide Field Camera 3

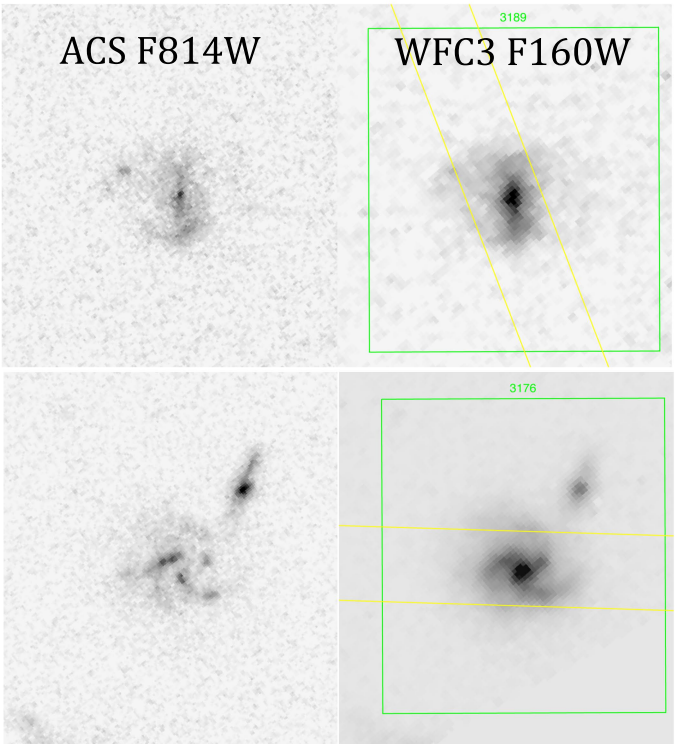

Figure 5.9 Two examples of galaxies which have no significant bulge component in the HST ACS F814W imaging, but a bulge is revealed when observed with the redder rest-frame optical imaging of the HST WFC3 F160W filter. These two galaxies are highlighted with large fuchsia circles in both Figs. 5.6 & 5.7.

(WFC3) provides both a F125 and F160W filter (roughly J and H band) which can help us achieve the bulge-to-disc decompositions we seek. While imaging from the WFC3 F160W is public for a subset of our $z > 1$ discs at present, the majority of the combined LRIS and DEIMOS samples are in GOODS North. This field will be covered by WFC3 towards the end of Summer 2012, and the data will be released to the public shortly thereafter (see Ch.6 Koekemoer et al., 2011). Until the WFC3 coverage is available for most of the dataset, and thus optical bulge-to-disc decompositions, the results presented in this chapter remain preliminary.

5.3.2 Possible Physical Implications

A number of hypotheses arise from this discovery of a bulgeless disc offset at high redshift, even if the significance and exact nature of the trend is unknown:

1. **Transition Mass:** As in all our TF analyses, we restrict our comparative linear regressions to those of fixed slope in order to determine whether significant differences occur in the zero-point normalisation (the free slopes are too uncertain to distinguish differences between them, as discussed in Ch. 4). However, rather than a simple zero-point offset, the features of Fig. 5.5 & 5.6 suggest that the slope of the bulgeless disc galaxies may be steepening compared to the local slope. Given the uncertainty in the free slope fits and the nature of the trend, a changing slope is indistinguishable from a 'transition' mass in the slope of the bulgeless discs relation. This is a mass below which the bulgeless discs fall off of the established relation, either to the fast side of the relation at a given stellar mass, or lag behind in stellar mass assembled at a given $V_{2.2}$.

   A similar phenomenon is observed locally with the low mass galaxies ($\log[M_*/M_\odot]<9$), which tend to fall below the extrapolation of the linear fit to more massive galaxies (Matthews et al., 1998; Stark et al., 2009). Taken together, these two results suggest a transition mass which is redshift-dependent. If we probe further down the mass function in our lower redshift bins, we may find a similar transition occurring in bulgeless galaxies at lower masses than where the transition is observed at high redshift ($\log[M_*/M_\odot]\sim10.5$), yet higher than that at $z \sim 0$ (Stark et al., 2009). For instance, in the middle redshift bin of the total mass relation in Fig. 5.5, we could be seeing a hint of a transition mass between $9.5 < \log[M_*/M_\odot] < 10.0$ since bulgeless discs are over-represented to the fast side of the relation. More data are needed to determine whether or not this is simply a coincidence.

If we are observing such a phenomenon, the physical significance of an evolving transition mass for bulgeless galaxies could be understood with a variant of the 'downsizing' concept (*e.g.*, Cowie et al., 1996) or an evolving 'mass floor' in galaxy formation theory (*e.g.*, Bouché et al., 2010). The role of environment for our sample would have to be subtle, since the majority of the discs are isolated field galaxies, but these models seek to explain why more massive galaxies formed earlier and faster than lower mass galaxies, regardless of whether they are in the field or in groups/clusters. These models are ultimately driven by the cosmological decline of the accretion rate, which shuts down the assembly of more massive galaxies first since they more quickly consume their accretion reservoirs.

For the physical mechanism, a combination of the evolution of the cosmic UV background together with photo-ionising radiation from the first stars could create a transition mass, above which the cooling efficiency is relatively higher, and below which, a lack of self-shielding keeps smaller, thinner discs from remaining neutral and thus molecular gas form collapsing to form GMCs. Galaxies which have formed bulges and maintain a thicker disc in a thicker, steeper potential-well could self-shield, and thus form stars more efficiently than a thin, bulgeless disc which is being adversely affected by the UV background and photo-ionising feedback in a shallower potential-well.

A number of observable trends are expected in this picture, such as lower metallicities at lower masses and star-formation rates (seen in Mannucci et al., 2010), and different column densities of neutral envelopes around low mass bulgeless discs opposed to discs with bulge components (and steeper potentials). This picture does not however explain why low-mass galaxies, which rotate relatively slowly tend to form bulgles, bars, or

thicker discs, while the faster-rotators tend to remain bulgeless. We turn to the dynamical nature of this picture in the next item.

2. **Clump Formation and Migration:** One possible explanation for the low ratios of rotation to velocity dispersion support in systems at $z\sim2$ ($V/\sigma < 2-5$, Förster Schreiber et al., 2006, 2009) is that gravitational disc instabilities create and then drive clumps into the central regions of galaxies, leading to the formation of stellar bulges (Noguchi, 1999; Immeli et al., 2004; Romeo et al., 2010). The low V/σ values stem from higher velocity dispersions produced as clumps migrate towards the centres of galaxies.

   Because we have radially-dependent dispersion measurements in addition to the rotation curves of our galaxies, we can test whether our results support the clump migration picture by examining the V/σ profiles of our sample in redshift bins. The intrinsic dispersion is determined by subtracting, in quadrature, the measured instrumental dispersion that are measured from skylines in the spectra.

   Our results in Figure 5.10 may possibly support the clump migration picture, since the V/σ values vary more in the highest redshift bins than at lower redshift. This could indicate a greater presence of clumps that have dissipated and/or driven towards the galaxy centres by lower redshifts. We see again in Fig. 5.10 a clear departure of the trend in the bulgeless discs in our highest DEIMOS redshift bin from the rest of the sample. The renegade discs' V/σ values continue to rise to ~ 8 whereas the rest of the subsample means level off between $5 < V/\sigma < 6$. There is a clear spread in V/σ values from 2–15 across all redshift bins (most <10), which could also support the idea that galaxies are transitioning from V/σ values of 2–6 at $z\sim2$ to the local values of 10–20, driven by the dynamical cooling of discs as they stabilise. However, besides the high redshift bulgeless

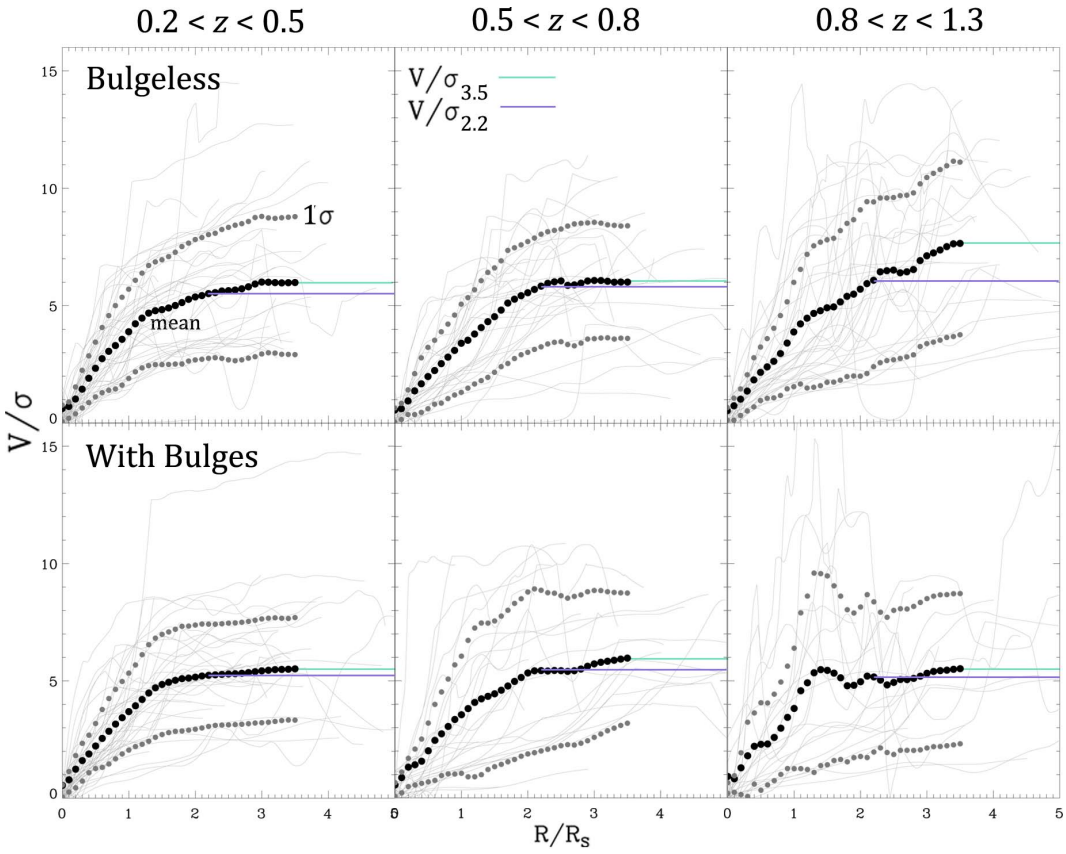

Figure 5.10 Radial profiles (in dimensionless units of disc scale radii, R/R_s) of the ratio of rotational velocity to velocity dispersion (V/σ) for each galaxy in our DEIMOS sample over three different redshift bins. We separate the profiles of the bulgeless galaxies **(top row)** from the galaxies with bulge components **(bottom row)**. In addition to each profile, plotted in light grey, we over plot the mean of the profiles in each panel at intervals of $1/10^{th}$ of a scale radius. In addition to the mean (plotted with black circles), we plot the robust sigma of the distribution of V/σ values at that given radius (plotted with smaller grey circles). To guide the eye as to potential differences between profiles, we plot a line extending from the V/σ value at 2.2 times the scale radius ($V/\sigma_{2.2}$, with a horizontal purple line) as well as at 3.5 times the scale radius ($V/\sigma_{3.5}$, with a horizontal teal line). This reveals the dramatic difference in the mean profile of the bulgeless discs at high z **(top right panel)** which continues to rise towards $V/\sigma \sim 8$, whereas the rest of the panel means appear to flatten between $5 < V/\sigma < 6$. We end the calculation of means at 3.5 scale radii since less than half of the profiles are traced past that point, and the determination becomes much more uncertain.

discs, there is no clear evidence for evolution in the mean V/σ profiles between redshift bins.

On the other hand, we see no trend of increasing pressure support toward the inner regions of galaxies with decreasing redshift. However it is important to note, as we did in Ch. 2, that the velocity dispersion that we measure is not the stellar velocity dispersion, or even the dispersion of the bulk of the gas (which is likely to be neutral and molecular), but the dispersion of the ionised gas. This signal could be heavily influenced by momentum or energy driven winds by stellar feedback, which could dominate the spread in velocities over any underlying dynamical pressure support. So a central bulge component velocity dispersion is unlikely to be well-reflected in the ionised gas, of which bulges contain relatively little.

A further problem with this picture is that large, central stellar velocity dispersions can support an increased stellar mass in the form of a bulge without significantly changing the rotational velocity of the surrounding disc. This would move galaxies above the TF relation as their bulges grow, which is not supported in our results.

Even if we were able to comprehensively test this picture, it does not explain why bulgeless galaxies would arrive on the TF relation by intermediate redshift without forming bulges. Indeed, in the clump migration picture, gas-rich bulgeless and barless discs would continue to suffer gravitational instabilities and clump formation until a bulge had formed and the disc had stabilised. An additional mechanism is needed to explain the stabilising of bulgeless discs which form no substantial bulge or bar to the present day.

3. **Higher gas fractions:** One final promising explanation of the offset we see for bulgeless discs is that we could be under-predicting their gas-fractions as compared to the rest of the galaxies in the sample. To explore

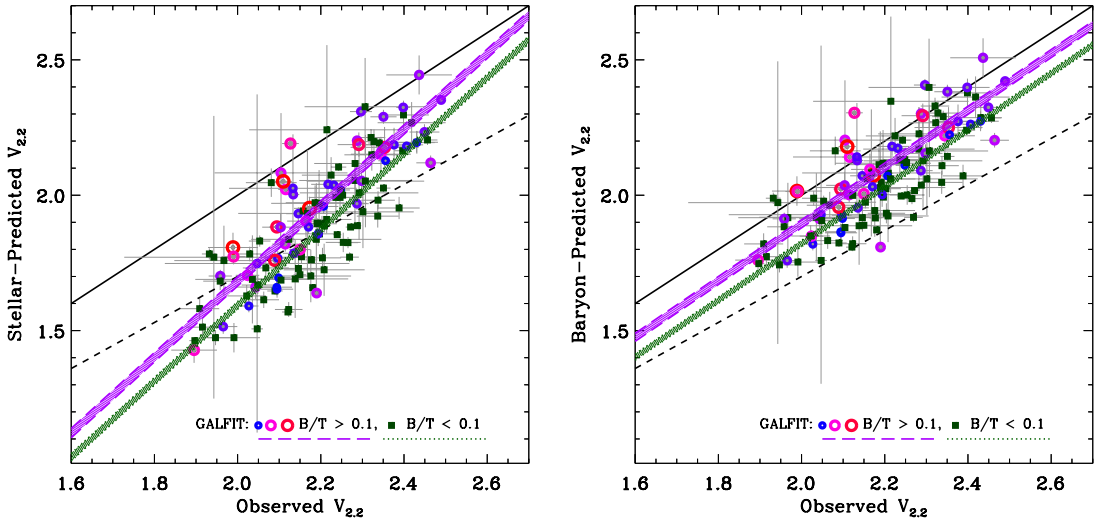

Figure 5.11 Velocities predicted by the stellar content of disc compared with measured velocities of disc **(left)**, and likewise with the baryonic mass estimates **(right)**. Symbols are as in Fig. 5.5. Even with gas estimates, we still see an offset between galaxies with and without bulges, since the estimates are based on stellar mass and redshift. The 1:1 ratio line is plotted with a solid black line, and the universal baryon fraction from the latest constraints of ΛCDM (Komatsu et al., 2011) is plotted with a dashed line. As determined in §5.1, we see no missing baryon problem with in $r_{2.2}$, and the influence of dark matter is minor. From this point on in this section, $V_{\rm pred}$ will refer to the velocity predicted by the baryonic estimate.

this possibility without access to direct gas mass data, we conduct an empirically-motivated analytical exercise of the following:

To begin we examine an alternative form of the Tully-Fisher relation, comparing the predicted velocity ($V_{\rm pred}$) from the luminous component with the velocity that is observed ($V_{\rm obs}$) at $r_{2.2}$. We plot this variant of the TF relation using both the stellar mass (left side of Fig. 5.11) and the estimated baryonic mass (right side of Fig. 5.11) to predict the velocity, and the bulgeless discs offset persists, even when we include the gas mass. Since more gas mass is predicted for lower mass galaxies, the slope of the relation changes to be more in line with the 1:1 ratio. From this point onwards, $V_{\rm pred}$ will refer to the velocity predicted by the total baryonic estimate, rather than the stellar mass alone.

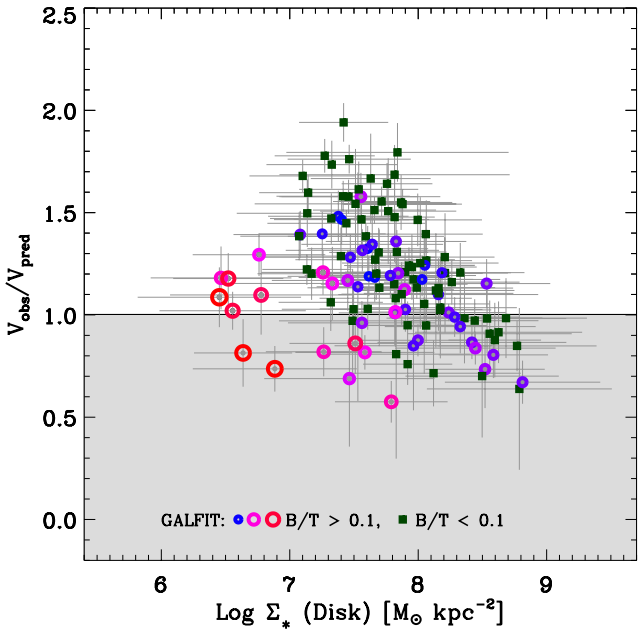

Figure 5.12 $V_{\rm obs}/V_{\rm pred}$ ratio as a function of stellar surface density of the disc (bulge component subtracted). Symbols are as in Fig. 5.5. We see an interesting departure of the high-z bulgeless discs from the galaxies with bulge components in this sample. The renegade discs cluster above the $V_{\rm obs}/V_{\rm pred}$ of 1.5, however no clear trend is present in this figure.

Next we plot the ratio of $V_{\rm obs}/V_{\rm pred}$, as a condensed TF parameter, as a function of a variety of measured and derived quantities of the galaxies, especially looking for offsets between the offset bulgeless discs and the rest of the sample. For instance we found no correlation with inclination, disc size, PA, $S_{0.5}$, or disc instability parameter Q (Toomre, 1964). There is an intriguing offset of the bulgeless discs when plotting $V_{\rm obs}/V_{\rm pred}$ against disc surface density (Fig. 5.12), however no clear trend or correlation is evident.

In the following plots, we consider only the mass range which is shared in all redshift bins, so that mass incompleteness towards high redshift does not lead to any bias (Fig. 5.13).

Two results show the clearest distinction between the offset high-z bulgeless discs and the rest of the sample, and both of the parameters being

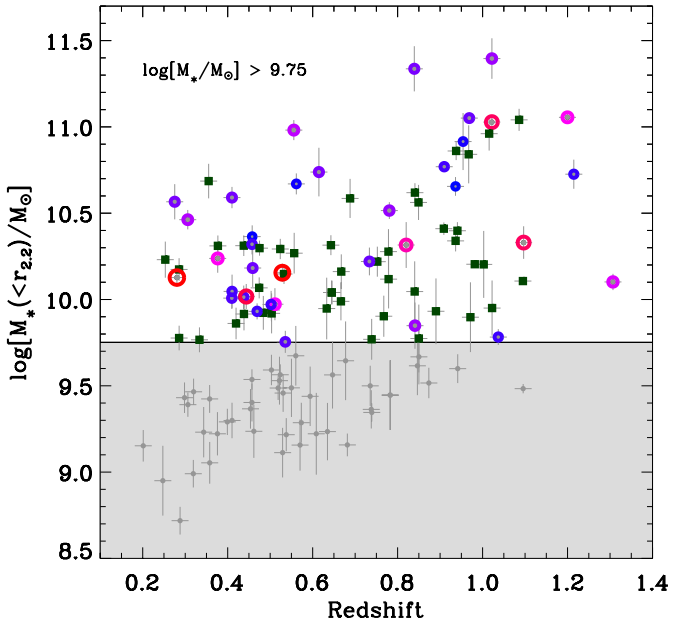

Figure 5.13 We show the shared mass range between galaxies, to consider when determining trends, or else redshift-dependent trends could be biased with mass-dependent ones. The lower mass galaxies at lower redshift are plotted with grey points in the following figures, while the galaxies of share mass range are continued to be plotted in colour, with circles for galaxies with bulges, and squares for bulgeless galaxies.

compared are ultimately determined by the gas fraction. These are (a) the surface density of the star-formation rate ($\Sigma_{\rm SFR}$, top of Fig. 5.14) and (b) the ratio between our gas estimates from §5.1.3 and the Kennicutt-Schmidt (K-S) relation (bottom of Fig. 5.14). The K-S gas mass is determined from the rest-frame *B*-magnitude surface brightness, which is used to estimate a SFR density and thus a gas mass according to the inverted K-S relation (Kennicutt, 1998).

These figures identify a group of galaxies which have a diminished B-band magnitude per area than expected in relation to the rest of the sample, given their mass and rotation velocity. If we correct the bulgeless discs gas fraction such that they are in line with the rest of the sample in the bottom of Fig. 5.14, their gas fractions will better reflect their rotation

velocities together with their SFRs.

This empirically-drives prediction of a different SFR-to-gas ratio recipe for bulgeless discs at $z \sim 1$ can be physically motivated by considering less metal-enriched gas in the discs of bulgeless discs, and thus less efficient SFR, reminiscent of a transition mass or threshold mass in disc galaxy assembly. The relative youth of the bulgeless discs may be caused by the lack of enriching outflows which have not re-condensed. This lengthened 'fountain' duty-cycle could be due to their shallower gravitational potential and lower star-formation surface densities (*i.e.* Oppenheimer & Davé, 2008; Finlator & Davé, 2008, etc.). Thus the outflows are slower and the metals more likely to escape in supernova-driven winds.

Regardless of the exact physical motivation, this correction is effectively a M_B based correction for the baryonic mass, determined by M_*, and relying on a combination of the trends discussed in §5.1.3 and Kennicutt (1998). Since baryons appear to dominate within 2.2 scale radii, we experiment with a baryon-based solution rather than assume we are seeing a change in evolution of the dark matter halo. It would also be unsurprising if locally-derived methods of estimating the gas masses fail in galaxies which are younger, less metal-rich, and less-efficient star formers, which these discs may be.

When we force the bulgeless discs to follow the same trend as the galaxies with bulges in Figure 5.14, we no longer see the bulge-dependent trend in V_{obs}/V_{pred} ratio with redshift (Fig. 5.15). However, if we estimate our dynamical masses with the oblated potentials for the bulgeless disc galaxies and spherical potentials for the galaxies with significant bulges (see §5.1.1), then both subsamples align (bottom of Fig. 5.15).

This exercise to find a common Baryonic TF relation for all galaxies in our sample is contrived, and should not be taken as more than a demonstration of the implications of a universal Baryonic TF relation, which

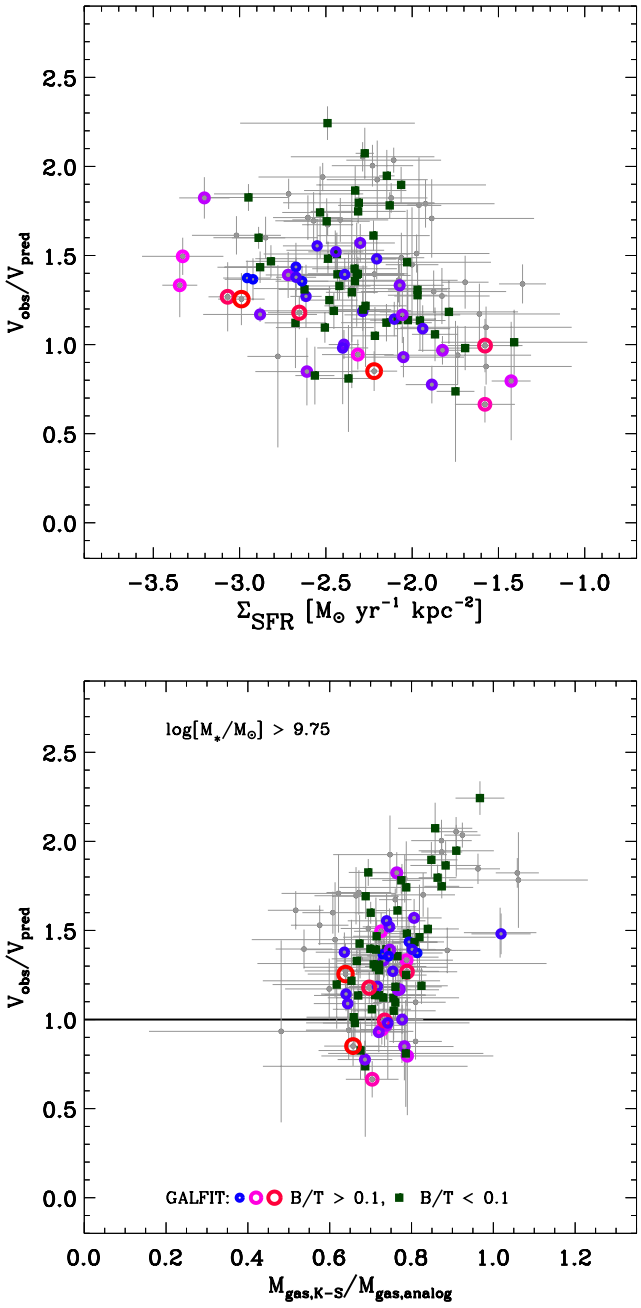

Figure 5.14 **Top:** The $V_{\rm obs}/V_{\rm pred}$ ratio as a function of star formation rate surface density (symbols are as in Fig. 5.5). **Bottom:** The $V_{\rm obs}/V_{\rm pred}$ ratio as a function of the ratio between the gas mass estimated in §5.1.3 (analog) and the Kennicutt-Schmidt (K-S) relation. We find that the group of offset galaxies in both panels are the offset bulgeless discs at high redshift. We predict a gas mass for the bulgeless discs that is much more similar to that found with the inverted Kennicutt-Schmidt relation than the rest of the sample (for which the methods in §5.1.3 predict gas masses which are 30±10% higher than the K-S relation). We predict that these galaxies are less mature, lower-metallicity, and thus less-efficient star-formers which may have a higher gas fraction than what would be predicted with locally-derived methods.

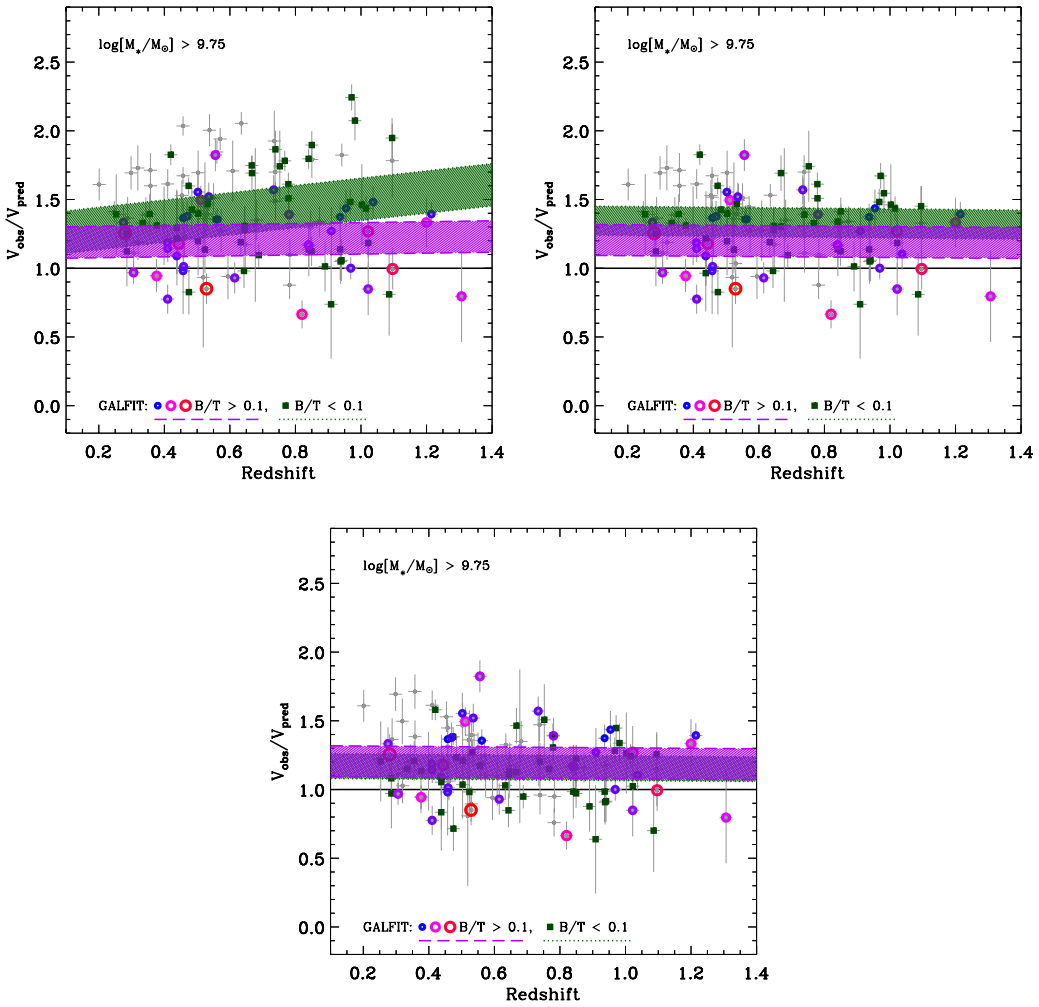

Figure 5.15 **Top left:** The redshift dependence of the V_{obs}/V_{pred} ratio, where we note the high redshift bulgeless discs spinning faster than expected given the rest of the sample. **Top right:** With an applied gas mass correction based on Fig. 5.14, we no longer have divergent, z-dependant trends in this alternative view of the un-binned Tully-Fisher relation. However there is still an offset in the bulgeless galaxies from the galaxies with significant bulges. **Bottom:** If we treat the potential of the bulgeless galaxies as oblate spheres, rather than typical spherically symmetric potential, then the bulgeless discs are no longer spinning faster than predicted with respect to the rest of the sample, and a universal Baryonic Tully-Fisher relation is restored.

is confirmed locally (*e.g.*, McGaugh, 2012). It does produce an interesting prediction of the gas mass differences between varying samples, and looking towards the future, we hope to verify these predictions using observatories like ALMA for the molecular gas component, and MeerKAT and ultimately the SKA for the neutral hydrogen component.

5.4 Summary of Chapter 5

In this chapter, we have used our data to illustrate the potential of comparing dynamical and baryonic masses to better understand the contributions that they matter make in the M_*-TF relation. Although we are uniquely placed to explore our extended rotation curves and derived stellar masses at intermediate and high redshift, our gas mass estimates are clearly approximate at this stage.

We estimate dynamical masses using both spherical and oblate potentials which we expect bracket the likely values. We compute baryonic masses by estimating the additional mass in cold gas. We find that baryons may contribute between 50-100% of the total mass within the radii at which we can confidently observe dynamics of the gas in our disc sample. Such a high fraction of baryons influences significantly the overall profile of the dark matter halo. This exercise therefore suggests that even if dark matter is present in equal amounts, it must be tightly coupled to the baryonic content.

The emergence of mature spiral galaxies with well-ordered rotational properties can be tracked with the M_*-TF relation. We find a significant Tully-Fisher offset for high redshift bulgeless disc galaxies compared to the rest of our sample and the local relation. This promising trend suggests that at $z \sim 1$ bulgeless discs are 0.5 dex less massive in stellar mass at a given velocity, and we explore the possible implications of this result.

Progress in studies of the evolution of the TF relation will continue as more data are collected and as instrumentation improves. These observation will sharpen our view of how disc galaxies assembled and evolved over the last

two-thirds of the Universe. We discuss various possible scenarios, including a transition mass in pure disc galaxy formation, the formation and migration of clumps at high redshift, or the underestimation of gas mass in bulgeless discs at high redshift.

In Chapter 6, we will summarise both the lessons learned from this body of work, as well as the results form the analysis and discussion. We will then turn to the future, suggesting improvements on the methods presented here from what has been learned, as well as ways forward that will likely bear interesting results towards our further understanding of disc galaxy assembly and evolution.

Chapter 6

Conclusions and Future Directions

We have attempted in this thesis to improve our understanding of disc galaxy assembly by tracking the evolution of the Tully-Fisher relation from intermediate to high redshifts. Our achievements and conclusions we can draw are primarily in four categories::

1. An appropriate modelling method for **rotation curves** at intermediate to high redshifts (§6.1).

2. A dataset of deep Keck spectroscopy of galaxies selected from HST imaging, which reveals **improved precision velocity extractions** compared to previous studies of similar size and scope, for application to scaling relations (§6.2).

3. Tracking **Tully-Fisher relations to $z \sim 1$ and beyond** with similar precision and accuracy as that found in many local studies, showing an evolving B-magnitude relation, while little, if any, evolution in the stellar mass relation (§6.3).

4. With this significant improvement in our knowledge of disc galaxy evolution over two-thirds of the age of the universe, we address new questions which have arisen regarding the **drivers of disc galaxy evolution**,

including the role that bulges may play in governing disc dynamical maturity (§6.4).

In the following subsections we summarise the specific points which are concluded in each category/chapter in bulleted lists. Finally in 6.5, we discuss the future directions to which this work should lead.

6.1 Rotation curves

- We adopt the arctangent (arctan) functional form to represent intermediate redshift rotation curves measured from optical emission lines.
- We characterise this functional form with a fiducial rotation velocity ($V_{2.2}$) at 2.2 times the scale radius ($r_{2.2}$), and justify this choice amongst similar options (*e.g.*, $V_{\rm opt}$, V_{80}) and options which can easily diverge (*e.g.*, V_a, $V_{\rm max}$).
- We have developed a rotation curve fitting procedure, CURVATION, to model rotation curves, which has been optimised for intermediate to high redshift optical emission line data from multi-slit spectroscopy.
- Subtle features of the code we demonstrate are important include adopting a two half-Gaussian (rather than a symmetric Gaussian) emission line profile in spatial bins, as well as implementation of the spatial-dependent velocity dispersion and emission brightness profile of the trace in the modelling process.

6.2 Precision measurements and velocity extractions

- Using spectra with extended 6-8 hour integration times secured with the DEIMOS instrument on the Keck II telescope we have measured 129

rotation curves of 238 HST targets selected with z_{AB}<22.5 in the redshift range 0.2<z<1.3 in the two GOODS fields.

- Using LRIS on Keck I we determine reliable rotational velocities for 42 of 70 targeted star-forming galaxies with z_{AB}<24 selected from the redshift range $1.0 \lesssim z < 1.7$ in 5 deep HST extra-galactic fields.

- Also targeted with DEIMOS/LRIS were 48/14 spectroscopically passive galaxies and 59/14 spectroscopically compact galaxies, respectively, which are interesting in their own right, but do not provide enough emission extension to be included in our rotation curve analysis (and thus Tully-Fisher relations).

- We use GALFIT to conduct a bulge-disc analysis, providing important measurements for our rotation curve deprojection analysis such as the disc scale radius, disc position angle (PA), and disc minor-to-major axis ration (b/a), and well as the bulge-to-total ratio (B/T).

- Using associated HST imaging data, we derive modelled velocities corrected for the effects of inclination, seeing and the 1-D nature of our multi-slit geometry to a fiducial radius, $r_{2.2}$. Most rotation curves flatten within $r_{2.2}$, and 90% are traceable to $r_{2.2}$, and we demonstrate the reliability of our velocity measurements with which to construct Tully-Fisher relations.

- We find that applying CURVATION to spectra integrated for 1hr as opposed to 6hrs, yields rotation velocities that are 13% higher on average, although this remains consistent within the considerably larger error bars of the 1 hr measurements. We also trace, on average, 30% further along the disc with the 6 hr data, and $\sim$1/2 of the objects for which we measure extended emission with 6 hr data, would be considered compact or passive category with only 1 hr exposures.

- When we compare the results of the overlapping sample between the TKRS survey and our work (which also uses Keck DEIMOS, which differ only in the velocity extraction method and the exposure time) we find that TKRS V_{rot} mean is 68% of our $V_{2.2}$ mean, and the fractional error bars are almost 7 times larger.

- We test the reliability of our extracted velocities from LRIS with reference to our higher resolution DEIMOS data at similar redshifts, allowing us to quantify some of the additional uncertainties in the LRIS measurements

6.3 Evolution of the Tully-Fisher relations

- In addition to demonstrating the validity of our observational approach and our improved modelling techniques, our results clearly show the TF relation is well-established at redshift $z \simeq 1$.

- We demonstrate a significantly reduced scatter around our intermediate redshift TF relations compared to that seen in intermediate redshift earlier studies. The scatter around the M_*-TF relation is typically 0.2 dex of $M_*/M_\odot$, which is 2-3 times less than earlier work at the same redshift, and comparable to that determined locally. It is also smaller than that achieved by Weiner et al. (2006a) and Kassin et al. (2007) who introduced an additional dispersion term in order to achieve a tight relation.

- We find that the M_*-TF relation for this subsample is well-determined with up to 60% increase in scatter compared to the local relation defined by Pizagno et al. (2005).

- In the DEIMOS data alone, we find a modest but statistically-insignificant evolution in the M_*-TF relation with redshift corresponding to a growth in stellar mass at fixed velocity of $\Delta M_* = 0.04 \pm 0.07$ dex with cosmic time from a redshift $\langle z \rangle \simeq 1.0$ to 0.3. This is consistent with the results

of recent numerical and semi-analytic simulations (Portinari & Sommer-Larsen, 2007; Somerville et al., 2008; Dutton et al., 2011a).

- By including constraints in the M_*-TF zero-point this scope for evolution tightens to $\Delta\, M_* = 0.02 \pm 0.02$ dex with cosmic time from a redshift $\langle z \rangle \simeq 1.7$ to 0.2. This result is consistent with the semi-analytic models of Benson (2012), and other known models depart from this observed trend.

- More pronounced evolution is seen in the M_B-TF relation corresponding to a decline in luminosity of 0.85 ± 0.28 mag from $\langle z \rangle \simeq 1.0$ to 0.3, consistent with predictions from Portinari & Sommer-Larsen (2007). The origin of this evolution can be understood by examining the star formation rate and mass-dependent correlation between M_* and M_B as a function of redshift.

6.4 Physical nature of disc galaxy evolution

- We use our data to illustrate the potential of comparing dynamical and baryonic masses to better understand the contributions of dark and baryonic matter in the M_*-TF relation, which gas mass estimates which are clearly approximate at this stage.

- We estimate dynamical masses using both spherical and oblate potentials which we expect to bracket the likely values. We also calculate the dynamical mass using the Freeman (1970) exponential disc potential to compare with the other potentials.

- We compute baryonic masses by estimating the additional mass in cold gas with an empirically motivated analytical method using the galaxies' masses and redshifts. We compare this to a method which utilises the Kennicutt-Schmidt relation (Kennicutt, 1998), and find that, on average, our estimates are 30% greater.

- We find that baryons may contribute between 50-100% of the total mass within the radii at which we can confidently observe dynamics of the gas in our sample. Such a high fraction of baryons significantly influence the overall profile of the dark matter halo. Even if dark matter is present in an equal amount, it will be tightly coupled to the baryonic content.

- The modest evolution seen in the TF relation over $0 < z < 1.7$ contrasts markedly with results emerging at $z > 2$. At face value it seems there is a dramatic change in the kinematic properties over a very short period of cosmic history, however a wider range of sample stellar masses is required at $z > 2$ to understand the validity and significance of this result.

- Comparing our results with various semi-analytical models, the addition of feedback appears to be key in reproducing the observed trends.

- We find a tantalising signal that $z < 0.8$ bulgeless discs galaxies are offset (-0.5 dex in stellar mass) from the TF relation of the rest of the sample, including the local relation. We find that the offset significance is at the $+4\sigma$ level in the DEIMOS data, but with the increased uncertainty in the LRIS measurements, this offset is only at the 2σ level.

- We propose a variety of hypotheses to explain these results, including:

  - an evolving transition mass or 'downsizing' mass floor in bulgeless disc galaxies
  - the formation of massive clumps in the discs of high redshift galaxies, which migrate to their centres to form bulges by the present day
  - the under-estimation of gas mass in the discs of bulgeless galaxies at high redshift

  A complete testing of these hypothetical explanations must await further analysis.

6.5 Future Directions

While we have attempted to construct a self-contained body of work in this thesis, there are a number of questions which have arisen in the process which should be explored in future projects and papers. We list promising inquiries here in our final section, broken down into 4 categories: work which can be done with the present dataset, *per se* (§6.5.1); work which can be done with new data on existing facilities in addition to the present dataset (§6.5.2); further comparisons to be made with our results to galaxy formation models and theory (§6.5.3); and finally, new rotation curve datasets to be gathered with new instrumentation, which will greatly improve our ability to reach our ultimate science goals and allow us to peer further back into time to the earliest scenes of galaxies formation and assembly (§6.5.4).

6.5.1 Further paths of analysis with this dataset

1. **A study on secular growth verses substructure accretion growth:** There is high enough resolution and signal-to-noise in the DEIMOS dataset to conduct a study correlating star-forming knots/clumps seen in rotation curves with HST high-resolution broad-band colour in the galaxies of our sample. By comparing the V/σ and Toomre Q profiles (sensitive to the velocity characteristics and stability of the ionised gas) with colour maps of the HST data, we can potentially distinguish which clumps have been accreted as clumpy minor mergers, and which have been triggered within the disc from existing or inflowing gas.

   Clump component models could be constructed where spectroscopic data are available. SEDs for individual clumps could be fit for star-formation and dust-content. Likelihood distributions of star formation histories then could be compared to likely dynamical timescales of the clumps within the rotation curve. Clumps which appear to be purely young stellar systems will have been created from in-situ or accreted gas, where

as clumps with very old stellar components would have been recently accreted, as resonances in the disc would not allow the survival of such substructure for the time necessary for the stellar populations to age. By combining both internal and external views of disc assembly, we could better constrain key drivers in disc assembly.

2. **A more detailed study of bugles and bulge growth:** We have focused primarily on discs in this thesis; a natural extension would be to study the bulges. By analysing bulge colour, bulge-to-disc ratio, and any velocity dispersion seen in emission or stellar continuum absorption, we may be able to distinguish between bulge types: classical bulges, pseudo bulges, or even large central star bursts masquerading as bulges. The clump formation/migration picture could be further informed by this study, if various bulge types tend to see clumpier or more unstable discs as per idea (1).

3. **A closer look at the mergers in our sample:** While most mergers appear to be minor in our dataset, there are a few objects which appear to be major mergers. However the rotation curves of these mergers tend to appear largely regular, where the emission line gas appears to be tracing a fairly normal gravitational potential well. A further systematic study of both minor and major mergers in this sample is warranted, given the high signal to noise and resolution far out in the discs of these star-forming systems.

4. **A Fully-Bayesian rotation curve modelling code:** A major drawback to the CURVATION procedure is that we do not know the intrinsic dispersion and emission brightness profiles of the best-fit galaxy. It may be possible to produce such profiles in the modelling scheme with intrinsic emission brightness and velocity dispersion profile likelihoods, in

a fully Bayesian procedure. As we are at the end of the 2D slit spectroscopy era, and at the beginning of that of the 3D IFU, such a modelling scheme should be implemented in 3D. While the computation time needed for such a determination will likely be large, the results and value added to emission line studies for resolved dynamics, metallicity, and star-formation in discs would be worthy of the investment.

6.5.2 Improved analysis of this dataset with additional data

1. **Improved bulge-to-disc decompositions at high redshift:** The full release of the HST WFC3 data in the CANDELS fields (Koekemoer et al., 2011) will allow us to compare most of our ACS-based bulge-to-disc decompositions, which are in rest-frame blue/UV at the highest redshifts, to those in rest-frame optical. As demonstrated in Fig. 5.9 of §5.3.1, this is a crucial check to make, as bulge components can be absent in rest-frame blue/UV light. This will allow us to confirm our results of the bulgeless discs offset at high redshift, and conduct studies such as that of idea (3) in the previous subsection.

2. **Improving TF constraints by extending the sample to lower stellar masses:** Clearly the larger the range in stellar masses probed in TF relation studies, the better constrained the slopes and zero-points are, resulting in the better determination of evolutionary signals. Further motivation to probe down the mass function is the trend of bulgeless discs offsets introduced in §5.3, which may suggest similar behavior at lower masses in the lower redshift bins.

   There are a number of other interesting hypotheses regarding the low mass Tully-Fisher relationship, including its likeness to the stellar-to-halo mass (SHM) relationship. Currently only ∼20 galaxies constrain the local SHM relation between $10^8 - 10^9$ $M_\odot$.

6.5.3 Further work comparing to disc formation models and theory

1. **A GALACTICUS component analysis:** An in-depth comparison between semi-analytic and hydrodynamic models may provide valuable insight on the observed trends, and could inform our understanding of the primary drivers of the emerging Tully-Fisher relation at $z \sim 1.7$. What in the formation processes of L^* disc galaxies are leading them to largely stabilise by $z \sim 1$?

2. **'Mock observing' numerical simulations for understanding the Tully-Fisher relation:** Tools have been developed within the hierarchical ΛCDM paradigm to circumvent the complex problem of modelling baryonic feedback in cosmological simulations, including Halo Occupation Distributions (HOD, *e.g.*, Peacock & Smith, 2000) and Abundance Matching (AM, *e.g.*, Vale & Ostriker, 2004), which result in stellar-to-halo mass (SHM) relations for galaxies in the given paradigm. Because these methods necessarily lie within the CDM framework, it has been difficult for them to ultimately inform why the TF relation exists, which is mysterious from an empirical standpoint alone.

   One possible way forward in both understanding the TF relation and resolving sub-structure abundance tension in ΛCDM-cosmology simulations is by carefully comparing 'like with like' in models and observations. By mock observing the projected angular momentum of simulated stars and gas in galaxies and constructing truly self-consistent SHM-like relations via the stellar mass TF relation, whatever differences in the shape and normalisation of the relation to those based on AM and HOD methods will crucially inform the verification process. Either we will finally converge on a self-consistent model and avoid circular arguments within the ΛCDM framework, or we will see a marked deviation with respect

to redshift and/or mass with predictions. If the latter, then alternative cosmological models should be tested for their comparative performance.

6.5.4 Prospects for disc dynamics studies on new and future instruments

They next decade will see a variety of new instruments and telescopes, and we highlight here some of the exciting opportunities that they will bring for measuring disc dynamics at intermediate and high redshifts.

1. **The Multi-Object Spectrometer For Infra-Red Exploration (MOSFIRE)**, which has just completed commissioning on Keck, will extend the observable redshift range well into the infrared, with Hα can be observed out to z$\sim$2.7, and [OII] to z$\sim$6.5 for studies on the evolution of dynamics. Slits cannot be tilted due to instrument design, so targets for emission line rotation curve studies must be carefully selected to have their major axes in line with the mask placement. This will substantially reduce the multiplexing capability of MOSFIRE for this type of high redshift study, although given the high density of discs on the sky, studies of this nature will be practical together with one other parallel observing campaign of similar source density.

2. **The K-band Multi-Object Spectrograph**, now commissioning on the VLT, will provide unprecedented multiplexing capabilities for IFU studies, making large samples of discs with velocity field measurements far less expensive to accrue. At present, multiplexing capabilities of slit spectrographs such as VIMOS (VLT), IMACS (Magellan), as well as DEIMOS, LRIS, and now MOSFIRE (Keck) enable extended exposures on survey sources without a penalty in spectral or spatial resolution along the major axis, for large samples of galaxies which are practically impossible to accrue with pre-KMOS multiplexing capabilities. KMOS will mitigate this current deficiency in the technology, especially since 3D spectroscopy

offers clear advantages in optimal fitting of complex velocity fields (Puech et al., 2008; Jones et al., 2010; Genzel et al., 2011; Förster Schreiber et al., 2011; Contini et al., 2012).

3. **The Atacama Large Millimetre Array (ALMA)** may soon reveal extended far-infrared/millimetre emission lines in disc galaxies with Cycle 0 results, for instance the 158-mm dominant gas cooling line of [CII]. however building vast samples of these observations will be costly (the effective field of view will only contain a few high redshift disc targets for [CII] at once), and time on ALMA is extremely competitive.

4. **30-metre class telescopes: The European Extremely Large Telescope (EELT)**, **The Thirty Meter Telescope (TMT)** and the **Giant Magellan Telescope (GMT)**, with state-of-the-art adaptive optics technology and huge collecting area, spectra from this new class of giant ground-based telescopes will be able to probe to previously unresolved smaller and lower mass galaxies at high redshifts in an exciting new regime of parameter space to explore. With so much more photon-collecting area, and thus shorter exposure times on high resolution instruments, we will be able to collect extremely precise emission line kinematics at higher magnification and resolve the clumpy, confused morphologies which have eluded astronomers at $z > 2$ for decades.

5. **The James Webb Space Telescope (JWST)** spectra will be free of skylines and reach further into the infra-red than possible on the ground with incredible sensitivity, which will allow the tracing of emission lines across the discs of galaxies to unprecedentedly low masses and faint emitters at low surface brightness and high redshift.

6. **The Square Kilometre Array (SKA)** will be an incredibly powerful instrument for the measurement of HI in galaxies at intermediate redshifts. The measurement of HI in individual galaxies will not be possible

beyond $z \sim 0.2$ until the completion of the SKA, however even then, its resolving power will only just reach z$\sim$1. Stacked samples will be possible to greater distances and higher redshifts, but for kinematic studies, we seek routes to resolving individual galaxies' velocity fields.

Appendix A

Sample figures

We show here the galaxies in the sample with the same index order as Table 3.4. To the left are the HST images, and to the right are the available emission lines, their respective models and residuals for each galaxy.

Table A.1 Sample Images and Their Spectral Lines and Models

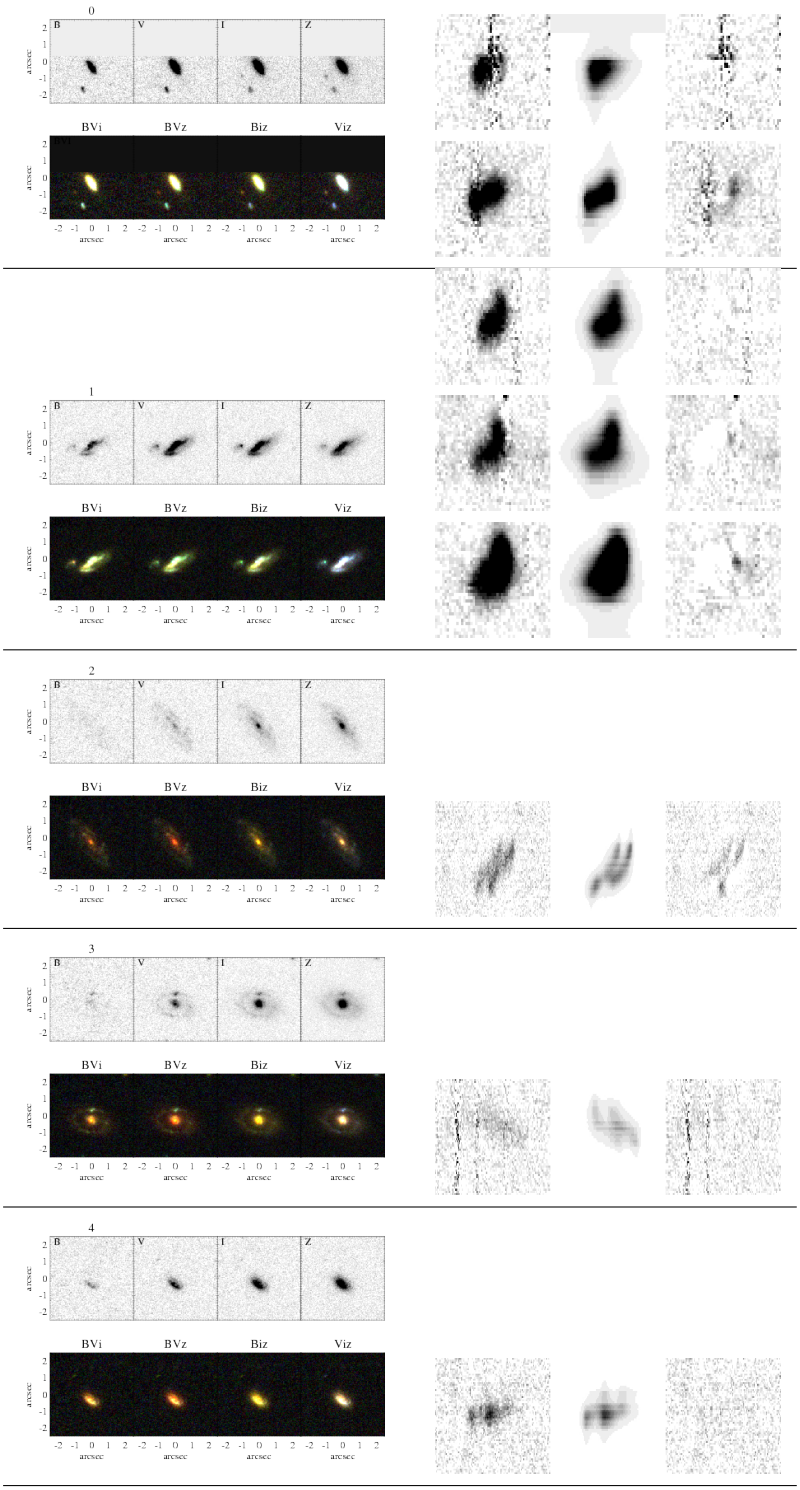

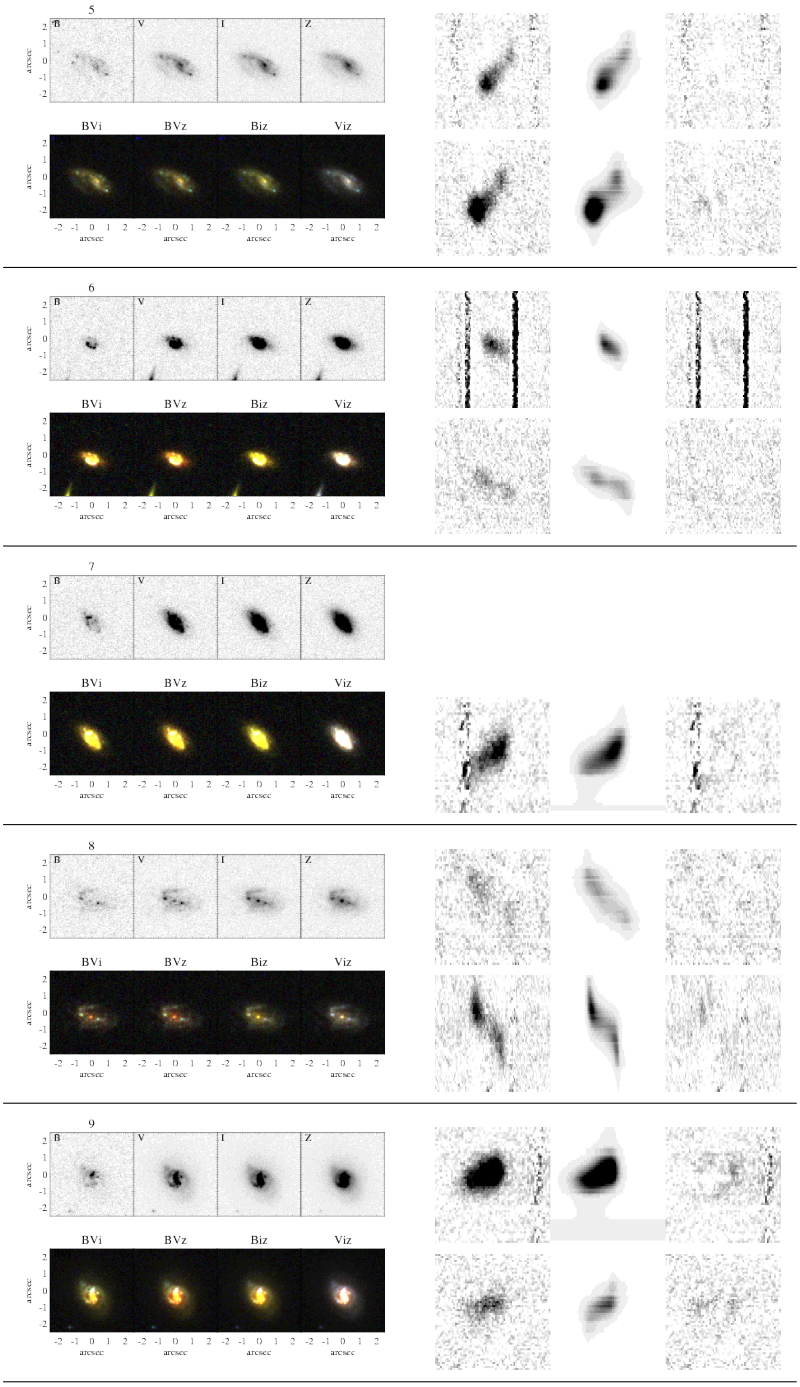
5
B
V
I
Z
BVi
BVz
Biz
Viz
arcsec
6
7
8
9

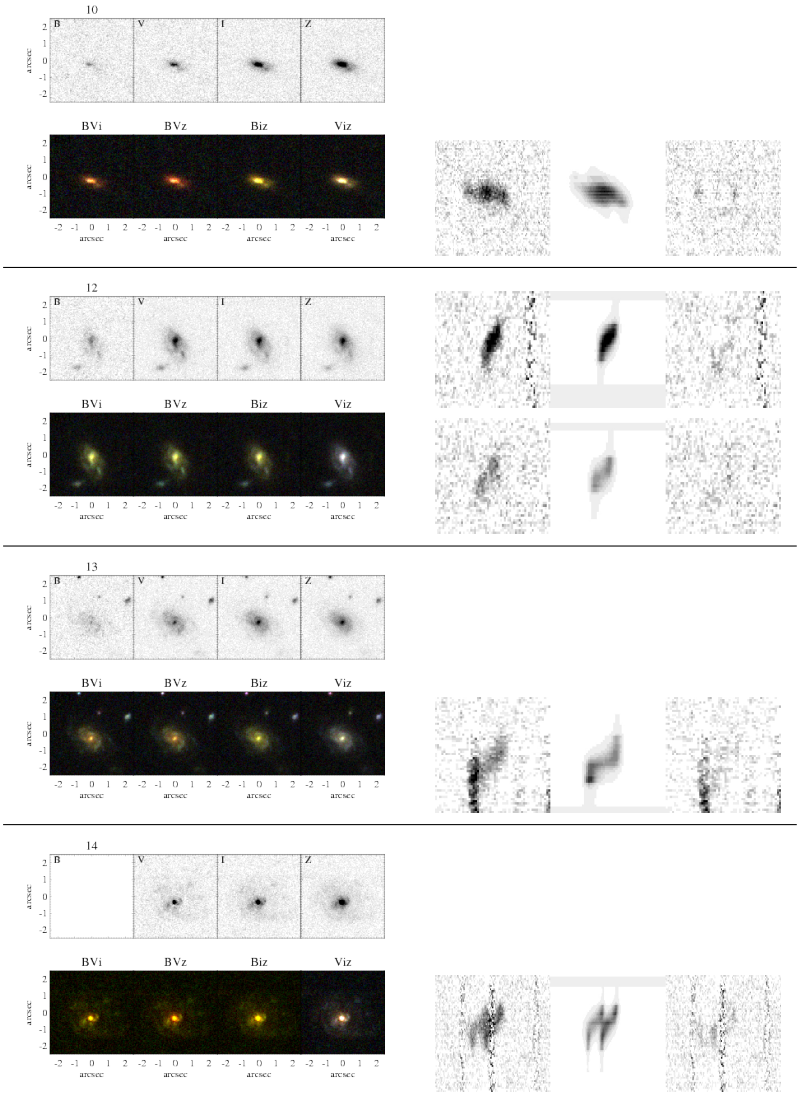
10
B
V
I
Z
BVi
BVz
Biz
Viz
arcsec
12
13
14

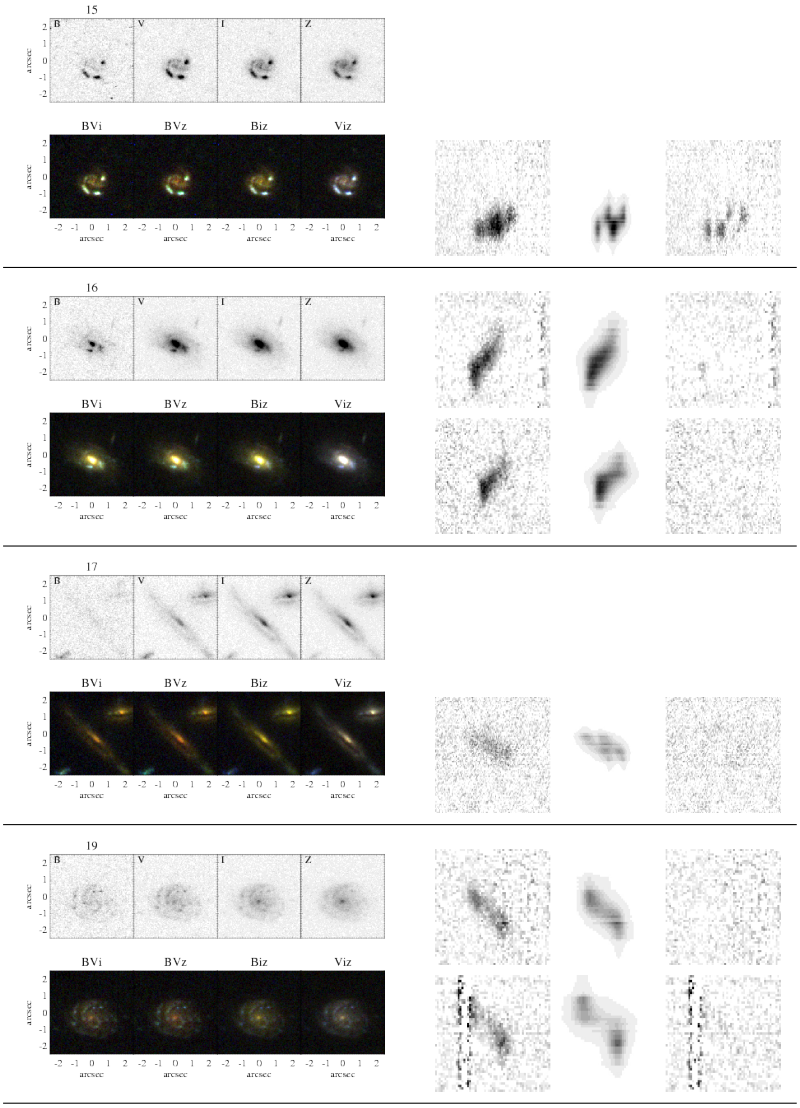
15
B
V
I
Z
BVi
BVz
Biz
Viz
arcsec
16
17
19

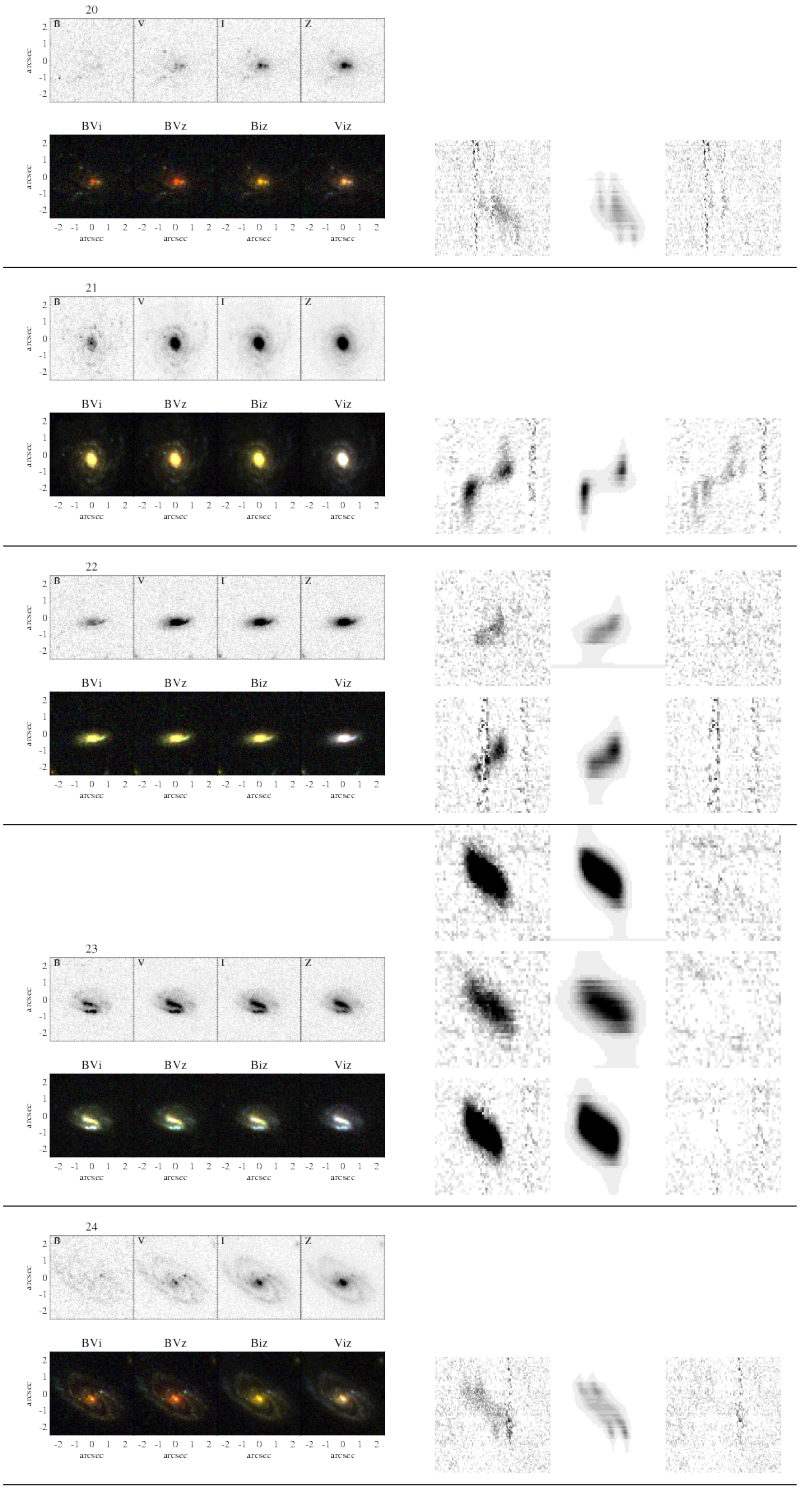
20
B
V
I
Z
BVi
BVz
Biz
Viz
arcsec
21
22
23
24

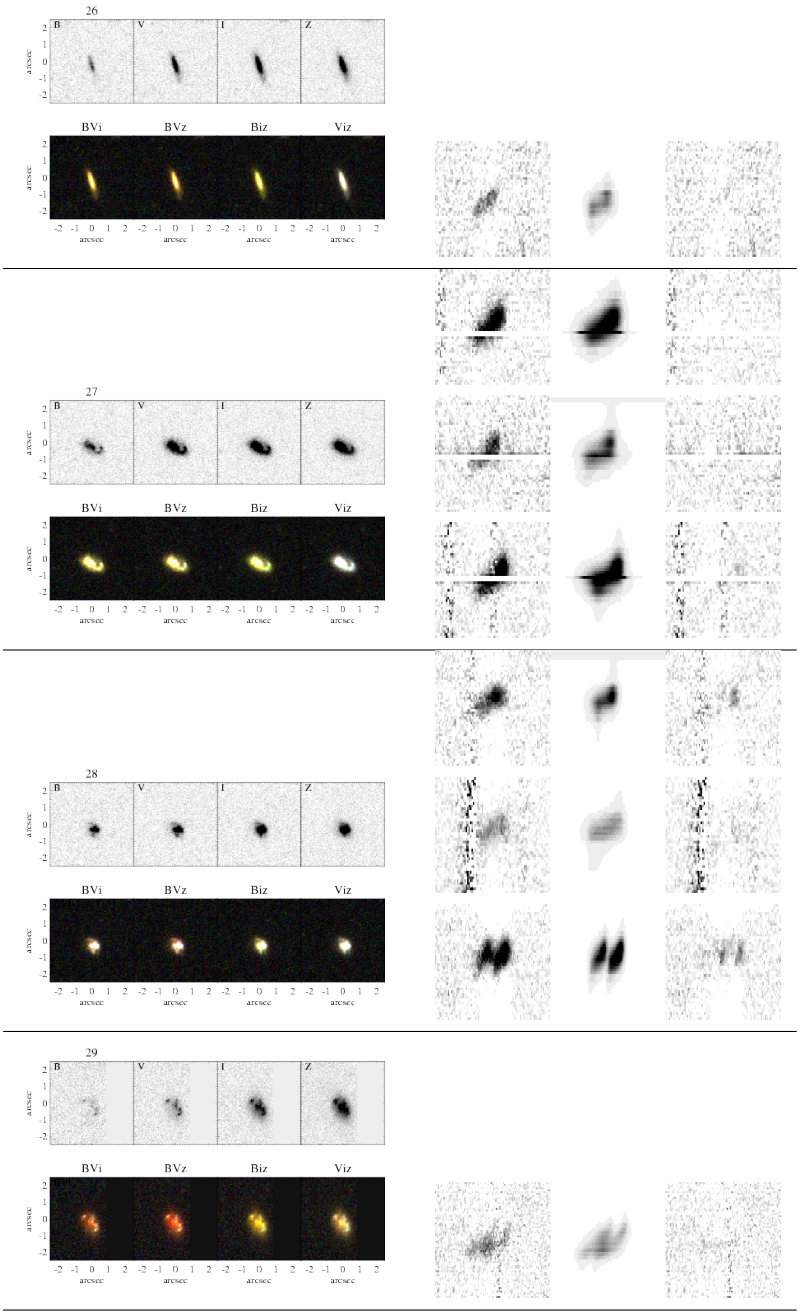
26
B
V
I
Z
BVi
BVz
Biz
Viz
arcsec
27
28
29

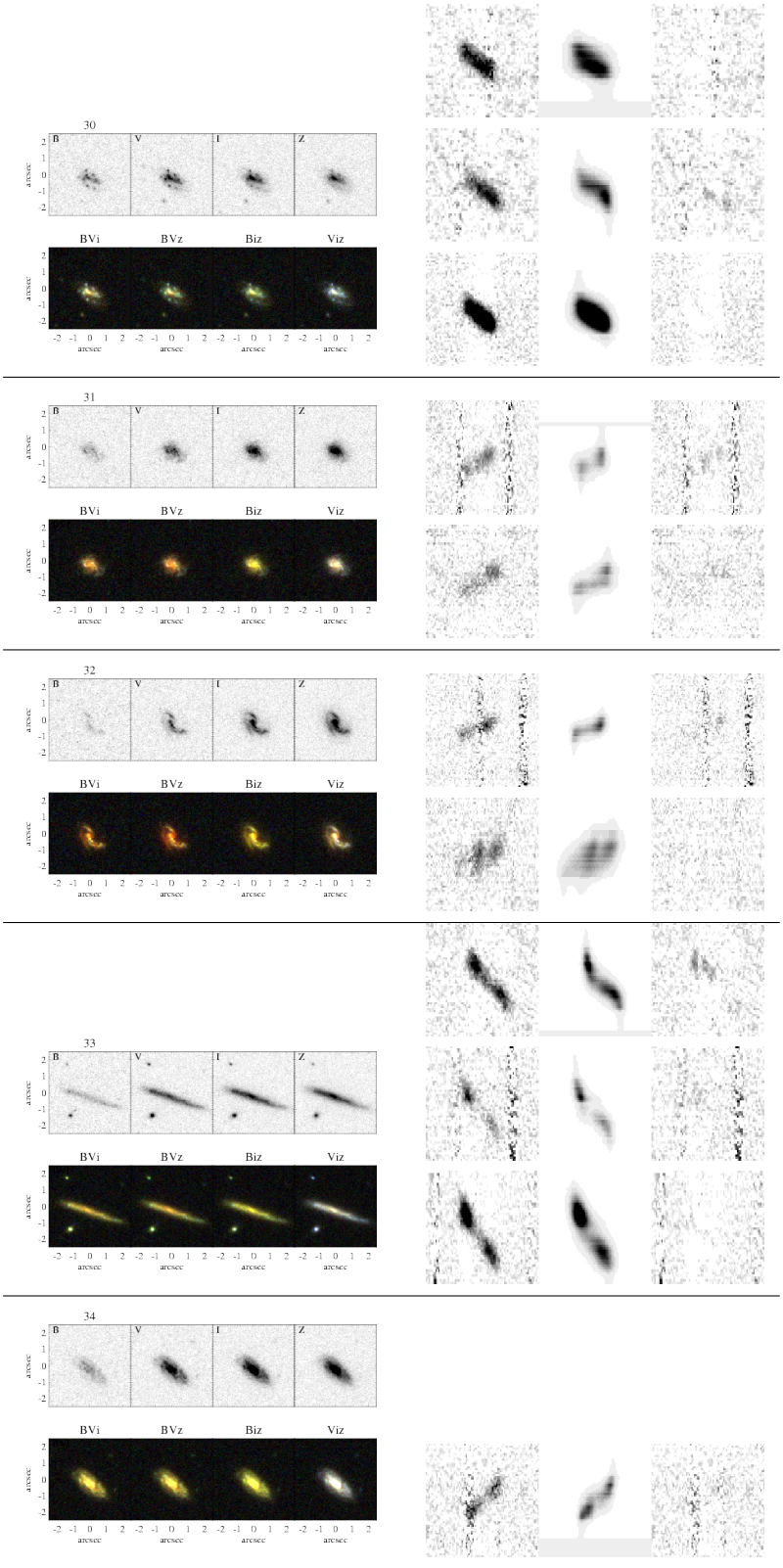
30
B
V
I
Z
BVi
BVz
Biz
Viz
arcsec
31
32
33
34

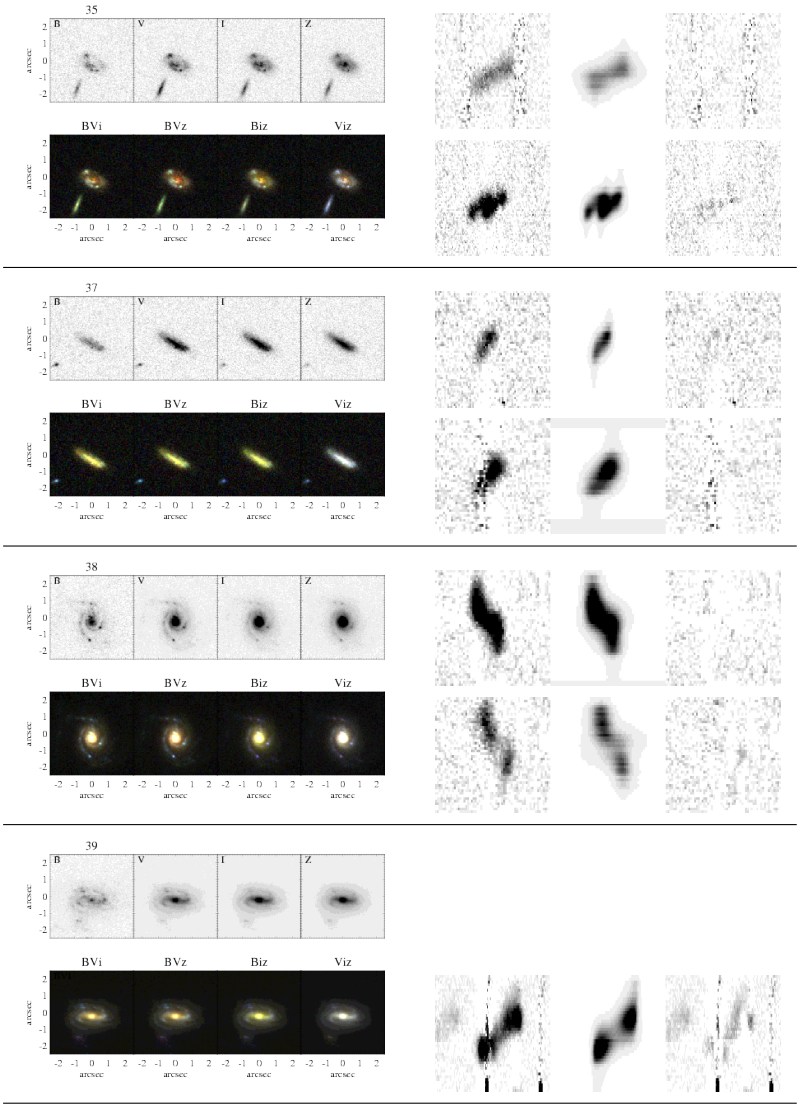
35
B
V
I
Z
BVi
BVz
Biz
Viz
arcsec
37
38
39

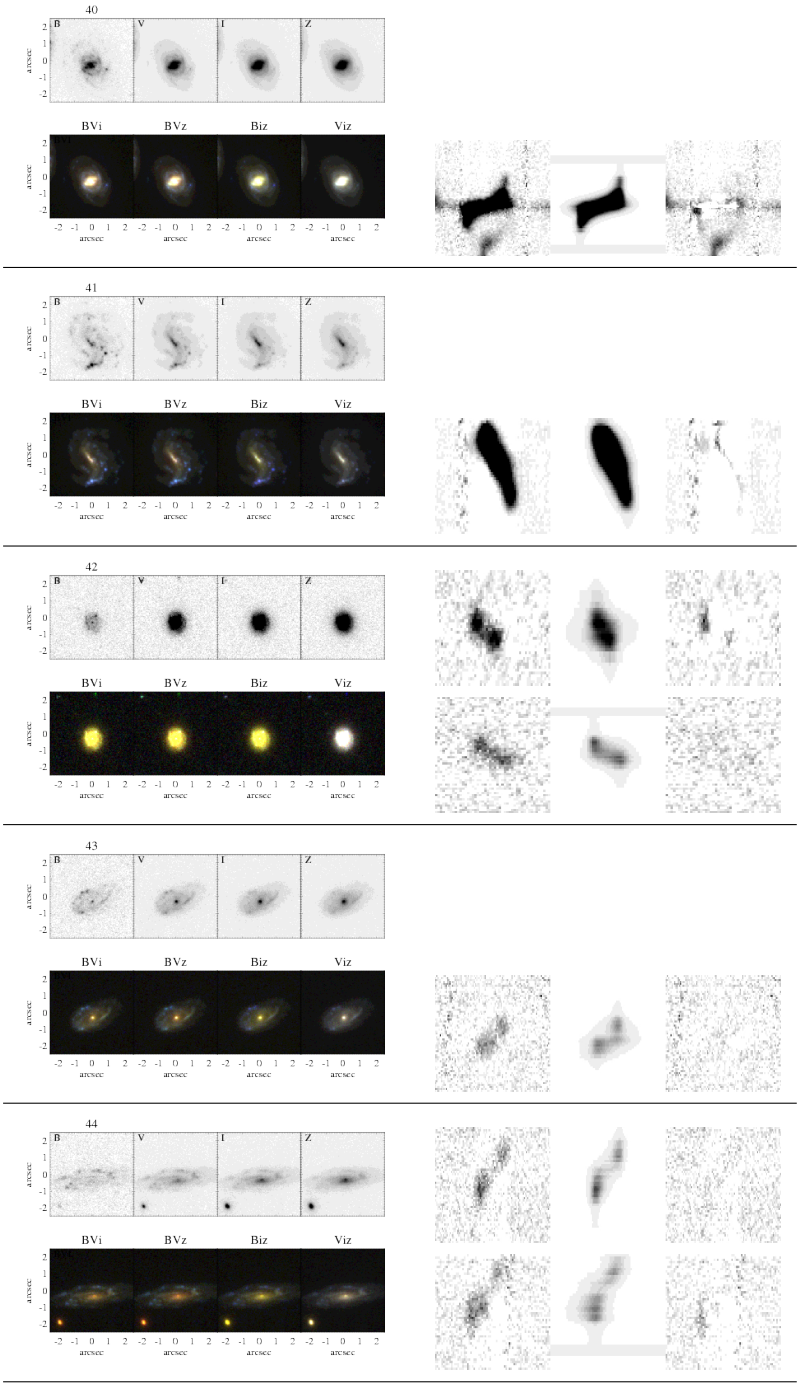
40
B
V
I
Z
BVi
BVz
Biz
Viz
arcsec
41
42
43
44

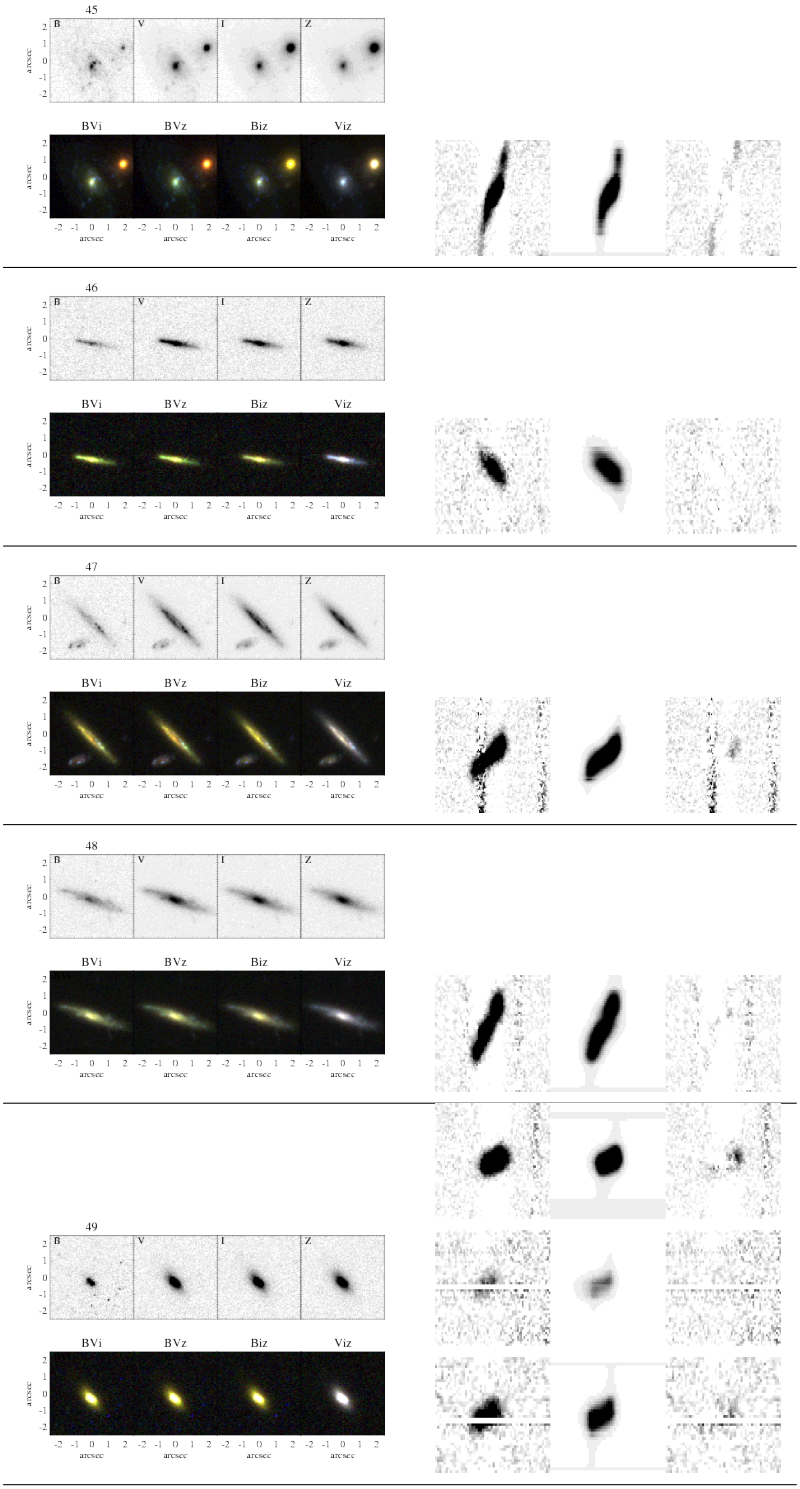
45
B
V
I
Z
BVi
BVz
Biz
Viz
arcsec
46
47
48
49

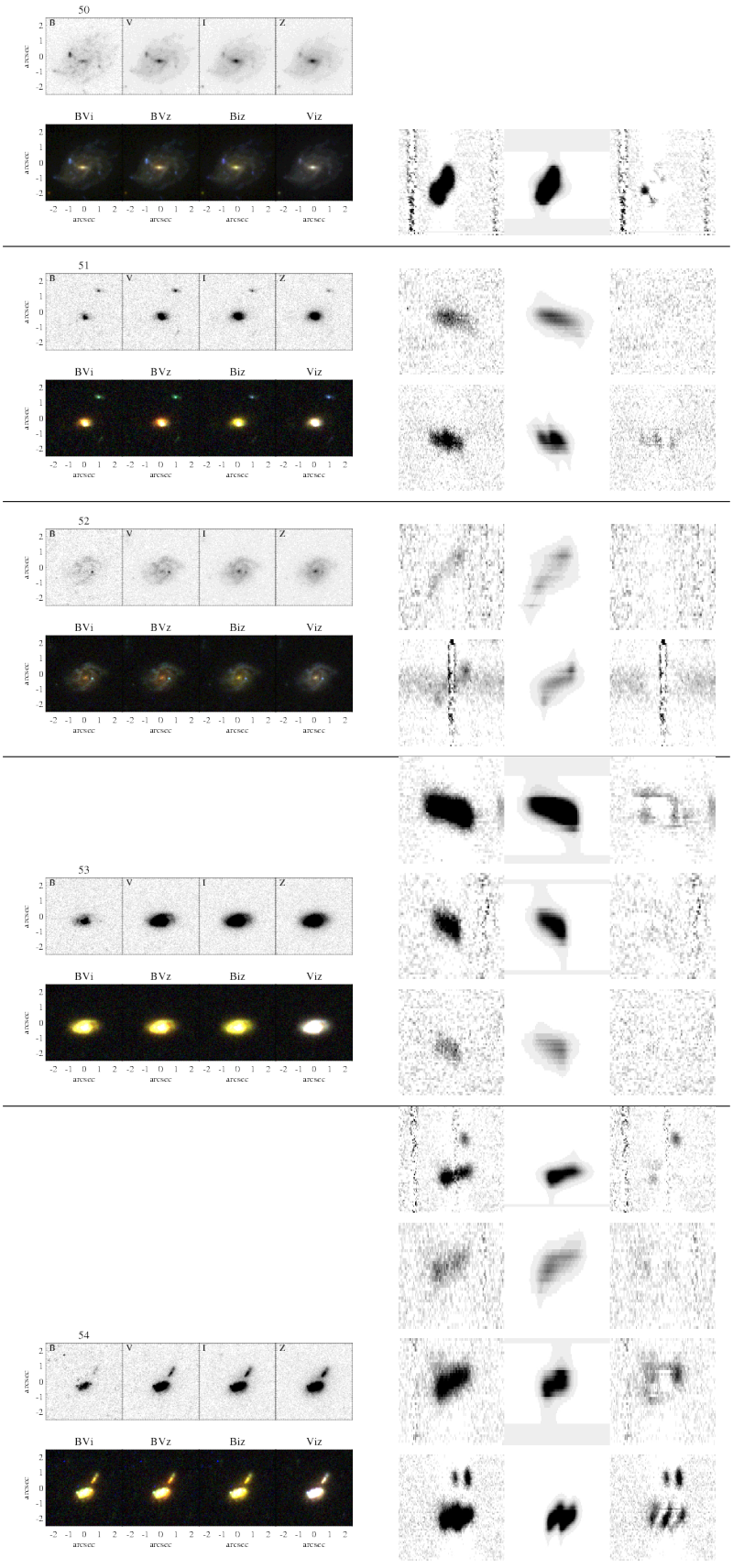
50
B
V
I
Z
BVi
BVz
Biz
Viz
arcsec
51
52
53
54

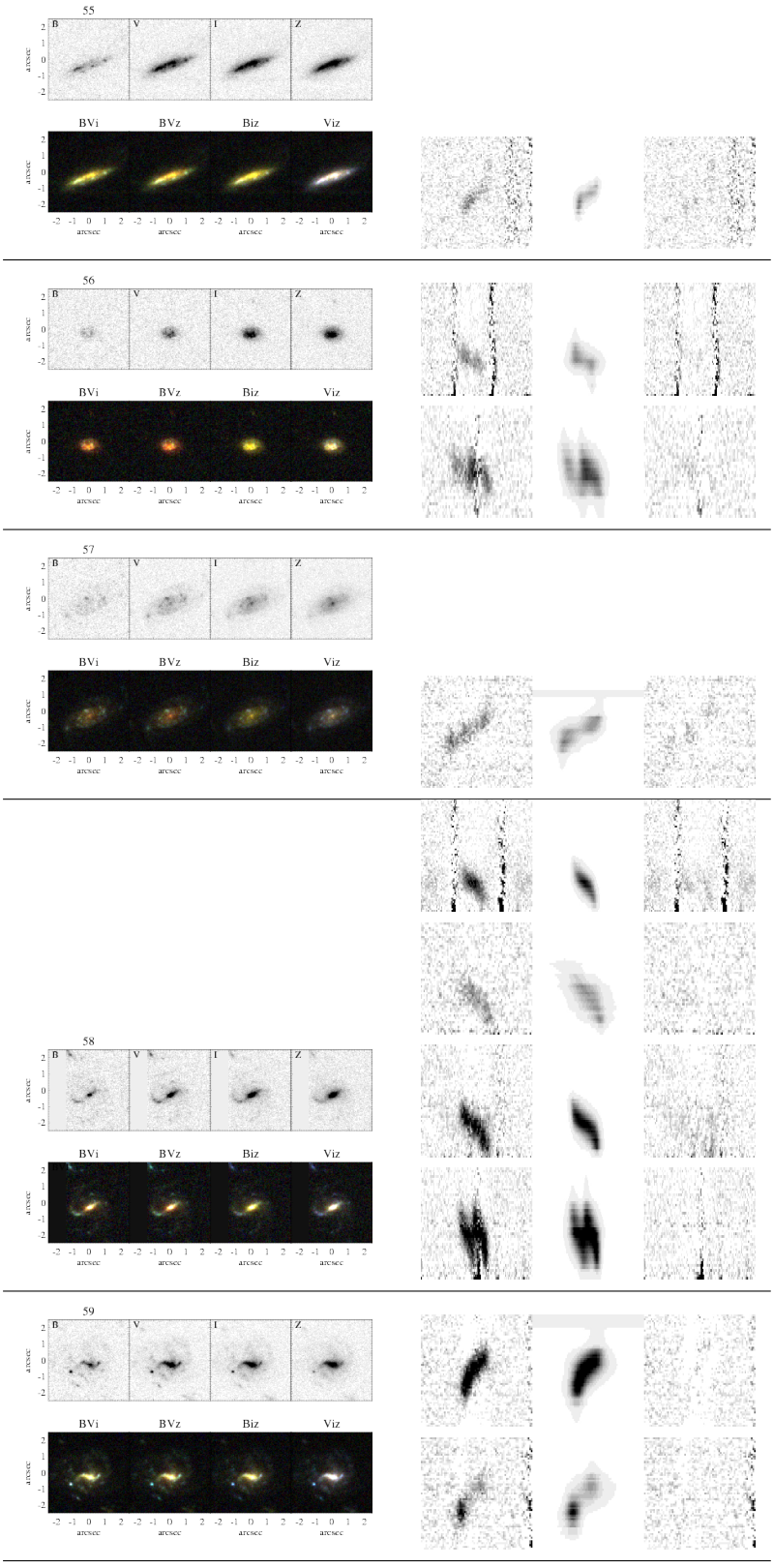
55
B
V
I
Z
BVi
BVz
Biz
Viz
arcsec
56
57
58
59

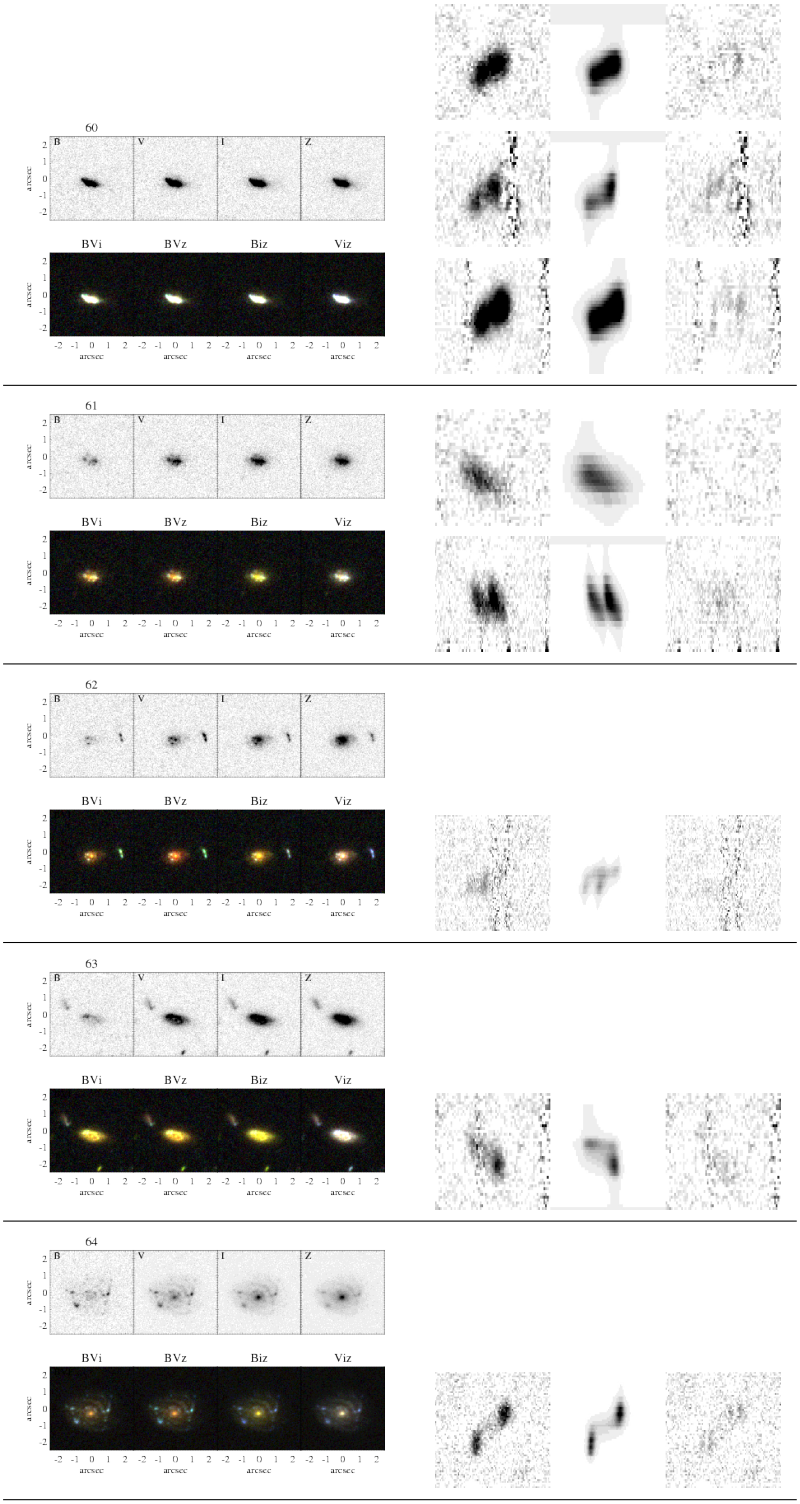
60
B
V
I
Z
BVi
BVz
Biz
Viz
arcsec
61
62
63
64

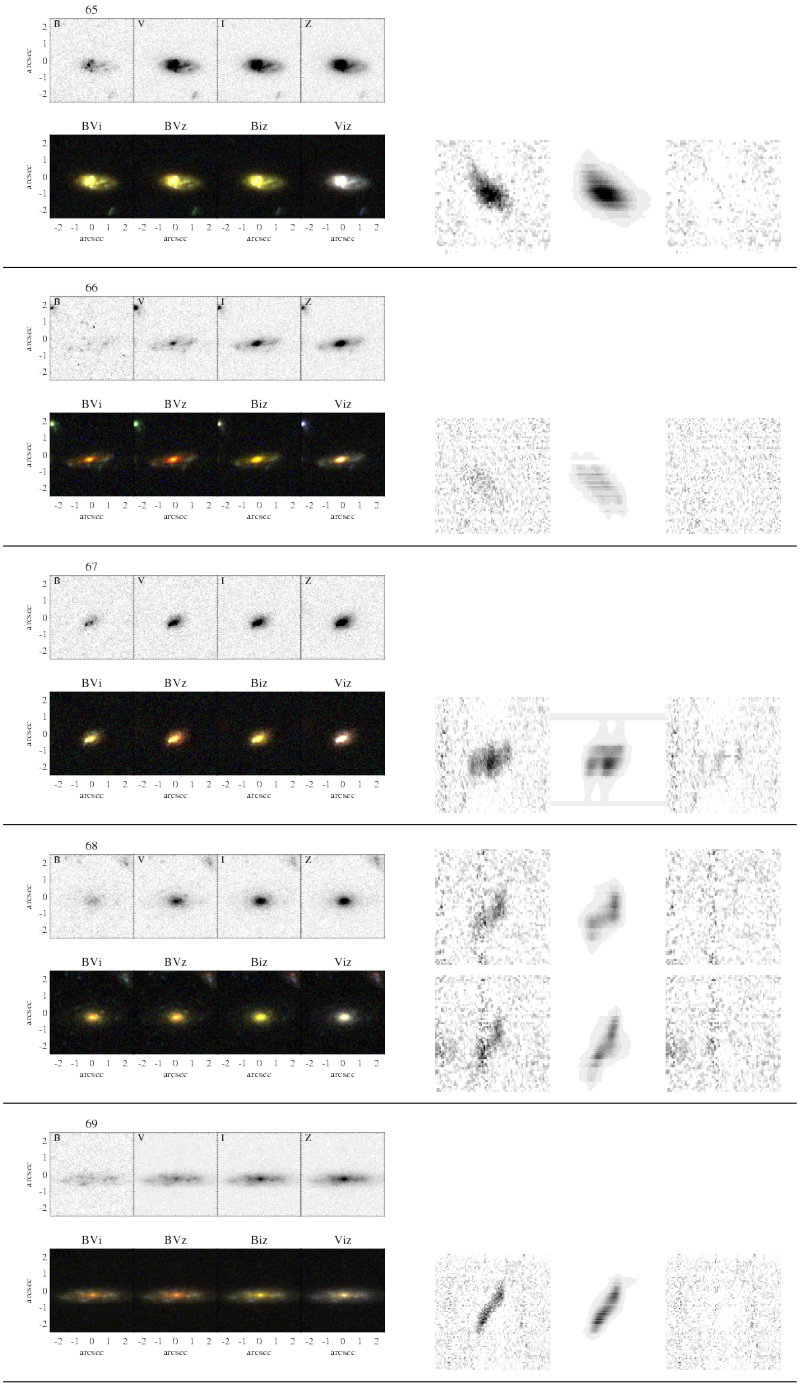
65
B
V
I
Z
BVi
BVz
Biz
Viz
arcsec
66
67
68
69

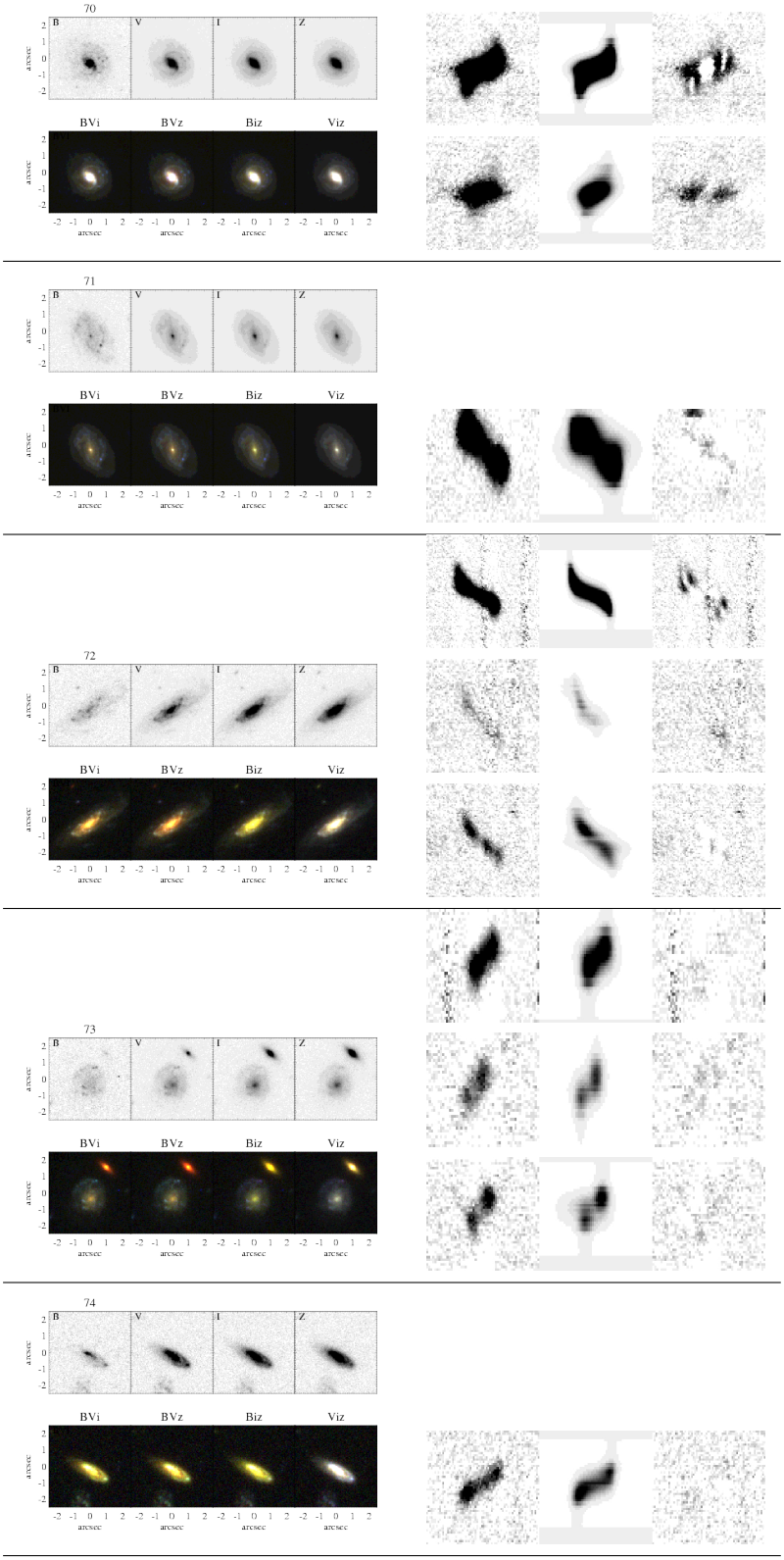
70
B
V
I
Z
BVi
BVz
Biz
Viz
arcsec
71
72
73
74

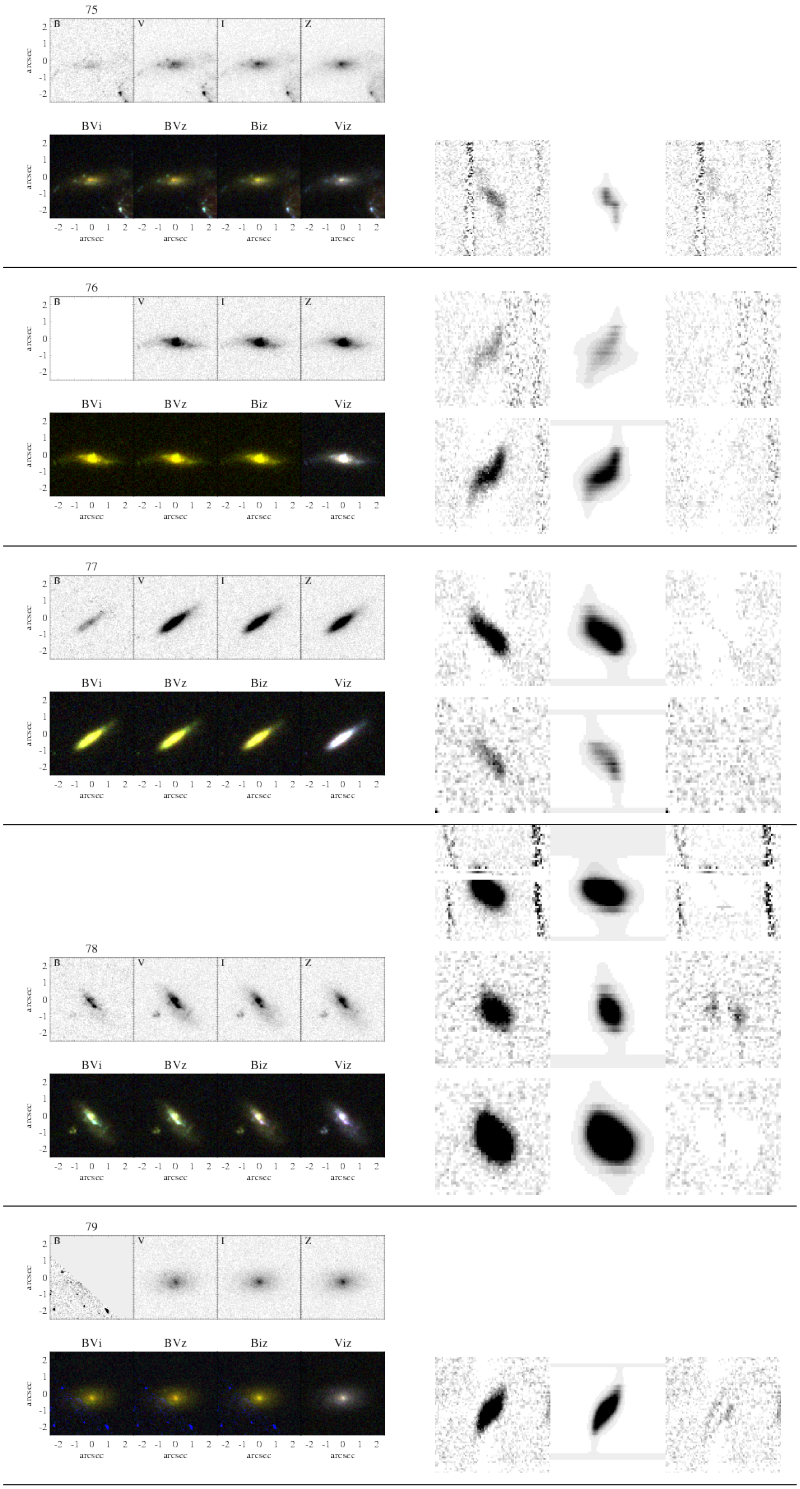
75
B
V
I
Z
BVi
BVz
Biz
Viz
arcsec
76
77
78
79

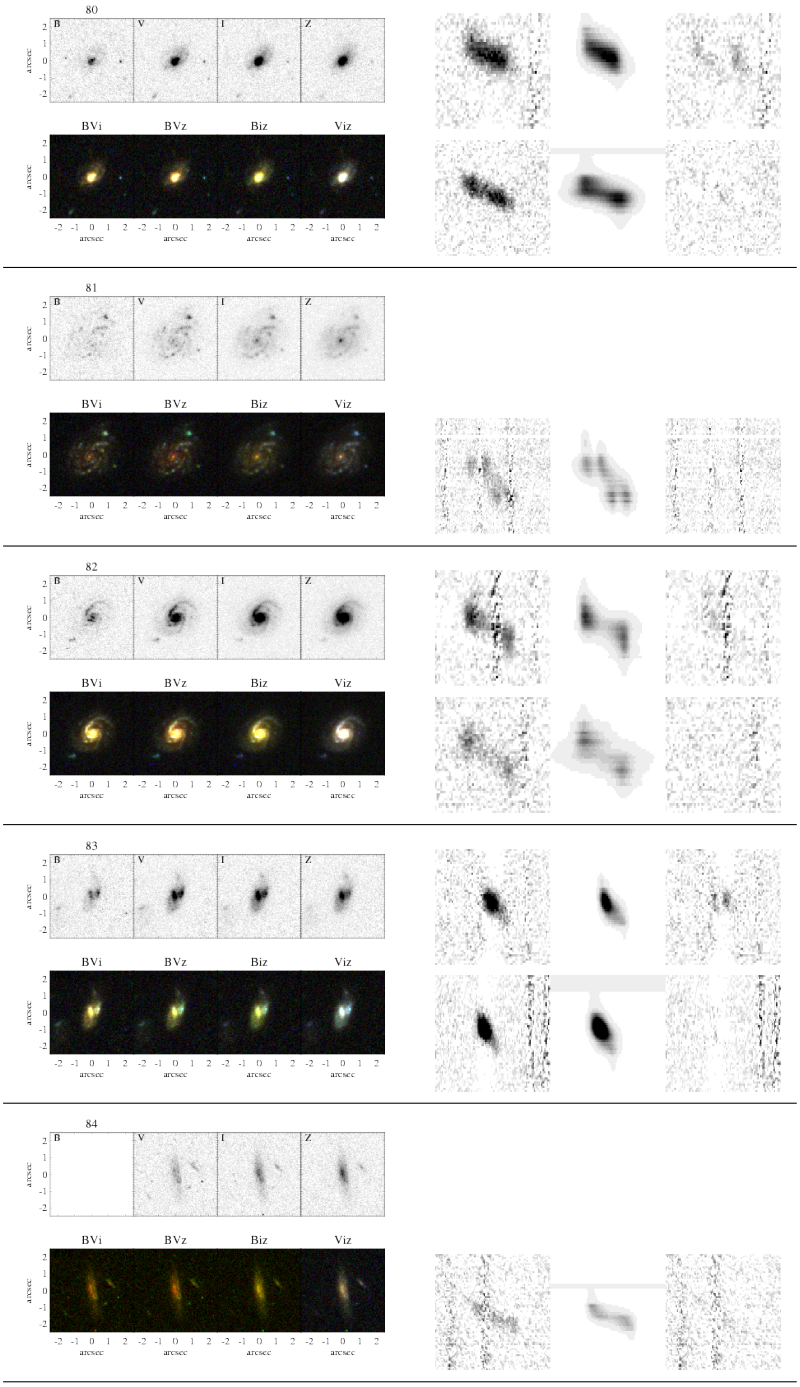
80
B
V
I
Z
BVi
BVz
Biz
Viz
arcsec
81
82
83
84

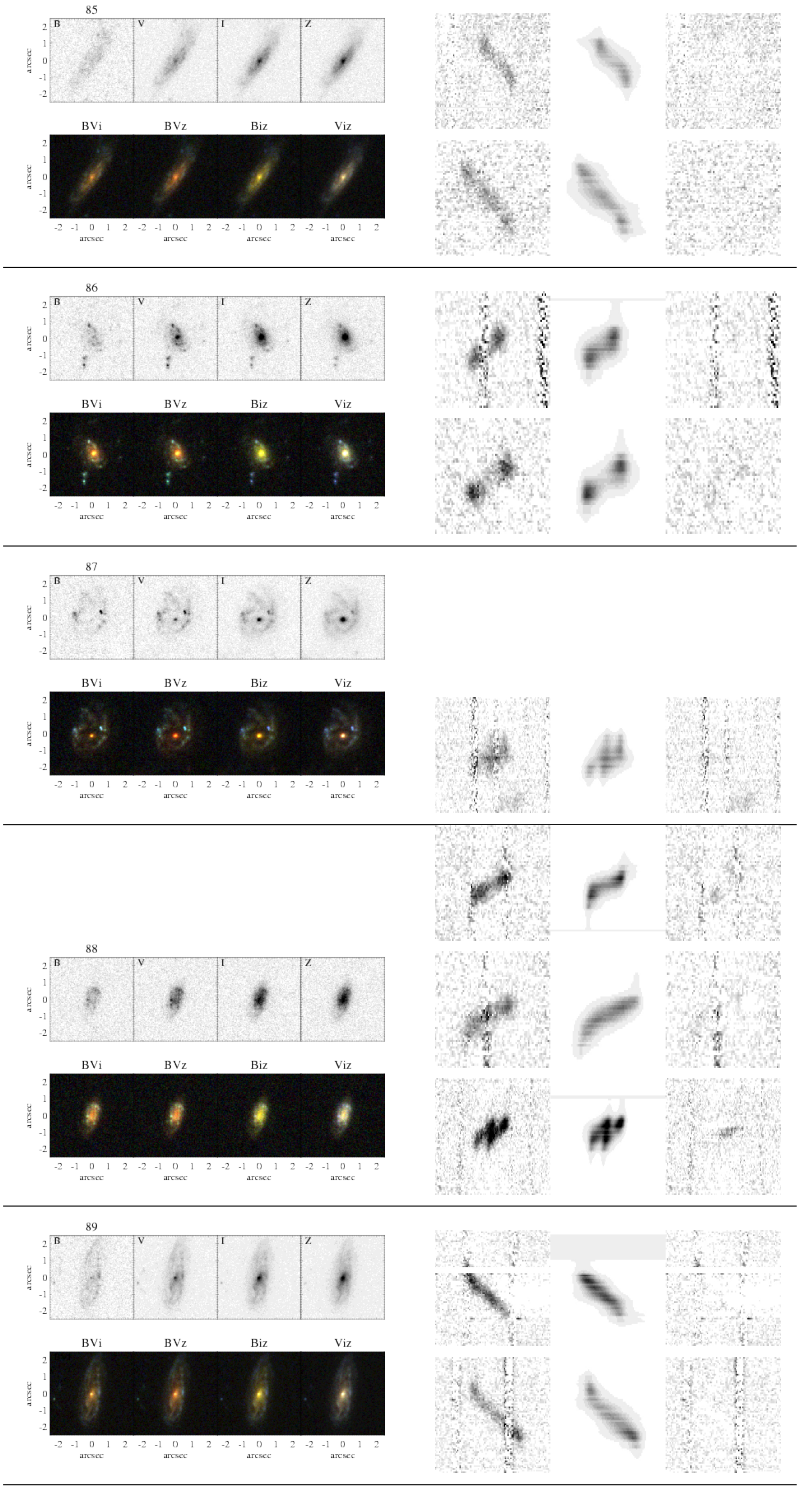
85
B
V
I
Z
BVi
BVz
Biz
Viz
arcsec
86
87
88
89

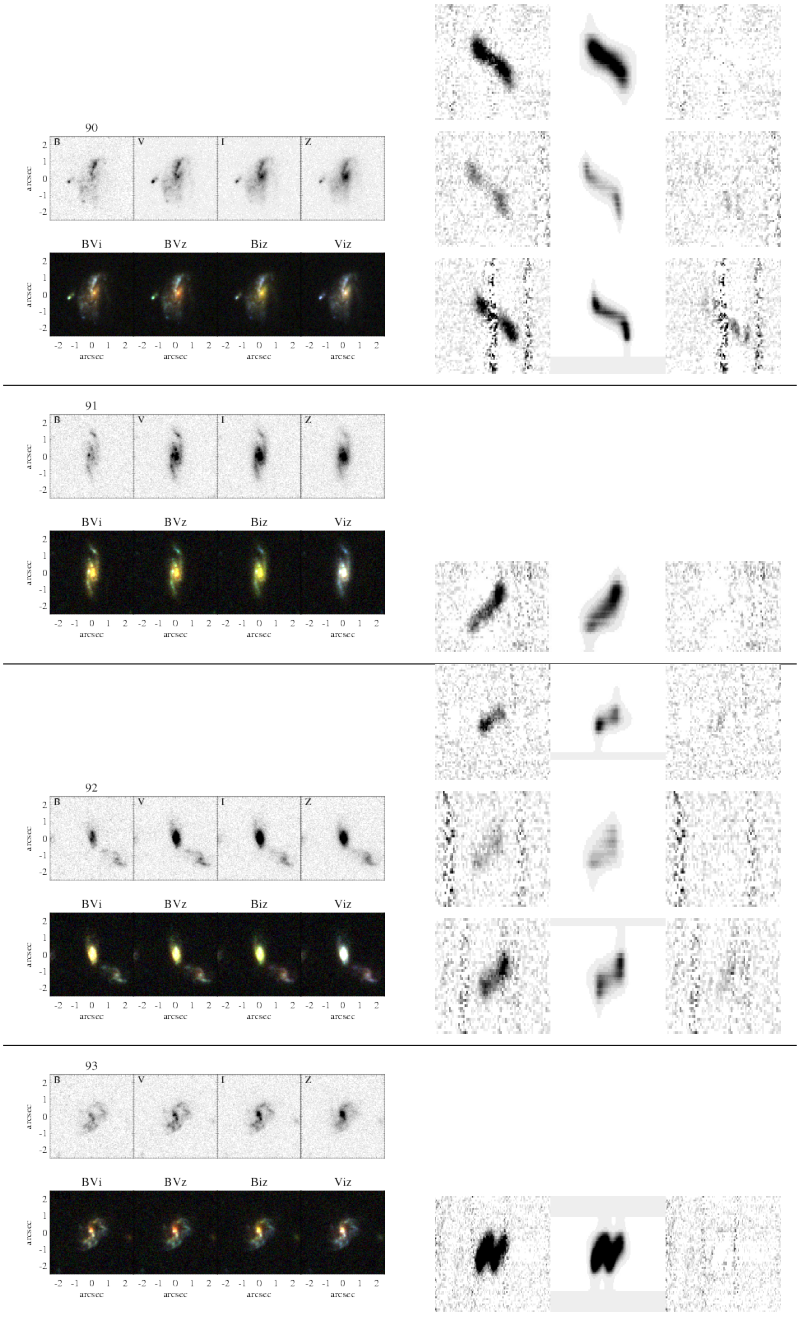
90
B
V
I
Z
BVi
BVz
Biz
Viz
arcsec
91
92
93

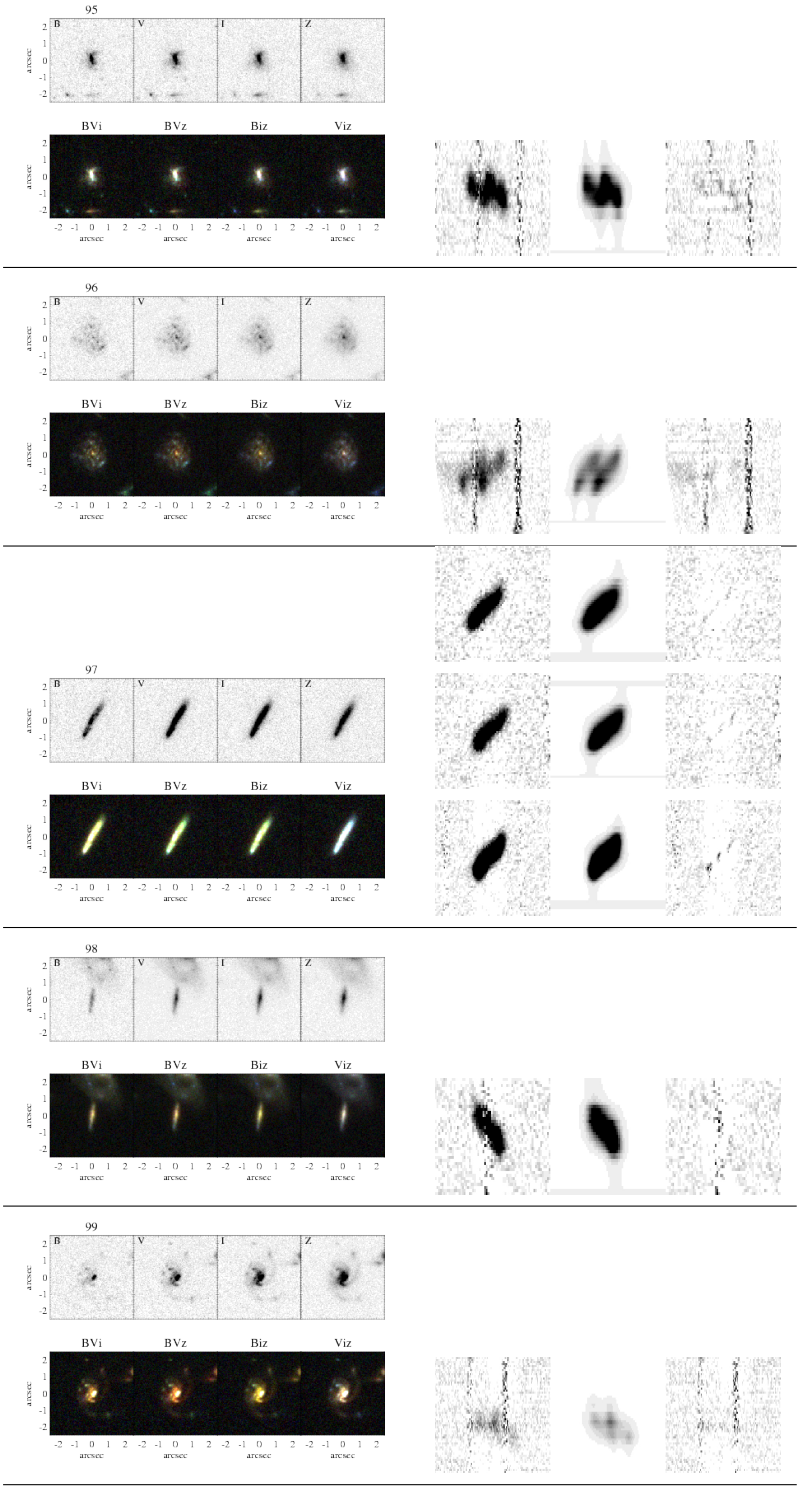
95
B
V
I
Z
BVi
BVz
Biz
Viz
arcsec
96
97
98
99

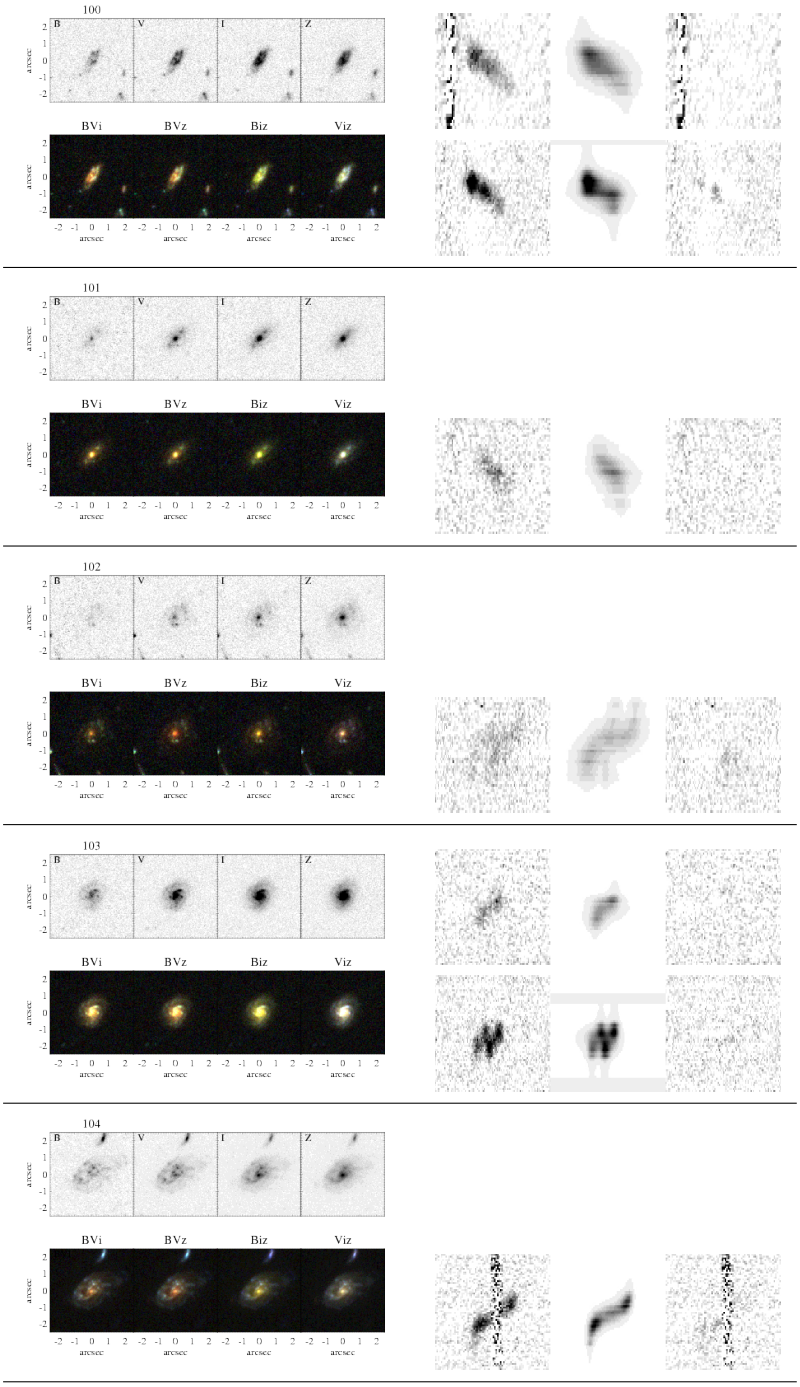
100
B
V
I
Z
BVi
BVz
Biz
Viz
arcsec
101
102
103
104

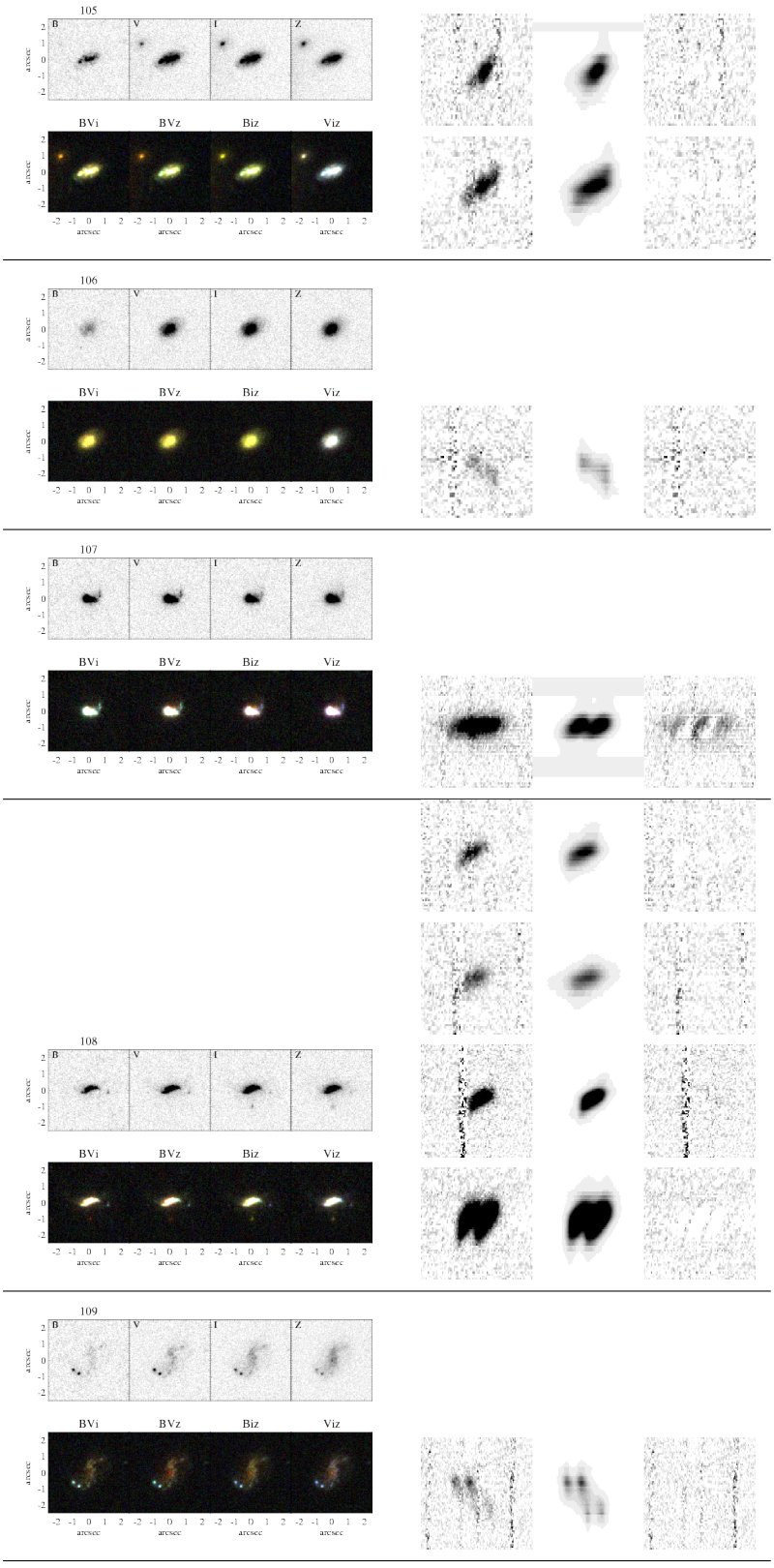
105
B
V
I
Z
BVi
BVz
Biz
Viz
arcsec
106
107
108
109

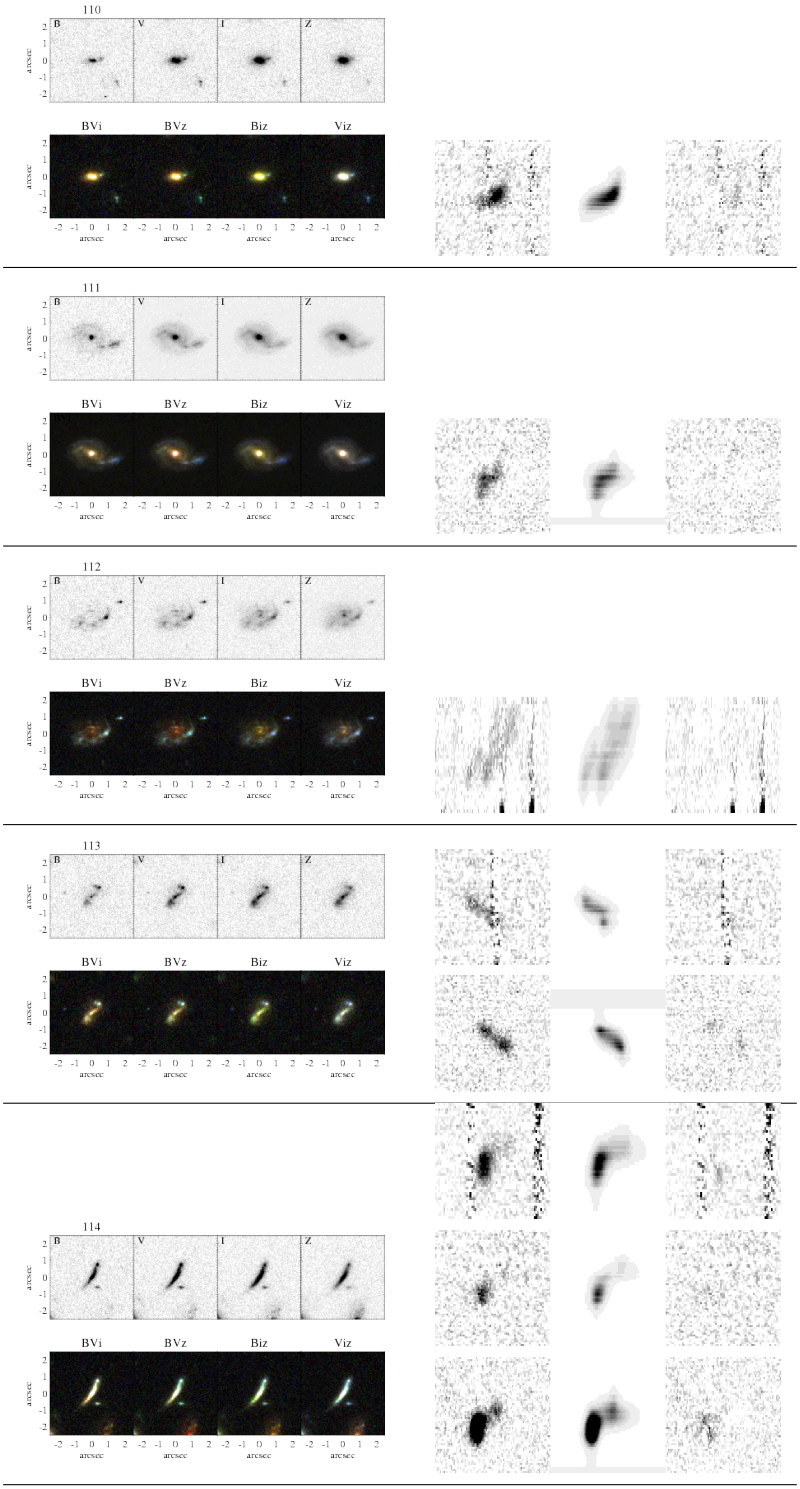
110
B
V
I
Z
BVi
BVz
Biz
Viz
arcsec
111
112
113
114

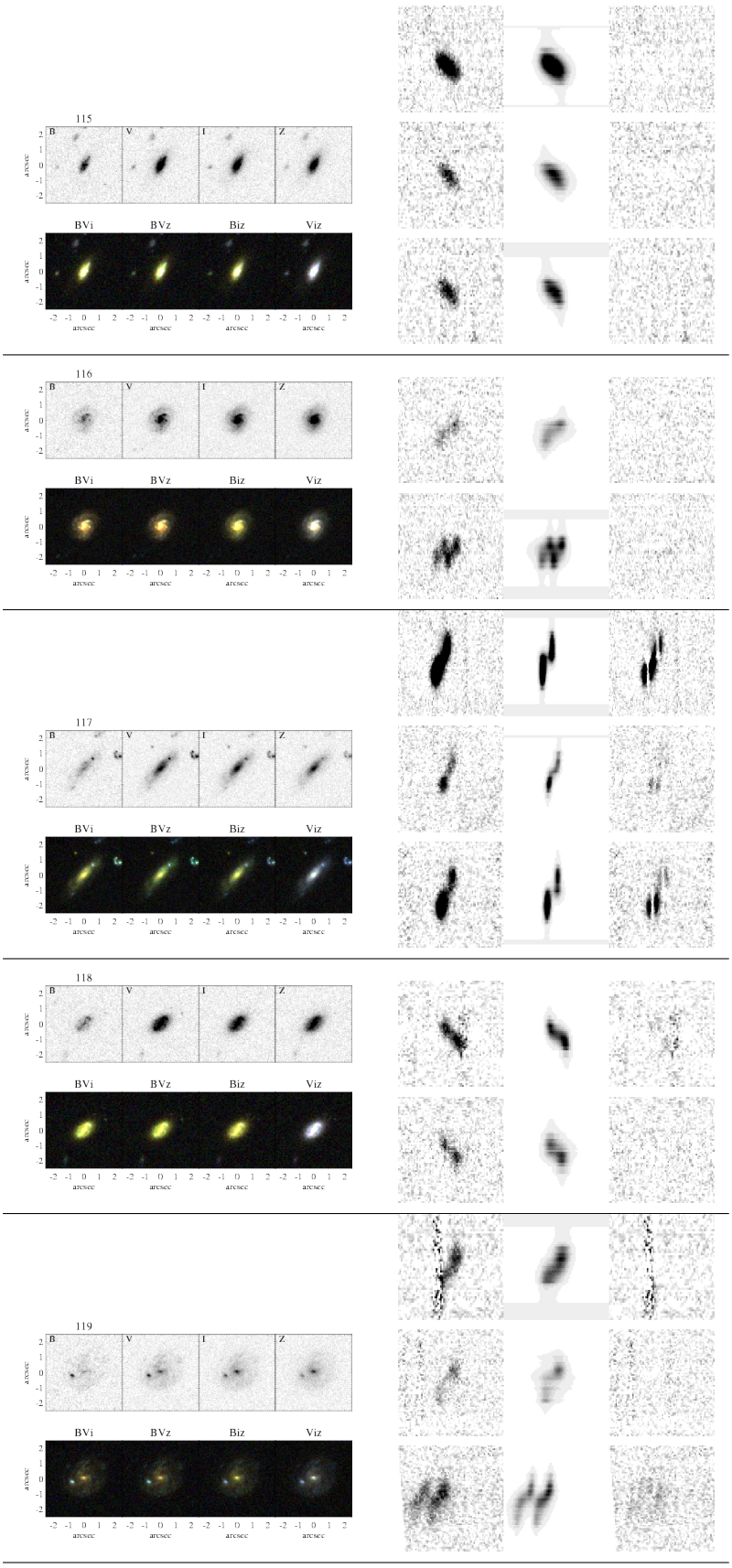
115
B
V
I
Z
BVi
BVz
Biz
Viz
arcsec
116
117
118
119

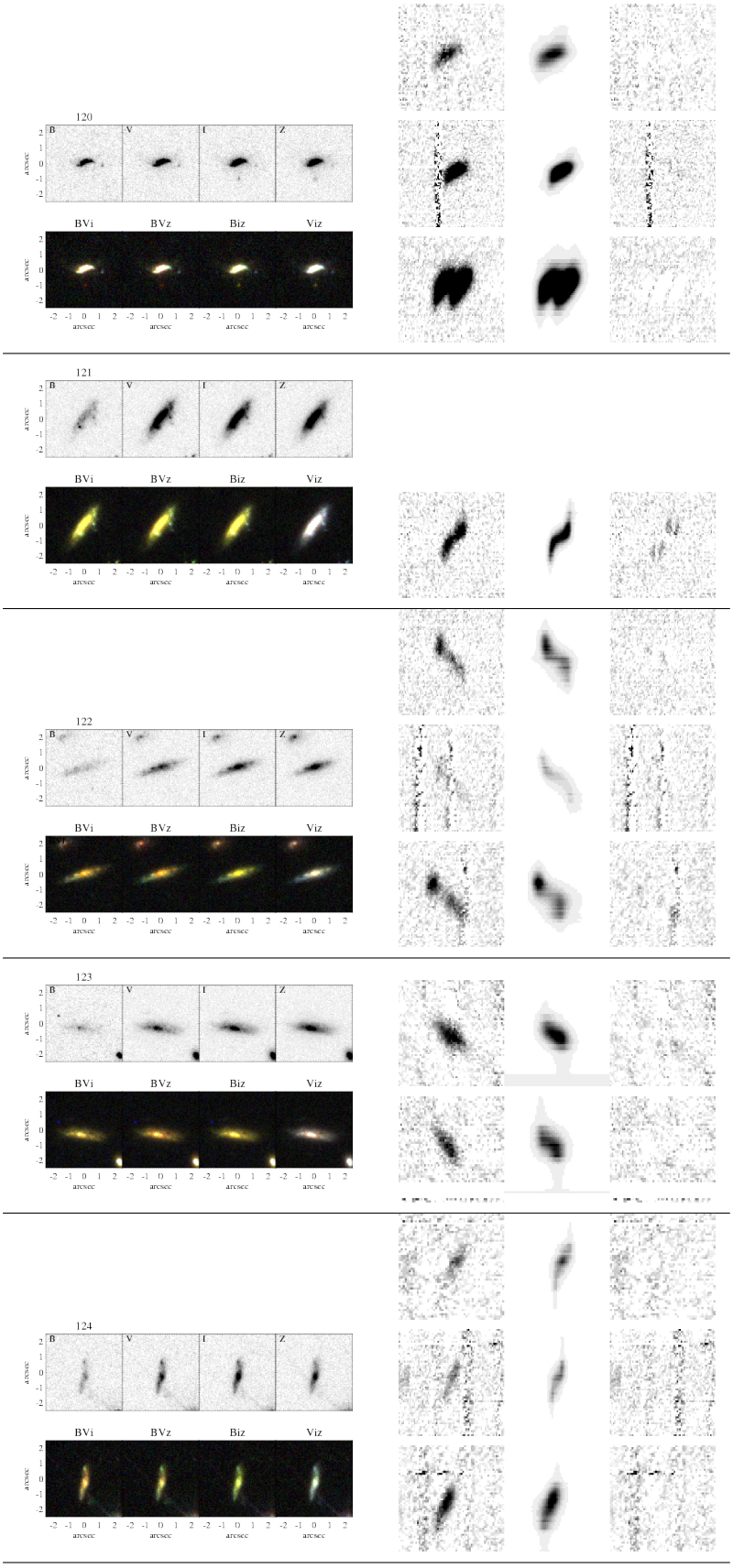
120
B
V
I
Z
BVi
BVz
Biz
Viz
arcsec
121
122
123
124

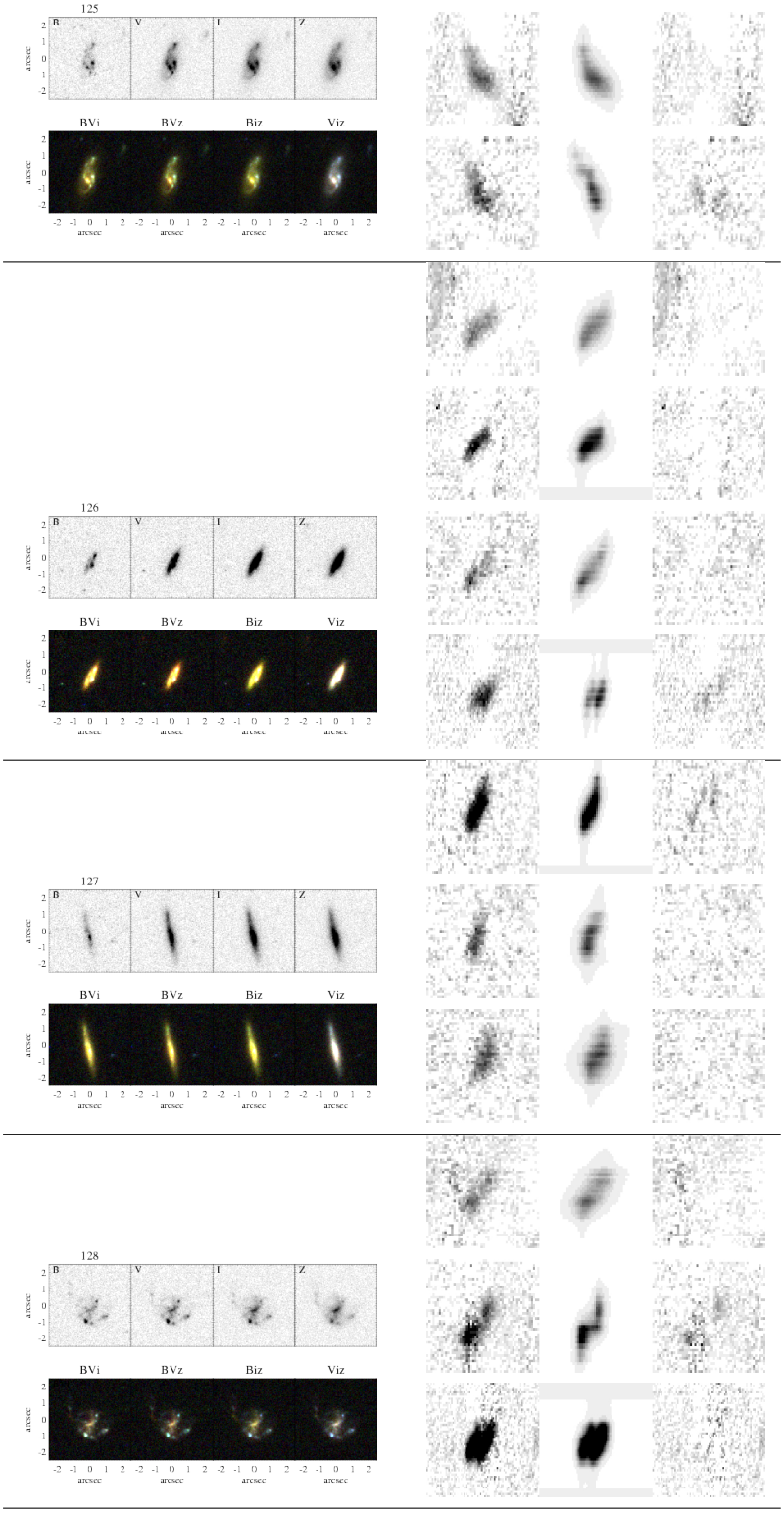
125
B
V
I
Z
BVi
BVz
Biz
Viz
arcsec
126
127
128

References

Aaronson, M., Huchra, J., & Mould, J. 1979, ApJ, 229, 1

Abraham, R. G., et al. 2007, ApJ, 669, 184

Abraham, R. G., van den Bergh, S., Glazebrook, K., Ellis, R. S., Santiago, B. X., Surma, P., & Griffiths, R. E. 1997, VizieR Online Data Catalog, 2107, 70001

Allen, R. J. 1970, A&A, 7, 330

Atkinson, N., Conselice, C. J., & Fox, N. 2007, astro-ph arXiv:0712.1316

Aumer, M., & Binney, J. J. 2009, MNRAS, 397, 1286

Balkowski, C., Bottinelli, L., Chamaraux, P., Gouguenheim, L., & Heidmann, J. 1974, A&A, 34, 43

Bamford, S. P., Aragón-Salamanca, A., & Milvang-Jensen, B. 2006, MNRAS, 366, 308

Begum, A., Chengalur, J. N., Karachentsev, I. D., & Sharina, M. E. 2008, MNRAS, 386, 138

Bell, E. F., & de Jong, R. S. 2001, ApJ, 550, 212

Bell, E. F., McIntosh, D. H., Katz, N., & Weinberg, M. D. 2003, ApJS, 149, 289

Benson, A. 2012, New Astronomy, 17, 175

Benson, A. J., Bower, R. G., Frenk, C. S., Lacey, C. G., Baugh, C. M., & Cole, S. 2003, ApJ, 599, 38

Bertin, E., & Arnouts, S. 1996, A&AS, 117, 393

Binney, J., & Tremaine, S. 1987, Galactic dynamics (Princeton University Press)

Blumenthal, G. R., Faber, S. M., Flores, R., & Primack, J. R. 1986, ApJ, 301, 27

Böhm, A., & Ziegler, B. L. 2007, in Astronomical Society of the Pacific Conference Series, Vol. 379, Cosmic Frontiers, ed. N. Metcalfe & T. Shanks, 278

Böhm, A., et al. 2004, A&A, 420, 97

Bosma, A. 1978, Ph.D. thesis, PhD Thesis, Groningen Univ., (1978)

Bouché, N., et al. 2007, ApJ, 671, 303

Bouché, N., et al. 2010, ApJ, 718, 1001

Bournaud, F., Elmegreen, B. G., & Elmegreen, D. M. 2007, ApJ, 670, 237

Brewer, B. J., et al. 2012, MNRAS, 422, 3574

Brinchmann, J., & Ellis, R. S. 2000, ApJ, 536, L77

Broadhurst, T. J., Ellis, R. S., & Shanks, T. 1988, MNRAS, 235, 827

Bruzual, G., & Charlot, S. 2003, MNRAS, 344, 1000

Buchhorn, M. 1992, Ph.D. thesis, Australian National Univ., (1992)

Bundy, K., Ellis, R. S., & Conselice, C. J. 2005, ApJ, 625, 621

Bundy, K., et al. 2006, ApJ, 651, 120

Bundy, K., Fukugita, M., Ellis, R. S., Targett, T. A., Belli, S., & Kodama, T. 2009, ApJ, 697, 1369

Capak, P., et al. 2004, AJ, 127, 180

Cappellari, M., et al. 2006, MNRAS, 366, 1126

Catinella, B., et al. 2012, MNRAS, 420, 1959

Chabrier, G. 2003, PASP, 115, 763

Chapman, S. C., Scott, D., Windhorst, R. A., Frayer, D. T., Borys, C., Lewis, G. F., & Ivison, R. J. 2004, ApJ, 606, 85

Chiu, K., Bamford, S. P., & Bunker, A. 2007, MNRAS, 377, 806

Coil, A. L., et al. 2004, ApJ, 609, 525

Cole, S., et al. 2001, MNRAS, 326, 255

Colless, M., Ellis, R. S., Taylor, K., & Hook, R. N. 1990, MNRAS, 244, 408

Conselice, C. J., Bundy, K., Ellis, R. S., Brichmann, J., Vogt, N. P., & Phillips, A. C. 2005, ApJ, 628, 160

Contini, T., et al. 2012, A&A, 539, A91

Cooper, M. C., Newman, J. A., Davis, M., Finkbeiner, D. P., & Gerke, B. F. 2012, Astrophysics Source Code Library, 3003

Courteau, S. 1992, Ph.D. thesis, California Univ., Santa Cruz.

Courteau, S. 1996, ApJS, 103, 363

Courteau, S. 1997, AJ, 114, 2402

Courteau, S., Dutton, A. A., van den Bosch, F. C., MacArthur, L. A., Dekel, A., McIntosh, D. H., & Dale, D. A. 2007, ApJ, 671, 203

Courteau, S., & Rix, H.-W. 1999a, ApJ, 513, 561

Courteau, S., & Rix, H.-W. 1999b, ApJ, 513, 561

Courtois, H. M., Hoffman, Y., Tully, R. B., & Gottlöber, S. 2012, ApJ, 744, 43

Cowie, L. L., Songaila, A., Hu, E. M., & Cohen, J. G. 1996, AJ, 112, 839

Cresci, G., et al. 2009, ApJ, 697, 115

Daddi, E., et al. 2010, ApJ, 713, 686

Dalcanton, J. J., Spergel, D. N., & Summers, F. J. 1997, ApJ, 482, 659

Davis, M., DEEP Team, & Extended Groth Strip Collaboration. 2005, in Bulletin of the American Astronomical Society, Vol. 37, American Astronomical Society Meeting Abstracts, 1299

Davis, M., et al. 2003, in Society of Photo-Optical Instrumentation Engineers (SPIE) Conference Series, Vol. 4834, Society of Photo-Optical Instrumentation Engineers (SPIE) Conference Series, ed. P. Guhathakurta, 161

de Vaucouleurs, G. 1948, Annales d'Astrophysique, 11, 247

de Vaucouleurs, G. 1959, Handbuch der Physik, 53, 311

Dekel, A., & Birnboim, Y. 2006, MNRAS, 368, 2

Dieter, N. H. 1962a, AJ, 67, 313

Dieter, N. H. 1962b, AJ, 67, 317

Djorgovski, S., & Davis, M. 1987, ApJ, 313, 59

Dressler, A., & Faber, S. M. 1990, ApJ, 354, L45

Dutton, A. A. 2012, MNRAS, 3354

Dutton, A. A., et al. 2011a, MNRAS, 410, 1660

Dutton, A. A., et al. 2011b, ArXiv e-prints

Dutton, A. A., Conroy, C., van den Bosch, F. C., Prada, F., & More, S. 2010a, MNRAS, 407, 2

Dutton, A. A., et al. 2010b, ArXiv e-prints

Dutton, A. A., & van den Bosch, F. C. 2009, MNRAS, 396, 141

Dutton, A. A., van den Bosch, F. C., Dekel, A., & Courteau, S. 2007, ApJ, 654, 27

Eke, V. R., Navarro, J. F., & Steinmetz, M. 2001, ApJ, 554, 114

Ellis, R., & Silk, J. 2009, New frontiers in cosmology and galaxy formation: challenges for the future (Cambridge University Press), 133

Ellis, R. S. 2008, Observations of the High Redshift Universe (Saas-Fee Advanced Course 36, Swiss Soc. Astrophys. Astron.), 259

Elmegreen, B. G., & Elmegreen, D. M. 2005, ApJ, 627, 632

Ewen, H. I., & Purcell, E. M. 1951, Nature, 168, 356

Faber, S. M., & Jackson, R. E. 1976, ApJ, 204, 668

Faber, S. M., et al. 2003, in Society of Photo-Optical Instrumentation Engineers (SPIE) Conference Series, Vol. 4841, Society of Photo-Optical Instrumentation Engineers (SPIE) Conference Series, ed. M. Iye & A. F. M. Moorwood, 1657

Fall, S. M., & Efstathiou, G. 1980, MNRAS, 193, 189

Fernández Lorenzo, M., Cepa, J., Bongiovanni, A., Castañeda, H., Pérez García, A. M., Lara-López, M. A., Pović, M., & Sánchez-Portal, M. 2009, A&A, 496, 389

Fernández Lorenzo, M., Cepa, J., Bongiovanni, A., Pérez García, A. M., Lara-López, M. A., Pović, M., & Sánchez-Portal, M. 2010, A&A, 521, A27

Finlator, K., & Davé, R. 2008, MNRAS, 385, 2181

Flores, H., Hammer, F., Puech, M., Amram, P., & Balkowski, C. 2006, A&A, 455, 107

Förster Schreiber, N. M., et al. 2009, ApJ, 706, 1364

Förster Schreiber, N. M., et al. 2006, ApJ, 645, 1062

Förster Schreiber, N. M., Shapley, A. E., Erb, D. K., Genzel, R., Steidel, C. C., Bouché, N., Cresci, G., & Davies, R. 2011, ApJ, 731, 65

Freedman, W. L. 1985, in IAU Colloq. 82: Cepheids: Theory and Observation, ed. B. F. Madore, 225

Freedman, W. L., et al. 2011, AJ, 142, 192

Freeman, K. C. 1970, ApJ, 160, 811

Freeman, K. C. 1993, in Astronomical Society of the Pacific Conference Series, Vol. 49, Galaxy Evolution. The Milky Way Perspective, ed. S. R. Majewski, 125

Fukugita, M., & Peebles, P. J. E. 2004, ApJ, 616, 643

Genzel, R., et al. 2008, ApJ, 687, 59

Genzel, R., et al. 2011, ApJ, 733, 101

Genzel, R., et al. 2006, Nature, 442, 786

Giavalisco, M., et al. 2004, ApJ, 600, L93

Gilmore, G. F., King, I. R., & van der Kruit, P. C. 1990, The Milky Way As A Galaxy (University Science Books, CA), 212

Giovanelli, R., & Haynes, M. P. 1983, AJ, 88, 881

Glazebrook, K., Ellis, R., Santiago, B., & Griffiths, R. 1995, MNRAS, 275, L19

Gnedin, O. Y., Weinberg, D. H., Pizagno, J., Prada, F., & Rix, H. 2007, ApJ, 671, 1115

Gnerucci, A., et al. 2011, A&A, 528, A88

Governato, F., et al. 2010, Nature, 463, 203

Governato, F., Willman, B., Mayer, L., Brooks, A., Stinson, G., Valenzuela, O., Wadsley, J., & Quinn, T. 2007, MNRAS, 374, 1479

Hammer, F., Flores, H., Elbaz, D., Zheng, X. Z., Liang, Y. C., & Cesarsky, C. 2005, A&A, 430, 115

Häussler, B., et al. 2007, ApJS, 172, 615

Haynes, M. P., & Giovanelli, R. 1984, AJ, 89, 758

Heidmann, J. 1969, Astrophys. Lett., 3, 19

Holmberg, E. 1958, Meddelanden fran Lunds Astronomiska Observatorium Serie II, 136, 1

Hopkins, A. M., & Beacom, J. F. 2006, ApJ, 651, 142

Hubble, E. P. 1925, Popular Astronomy, 33, 252

Immeli, A., Samland, M., Westera, P., & Gerhard, O. 2004, ApJ, 611, 20

Jäger, K., Ziegler, B. L., Böhm, A., Heidt, J., Möllenhoff, C., Hopp, U., Mendez, R. H., & Wagner, S. 2004, A&A, 422, 907

Jones, T., Ellis, R., Jullo, E., & Richard, J. 2010, ApJ, 725, L176

Kapferer, W., et al. 2006, A&A, 447, 827

Kassin, S. A., de Jong, R. S., & Weiner, B. J. 2006, ApJ, 643, 804

Kassin, S. A., et al. 2007, ApJ, 660, L35

Kauffmann, G., et al. 2003, MNRAS, 346, 1055

Kelly, B. C. 2007, ApJ, 665, 1489

Kelson, D. D. 2003, PASP, 115, 688

Kennicutt, R. C., Jr. 1998, ApJ, 498, 541

Kennicutt, R. C., Jr., Tamblyn, P., & Congdon, C. E. 1994, ApJ, 435, 22

Koekemoer, A. M., et al. 2011, ApJS, 197, 36

Komatsu, E., et al. 2011, ApJS, 192, 18

Kormendy, J., Drory, N., Bender, R., & Cornell, M. E. 2010, ApJ, 723, 54

Kravtsov, A. V., Klypin, A. A., Bullock, J. S., & Primack, J. R. 1998, ApJ, 502, 48

Kriek, M., et al. 2010, ApJ, 722, L64

Krist, J. 1993, in Astronomical Society of the Pacific Conference Series, Vol. 52, Astronomical Data Analysis Software and Systems II, ed. R. J. Hanisch, R. J. V. Brissenden, & J. Barnes, 536

Krist, J. E., Hook, R. N., & Stoehr, F. 2011, in Society of Photo-Optical Instrumentation Engineers (SPIE) Conference Series, Vol. 8127, Society of Photo-Optical Instrumentation Engineers (SPIE) Conference Series

Kron, R. G. 1980, ApJS, 43, 305

Kroupa, P. 2002, Science, 295, 82

Kuijken, K., & Dubinski, J. 1995, arXiv:astro-ph/9502051

Law, D. R., Steidel, C. C., Erb, D. K., Pettini, M., Reddy, N. A., Shapley, A. E., Adelberger, K. L., & Simenc, D. J. 2007, ApJ, 656, 1

Le Fèvre, O., et al. 2004, A&A, 428, 1043

Leavitt, H. S. 1908, Annals of Harvard College Observatory, 60, 87

Leroy, A. K., Walter, F., Brinks, E., Bigiel, F., de Blok, W. J. G., Madore, B., & Thornley, M. D. 2008, AJ, 136, 2782

Lilly, S. J., Cowie, L. L., & Gardner, J. P. 1991, ApJ, 369, 79

Lilly, S. J., Le Fevre, O., Hammer, F., & Crampton, D. 1996, ApJ, 460, L1

Madau, P., Ferguson, H. C., Dickinson, M. E., Giavalisco, M., Steidel, C. C., & Fruchter, A. 1996, MNRAS, 283, 1388

Madau, P., Pozzetti, L., & Dickinson, M. 1998, ApJ, 498, 106

Madore, B. F., McAlary, C. W., McLaren, R. A., Welch, D. L., Neugebauer, G., & Matthews, K. 1985, ApJ, 294, 560

Mannucci, F., Cresci, G., Maiolino, R., Marconi, A., & Gnerucci, A. 2010, MNRAS, 408, 2115

Maraston, C., Daddi, E., Renzini, A., Cimatti, A., Dickinson, M., Papovich, C., Pasquali, A., & Pirzkal, N. 2006, ApJ, 652, 85

Markwardt, C. B. 2009, in Astronomical Society of the Pacific Conference Series, Vol. 411, Astronomical Society of the Pacific Conference Series, ed. D. A. Bohlender, D. Durand, & P. Dowler, 251

Matthews, L. D., van Driel, W., & Gallagher, J. S., III. 1998, AJ, 116, 2196

McCracken, H. J., et al. 2010, ApJ, 708, 202

McGaugh, S. S. 2005, ApJ, 632, 859

McGaugh, S. S. 2011, Physical Review Letters, 106, 121303

McGaugh, S. S. 2012, AJ, 143, 40

McGaugh, S. S., Schombert, J. M., Bothun, G. D., & de Blok, W. J. G. 2000, ApJ, 533, L99

Metevier, A. J., Koo, D. C., Simard, L., & Phillips, A. C. 2006, ApJ, 643, 764

Meyer, M. J., Zwaan, M. A., Webster, R. L., Schneider, S., & Staveley-Smith, L. 2008, MNRAS, 391, 1712

Miller, S. H., Bundy, K., Sullivan, M., Ellis, R. S., & Treu, T. 2011, ApJ, 741, 115

Miller, S. H., Ellis, R. S., Sullivan, M., Bundy, K., Newman, A. B., & Treu, T. 2012, ApJ, 753, 74

Milvang-Jensen, B., Aragón-Salamanca, A., Hau, G. K. T., Jørgensen, I., & Hjorth, J. 2003, MNRAS, 339, L1

Mo, H. J., & Mao, S. 2000, MNRAS, 318, 163

Mo, H. J., Mao, S., & White, S. D. M. 1998, MNRAS, 295, 319

Moran, S. M., Miller, N., Treu, T., Ellis, R. S., & Smith, G. P. 2007, ApJ, 659, 1138

Newman, A. B., Ellis, R. S., Treu, T., & Bundy, K. 2010, ApJ, 717, L103

Newman, J. A., et al. 2012, ArXiv e-prints, arxiv:1203.3192

Noguchi, M. 1999, ApJ, 514, 77

Noordermeer, E., van der Hulst, J. M., Sancisi, R., Swaters, R. S., & van Albada, T. S. 2007, MNRAS, 376, 1513

Oke, J. B., et al. 1995, PASP, 107, 375

Oliver, S., et al. 2010, MNRAS, 405, 2279

Oort, J. H. 1940, ApJ, 91, 273

Oppenheimer, B. D., & Davé, R. 2008, MNRAS, 387, 577

Palunas, P., & Williams, T. B. 2000, AJ, 120, 2884

Peacock, J. A., & Smith, R. E. 2000, MNRAS, 318, 1144

Pease, F. G. 1918, Proceedings of the National Academy of Science, 4, 21

Peeples, M. S., & Shankar, F. 2010, ArXiv e-prints

Peng, C. 2010, in Bulletin of the American Astronomical Society, Vol. 42, Bulletin of the American Astronomical Society, 578

Perlmutter, S., et al. 1999, ApJ, 517, 565

Persic, M., & Salucci, P. 1991, ApJ, 368, 60

Pierce, M. J., & Tully, R. B. 1988, ApJ, 330, 579

Pierce, M. J., & Tully, R. B. 1992, ApJ, 387, 47

Piontek, F., & Steinmetz, M. 2011, MNRAS, 410, 2625

Pizagno, J., et al. 2005, ApJ, 633, 844

Pizagno, J., et al. 2007, AJ, 134, 945

Pontzen, A., & Governato, F. 2012, MNRAS, 421, 3464

Portinari, L., & Sommer-Larsen, J. 2007, MNRAS, 375, 913

Puech, M., et al. 2008, A&A, 484, 173

Read, J. I., & Trentham, N. 2005, Royal Society of London Philosophical Transactions Series A, 363, 2693

Retzlaff, J., Rosati, P., Dickinson, M., Vandame, B., Rité, C., Nonino, M., Cesarsky, C., & GOODS Team. 2010, A&A, 511, A50

Reyes, R., Mandelbaum, R., Gunn, J. E., Nakajima, R., Seljak, U., & Hirata, C. M. 2011a, ArXiv e-prints

Reyes, R., Mandelbaum, R., Gunn, J. E., Pizagno, J., & Lackner, C. N. 2011b, MNRAS, 417, 2347

Riess, A. G., et al. 1998, AJ, 116, 1009

Rigopoulou, D., Franceschini, A., Aussel, H., Genzel, R., Thatte, N., & Cesarsky, C. J. 2002, ApJ, 580, 789

Rix, H., Guhathakurta, P., Colless, M., & Ing, K. 1997a, MNRAS, 285, 779

Rix, H.-W., de Zeeuw, P. T., Cretton, N., van der Marel, R. P., & Carollo, C. M. 1997b, ApJ, 488, 702

Roberts, M. S. 1962, AJ, 67, 431

Roberts, M. S. 1969, AJ, 74, 859

Robertson, B., Bullock, J. S., Cox, T. J., Di Matteo, T., Hernquist, L., Springel, V., & Yoshida, N. 2006, ApJ, 645, 986

Rockosi, C., et al. 2010, in Society of Photo-Optical Instrumentation Engineers (SPIE) Conference Series, Vol. 7735, Society of Photo-Optical Instrumentation Engineers (SPIE) Conference Series

Rogstad, D. H., & Shostak, G. S. 1972, ApJ, 176, 315

Romeo, A. B., Burkert, A., & Agertz, O. 2010, MNRAS, 407, 1223

Rubin, V. C., Burstein, D., Ford, W. K., Jr., & Thonnard, N. 1985, ApJ, 289, 81

Rubin, V. C., Ford, W. K. J., & . Thonnard, N. 1980, ApJ, 238, 471

Rubin, V. C., Thonnard, N., & Ford, W. K., Jr. 1978, ApJ, 225, L107

Ryder, S. D., & Dopita, M. A. 1994, ApJ, 430, 142

Sackett, P. D. 1997, ApJ, 483, 103

Sales, L. V., Navarro, J. F., Theuns, T., Schaye, J., White, S. D. M., Frenk, C. S., Crain, R. A., & Dalla Vecchia, C. 2011, ArXiv e-prints

Salpeter, E. E. 1955, ApJ, 121, 161

Sancisi, R., & van Albada, T. S. 1987, in IAU Symposium, Vol. 117, Dark matter in the universe, ed. J. Kormendy & G. R. Knapp, 67

Schlegel, D. J. 1995, Ph.D. thesis, UNIVERSITY OF CALIFORNIA, BERKELEY.

Scoville, N., et al. 2007, ApJS, 172, 38

Seljak, U., et al. 2005, Phys. Rev. D, 71, 103515

Sérsic, J. L. 1963, Boletin de la Asociacion Argentina de Astronomia La Plata Argentina, 6, 41

Shapiro, K. L., et al. 2008, ApJ, 682, 231

Shlosman, I. 2009, in Astronomical Society of the Pacific Conference Series, Vol. 419, Astronomical Society of the Pacific Conference Series, ed. S. Jogee, I. Marinova, L. Hao, & G. A. Blanc, 39

Shostak, G. S. 1975, ApJ, 198, 527

Simard, L., & Pritchet, C. J. 1998, ApJ, 505, 96

Simard, L., et al. 2002, ApJS, 142, 1

Slipher, V. M. 1914, Lowell Observatory Bulletin, 2, 66

Somerville, R. S., et al. 2008, ApJ, 672, 776

Spergel, D. N., et al. 2007, ApJS, 170, 377

Sprayberry, D., Bernstein, G. M., Impey, C. D., & Bothun, G. D. 1995, ApJ, 438, 72

Stark, D. P., Swinbank, A. M., Ellis, R. S., Dye, S., Smail, I. R., & Richard, J. 2008, Nature, 455, 775

Stark, D. V., McGaugh, S. S., & Swaters, R. A. 2009, AJ, 138, 392

Steinmetz, M., & Navarro, J. F. 1999, ApJ, 513, 555

Strauss, M. A., & Willick, J. A. 1995, Phys. Rep., 261, 271

Tacconi, L. J., et al. 2010, Nature, 463, 781

Toomre, A. 1964, ApJ, 139, 1217

Tremaine, S., et al. 2002, ApJ, 574, 740

Trimble, V. 1995, PASP, 107, 1133

Trott, C. M., Treu, T., Koopmans, L. V. E., & Webster, R. L. 2010, MNRAS, 401, 1540

Tully, R. B., & Fisher, J. R. 1977, A&A, 54, 661

Tully, R. B., Pierce, M. J., Huang, J., Saunders, W., Verheijen, M. A. W., & Witchalls, P. L. 1998, AJ, 115, 2264

Vale, A., & Ostriker, J. P. 2004, MNRAS, 353, 189

van den Bergh, S., Abraham, R. G., Ellis, R. S., Tanvir, N. R., Santiago, B. X., & Glazebrook, K. G. 1996, AJ, 112, 359

van den Bosch, F. C. 2000, ApJ, 530, 177

Vergani, D., et al. 2012, ArXiv e-prints, astro-ph/1202.3107

Verheijen, M. A. W. 1997, Ph.D. thesis, PhD thesis, Univ. Groningen, The Netherlands , (1997)

Verheijen, M. A. W. 2001, ApJ, 563, 694

Vogt, N. P. 1995, Ph.D. thesis, CORNELL UNIVERSITY.

Vogt, N. P., Forbes, D. A., Phillips, A. C., Gronwall, C., Faber, S. M., Illingworth, G. D., & Koo, D. C. 1996, ApJ, 465, L15

Vogt, N. P., et al. 1997, ApJ, 479, L121

Wechsler, R. H., Bullock, J. S., Primack, J. R., Kravtsov, A. V., & Dekel, A. 2002, ApJ, 568, 52

Weiner, B. J., et al. 2006a, ApJ, 653, 1049

Weiner, B. J., et al. 2006b, ApJ, 653, 1027

White, S. D. M., & Rees, M. J. 1978, MNRAS, 183, 341

Williams, M. J., Bureau, M., & Cappellari, M. 2010, MNRAS, 409, 1330

Willick, J. A. 1999, ApJ, 516, 47

Wirth, G. D., et al. 2004, AJ, 127, 3121

Wolf, C., et al. 2004, A&A, 421, 913

Zhao, H., Spergel, D. N., & Rich, R. M. 1995, ApJ, 440, L13

Zibetti, S., Gallazzi, A., Charlot, S., Pierini, D., & Pasquali, A. 2012, ArXiv e-prints

Ziegler, B. L., et al. 2002, ApJ, 564, L69

Zwaan, M. A., van der Hulst, J. M., de Blok, W. J. G., & McGaugh, S. S. 1995, MNRAS, 273, L35